Progress Towards an Optimized $^{129}Xe/^{3}He$ Zeeman Maser and a Test of Boost Symmetry

by

Federico Canè

Submitted to the Department of Physics
in partial fulfillment of the requirements for the degree of

Doctor of Philosophy

at the

MASSACHUSETTS INSTITUTE OF TECHNOLOGY

February 2006

Author .....
Department of Physics
January 15, 2006

Certified by .....
Doctor Ronald L. Walsworth
Senior Lecturer on Physics, Harvard University
Senior Physicist, Smithsonian Institution
Thesis Supervisor

Certified by .....
Professor Daniel Kleppner
Lester Wolfe Professor of Physics
Thesis Supervisor

Accepted by .....
Professor Thomas J. Greytak
Chairman
Associate Department Head for Education

Progress Towards an Optimized ^{129}Xe/^{3}He Zeeman Maser and a Test of Boost Symmetry

by

Federico Canè

Submitted to the Department of Physics
on January 15, 2006, in partial fulfillment of the
requirements for the degree of
Doctor of Philosophy

Abstract

We report on a search for an annual variation of a daily sidereal modulation of the frequency difference between co-located ^{129}Xe and ^{3}He Zeeman masers that sets a stringent limit on boost-dependent Lorentz and CPT violation involving the neutron, consistent with no effect at the level of 150 nHz. In the framework of the general Standard-Model Extension, our result provides the first clean test for the fermion sector of the symmetry of spacetime under boost transformations at a level of 10^{-27} GeV [1]. We also report progress on the optimization and operation of the Harvard-Smithsonian ^{129}Xe/^{3}He dual noble gas maser. The ^{129}Xe/^{3}He maser is the first device to sustain simultaneous active maser oscillations on distinct transitions in two intermingled atomic species, and it allows sensitive differential measurement of the ^{129}Xe and ^{3}He nuclear spin-1/2 Zeeman transition frequencies [2, 3, 4]. The optimized ^{129}Xe/^{3}He maser will be used for highly sensitive tests of Lorentz and CPT symmetry.

Thesis Supervisor: Doctor Ronald L. Walsworth
Title: Senior Lecturer on Physics, Harvard University
Senior Physicist, Smithsonian Institution

Thesis Supervisor: Professor Daniel Kleppner
Title: Lester Wolfe Professor of Physics

Ai miei genitori.

Acknowledgments

I would like to thank my co-supervisor at MIT, Daniel Kleppner, for enabling me to pursue my research at the Harvard-Smithsonian Center for Astrophysics, and the other members of my thesis committee, Professors Wolfgang Ketterle and Nergis Mavalvala, for the interest shown in my research project over the years and for their feedback on this thesis. I gladly acknowledge also the characteristically brisk and yet always warm mentoring of Professor Michael Feld, my academic advisor at MIT.

I am very grateful to my research advisor, Ron Walsworth, for granting me great independence in conducting research, for seconding my inclinations and allowing me to learn from my mistakes, without ever failing to provide support and encouragement. I am equally grateful to David Phillips, the staff scientist who closely supervised much of the work presented in this thesis. David's enthusiasm for research and his willingness to discuss even the most technical issues were invaluable to me during the sometimes daunting pursuit of a precision measurement.

To David Bear and Rick Stoner I am very thankful for the excellent work done on the ^{129}Xe/^{3}He maser before I joined the group. In particular, Rick never stopped following our progress and providing useful feedback; many calculations presented in this thesis extend, or are inspired by, his previous work. I consider myself lucky to have had in the last year and a half a very capable collaborator, Alex Glenday, without whose help I would never have managed to write this thesis, while still making progress in the experiment. I also thank Alan Kostelecký, of Indiana University, for many useful discussions and Kevin Bennett, for his assistance in the realization of several prototypes in the machine shop of the Observatory.

Many current and past members of the Walsworth group helped me in several ways. Chris Smallwood, Alois Mair, and Matt Rosen were involved in the ^{129}Xe/^{3}He

maser experiment in various capacities. Marc Humphrey and Leo Tsai, besides being good colleagues, were also excellent group computer system administrators: to me they represent American efficiency and cheerfulness at their best. Our group's very international version of the Three Graces, embodied in Irina Novikova, Yanhong Xiao, and Tina Pavlin, recently brought us a new combination of professionalism, humbleness, and gentleness: thanks girls! I also enjoyed the friendly solidarity of Ross Mair, Mason Klein, and Ruopeng Wang. It was an honor when Bob Vessot and Ed Mattison, the two most senior scientists in our group, shared their anecdotes and wisdom with us. In particular, I am grateful to Ed for his kind words in hard times.

Outside of the lab I enjoyed the friendships of many, without whose company attending classes, preparing for exams, participating to debates and watching movies, or simply going out, would have been of little interest: Nikolas Meitanis, Alessandra and Alberto De Sole, and Peter Rakich are some of the dearest friends.

This work is dedicated to my parents and it is only a small token of recognition of their encouragement and love. My brother's growing family constantly inspired great warmth from afar, while, in Cambridge, Rada's smile was always, to me, the brightest sun.

Contents

Chapter 1

Introduction

We do not usually think that the energy levels of an atom depend on its orientation with respect to the "fixed stars," or on the velocity of the laboratory. Our intuition is based on the belief that nature is invariant under Lorentz transformations (i.e., rotations and velocity boosts). This belief pervades most modern descriptions of nature, from the standard model of particle physics to general relativity. Experimental investigations of the validity of Lorentz symmetry therefore provide valuable tests of modern theoretical physics. This thesis presents such a test as well as progress towards improved experimental sensitivity.

Atomic physics experiments are often in a unique position to provide world class tests of fundamental theories. In particular, the ^{129}Xe/^{3}He maser has an absolute energy sensitivity allowing us to detect daily modulations of its Zeeman levels as small as 10^{-22} eV (10^{-31} GeV in the units typically used in particle physics). This characteristic makes it ideally suited to test Lorentz invariance.

1.1 The ^{129}Xe/^{3}He Maser

The ^{129}Xe/^{3}He maser was first proposed by Walsworth in 1991 and has been developed at the Harvard-Smithsonian Center for Astrophysics, initially in collaboration with researchers at the University of Michigan [2, 3, 65]. A schematic diagram of this device is given in Fig. 1-1 and typical system parameters are listed in Tab. 1.1.

In the ^{129}Xe/^{3}He maser, co-located ensembles of ^{129}Xe and ^{3}He atoms at pressures of few hundred Torr are held in a double-chamber glass cell placed in a homogeneous magnetic field of a few gauss. Both species have spin-1/2 nuclei and the same sign nuclear magnetic dipole moment, but no higher-order electric or magnetic nuclear multipole moments. In one chamber of the glass cell (pump bulb) the noble gas atoms are nuclear-spin-polarized by spin-exchange collisions with optically-pumped Rb vapor [5]. The noble gas atoms can diffuse into the second chamber (maser bulb) located at the center of a single pick-up coil connected to a circuit resonant both at the ^{3}He and ^{129}Xe Zeeman frequencies (both on the order of a few kHz). Initially, spontaneous and thermal transitions in the maser bulb excite the resonant circuit which in turn stimulates emission from other incoming atoms. After depositing their energy in the resonant circuit the noble gas atoms diffuse back to the pump bulb where they are re-polarized by spin-exchange. Thus, active maser oscillation of both species can continue indefinitely. One species may then serve as a co-magnetometer for the other, by locking its frequency to a stable reference through adjustment of the applied field.

Operation of the two species maser as a stable oscillator requires a two chamber design to separate the spin-exchange pump and maser operations. Different Rb vapor densities are obtained in the two regions by maintaining a strong temperature differential. The pump bulb is kept at a temperature of $T_P \approx 114°$ C, while the maser

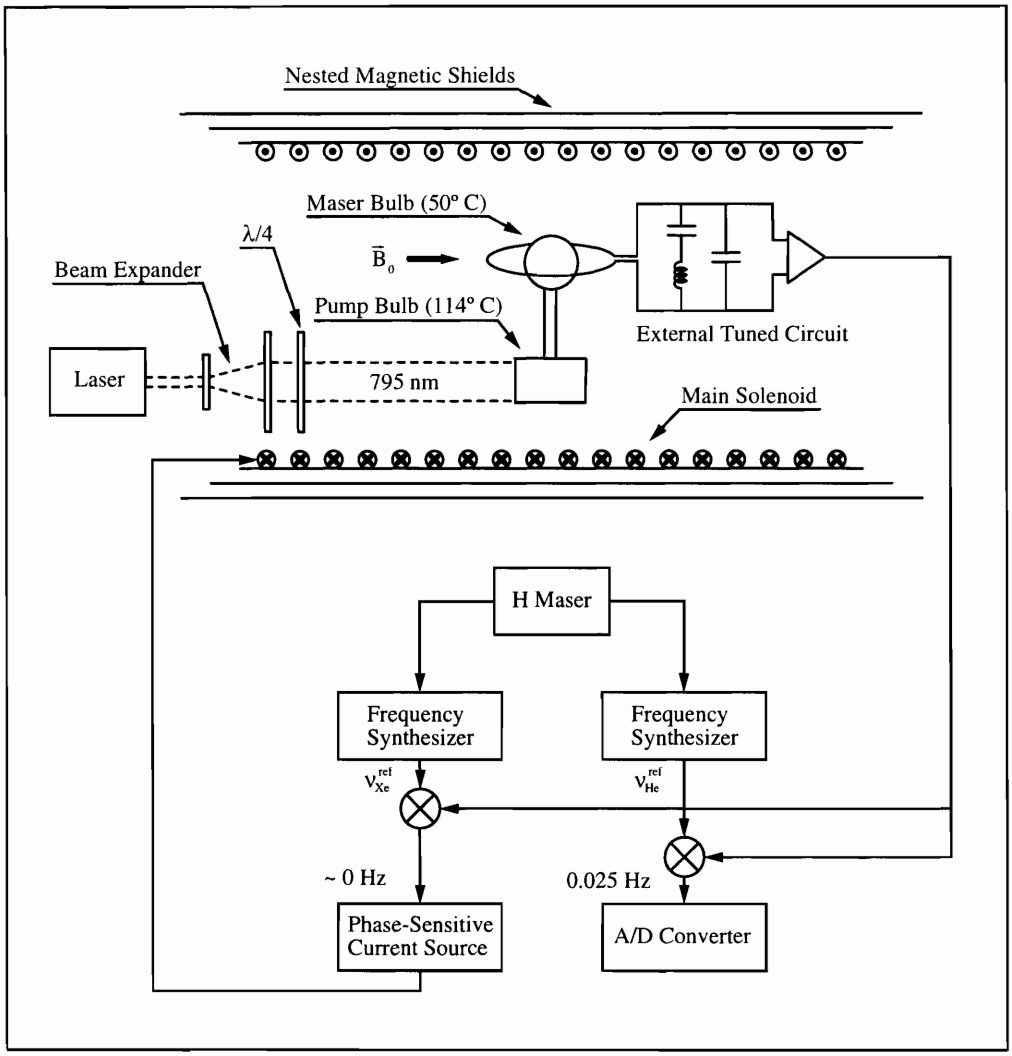

Figure 1-1: Schematic diagram of the $^{129}Xe/^{3}He$ Zeeman maser.

bulb is kept at $T_M \approx 50°$ C, inducing a suppression of two orders of magnitude in the Rb density between the first and the second bulb (see Tab. 1.1). The Rb density differentiation is crucial because the ^{129}Xe-Rb spin-exchange rate is two orders of magnitude greater than the ^{3}He-Rb spin-exchange rate. Thus, in a single bulb a Rb density adequate to maintain a ^{3}He population inversion able to sustain ^{3}He maser oscillation would also induce excessive de-coherence of the ^{129}Xe ensemble and degrade ^{129}Xe maser oscillation. Moreover, the frequency stability in a single-chamber ^{129}Xe/^{3}He maser would be severely limited by noble gas Zeeman frequency shifts induced by collisional contact hyperfine interaction with optically pumped Rb. In the two chamber design the high Rb density of the pump bulb favors spin-exchange optical pumping, while the low Rb density in the maser bulb prevents unwanted Rb-induced spin-exchange relaxation and frequency shifts from adversely affecting either maser.

Electron spin polarization is induced in Rb via optical pumping [6]. We use a laser tuned at the Rb D_1 transition ($\lambda \approx 795$ nm), whose light is circularly polarized and focused onto the pump bulb. Approximately 80 Torr of N_2 gas in the cell promote collisional de-excitation of the optically pumped Rb atoms, thus preventing radiation trapping, which would limit the efficiency of the optical pumping process [6]. Spin-exchange collisions between the ^{129}Xe and ^{3}He atoms and optically-pumped Rb vapor [5, 7] polarize the noble gas nuclei.

A typical maser cell consists of a roughly cylindrical pump bulb joined by a straight transfer tube to a roughly spherical maser bulb. The inner surface of the cell is treated with a silane coating to minimize spin relaxation of the ^{129}Xe atoms at the walls [8]. Due to the generally weak interactions of noble gas atoms during atomic collisions, the ^{3}He and ^{129}Xe ensembles can have long Zeeman coherence (T_2) times, provided that they are kept in a homogeneous magnetic field. For this purpose

Description	Parameter	^{3}He	^{129}Xe	Units
Gyromagnetic ratio	γ_{ng}	2π 3,243.72	2π 1,177.79	Hz/G
Operating frequency	ν_{ng}	19,607	7,119	Hz
Polarization lifetime	T_1^*	6,000	370	s
Coherence time	T_2^*	88	229	s
Maser signal amplitude		21	25	μV
Maser power	W_{ng}	30×10^{-9}	62×10^{-9}	erg/s
Fill pressure	$\mathcal{P}_{ng,Fill}$	600	30	Torr
N_2 fill pressure	$\mathcal{P}_{N_2,Fill}$	80		Torr
Pump bulb temperature	T_P	114		$^\circ$ C
Maser bulb temperature	T_M	50		$^\circ$ C
Pump bulb Rb density	[Rb]	1.4×10^{13}		cm^{-3}
Maser bulb Rb density	$[\mathrm{Rb}]_M$	1.5×10^{11}		cm^{-3}
Static magnetic field	B_0	6.04		G
Pump bulb volume	V_P	6		cm^3
Maser bulb volume	V_M	4		cm^3
Transfer tube cross-section	$A_{tt} = \pi\rho_0^2$	$\pi\ 0.2^2 = 0.13$		cm^2
Transfer tube length	L	3		cm

Table 1.1: Typical parameters characterizing the ^{129}Xe/^{3}He maser.

the ^{129}Xe/^{3}He maser is housed inside three concentric cylindrical magnetic shields screening the experiment from inhomogeneous DC magnetic fields and ambient RF noise. A stable magnetic field is used to split the noble gas Zeeman sublevels. This field is created with a single-layer solenoid located inside the magnetic shields together with field-gradient correction coils. The resultant field homogeneity ($\nabla B \sim$ 20 μG/cm for $B_0 \approx 1.5$ G) allows spin coherence relaxation times (T_2) of hundreds of seconds in the ^{129}Xe and ^{3}He ensembles, which are a prerequisite for stable maser operation.

The ^{129}Xe and ^{3}He maser signals from the pick-up coil (typically with amplitudes of few μV) are amplified and sent to a pair of digital lock-in detectors. Active feedback to the solenoid's magnetic field locks the phase of one of the two masers (typically ^{129}Xe) to a reference signal (ν_{Xe}^{ref} in Fig. 1-1), thereby isolating the experiment from common-mode systematic effects, such as stray magnetic field fluctuations.

Excellent absolute frequency stability is achieved in the free-running maser. For instance, Zeeman frequency measurements with sensitivity of approximately 300 nHz are possible with averaging intervals of about 2,000 s.

All reference frequencies used in the experiment are derived from the same hydrogen maser clock. This eliminates phase and frequency shifts among the reference oscillators. Even more importantly, the magnetic field independent hydrogen maser frequency is unaffected by the Lorentz and CPT violating interactions that we wish to detect with our masers. Thus, the hydrogen maser is the stable reference clock in our clock-comparison experiment, as we see in the next section.

1.2 Testing Lorentz and CPT Invariance

The ^{129}Xe/^{3}He maser is used to monitor the relative phases and Larmor frequencies of the co-located ^{3}He and ^{129}Xe masers as the laboratory reference frame is rotated and velocity-boosted with respect to the distant stars thanks to the movement of the Earth. The ^{129}Xe/^{3}He maser is usually operated with the ^{129}Xe maser phaselocked and the ^{3}He maser free-running. The Lorentz-invariance signature that we look for is a sidereal modulation of the ^{3}He frequency.

Our atomic clock comparisons are motivated by the Standard-Model Extension (SME) developed by Kostelecký and others [9, 10, 11, 12]. The SME parameterizes arbitrary coordinate-independent Lorentz violation. Since violation of CPT symmetry (the product of Charge conjugation, Parity inversion, and Time reversal) must come with Lorentz violation [13, 14], the SME also parameterizes general CPT violation. Observable Lorentz and CPT violation could be a remnant of Planck-scale physics. One attractive origin is spontaneous Lorentz breaking in a fundamental theory [15, 16, 17, 18, 19], but other sources are possible [20].

The SME provides a widely-accepted formalism for the interpretation and comparison of experimental searches for violations of Lorentz and CPT symmetry. The SME and its predictions for the ^{129}Xe/^{3}He maser are described in detail in Chapter 3. Here we anticipate some results.

The leading-order energy shift due to Lorentz violations for a fermion, f, in state $|J, m_J\rangle$ is a sum of two terms[1] [21],

$$\langle J, m_J | h^f | J, m_J \rangle = \widehat{m}_J E_d^f + \widetilde{m}_J E_q^f. \tag{1.1}$$

In this expression, $\widehat{m}_J$ and $\widetilde{m}_J$ are given by

$$\widehat{m}_J = \frac{m_J}{J}, \qquad \widetilde{m}_J = \frac{3m_J^2 - J(J+1)}{3J^2 - J(J+1)}. \tag{1.2}$$

The dipole and quadrupole energy shifts E_d^f and E_q^f are independent of m_J and depend on Lorentz-violating terms introduced by the SME. Note that for spin-1/2 fermions in states of vanishing angular momentum ($l = 0$), the quadrupole energy shift always vanishes. This is the case in the clock transitions that we compare, those of a hydrogen maser and of a spin-1/2 Zeeman maser.

In the case of the hydrogen maser, there are two Lorentz-violating perturbations, h^p and h^e, acting on the proton and on the electron respectively. Since both the proton and the electron in the clock hyperfine levels $|1, 0\rangle$ and $|0, 0\rangle$ (depicted in Fig. 1-2 (a)) are in a superposition of their spin-up and spin-down states, the expectation value of h^p and h^e vanishes for both levels and the hydrogen maser frequency is unaffected by the Lorentz-violating contributions.[2]

[1]Here, $\vec{J}$ is the total angular momentum of the fermion f, not the angular momentum of the system to which it may belong.

[2]As Fig. 1-2 (a) suggests, the $|1, \pm 1\rangle$ levels of the hydrogen maser are affected by the Lorentz-violating interactions described by the SME. A Lorentz symmetry test searching for sidereal vari-

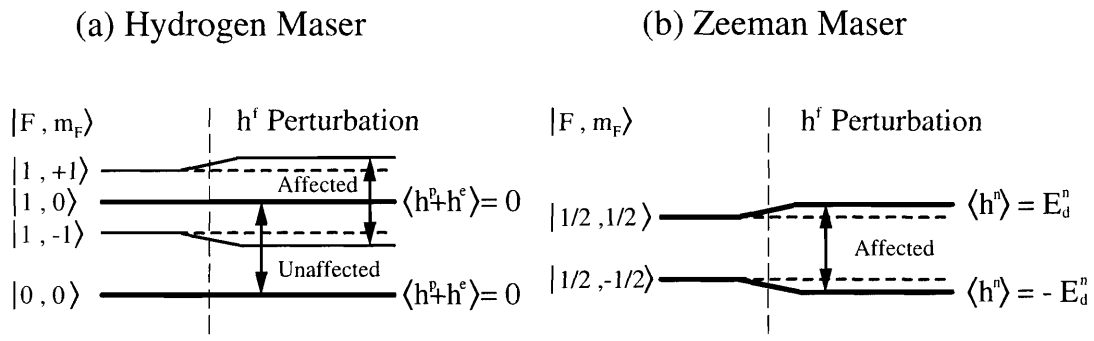

Figure 1-2: Clock transitions for the hydrogen maser and for a spin-1/2 Zeeman maser in the presence of a magnetic field and a Lorentz-violating perturbation h^f given by Eq. (1.1).

The same is not true for the ^{129}Xe and ^{3}He Zeeman maser frequencies. In both isotopes the unpaired neutron is assumed to carry the entire angular momentum of the nucleus and be in a bound $s_{1/2}$ wave. The Lorentz-violating perturbation for the neutron, h^n, produces equal and opposite energy shifts for the two Zeeman levels, as shown in Fig. 1-2 (b), thus affecting the Larmor precession frequency.

For a neutron at rest the SME predicts the following effective hamiltonian,

$$h^n = -2\,\vec{I}\cdot\vec{b}, \tag{1.3}$$

where $\vec{I}$ is the spin operator of the neutron and $\vec{b}$ indicates a combination of SME coefficients that vanishes if Lorentz-symmetry is exact. The SME assumes that $\vec{b}$ is the spatial part of a four-vector b_μ, assumed to be static in the Sun's rest frame where its components are: $b_\Sigma = \{b_T, b_X, b_Y, b_Z\}$. In the laboratory, $b_i = \Lambda_i{}^\Sigma\, b_\Sigma$. $\Lambda_\mu{}^\Sigma$ is the Lorentz transformation from the Sun's system of space-time coordinates to the laboratory system and depends on the sidereal time, T, on the Earth's rotation

ations in this transition was carried out in our group [22]. Note also that in the present treatment we have disregarded spin independent, Lorentz-violating frequency shifts that would shift all hyperfine levels equally producing no observable results in the maser frequency. A more accurate treatment of this topic is presented in Ref. [23].

and revolution frequencies, $\omega_\oplus$ and $\Omega_\oplus$, and on the velocity $\beta_\oplus \simeq 9.9 \times 10^{-5}$ of the Earth on its orbit.

The perturbation h^n acquires a time dependence through ${\Lambda_\mu}^\Sigma$. The ^{129}Xe and ^{3}He Zeeman levels are shifted equally,[3] but since the gyromagnetic ratios, γ_{ng}, for the two species are different (see Tab. 1.1) and the ^{129}Xe maser is used as a co-magnetometer, the free-running ^{3}He maser has a time dependence that can be written as follows:

$$\delta\nu_{He} = \nu_{He} - \frac{\gamma_{He}}{\gamma_{Xe}}\nu_{Xe} = \delta\nu_X \ \sin\ \omega_\oplus T + \delta\nu_Y \ \cos\ \omega_\oplus T, \tag{1.4}$$

where

$$\begin{aligned} \delta\nu_X &= k\ (\lambda_s + \beta_\oplus(\Lambda_{ss}\sin\Omega_\oplus T + \Lambda_{sc}\cos\Omega_\oplus T)), \\ \delta\nu_Y &= k\ (\lambda_c + \beta_\oplus(\Lambda_{cs}\sin\Omega_\oplus T + \Lambda_{cc}\cos\Omega_\oplus T)). \end{aligned} \tag{1.5}$$

$k = -8.46 \times 10^{32}$ nHz/GeV is given by the SME [24, 25] and the coefficients λ_c, λ_s, Λ_{ss}, $\Lambda_{sc}, \ldots$ are Sun-frame Lorentz-violating coefficients.[4]

In Chapter 3 we show that our experiments put a bound on $\Lambda_{ss}, \Lambda_{sc}, \Lambda_{cs}, \Lambda_{cc} < 10^{-27}$ GeV, while our previous experiments [24, 25], bounded $\lambda_s, \lambda_c < 10^{-31}$ GeV. Significant improvements on both bounds should be possible using the optimized ^{129}Xe/^{3}He maser described in this thesis.

[3]The valence neutron is treated in the same way for both species [21], therefore the energy shift is the same.

[4]These coefficients are a function of b_Σ, as well as other SME coefficients arising from the motion of the valence neutron in its bound nuclear $s_{1/2}$ state.

1.3 Thesis Organization

This thesis is organized in six chapters. After an introductory chapter we report, in roughly chronological order, recent work on the ^{129}Xe/^{3}He maser.

In Chapter 2 we introduce spin-exchange optical pumping, the mechanisms responsible for polarization relaxation, and we solve the maser equations for a single bulb Zeeman maser. In this chapter, dedicated to theoretical principles, we chose to neglect the complications arising from the diffusive transport of polarization between pump bulb and maser bulb and to emphasize instead the analogies with standard maser theory. At the end of the chapter we review the techniques used to characterize instabilities and to assess the performance of our masers as precision oscillators. We then discuss the sources of noise that fundamentally limit the frequency stability of the ^{129}Xe/^{3}He maser and with it its Lorentz-invariance-violation sensitivity.

Chapter 3 deals with our experimental result obtained with the previous ^{129}Xe/^{3}He maser: the first test of boost invariance in the fermion sector (reported in Appendix A). The beginning of the chapter is meant as a preface to our result and an introduction to the SME. Our aim is to illustrate how Lorentz-violating interactions affecting fermions may produce observable effects in complex systems, such as the ^{129}Xe/^{3}He maser. We then compare and contrast our boost test to a classical test of Lorentz violation in electrodynamics: the Kennedy-Thorndike experiment. In the later part of the chapter, we show that our Zeeman masers are effectively NMR gyroscopes and as such are affected by frequency shifts induced by the Earth's rotation. These shifts however are constant in time for a maser at rest in the laboratory and thus a sidereal frequency modulation observed in our masers would be unequivocal sign of physics beyond the standard model. Finally, we summarize advantages and disadvantages of operating our ^{129}Xe/^{3}He maser on

a rotating platform.

Chapter 4 is dedicated to the design studies carried out mostly before the construction of the new $^{129}Xe/^{3}He$ maser. The chapter begins with an assessment of the frequency stability and Lorentz-invariance-violation sensitivity of the previous maser. We discuss its known limitations, particularly the layout of the oven and the temperature control system, and we present possible design improvements. We then introduce an extensive model of optical pumping (considering narrow and broad-band light sources), polarization transport, and maser dynamics in the double-bulb cell. This model illustrates some of the $^{129}Xe/^{3}He$ maser's complexity and was used in the process of cell geometry and gas fill pressure optimization. Next, we attempt to understand the role that different diffusion coefficients and interaction times for the two noble gas species may play in causing imperfect co-magnetometry. At the end of this chapter we show that by choosing a spherical geometry for the maser bulb we can neglect self-interaction in our masers.

In Chapter 5 we describe the design and construction of the new $^{129}Xe/^{3}He$ maser. We review the new oven design with an improved blown air temperature control of the maser cell and we summarize the procedure for making $^{129}Xe/^{3}He$ maser cells. We then discuss the characteristics and stabilization schemes for the two lasers which are currently under test: a half Watt narrow-band laser and the 30 W, broad-band laser diode array (LDA) formerly used. Next, we review the magnetic field environment: magnetic shielding, main field characteristics, field stabilization, and various attempts to confine the maser action to the maser bulb region. We conclude the chapter by describing in detail the signal detection system.

The final chapter is dedicated to the current system performance. We provide the operational details of the temperature control system, of the laser stabilization schemes, and we assess their performance. We describe the methods for measuring

the primary parameters of the $^{129}Xe/^{3}He$ maser and we compare our observations with the predictions of our modified Bloch theory. We then study the effects of peripheral pick-up coil fields on the maser frequency. The importance of peripheral fields was discovered during our first experimental study of co-magnetometry imperfection, which is described next. Finally, we present an assessment of maser frequency stability and current sensitivity to Lorentz invariance violation.

Chapter 2

Theoretical Principles

A maser uses the stimulated emission of radiation by excited atoms or molecules to generate or amplify coherent monochromatic electromagnetic radiation in the "long wavelength" (audio to microwave) range. The radiation emitted from the noble gas atoms in our masers is in the audio-frequency range and our spin 1/2 masers have all of the characteristics described by standard maser theory, as we briefly show in this chapter. We begin by introducing spin-exchange optical pumping, which is used to achieve population inversion (i.e., a population imbalance in which more atoms are in the highest energy state). We then present the relaxation mechanisms that tend to re-establish thermal equilibrium between populations and coherences of the two Zeeman levels. Next, we show how the maser equations of motion take a simple form if, in analogy with the well known Bloch vector, we employ an average spin polarization vector to characterize the whole masing ensemble.

For simplicity, we defer until Ch. 4 the treatment of the complications arising from the details of the geometry of our maser. Here, we will simply assume without loss of generality that a given, steady-state flux of polarized atoms enters the maser bulb. As in standard maser theory, the flux of polarized atoms must exceed a

threshold value to sustain continuous maser oscillation. We also show that our tank circuit behaves like a resonant cavity: It provides the feedback necessary to stimulate emission; a mistuning of the circuit's resonant frequency from the atomic Zeeman frequency induces cavity pulling of the maser frequency; and in steady state the resistive circuit dissipates the energy that the atoms gain during the initial state-preparation.

In the last section of the chapter we review the techniques used throughout this thesis to characterize various types of instabilities and in particular to assess the performance of our masers as precision oscillators. We then show how phase and frequency data are extracted from the maser signals and we discuss the sources of noise that fundamentally limit the stability of the observed Zeeman frequencies.

2.1 Spin-Exchange Optical Pumping

An active maser dissipates energy in order to self-sustain its oscillation. In our device this energy is transfered to the noble gas atoms when they are spin polarized in their most energetic Zeeman level.

The ^{129}Xe and ^{3}He nuclei are polarized by spin-exchange interactions with optically pumped Rb vapor [26, 6, 27]. This process occurs in two stages. First, Rb is polarized by optical pumping with circularly polarized light tuned to the Rb D_1 transition. Second, polarization from the Rb valence electrons is transferred to the ^{129}Xe and ^{3}He nuclei during collisions between the Rb and noble gas atoms. The spin-exchange process is similar for both noble gas species, but the angular momentum transfer rate from the Rb to the ^{129}Xe atoms is approximately 2,500 times the transfer rate from the Rb to the ^{3}He atoms.

The two naturally occurring isotopes of Rb, ^{85}Rb ($S = 1/2, I = 5/2$) and ^{87}Rb

($S = 1/2, I = 3/2$), have ground state hyperfine splittings of 3,036 MHz and 6,835 MHz, respectively. A typical maser cell contains a gas mixture of 600-1,500 Torr ^{3}He, 30-200 Torr ^{129}Xe, and 50-100 Torr N_2. The presence of these gases broadens the Rb D_1 line to a width of approximately 10-30 GHz, which is larger than the hyperfine splitting of either isotopic ground state.[1] Figure 2-1 shows a simplified level diagram for both isotopes of Rb, with the (unresolved) hyperfine levels not depicted. The $m_s = +1/2$ and $m_s = -1/2$ Zeeman sublevels are split by the experiment's solenoidal magnetic field: $\Delta\nu_z \approx 467$ kHz/G.[2] While the Zeeman splitting is also not resolved for typical magnetic fields of approximately 1 G, spin depolarization of the Rb ground electronic state is very slow; hence the two m_s sublevels are resolved in angular momentum space. Circularly polarized σ^+ light selectively drives the D_1 transition $^2s_{1/2} \rightarrow {}^2p_{1/2}$, with $\Delta m = +1$. Spontaneous radiative decay from the excited state occurs with a probability of 2/3 to return to the $m_s = -1/2$ ground state and a probability of 1/3 to return to the $m_s = +1/2$ ground state, which is the desired, spin-polarized state. When a Rb atom undergoes such radiative decay, it emits a photon that in general will have neither the same polarization nor propagation direction as the optical pumping light. Re-absorption of these emitted photons by ground state $m_s = 1/2$ Rb atoms limits the efficiency of the optical pumping process [6]. The addition of approximately 80 Torr of N_2 buffer gas to each maser cell provides a mechanism for radiationless de-excitation of the Rb valence electron. The Rb-N_2 cross-section for collisional Rb de-excitation is several orders of magnitude larger than the Rb-^{3}He and Rb-^{129}Xe cross-sections, with a decay time of approximately 2 ns. The spontaneous radiative decay time

[1]The pressure broadening coefficients for the Rb D_1 transition are approximately 14 GHz/atm for N_2 and 18 GHz/atm for ^{129}Xe and ^{3}He [8].

[2]The quoted $\Delta\nu_z$ is that of ^{85}Rb, the most abundant isotope (72.15%). For ^{87}Rb, $\Delta\nu_z \approx$ 700 kHz/G [28].

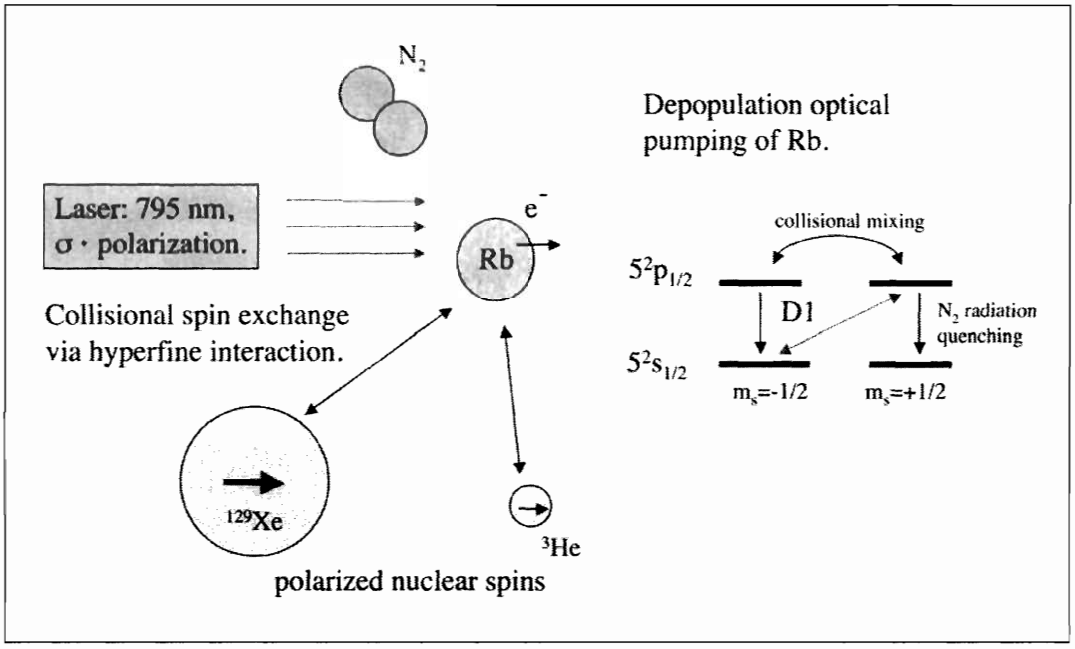

Figure 2-1: Simplified representation of spin-exchange optical pumping. Rb is polarized by circularly polarized σ^+ light. In a pressure-broadened cell the hyperfine levels cannot be energetically resolved and are not shown. The $m_s = 1/2$ and $m_s = -1/2$ Zeeman sublevels are split by the experiment's solenoidal magnetic field in both the $5^2s_{1/2}$ and $5^2p_{1/2}$ electronic states, and are resolved in angular momentum space.

is approximately 30 ns; thus more than 90% of Rb atoms decay non-radiatively [29]. Collisional mixing between the Rb and ^{129}Xe, ^{3}He, and N_2 atoms also rapidly populates the two $^2p_{1/2}$ states equally. Hence non-radiative decay to either ground state m_s level occurs with equal probability. In this simple picture, and in the absence of spin-destruction mechanisms that connect the two m_s ground states, an average of two σ^+ photons is required to polarize one Rb valence electron (a more complete description, including the effect of the Rb hyperfine interaction, is found in [26]).

The rate equation governing the Rb polarization, P_{Rb}, represents the competition between the optical pumping rate, γ_{opt}, and the rate of spin-relaxation of the Rb atom between the ground state sublevels, Γ_{Rb}. The time dependence of the Rb

polarization is

$$\frac{dP_{Rb}}{dt} = \gamma_{opt}(1 - P_{Rb}) - \Gamma_{Rb}P_{Rb}. \tag{2.1}$$

The solution of this equation for $P_{Rb}(0) = 0$ is:

$$P_{Rb}(t) = \frac{\gamma_{opt}}{\gamma_{opt} + \Gamma_{Rb}} \left(1 - e^{-(\gamma_{opt}+\Gamma_{Rb})t}\right). \tag{2.2}$$

For typical maser operating conditions, P_{Rb} reaches its equilibrium value of $30-90\%$ in a few milliseconds depending on the operating temperature and the intensity of the pumping light. In steady state we have:

$$P_{Rb} = \frac{\gamma_{opt}}{\gamma_{opt} + \Gamma_{Rb}}. \tag{2.3}$$

As we will see in Sect. 4.3.1, γ_{opt} depends on the local flux of on-resonant optical pumping photons, which decreases along the cell as light is absorbed.

Spin-rotation interactions between Rb and other atoms in the optical pumping region are the dominant contribution to Γ_{Rb} [29],

$$\Gamma_{Rb} = k_{Rb,He}[^3\mathrm{He}] + k_{Rb,Xe}[^{129}\mathrm{Xe}] + k_{Rb,Rb}[\mathrm{Rb}] + k_{Rb,N_2}[\mathrm{N_2}], \tag{2.4}$$

where the $k_{Rb,a} = \langle v_a \sigma_{Rb,a} \rangle$ are velocity averaged cross sections resulting from collisions of Rb atoms with atoms of type a and $[a]$ indicates their number density. Table 2.1 gives values for the relevant $k_{Rb,a}$. For typical ^{129}Xe/^{3}He maser conditions, Γ_{Rb} is dominated by spin-rotation interactions of the Rb and ^{129}Xe atoms [30].

The polarization of a Rb valence electron is transferred to a noble gas nucleus

species a	$k_{Rb,a}$ (cm^3/s)	$[a]$ (cm^{-3})
^{3}He	2.3×10^{-18}	10^{19}
^{129}Xe	8.8×10^{-15}	10^{18}
Rb	4.2×10^{-13}	10^{13}
N_2	8.0×10^{-18}	10^{18}

Table 2.1: Values for the spin-rotation rate constants k_{Rb-a} and typical gas and vapor number densities, $[a]$, in the ^{129}Xe/^{3}He maser.

by a spin-exchange interaction of the form:

$$H = -2g_{ng}\mu_B\mu_{ng}\sum_{i=1}^{N}\left[\frac{\vec{S}_i\cdot\vec{I}}{r_i^3} - 3\frac{(\vec{I}\cdot\vec{r}_i)(\vec{S}_i\cdot\vec{r}_i)}{r_i^5} + \frac{8\pi}{3}\delta(r_i)\vec{S}_i\cdot\vec{I}\right], \qquad (2.5)$$

where $\vec{I}$ represents the nuclear spin of the noble gas and $\vec{S}_i$ represents the spin of the Rb valence electron and of all the noble gas electrons [31, 32]. The last term in the Hamiltonian represents the Fermi contact interaction between the electrons and the noble gas nucleus and it is this interaction that dominates the spin-exchange process [31]. Furthermore, the total gas pressure in a typical maser cell is low enough to permit the formation of transient Rb-^{129}Xe Van der Waals molecules that increase the Rb-^{129}Xe hyperfine interaction time and therefore enhance the Rb-^{129}Xe spin-exchange rate [7].

As with the Rb polarization, the rate equation describing the polarization of ^{3}He and ^{129}Xe is characterized by a spin-exchange source term $\gamma_{se} = k_{se}[\mathrm{Rb}]$ and a relaxation term Γ_{ng}. In steady state:

$$\begin{aligned} P_{ng} &= \frac{P_{Rb}\gamma_{se}}{\gamma_{se}+\Gamma_{ng}} \\ &= \frac{\gamma_{opt}}{\gamma_{opt}+\Gamma_{Rb}}\,\frac{\gamma_{se}}{\gamma_{se}+\Gamma_{ng}}. \end{aligned} \qquad (2.6)$$

Relaxation mechanisms for polarized noble gases will be discussed in the next sec-

tion. We note here that Γ_{ng} in our double-bulb cells also includes the rate at which atoms diffuse into and out of the pump bulb, which in turn depends on the steady state polarizations in the two bulbs. The steady state value of Eq. (2.6) will be obtained in Sect. 4.3, where we introduce a model for the diffusive polarization transfer.

Under typical operating conditions in the pump bulb, $k_{se,He} \approx 7 \times 10^{-20}$ and $k_{se,Xe} = (1.75 \pm 0.12) \times 10^{-16}$ cm^3 s^{-1} for binary collisions. The contribution of Rb-^{129}Xe Van der Waals molecules to ^{129}Xe spin-exchange can be on the same order of magnitude or even greater than that of binary collisions. Its magnitude depends sensitively on the density and species of the buffer gases present in the cell; in our case we also have both N_2 and ^{3}He. Buffer gases are needed for molecule formation, since this begins with a three body collision in which the momentum carried away by the buffer gas allows for the binding of the molecule. However, when buffer gas pressures become too high, they limit the lifetime of the Rb-^{129}Xe molecules, thus suppressing this spin-exchange mechanism. Unfortunately, reliable measurements of the Van der Walls contributions to spin-exchange are not available for the gas mixtures and relatively low pressures that we employ and this limits our ability to make accurate quantitative predictions.

Typical times to reach equilibrium polarization are: ^{129}Xe $\approx$ 10 minutes, ^{3}He $\approx$ 2 hours. Typical equilibrium noble gas polarizations in the pump bulb are: $P_{Xe} \approx 0.4$ and $P_{He} \approx 0.02$. In Sect. 4.3.1 we will present a numerical simulation of the optical pumping process and we will discuss pros and cons of using broad- or narrow-band lasers.

2.2 Spin Relaxation

In this section we briefly review the known spin-relaxation and decoherence processes affecting ^{129}Xe and ^{3}He. The long spin-relaxation times that we find are perhaps the most remarkable properties of these two isotopes and derive from their having nuclear spin 1/2 and no net electronic spin. These atoms interact with their environment only through the relatively weak magnetic dipole, since all higher order electric and magnetic momenta vanish for systems of particles with total spin $\leq 1/2$. Here, we consider the effects of wall collisions, self-interaction and magnetic field inhomogeneities, but not mechanisms such as maser action (radiation damping) and diffusion into and out of the two bulbs, which will be addressed in Sect. 2.3.1 and Sect. 4.3 respectively.

2.2.1 Longitudinal Relaxation (T_1)

Magnetic impurities on the glass surface disorient the spins of polarized noble gases during wall collisions. This depolarization mechanism is the dominant source of relaxation in the relatively small, high surface-to-volume ratio cells used in our masers. The relaxation rate depends on the specifics of cell geometry, wall coatings, gas fill pressures, gas temperature, etc. For ^{3}He, we have observed (see Sect. 6.4) relaxation times $T_1 \approx 2 - 7$ h, which we attribute to wall relaxation and are in keeping with the literature [6]. For ^{129}Xe, the wall relaxation times are typically much shorter. We carefully clean our cells and then cover the inner surface with silane coatings (see Sect. 5.2.1) that are known to lengthen the ^{129}Xe relaxation times to about $T_{1,Wall} \approx 20$ minutes. This time constant is difficult to observe experimentally in our double-bulb cells, because the spin-exchange interaction with Rb seen in the last section and polarization transport affect the ^{129}Xe polarization

on comparable time-scales (see Sect. 6.4).

Compared to wall relaxation, the self-relaxation of ^{3}He due to the magnetic dipole-dipole interaction (given by $T_{1,He-He} = 744$ h/[He] [29], where the ^{3}He density [He] is measured in amagat[3]) is negligible. The self-relaxation of ^{129}Xe due to magnetic dipole-dipole interactions is negligible compared to the spin rotation relaxation in ^{129}Xe/^{129}Xe Van der Waals molecules, which is given by $T_{1,Xe-Xe} \approx (1 + 0.25[\mathrm{He}]/[\mathrm{Xe}])$ 3.5 h [33], where we have assumed that ^{3}He is the most dense buffer gas in the cell and it contributes to the breaking of the ^{129}Xe-^{129}Xe molecules.

Noble gas atoms can be depolarized also by diffusion through magnetic field inhomogeneities at the rate

$$\frac{1}{T_{1,Magn}} = \frac{D_{ng}\left|\vec{\nabla}B_{\perp}\right|^2}{B_0^2}, \tag{2.7}$$

where $B_\perp$ is the component of the static magnetic field transverse to the main applied field $B_0 \approx 1.5$ G [6]. The noble gas diffusion coefficients D_{ng} are largest in the hot pump chamber, with rough values $D_{Xe} \approx 0.4$ cm^2/s and $D_{He} \approx 1.5$ cm^2/s (see Sect. 4.3.3). In our apparatus we limit $\vec{\nabla}B_0(\vec{r})$ to approximately 20 μG/cm for $B_0 \approx 1.5$ G (see for instance Sect. 6.5 and [34]). Assuming that $\vec{\nabla}B_\perp$ is ten times larger than $\vec{\nabla}B_0(\vec{r})$ (an extremely conservative estimate), the resulting magnetic-gradient-induced relaxation rates are thus entirely negligible ($T_{1,Magn} > 1$ y). Since the mechanisms that lead to spin relaxation are independent, the total rate of longitudinal spin relaxation is the sum of all rates for each process:

$$\frac{1}{T_1} = \frac{1}{T_{1,Wall}} + \frac{1}{T_{1,ng-ng}} + \frac{1}{T_{1,Magn}}. \tag{2.8}$$

[3] 1 amagat $= 2.69 \times 10^{19}$ is the density at STP.

2.2.2 Transverse Relaxation (T_2)

In addition to the mechanisms discussed in the previous section the dominant mechanism for transverse spin relaxation in the maser bulb arises from axial magnetic field inhomogeneities of the form $\vec{\nabla}B_0(\vec{r})$. Noble gas nuclei at different locations experience slightly different magnetic fields and precess at slightly different rates, thus inducing decoherence. Motional averaging (i.e., diffusion) reduces the effective field inhomogeneity. In a spherical maser bulb the dephasing rate takes the form [35]:

$$\frac{1}{T_{2,Magn}} \approx \frac{8R^4\gamma_{ng}^2|\vec{\nabla}B_0(\vec{r})|^2}{175D_{ng}}, \tag{2.9}$$

where D_{ng} is the total noble diffusion coefficient, γ_{ng} is the noble gas gyromagnetic ratio and R (≈ 1 cm) is the radius of the spherical maser bulb. The components of $\vec{\nabla}B_0(\vec{r})$ include contributions from the solenoid field, from residual magnetization of the μ-metal shields, and from fields produced by the polarized noble gas atoms. Using the diffusion coefficients and the magnetic field inhomogeneity given in the last section ($D_{Xe} \approx 0.4$ cm^2/s, $D_{He} \approx 1.5$ cm^2/s, and $\vec{\nabla}B_0(\vec{r}) \approx 20$ μG/cm), we obtain $T_2 = 400$ and 200 s for ^{129}Xe and ^{3}He respectively, in good agreement with measured values (see Sect. 6.5).

In conclusion, the total decoherence rate is then given by

$$\frac{1}{T_2} = \frac{1}{T_1} + \frac{1}{T_{2,Magn}}, \tag{2.10}$$

and the magnetic field gradients usually dominate the decoherence process. As we will see in Sect. 5.4.2, careful trimming of three shim coils allows us to maximize transverse decoherence times.

2.3 Bloch Equations and Masing

The Hamiltonian for a magnetic moment $\vec{\mu}$ in the presence of a static magnetic field B_0 along $\hat{z}$ and a quasi-resonant drive of frequency ω_M, phase α, and amplitude B_1 along $\hat{x}$ is:

$$H = -\vec{\mu} \cdot \vec{B} = \gamma_{ng} \vec{I} \cdot (B_1 \cos(\omega_M t + \alpha), 0, B_0)\,, \tag{2.11}$$

where $\vec{I}$ is represents the nuclear spin and $\gamma_{ng} > 0$ is the absolute value of the noble gas gyromagnetic ratio, which is negative for both ^{129}Xe and ^{3}He. In matrix notation the Hamiltonian is:

$$H = \frac{\hbar}{2} \begin{pmatrix} \omega_0 & 2\omega_R \cos(\omega_M t + \alpha) \\ 2\omega_R \cos(\omega_M t + \alpha) & -\omega_0 \end{pmatrix}, \tag{2.12}$$

where $\omega_0 = \gamma_{ng} B_0$ and the Rabi frequency $\omega_R = \gamma_{ng} B_1/2$. It is convenient to make the rotating wave approximation, i.e., to neglect the counter-rotating term, so that:

$$H \approxeq \frac{\hbar}{2} \begin{pmatrix} \omega_0 & \omega_R e^{-i(\omega_M t + \alpha)} \\ \omega_R e^{i(\omega_M t + \alpha)} & -\omega_0 \end{pmatrix}. \tag{2.13}$$

The equations of motion governed by this Hamiltonian can be solved more easily in the frame rotating at the frequency of the quasi-resonant drive. In the frame rotating at ω_M the Hamiltonian takes the following form:

$$H' = \frac{\hbar}{2} \begin{pmatrix} -\delta & \omega_R e^{-i\alpha} \\ \omega_R e^{i\alpha} & \delta \end{pmatrix} \tag{2.14}$$

$$= \frac{\hbar}{2} \vec{\sigma} \cdot (\omega_R \cos\alpha, \omega_R \sin\alpha, -\delta) = \frac{\hbar}{2}\, \vec{\sigma} \cdot \vec{\Omega}, \tag{2.15}$$

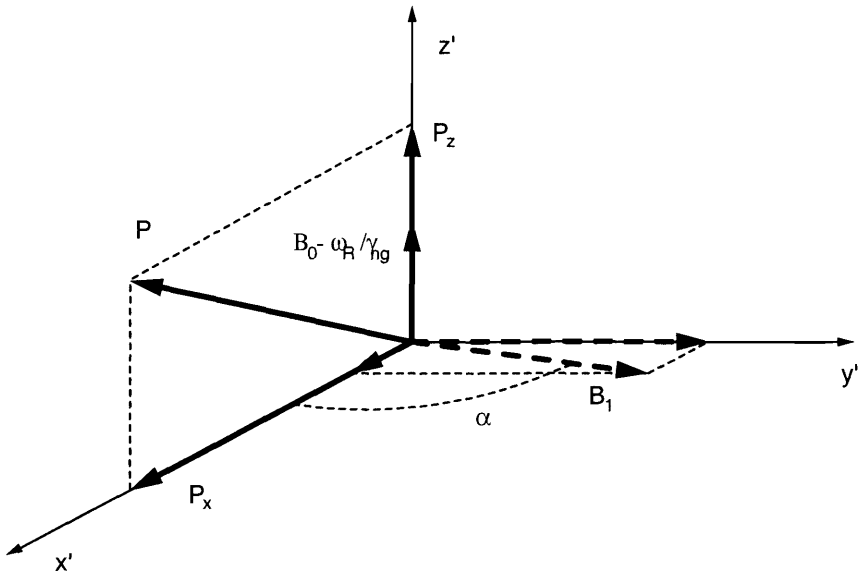

Figure 2-2: The polarization vector $\vec{P}$ in the frame rotating at the maser frequency. The $\hat{x}'$ axis is chosen along the direction of the perpendicular polarization. The B_1 field is the feedback field produced by the pick-up coil. The phase of this field is shifted by an angle α depending on the detuning of the coil from the Zeeman frequency.

where we have defined the frequency shift $\delta = \omega_M - \omega_0$ and σ_i are the Pauli matrices. In terms of the spin density matrix ρ' for the ensemble of noble gas atoms in the rotating frame,[4] Eq. (2.11) can be rewritten in the following form:

$$\dot{\rho}' = \frac{1}{i\hbar}\left[H', \rho'\right]. \tag{2.16}$$

The spin density matrix can be rewritten using the Pauli matrices $\vec{\sigma}$, the identity matrix $I_{2\times 2}$, and a polarization vector $\vec{P}$:

$$\rho' = \tfrac{1}{2}\left(I_{2\times 2} + \vec{\sigma}\cdot\vec{P}\right). \tag{2.17}$$

[4]The prime indicates coordinates in the rotating frame.

The polarization vector is defined using the populations (ρ'_{bb}, ρ'_{aa}) and coherences (ρ'_{ba}, ρ'_{ab}) of the spin density matrix:

$$\begin{aligned} P_x &= \rho'_{ab} + \rho'_{ba}, \\ P_y &= -i\left(\rho'_{ab} - \rho'_{ba}\right), \\ P_z &= \rho'_{bb} - \rho'_{aa}. \end{aligned} \tag{2.18}$$

One can then show that the equation of motion in Eq. (2.16) takes the following vector form:

$$\dot{\vec{P}} = \vec{\Omega} \times \vec{P} \tag{2.19}$$

with $\vec{\Omega}$ as defined in Eq. (2.15).

In an active maser the polarization perpendicular to the B_0 field, $P_\perp$, is coupled through a resonant cavity or circuit back on the atomic ensemble thus creating a tipping field that self-sustains the oscillation. The equations of motion for a simple maser[5] can be derived using Eq. (2.19) and assuming a source of polarization such that, in absence of masing, the longitudinal polarization would reach the value $P_{z,0}$ in the presence of longitudinal spin relaxation characterized by the time T_1. For the maser, the polarization vector $\vec{P}$ of Eq. (2.19) refers to an average over the ensemble of $[\mathrm{ng}]V_{Bulb}$ atoms, where [ng] is the number density of the noble gas atoms and V_{Bulb} is the volume of the bulb in which they are contained. In our system the source is a flux of polarized atoms ϕ (in units of number of atoms per second) that diffuse into the maser bulb. In terms of the flux the source term is:

$$P_{z,0} = \frac{\phi T_1}{[ng]V_{Bulb}}. \tag{2.20}$$

[5]The general case of the double-bulb maser will be discussed in Sect. 4.3.4.

In compact form the maser equation of motion including relaxation is [36]:

$$\dot{\vec{P}} = (\omega_R \cos\alpha, \omega_R \sin\alpha, -\delta) \times \vec{P} + \frac{P_{z,0}\hat{z} - \vec{P}}{\{T_2, T_2, T_1\}}. \tag{2.21}$$

Since the oscillator is self-driven ω_R depends on the polarization $\vec{P}$ and this makes Eq. (2.21) nonlinear. In order to solve this equation in steady state we must review the feedback mechanism that generates the quasi-resonant driving field B_1 and find an expression for $\omega_R(\vec{P})$.

2.3.1 Feedback Circuit and Radiation Damping Time

The quasi resonant field B_1 of the maser is produced by a coil surrounding the atoms. This coil is connected to a resonant tank-circuit (see Fig. 2-3) and is excited by the magnetic flux picked up from the precessing atoms, whence the name "pick-up coil." The spatially dependent magnetic field per unit current produced by the pick-up coil, $\vec{\xi}(\vec{r})$, satisfies the following equation:

$$\vec{B}_1(\vec{r}, t) = \vec{\xi}(\vec{r})\, I_{pu}(t). \tag{2.22}$$

The magnetization associated to the ensemble of atoms is:

$$\vec{M}(\vec{r}, t) = -\frac{\hbar\gamma_{ng}}{2}[ng]\,\vec{P}(\vec{r}, t). \tag{2.23}$$

The polarization $\vec{P}$ is defined in Eq. (2.18) and now refers to an ensemble of atoms. The voltage induced in the coil can be written in the following form [37]:

$$V_{pu}(t) = -\frac{\partial}{\partial t}\int_{V_{Bulb}} d^3\vec{r}' \left\{\vec{\xi}(\vec{r}') \cdot \vec{M}(\vec{r}', t)\right\}. \tag{2.24}$$

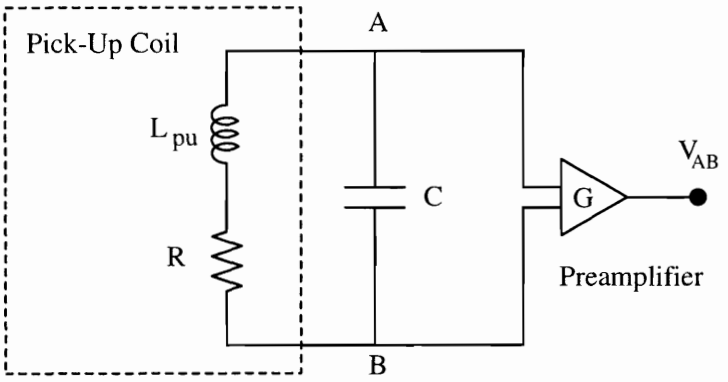

Figure 2-3: Simple RLC circuit that could be used as the feed-back circuit of a single species noble gas maser (the double-resonant circuit that we actually use is described in Sect. 5.5). The atoms' oscillation induces a current in the pick-up coil with inductance L_{pu} and resistance R. The maser signal is the sinusoidal voltage, V_{AB}, detected across the tuning capacitor, C, after low-noise amplification with gain G.

Assuming the pick-up coil is part of a simple RLC series circuit (the more general case for the two species maser is treated in Sect. 5.5) then the resonant frequency $\omega_c = 1/\sqrt{L_{pu}C}$ and the quality factor $Q = \omega_c L_{pu}/R$, which responds to the atoms' excitation by generating a driving field of average spatial intensity $B_1(t) = \xi_o I_{pu}(t)$, where:

$$\xi_0 = \frac{1}{V_{Bulb}} \int_{V_{Bulb}} d^3\vec{r}\,\xi(\vec{r}). \tag{2.25}$$

The pick-up current $I(t)$ is amplified by ρ_c and de-phased by an angle α, due to the tuned circuit:[6]

$$\begin{aligned} I_{pu}(t) &= \frac{V_{pu}(t)}{R + i\omega_M L_{pu} + \frac{1}{i\omega_M C}} \\ &= \frac{V_{pu}(t)\rho_c(\omega_M)e^{i\alpha}}{i\omega_M L_{pu}}, \end{aligned} \tag{2.26}$$

[6]In the following equations, when only the right-hand side of the equation is complex, we implicitly assume extraction of the real part. We also assume that $V_{pu} \propto e^{i\omega_M t}$.

where have introduced the following definitions:

$$\sin\alpha = \frac{\omega_c}{\omega}\frac{\rho_c(\omega)}{Q}, \tag{2.27}$$

$$\cos\alpha = \rho_c(\omega)\left[1-\left(\frac{\omega_c}{\omega}\right)^2\right], \tag{2.28}$$

$$\rho_c(\omega) = \frac{Q}{\sqrt{Q^2\left[1-\left(\frac{\omega_c}{\omega}\right)^2\right]^2+\left(\frac{\omega_c}{\omega}\right)^2}}. \tag{2.29}$$

Factoring out the fast oscillation from the definition of the perpendicular polarization $P_\perp$ gives the pick-up coil voltage,

$$V_{pu}(t) \cong -\frac{\hbar\gamma_{ng}}{2}[ng]\,P_\perp(t)\,\xi_o V_{Bulb}\frac{\partial}{\partial t}(e^{i\omega_M t}). \tag{2.30}$$

We then find that the Rabi frequency (see Eq. (2.12)) is

$$\omega_R = \frac{\rho_c(\omega_M)}{Q}\frac{1}{\tau_{RD}}\frac{P_\perp}{P_{z,0}}, \tag{2.31}$$

where we have defined the radiation damping time as

$$\tau_{RD}^{-1} = \frac{\hbar\gamma_{ng}^2}{4}\frac{\xi_o^2 Q V_{Bulb}}{L_{pu}}[ng]P_{z,0}. \tag{2.32}$$

The longitudinal polarization $P_{z,0}$ is the noble gas polarization in the maser chamber, that would be attained in the absence of masing. Including this quantity in the definition above has the advantage of making τ_{RD} a readily measurable parameter, as we shall see at the end of the next section. We also define an effective radiation damping time:

$$\frac{1}{\tau'_{RD}(\omega)} = \frac{\rho_c(\omega)}{Q}\frac{\sin\alpha}{\tau_{RD}}, \tag{2.33}$$

which depends on cavity tuning such that on resonance ($\omega = \omega_c$) it coincides with the radiation damping time, i.e., $\tau'_{RD}(\omega_c) = \tau_{RD}$.

2.3.2 Steady State Maser Solutions and Cavity Pulling

We are now ready to find the steady state maser solutions. For convenience we choose the $\hat{x}'$ axis of the rotating reference frame along the perpendicular polarization so that $P_x = P_\perp$ (see Fig. 2-2), setting $P_y = 0$. In component terms Eq. (2.21) becomes:

$$\dot{P}_x = \dot{P}_\perp = \omega_R \sin\alpha \; P_z - \frac{P_\perp}{T_2}, \tag{2.34}$$

$$\dot{P}_y = -\delta P_\perp - \omega_R \cos\alpha \; P_z, \tag{2.35}$$

$$\dot{P}_z = -\omega_R \sin\alpha \; P_\perp - \frac{P_z - P_{z,0}}{T_1}. \tag{2.36}$$

In steady state the left-hand side of these equations vanishes. The equilibrium values for the maser polarization are:

$$\frac{P_{z,eq}}{P_{z,0}} = \frac{\tau'_{RD}}{T_2}, \tag{2.37}$$

$$\frac{P_{\perp,eq}}{P_{z,0}} = \sqrt{\frac{\tau'_{RD}}{T_1}\left(1 - \frac{\tau'_{RD}}{T_2}\right)}. \tag{2.38}$$

From Eq. (2.35) and $\dot{P}_y = 0$ we derive the maser frequency shift, δ_{eq}, from the atomic frequency in steady state:

$$\begin{aligned} \delta_{eq} &= \omega_{M,eq} - \omega_0 = -\frac{1}{T_2}\cot\alpha \\ &= -\frac{Q}{T_2}\left(\frac{\omega_M}{\omega_c} - \frac{\omega_c}{\omega_M}\right) \approx -\frac{Q}{Q_{line}}(\omega_0 - \omega_c). \end{aligned} \tag{2.39}$$

We assume that the resonator is tuned close to the atomic frequency and that its quality factor $Q \ll \omega_0 T_2$, so that in the right-hand side of the the equation we replace ω_M with ω_0. We have also introduced the line quality factor $Q_{line} = \omega_0 T_2/2$. This shift in maser frequency is called the "cavity-pulling shift" because it is caused by the detuning of the cavity, which pulls the oscillator frequency slightly away from the atomic frequency towards the resonant frequency of the cavity, and it is characteristic of any active oscillator.

Observation of Radiation Damping Time

The effective radiation damping time can be directly measured by pumping the atoms in the low energy state (see Fig. 1-2) and measuring the free induction decay rates, $1/T_{2,On}$ and $1/T_{2,Off}$, of the perpendicular polarization when the resonator is turned on resonance (ω_R as given in Eq. (2.31)) and high off resonance ($\omega_R = 0$). Using Eq. (2.34) and noticing that for small tips $P_z \approx -P_{z,0}$, we find that the effective radiation damping time is simply given by the difference:

$$\frac{1}{\tau_{RD}'} = \frac{1}{T_{2,On}} - \frac{1}{T_{2,Off}}. \tag{2.40}$$

In Sect. 6.6.1, we will show observations of this parameter for both gas species, in the double-bulb maser.

2.3.3 Threshold Condition and Maser Power

The condition for having an indefinite maser oscillation is simply that the coherences in the spin density matrix do not vanish in steady state. In terms of the polarization vector this condition is simply $P_{\perp,eq} > 0$, which together with Eq. (2.38) yields the threshold condition for our maser $\tau_{RD}' < T_2$. This condition is equivalent to the

more customary statement that the flux of incoming polarized particles ϕ is greater than the threshold flux ϕ_{th}, which using Eq. (2.20) and Eq. (2.33) is

$$\phi_{th} = \frac{4L_{pu}}{T_1 T_2 \sin\alpha \hbar \gamma_{ng}^2 \xi_0^2 \rho_c(\omega_M)} \approx \frac{4R}{T_1 T_2 \hbar \omega_M \gamma_{ng}^2 \xi_0^2}, \tag{2.41}$$

where in the last equation we have assumed that the cavity is tuned to the atomic resonance ($\omega_c \rightarrow \omega_0$).

Conservation of the total number of particles in the maser cell requires that for each polarized particle that enters the maser bulb an unpolarized particle leaves the bulb. Each polarized particle that does not end up contributing to $P_{z,eq}$, deposits an energy $\hbar\omega_M/2$. The total power deposited by the incoming atoms is therefore:

$$W = \frac{\hbar\omega_M}{2}\left(1 - \frac{P_{z,eq}}{P_{z,0}}\right)\phi = \frac{\hbar\omega_M}{2}\left(\phi - \phi_{th}\right). \tag{2.42}$$

One can verify, making use of Eq. (2.30) and Eq. (2.26), that this is also the steady state maser power dissipated in the resonant circuit:

$$\begin{aligned} W &= \langle V_{pu}(t) I(t) \rangle \\ &= \frac{\hbar\omega_M}{2}[ng] V_{Bulb} \frac{P_{\perp,eq}^2}{\tau'_{RD} P_{z,0}} \qquad (2.43) \\ &= \frac{\hbar\omega_M}{2}\frac{[ng] V_{Bulb} P_{z,0}}{T_1}\left(1 - \frac{\tau'_{RD}}{T_2}\right). \qquad (2.44) \end{aligned}$$

Detected Maser Signal and Noise Considerations

We measure the amplitude of the oscillating maser as the voltage V_{AB} across the capacitor C of the resonant RLC circuit detected after a low noise preamplification

stage of gain G (see Fig. 2-3):

$$V_{AB} = G\frac{I}{i\omega_M C} = GQV_{pu} = GQ\sqrt{RW} = G\sqrt{\omega_M L_{pu} QW}. \tag{2.45}$$

Assuming that the resonator is perfectly tuned to the atomic resonance ($\alpha = \pi/2$) and noticing that $\tau_{RD} \propto 1/Q$, we can express the maser signal as

$$S = V_{AB} \propto \sqrt{\frac{1}{\tau_{RD}}\left(1 - \frac{1}{\sin\alpha}\frac{\tau_{RD}}{T_2}\right)}, \tag{2.46}$$

where we have used the definition of maser power given in Eq. (2.44). While the signal, S, grows with shorter radiation damping time, τ_{RD}, the value of τ_{RD} that optimizes the SNR depends on the properties of the noise. Johnson noise in the coil is detected and amplified exactly as the maser signal. The power available at temperature T in a bandwidth B is $W_J = 4k_BTB$, where k_B is the Boltzmann constant. The SNR is therefore

$$\frac{S}{N_J} = \frac{GQ\sqrt{RW_{Maser}}}{GQ\sqrt{RW_J}} \propto \sqrt{\left(1 - \frac{1}{\sin\alpha}\frac{\tau_{RD}}{T_2}\right)}, \tag{2.47}$$

improving as τ_{RD} is reduced. Pickup of ambient magnetic noise, δB_{Amb}, however will be amplified by the resonator as well:

$$\frac{S}{N_{Amb}} \propto \frac{\sqrt{QW}}{Q\delta B_{Amb}} \propto \sqrt{\tau_{RD}\left(1 - \frac{1}{\sin\alpha}\frac{\tau_{RD}}{T_2}\right)}. \tag{2.48}$$

The best SNR is then obtained for $\tau_{RD} = T_2 \sin\alpha\ /2$, which also maximizes $P_{\perp,eq}$, optimizing the ratio of atomic magnetic induction to ambient noise.

In our apparatus Johnson noise dominates and minimizing τ_{RD} improves the SNR. However, the detection noise discussed here only contributes to white phase

noise ($\delta\varphi = \delta V_{AB}/V_{AB}$). As we shall see at the end of this chapter (Sect. 2.4), this noise is averaged out over the long observation times employed in our experiments and does not limit the stability of our masers, when applied to tests of Lorentz and CPT symmetry on time-scales of approximately one day.

2.3.4 Near-Equilibrium Transient Behaviour

While we are mostly interested in the steady state solutions given in Sect. 2.3.2, the reaction of the masers to small perturbations and their return to steady state is also important. Therefore we linearize Eqs. (2.37-2.39) near equilibrium using the following definitions:

$$P_z(t) = P_{z,eq} + \delta P_z(t), \tag{2.49}$$

$$P_\perp(t) = P_{\perp,eq} + \delta P_\perp(t), \tag{2.50}$$

$$\delta(t) = \delta_{eq} + \delta_{ne}(t). \tag{2.51}$$

Substituting these equations into Eqs. (2.34-2.36), we obtain the following identity,

$$\delta_{ne}(t) = -\frac{\cot\alpha}{\tau'_{RD}}\frac{\delta P_z(t)}{P_{z,0}}, \tag{2.52}$$

and two first order differential equations that can be written in matrix form:

$$\frac{d}{dt}\begin{pmatrix} \delta P_z(t) \\ \delta P_\perp(t) \end{pmatrix} = \begin{pmatrix} -\frac{1}{T_1} & -2\sqrt{\frac{1}{T_1}\left(\frac{1}{\tau'_{RD}} - \frac{1}{T_2}\right)} \\ \sqrt{\frac{1}{T_1}\left(\frac{1}{\tau'_{RD}} - \frac{1}{T_2}\right)} & 0 \end{pmatrix}\begin{pmatrix} \delta P_z(t) \\ \delta P_\perp(t) \end{pmatrix} \tag{2.53}$$

The solutions to the equations above are in most practical situations underdamped oscillations. The eigenvalues of the 2×2 matrix above give the damping rate, γ_{damp},

and the oscillation frequency, ω_{osc} :

$$\gamma_{damp} = \frac{1}{2T_1} \tag{2.54}$$

$$\omega_{osc} = \sqrt{\frac{2}{T_1}\left(\frac{1}{\tau'_{RD}} - \frac{1}{T_2}\right) - \frac{1}{4T_1^2}}. \tag{2.55}$$

The oscillations begin not far from threshold, when $\tau'_{RD} < T_2(1+T_2/8T_1)^{-1}$ and their frequency becomes larger as we increase the flux of incoming polarized atoms. The period of these oscillations is well above threshold is $\pi\sqrt{2T_1\tau_{RD}}$ and is observed in the amplitudes of our maser signals, which are proportional to $P_\perp$ (see Sect. 6.6.2). Additionally there is a correlation between the phase φ_M and amplitude of the maser signals, which appears when the coil is detuned from the atomic resonance ($\alpha \neq \pi/2$). Integrating Eq. (2.52) and using also Eq. (2.53), we find:

$$\delta\varphi_M(t) = \int \delta_{ne}(t)dt = -\frac{\cot\alpha}{\tau'_{RD}}\left[\frac{1}{T_1}\left(\frac{1}{\tau'_{RD}} - \frac{1}{T_2}\right)\right]^{-\frac{1}{2}} \frac{\delta P_\perp(t)}{P_{z,0}}. \tag{2.56}$$

This correlation directly converts the underdamped oscillations in maser amplitudes seen above into frequency noise. This undesired effect can be avoided by properly tuning the resonant circuit to the Zeeman frequency ($\omega_c = \omega_0 \rightarrow \alpha = \pi/2$).

2.4 Characterization of Stability

The limit to the statistical precision of our Lorentz and CPT tests is the finite frequency stability of our masers. Our experimental diagnostics assess the stability of various quantities: maser frequencies and amplitudes, and also temperatures, photodiode voltages, etc. In this section we briefly introduce the Allan Deviation,

one of the many possible measures of stability.[7] The need for such estimators arises whenever the quantity to be characterized is a time series for which the traditional variance and higher moments do not converge in general. The Allan deviation is the standard deviation of the time series when the latter converges and is well defined when the standard deviation is not. The simple definition of the Allan deviation of the quantity $y(t)$ is:

$$\sigma_y(\tau) = \sqrt{\frac{1}{2(N-1)} \sum_{n=1}^{N-1} (y_{n+1} - y_n)^2}, \tag{2.57}$$

where $\{y_n = y(n\tau)\}$ is a series of measurements made at fixed measurement interval τ. The Allan deviation of a time series is essentially the standard deviation of the signal after it has been appropriately filtered. To see this we notice that the standard deviation σ_y^{st} for a signal $y(t)$ with zero mean is simply related to the integral of the signal's power spectral density, $S_y(f)$,

$$(\sigma_y^{st})^2 = \int_0^{f_h} S_y(f) df. \tag{2.58}$$

In the integral above we have considered a high frequency cutoff f_h always present in the equipment measuring $y(t)$.[8] The power spectral density, or "power spectrum," is computed from the Fourier transform of the auto-correlation function, $R_y(\tau)$,

$$R_y(\tau) = R_y(-\tau) = \frac{1}{T} \int_0^T y(t) y(t-\tau) dt, \tag{2.59}$$

$$S_y(f) = 4 \int_0^T R_y(\tau) \cos 2\pi f \tau \, d\tau. \tag{2.60}$$

[7] A comprehensive overview of the topics presented here can be found in [28], Appendix 2F.

[8] At the very least f_h is limited by the rate of data acquisition $f_0 \approx 1/2\pi\tau_0$ and we always choose $\tau \gg \tau_0$.

We will show the power spectrum of a signal when we wish to study the frequency dependence of its noise. The integral of $S_y(f)$ over a certain frequency range gives the fraction of the signal's variance for which that range range of frequencies is ultimately responsible (see Eq. (2.58)). This often provides useful information when studying harmonic perturbations of a signal. Returning now to the Allan deviation, it is possible to show that

$$\sigma_y^2(\tau) = \int_0^{f_h} |H_A(f)|^2 \, S_y(f) df, \tag{2.61}$$

where $H_A(f)$ is the Allan transfer function

$$|H_A(f)|^2 = 2\frac{\sin^4(\pi f \tau)}{(\pi f \tau)^2}. \tag{2.62}$$

When $f \to 0$, $|H_A(f)|^2 \propto f^2$, guaranteeing the convergence of the integral when the power spectrum of the signal y can be written as

$$S_y(f) = \sum_{\alpha=-2}^{2} h_\alpha f^\alpha. \tag{2.63}$$

In particular, the Allan variation in Eq. (2.61) converges for signals containing $1/f$ noise (also called pink noise, or flicker noise) and for signals performing a random walk ($1/f^2$). When y is an oscillator's frequency, $\alpha = 0, 1, 2$ respectively correspond to white frequency, flicker phase, and white phase noise. In the next section we give more specific information on the characterization of the noise in our masers.

2.4.1 Extraction of Phase and Frequency Data

The in-phase and out-of-phase portions of each maser signal (relative to an ultra-stable reference oscillator) are recorded at regular intervals, typically once every two seconds, providing discrete data streams drawn from the (idealized) continuous in-phase and out-of-phase signals:

$$\begin{aligned} x(t) &= R(t)\cos(2\pi\nu_b t + \delta\varphi(t)), \\ y(t) &= R(t)\sin(2\pi\nu_b t + \delta\varphi(t)), \end{aligned} \tag{2.64}$$

where the maser amplitude is given by $R(t) = \sqrt{x(t)^2 + y(t)^2}$, and $\nu_b(t) = \nu_{ng}(t) - \nu_{ref}$ represents the beat frequency between the detected maser signal and the signal from the reference oscillator. (The signal detection system is described in Sect. 5.5.) For example, the beat frequency of the free-running ^{3}He maser is typically set to 25 mHz. The phase evolution of each maser is determined from measurements of $x(t)$ and $y(t)$ as follows:

$$\varphi(t) = \arctan\ \frac{y(t)}{x(t)} = 2\pi\nu_b t + \delta\varphi(t). \tag{2.65}$$

If phase measurements are performed every τ_0 seconds, the average maser frequency over the interval τ is given by the least squares formula:

$$\nu(\tau) = \frac{c_1}{2\pi} = \frac{12}{2\pi\tau^2(N^2-1)}\left(N\sum_{i=1}^{N}\varphi_i t_i - \sum_{i=1}^{N}\varphi_i\sum_{i=1}^{N}t_i\right), \tag{2.66}$$

where $N = \tau/\tau_0$ is the total number of measurements in that interval. This expression is useful to derive the effect on the maser frequency of random perturbations of the maser phase and frequency (the so called "white phase" and "white frequency

noise"). The perturbations $\delta\varphi_n$ and $\delta\nu_n$, with $n = 0 \ldots N$, are normally distributed variables chosen with variances $\sigma^2_{\delta\varphi}(\tau_0)$ and $\sigma^2_{\delta\nu}(\tau_0)$, respectively. The modified phase

$$\varphi_n = 2\pi\nu_0 t_n + \delta\varphi_n + 2\pi \sum_{i=1}^{n} \delta\nu_i \tau_0, \tag{2.67}$$

yields the standard deviation $\sigma_\nu(\tau) = \sqrt{[\sigma_\nu^{wp}(\tau)]^2 + [\sigma_\nu^{wf}(\tau)]^2}$ where we have introduced the following white phase (wp) and the white frequency (wf) contributions,

$$\begin{aligned} \sigma_\nu^{wp}(\tau) &\approx \frac{\sqrt{3\tau_0}}{\pi\tau^{3/2}}\sigma_{\delta\varphi}(\tau_0) \propto \tau^{-3/2}, \\ \sigma_\nu^{wf}(\tau) &\approx \sqrt{\frac{6\tau_0}{5\tau}}\sigma_{\delta\nu}(\tau_0) \propto \tau^{-1/2}, \end{aligned} \tag{2.68}$$

and we have assumed that $\tau \gg \tau_0$. The observation time at which phase and frequency noise become of the same magnitude is given by

$$\bar{\tau} = \frac{1}{\pi}\sqrt{\frac{5}{2}}\frac{\sigma_{\delta\varphi}(\tau_0)}{\sigma_{\delta\nu}(\tau_0)}. \tag{2.69}$$

For these convergent types of noise the Allan deviation coincides with the standard deviation. Therefore Eqs. (2.68) show the dependence of the Allan deviation on the duration of the measurement interval for phase and frequency noise. The Allan deviation of a signal containing various types of noise is plotted in Fig. 2-4. The slope of the Allan deviation as a function of measurement interval allows us to identify the type of noise present in the oscillator frequency as we see in Tab. 2.2.

2.4.2 Maser Frequency and Phase Noise

Even under ideal operating conditions, the maser frequency resolution is fundamentally limited by two independent manifestations of thermal noise: white frequency

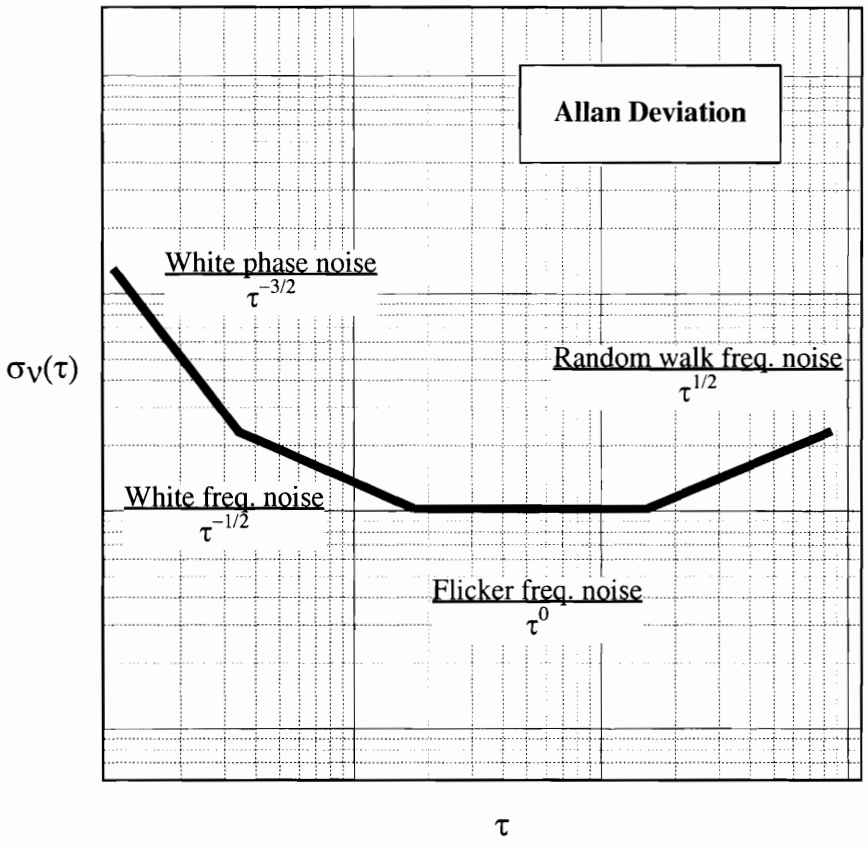

Figure 2-4: Log-Log plot of a generic Allan deviation. Different types of frequency noise dominate the frequency instability for different measurements intervals.

noise and added white phase noise. White frequency noise is caused by thermal radiation inducing a random walk in time of the phase of the coherent electromagnetic field produced by a noble gas maser, yielding the following limit on frequency [28]:

$$\sigma_\nu^{wf}(\tau) = \frac{1}{\pi T_2}\sqrt{\frac{k_B T_M}{2W_{ng}\tau}} \propto \tau^{-1/2}, \tag{2.70}$$

where T_M is the temperature of the masing region and W_{ng} is the radiated maser power.

μ	*Designation*
-1.5	White noise of phase
-0.5	White noise of frequency
0	Flicker noise of frequency
0.5	Random walk of frequency

Table 2.2: Common designations for the noise processes associated with values of μ in the expression $\sigma_\nu(\tau) \propto \tau^\mu$ [28].

Added white phase noise arises from the external amplification of the maser signals. The signal amplifiers multiply thermal noise present in the resonant signal detection circuits and also add noise due to their own finite temperature. The frequency stability limit is [28]:

$$\sigma_\nu^{wp}(\tau) = \frac{1}{2\pi\tau}\sqrt{\frac{k_B(T_{Coil}+T_{Amp})B}{W_{ng}}} \propto \tau^{-3/2}, \tag{2.71}$$

where $B \approx (\pi\tau)^{-1}$ is the measurement bandwidth and T_{Coil} and T_{Amp} are the pick-up coil and amplifier noise temperatures, respectively.

As we will see in Ch. 4, typical maser powers are $W_{He} = 0.5 - 30 \times 10^{-9}$ erg/s, $W_{Xe} = 5 - 40 \times 10^{-9}$ erg/s and the transverse coherence times T_2, are on the order of few hundred seconds. For $T_{Coil} = T_{Amp} = 30°$ C, $T_M = 50°$ C and $T_2 = 100$ s, approximate values for the expressions above are:

$$\sigma_\nu^{wf}(\tau) \approx \frac{15\ \mu\text{Hz}}{\sqrt{\tau W_{ng}/W_0}} \tag{2.72}$$

$$\sigma_\nu^{wp}(\tau) \approx \frac{820\ \mu\text{Hz}}{\sqrt{\tau^3 W_{ng}/W_0}} \tag{2.73}$$

where for convenience we have introduced $W_0 = 1 \times 10^{-9}$ erg/s, which is a typical maser power. For long measurement intervals, the thermal frequency noise dominates. In particular, $\sigma_\nu^{wf}(1{,}000\text{ s}) \approx 470\ n\text{Hz}\sqrt{W_0/W_{ng}}$ and $\sigma_\nu^{wf}(1\text{ day}) \approx$

51 $n\text{Hz}\sqrt{W_0/W_{ng}}$, so that ^{3}He maser powers lower than W_0, or interaction times shorter than 100 s may seriously limit the medium and long term stability of our masers. In order to improve the Lorentz Invariance and CPT violation sensitivity by a factor of 10 with respect to our previous results, we require that $\sigma_\nu^{wf}(1 \text{ day}) < 20$ nHz. This and other considerations will be explored further in the design studies for the new maser presented in Ch. 4.

Chapter 3

Testing Lorentz and CPT Symmetry Using a Two-Species Noble Gas Maser

3.1 Overview

All attempts to measure violations of fundamental laws of physics are ultimately precise measurements of zero when those laws withstand the test. Historically, in order to express the level of precision attained, in each experiment a set of coefficients were introduced whose existence would violate the law of physics in question and whose magnitude would be bound to a certain level by a null measurement. The general idea of this approach remains very useful, but makes it difficult to compare results obtained with different experiments and perform a systematic study of Lorentz and CPT violation across different fields of physics.

In this chapter we introduce the Standard Model Extension (SME) that allows us to interpret our tests of Lorentz and CPT symmetry. The SME is a very general

framework that introduces Lorentz and CPT violating terms to the Lagrangian describing elementary particles physics. Since the formalism of quantum field theory is not so common in atomic physics, we explicitly derive the perturbation induced, at low energies, by a symmetry breaking term that is particularly relevant for our experiment. We then present the full non-relativistic predictions of the SME, explicitly showing how Lorentz and CPT violating signals would arise in the $^{129}Xe/^{3}He$ maser and how we would detect them. We also compare our boost symmetry test, the first test of boost invariance[1] in the fermion sector (reported in App. A), with a classical test of Lorentz violation in electrodynamics: the Kennedy-Thorndike Experiment.

Finally, we show that our Zeeman masers are effectively NMR gyroscopes and as such are affected by frequency shifts induced by the Earth's rotation, which are constant in time when the masers are at rest in the laboratory. This completes the demonstration that any observed sidereal frequency modulations in our masers would be unequivocal sign of physics beyond the Standard Model. Having developed the necessary formalism, we then summarize advantages and disadvantages of operating our $^{129}Xe/^{3}He$ maser on a rotating platform.

3.2 The Standard Model Extension

Alan Kostelecký and coworkers [9, 10, 11, 12] have developed an extension to the Standard Model which provides a consistent and general framework for studying Lorentz violations, based at the level of the known elementary particles. The Lagrangian of the theory is formed using fields for the known elementary particles, and the possible Lorentz violations for each type of particle and interaction are con-

[1] "A restricted Lorentz transformation that describes the relation between two systems with parallel axes moving uniformly relatively to each other, i.e., without any spatial rotation, is called a pure Lorentz transformation or, in jargon, a boost" [38].

trolled by coefficients whose values are to be determined by experiment. Since atoms and ions are composed of these elementary particles, the behavior of different atoms and ions under rotations and boosts is determined by the coefficients for Lorentz violations in the theory. This Standard-Model Extension must emerge from any underlying theory that generates the Standard-Model and contains Lorentz violation [9]. It is a renormalizable field theory, and it has a variety of desirable features including energy momentum conservation, observer Lorentz covariance,[2] conventional quantization and hermiticity [11].

The purpose of this section is to illustrate how the SME connects experimental observations in complex systems, such as the ^{129}Xe/^{3}He maser, to fundamental Lorentz-violating interactions affecting fermions (neutrons in our case). Our masers oscillate on nuclear Zeeman transitions of ^{129}Xe and ^{3}He. Both are isotopes with nuclear spin $I = \frac{1}{2}$ and nuclei characterized to leading order by an unpaired neutron. The SME is simply the effective field theory that regulates the interaction of this neutron with several background tensor fields which could arise, for instance, from spontaneous Lorentz breaking in an underlying theory. The most general Lagrangian describing a single spin-$\frac{1}{2}$ Dirac fermion ψ of mass m in the presence of Lorentz violation is[3] [39, 16]

$$\mathcal{L} = \tfrac{1}{2} i \overline{\psi} \Gamma_\nu \overleftrightarrow{\partial^\nu} \psi - \overline{\psi} M \psi, \tag{3.1}$$

[2]The Lorentz-violating effects introduced by the SME on a physical system are described by the same set of equations for two observers in distinct inertial frames (observer Lorentz invariance). To actually observe Lorentz violation one must rotate or boost the system itself (particle Lorentz violation), in our case the ^{129}Xe/^{3}He maser, and detect changes in the system from within a fixed inertial frame (typically the Sun's rest frame).

[3]In this chapter we will use $\hbar = c = 1$ and standard definitions for operators like $A \overleftrightarrow{\partial}_\mu B \equiv A\partial_\mu B - (\partial_\mu A)B$ [9].

where

$$M = m + a_\mu \gamma^\mu + b_\mu \gamma_5 \gamma^\mu + \tfrac{1}{2} H_{\mu\nu} \sigma^{\mu\nu}, \tag{3.2}$$

$$\Gamma_\nu = \gamma_\nu + c_{\mu\nu} \gamma^\mu + d_{\mu\nu} \gamma_5 \gamma^\mu + e_\nu + i f_\nu \gamma_5 + \tfrac{1}{2} g_{\lambda\mu\nu} \sigma^{\lambda\mu}. \tag{3.3}$$

This represents an extension of the usual Lagrangian for a massive Dirac fermion field. The Dirac matrices $\{1, \gamma_5, \gamma^\mu, \gamma_5\gamma^\mu, \sigma^{\mu\nu}\}$ appearing in Eqs. (3.2) and (3.3) have conventional properties.

The Lorentz violation in Eq. (3.1) is governed by the coefficients a_μ, b_μ, $c_{\mu\nu}$, $d_{\mu\nu}$, e_μ, f_μ, $g_{\lambda\mu\nu}$, and $H_{\mu\nu}$. The hermiticity of $\mathcal{L}$ means that all the coefficients are real. The coefficients appearing in M have dimensions of mass, while those in Γ are dimensionless. Both $c_{\mu\nu}$ and $d_{\mu\nu}$ are traceless, while $H_{\mu\nu}$ is antisymmetric and $g_{\lambda\mu\nu}$ is antisymmetric in its first two indices.

The field operators in the terms with coefficients a_μ, b_μ, e_μ, f_μ, and $g_{\lambda\mu\nu}$ are odd under CPT, while the others are even. Since both the particle field and the background coefficients transform covariantly under rotations or boosts of an observer's inertial frame, the Lagrangian (3.1) remains invariant under observer Lorentz transformations. However, the background coefficients are unaffected by rotations or boosts of the particle or localized field in the same observer inertial frame, so the Lagrangian transforms nontrivially under particle Lorentz transformations [9, 10].

Lorentz-breaking effects are likely to be detectable only in experiments of exceptional sensitivity. Credible estimates for the order of magnitude of the coefficients are difficult to make in the absence of a realistic underlying theory. Various sources of suppression might arise. For example, if the origin of the Lorentz violation lies at the Planck scale M_P ($\approx 10^{19}$ GeV), one natural suppression factor would be some power of the ratio $r \approx m_l/M_P$, where m_l is a low-energy scale such as a particle mass.

Another natural factor could emerge from the coupling strengths in the underlying theory and could produce suppressions similar to those for the particle masses in the usual standard model, arising from the Yukawa couplings to the Higgs scalar field [9]. Other substantial suppression factors might also appear. A further potential complication is that some coefficients might be much more heavily suppressed than others. No specific assumptions are made about the absolute or relative magnitudes of the coefficients for Lorentz violation other than to suppose they are perturbative.

3.2.1 SME Low Energy Limit in a Simple Case

In order to illustrate how the Lagrangian (3.1) leads to a new interaction that violates Lorentz invariance by introducing a privileged direction in space-time, we study its predictions for a slow, free neutron, which we will assume to be stable (ultimately, we will be dealing with stable neutrons embedded in noble gas nuclei). For simplicity, we will assume that all SME coefficients vanish, with the only exception being the four vector $b^\mu = (b_0, \vec{b})$ in some frame (typically the Sun's rest frame).

For definiteness in what follows, we work within the Dirac-Pauli representation of the Dirac matrices, for which

$$\gamma^0 = \begin{pmatrix} 1 & 0 \\ 0 & -1 \end{pmatrix} \quad \text{and} \quad \gamma^j = \begin{pmatrix} 0 & \sigma^j \\ -\sigma^j & 0 \end{pmatrix}, \tag{3.4}$$

where σ^j are the usual Pauli matrices and $\gamma^5 = i\gamma^0\gamma^1\gamma^2\gamma^3$. The free Lagrangian (3.1) is then

$$\mathcal{L} = \tfrac{1}{2} i\overline{\psi}\gamma^\mu \overleftrightarrow{\partial}_\mu \psi - m\overline{\psi}\psi - b_\mu \overline{\psi}\gamma_5\gamma^\mu\psi, \tag{3.5}$$

where $\overline{\psi} = \psi^\dagger\gamma^0$. The last term, proportional to b is the small, Lorentz violating perturbation. The first two terms are nothing but the Dirac equation. Its four

eigenvalues $E_u^{(\alpha)}, E_v^{(\alpha)}$, with $\alpha = 1, 2$ and eigenvectors[4] are [40]:

$$|\psi^{(\alpha)}\rangle = \exp(-ip^{(\alpha)} \cdot x)|u^{(\alpha)}\rangle \quad , \qquad |\psi^{(\alpha)}\rangle = \exp(+ip^{(\alpha)} \cdot x)|v^{(\alpha)}\rangle, \tag{3.6}$$

where u is the positive energy solution for the neutron, v is the negative energy solution for the anti-neutron, while x and p are the position and momentum four-vectors, respectively. The spinors take the simple form

$$|u^{(\alpha)}\rangle = \sqrt{\frac{(E_u^{(\alpha)} + m)}{2m}} \begin{pmatrix} |\xi^{(\alpha)}\rangle \\ \frac{\vec{\sigma}\cdot\vec{p}}{E_u^{(\alpha)}+m}|\xi^{(\alpha)}\rangle \end{pmatrix} \quad , \tag{3.7}$$

$$|v^{(\alpha)}\rangle = \sqrt{\frac{(E_v^{(\alpha)} + m)}{2m}} \begin{pmatrix} \frac{\vec{\sigma}\cdot\vec{p}}{E_v^{(\alpha)}+m}|\xi^{(\alpha)}\rangle \\ |\xi^{(\alpha)}\rangle \end{pmatrix} \quad , \tag{3.8}$$

and $|\xi^{(1)}\rangle, |\xi^{(2)}\rangle$ are the well known Dirac spinors in 2 dimensions. In what follows we will concentrate exclusively on the equations that deal with the neutron. We need the neutron's eigenvectors in order to apply the standard perturbation theory, and since we are interested in the non-relativistic limit it is convenient to keep only terms up to second order[5] in p/m and find the appropriate normalization N,

$$|u^{(\alpha)}\rangle = N \begin{pmatrix} |\xi^{(\alpha)}\rangle \\ \frac{\vec{\sigma}\cdot\vec{p}}{2m}|\xi^{(\alpha)}\rangle \end{pmatrix} \quad , \quad N^2 = \frac{1}{1 + \frac{p^2}{4m^2}}. \tag{3.9}$$

The last term in Eq. (3.5) is the 4×4 perturbation matrix from which we can

[4]To be consistent with the most common low-energy formalism we use from now on the bra-ket notation. Hence, ψ becomes $|\psi\rangle$ and its dual $\psi^\dagger$ is $\langle\psi|$.

[5]The momentum p we are dealing with is the generalized momentum of this theory and does not coincide with the classical momentum. In fact, the neutron's velocity in the relativistic case depends on b_μ [9]: $\langle\vec{v}\rangle = \langle\frac{p-b_0}{E}\hat{p}\rangle$. This means that in this theory, when $b_0 \neq 0$, a particle at rest has nonzero (generalized) momentum!

obtain the 2×2 perturbation matrix $h^{'}$ valid up to second order in p/m:

$$\begin{aligned}
\langle u^{(\alpha)}| - b_\mu \gamma^0 \gamma_5 \gamma^\mu |u^{(\alpha)}\rangle &= \langle u^{(\alpha)}| \begin{pmatrix} -\vec{\sigma}\cdot\vec{b} & b_0 \\ b_0 & -\vec{\sigma}\cdot\vec{b} \end{pmatrix} |u^{(\alpha)}\rangle \\
&\approx N^2 \langle \xi^{(\alpha)}| - \vec{\sigma}\cdot\vec{b} + b_0 \frac{\vec{\sigma}\cdot\vec{p}}{m} - \frac{(\vec{\sigma}\cdot\vec{p})(\vec{\sigma}\cdot\vec{b})(\vec{\sigma}\cdot\vec{p})}{4m^2} |\xi^{(\alpha)}\rangle \\
&= \langle \xi^{(\alpha)}| h^{'} |\xi^{(\alpha)}\rangle. \qquad (3.10)
\end{aligned}$$

After some manipulation $h^{'}$ can be rewritten in the following form

$$h^{'} = -\vec{\sigma}\cdot\vec{b} + b_0 \frac{\vec{\sigma}\cdot\vec{p}}{m} - \frac{(\vec{b}\cdot\vec{p})(\vec{\sigma}\cdot\vec{p})}{2m^2} + \frac{(\vec{\sigma}\cdot\vec{b})p^2}{2m^2}, \qquad (3.11)$$

and $\vec{\sigma}$ is proportional to the spin operator $\vec{S} = \frac{\vec{\sigma}}{2}$. Thus we see that the energy of the neutron depends on the orientation of its spin with respect to the background field $\vec{b}$, which acts analogously to a magnetic field. Additionally for a moving neutron, there is a spin boost dependent energy proportional to the time-like component of b_0, as well as higher-order terms.

Sidereal Modulations

Next we will assume that the neutron is at rest in the laboratory[6] and is immersed in a magnetic field $\vec{B}$. The leading-order non-relativistic Hamiltonian takes the simple form

$$h = -\vec{\mu}_n \cdot \vec{B} + h^{'} = -\vec{\mu}_n \cdot \vec{B} - \vec{\sigma}\cdot\vec{b} \qquad (3.12)$$

where $h^{'}$ is the interaction Hamiltonian of Eq. (3.11) and and $\vec{\mu}_n$ is the magnetic moment of the neutron. Assuming that the magnetic field is directed along $\hat{y}$ and

[6]The valence neutron of a ^{129}Xe or ^{3}He atom at rest is in a bound state. This means that on average only the even powers of p/m do not vanish. We will deal with this issue in the next section.

that $h^{'}$ is a small perturbation, the precession frequency is

$$\begin{aligned} \omega_n &= \langle S, S_2 = -\tfrac{1}{2}|h|S, S_2 = -\tfrac{1}{2}\rangle - \langle S, S_2 = \tfrac{1}{2}|h|S, S_2 = \tfrac{1}{2}\rangle \\ &= \gamma_n B_0 + 2b_2, \end{aligned} \tag{3.13}$$

where γ_n is the gyromagnetic ratio of the neutron and $\vec{S} = \frac{\vec{\sigma}}{2}$ is the spin operator.

The frequency shift $\delta\omega_n = 2b_2$ acquires a time dependence because of the rotation of the Earth and its revolution around the Sun. The SME assumes that the Lorentz violating background fields are roughly homogeneous over astronomic distances and static, or quasi-static, in the Sun's rest frame on the time-scale of a solar year.

We refer to the parameters of the standard model extension that have been bound experimentally, in the Sun's rest frame, and capitalize the indexes $\Sigma = T, X, Y, Z$, while the laboratory indexes are usually lowercase letters, or numbers $\alpha = 0, 1, 2, 3 = t, x, y, z$. Following the SME conventions, we choose a set of laboratory coordinates such that the $\hat{x}$ axis points south, the $\hat{y}$ axis east, and the $\hat{z}$ axis vertically upwards in the laboratory. The Sun-centered frame uses celestial equatorial coordinates. The angle between the $\hat{X}\hat{Y}$ celestial equatorial plane and the Earth's orbital plane is $\eta = 23.4°$ (see Fig. 3-1). The Earth's sidereal angular rotation frequency is $\omega_\oplus \simeq 2\pi/(23 \text{ h } 56 \text{ min})$, and χ is the colatitude of the laboratory. The time $T_\oplus$ is measured in the Sun-centered frame from the beginning of the sidereal day, which begins when the $\hat{y}$ and $\hat{Y}$ axes align. With the reasonable approximation that the orbit of the Earth is circular,[7] the rotation, $R_\alpha{}^\Sigma$, from the Sun-centered celestial

[7]The eccentricity of the Earth's orbit is only 0.0167 [41].

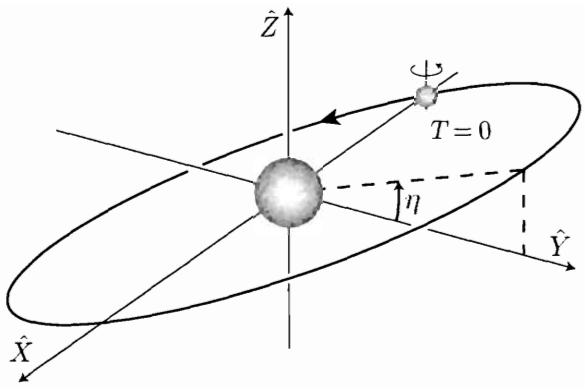

Figure 3-1: Earth's orbit around the Sun and Sun-centered frame using celestial equatorial coordinates. The angle between the $\hat{X}\hat{Y}$ celestial equatorial plane and the Earth's orbital plane is $\eta = 23.4°$. By convention, the origin of time coincides with the instant in which Earth crossed the equatorial plane during the vernal equinox of year 2000.

equatorial frame to the standard laboratory frame is given by:

$$R_\alpha{}^\Sigma = \begin{pmatrix} 1 & 0 & 0 & 0 \\ 0 & \cos\chi\ \cos\omega_\oplus T_\oplus & \cos\chi\ \sin\omega_\oplus T_\oplus & -\sin\chi \\ 0 & -\sin\omega_\oplus T_\oplus & \cos\omega_\oplus T_\oplus & 0 \\ 0 & \sin\chi\ \cos\omega_\oplus T_\oplus & \sin\chi\ \sin\omega_\oplus T_\oplus & \cos\chi \end{pmatrix}. \tag{3.14}$$

The velocity 3-vector of the laboratory in the Sun-centered frame is composed of terms proportional to the orbital velocity $\beta_\oplus$ and the rotation β_L:

$$\vec{\beta} = \beta_\oplus \begin{pmatrix} sin\Omega_\oplus T \\ -cos\eta\ cos\Omega_\oplus T \\ -sin\eta\ cos\Omega_\oplus T \end{pmatrix} + \beta_L \begin{pmatrix} -sin\omega_\oplus T_\oplus \\ cos\omega_\oplus T_\oplus \\ 0 \end{pmatrix}. \tag{3.15}$$

Here, $\Omega_\oplus$ is the angular frequency of the Earth's orbital motion. The time T is measured by a clock at rest at the origin from the instant in which Earth crossed

the equatorial plane during the vernal equinox of year 2000. T and $T_\oplus$ are equivalent, modulo the sidereal day period.

In what follows we ignore the laboratory's velocity due to the rotation of the Earth,[8] whose magnitude, $\beta_L = r_\oplus \omega_\oplus \sin\chi/c \simeq 1.1 \times 10^{-6}$ (where $r_\oplus$ is the radius of the Earth), is two orders of magnitude smaller than the orbital velocity $v_\oplus/c = \beta_\oplus \simeq 9.9 \times 10^{-5}$. To first order in $\vec{\beta}$ the 4×4 boost matrix is:[9]

$$B_\alpha{}^\Sigma = \begin{pmatrix} 1 & -\vec{\beta}^T \\ -\vec{\beta} & I_{3\times 3} \end{pmatrix}. \tag{3.16}$$

Since we assume observer Lorentz covariance a direct Lorentz transformation, $b_\alpha = (RB)_\alpha{}^\Sigma\, b_\Sigma$, yields the relevant coefficients in the laboratory frame. The neutron's precession frequency is

$$\begin{aligned} \omega_n = \gamma B_0 + 2b_2 = \;& \gamma B_0 - (2b_X + 2b_T\beta_\oplus \sin\Omega_\oplus T)\sin\omega_\oplus T_\oplus + \\ & (2b_Y - 2\cos\eta b_T \beta_\oplus \cos\Omega_\oplus T)\cos\omega_\oplus T_\oplus. \end{aligned} \tag{3.17}$$

Because of the Lorentz and CPT violating background field b_μ, the Earth's rotation induces daily sidereal modulations of the neutron precession frequency (of frequency $\omega_\oplus$), while the boost transformation induces a sinusoidal variation of the daily modulation amplitude over the course of the sidereal year (of frequency $\Omega_\oplus$) as the direction of the velocity of the Earth varies with respect to the Sun. Thus the effects of rotation and boost symmetry violation can be clearly distinguished. These equations indicate that the sensitivity of our experiment to violations of

[8] In Sect. 3.3.1 we will see that this approximation leads us to neglect boost effects responsible for a constant frequency shift and frequency modulations at twice the sidereal frequency, both of order β_L.

[9] The most general expression for the boost matrix will be introduced in Sect. 3.2.3.

Measurable parameters	SME Coefficients
λ_c	$2\ b_Y$
λ_s	$-2\ b_X$
Λ_{cc}	$-2\cos\eta\ b_T$
Λ_{cs}	0
Λ_{ss}	$-2\ b_T$
Λ_{sc}	0

Table 3.1: Observable coefficients of the sidereal modulations in the Zeeman frequency of a free neutron at rest on Earth as defined in Eq. (3.18). For the simple Lorentz-invariance violating theory introduced in Eq. (3.5), the observable coefficients are simply expressed in terms of few SME coefficients.

boost-symmetry is reduced by a factor of $\beta_\oplus \simeq 10^{-4}$ with respect to the sensitivity to rotation-symmetry violation. However, we will show in Sect. 3.2.3 that for some models of Lorentz violation that are isotropic in the frame of the cosmic microwave background, our experiment has greater sensitivity to boost-symmetry violation than to rotation-symmetry violation.

A Standard Notation

When all the background coefficients are considered, the expression for the neutron precession frequency (or equivalently the maser frequency), to first order in $\beta_\oplus$, contains additional terms. It is convenient to define a general, time dependent frequency shift as follows:

$$\delta\omega = \delta\omega_X\ \sin\omega_\oplus T_\oplus + \delta\omega_Y\ \cos\omega_\oplus T_\oplus, \tag{3.18}$$

where

$$\begin{aligned}\delta\omega_X &= \lambda_s + \beta_\oplus(\Lambda_{ss}\sin\Omega_\oplus T + \Lambda_{sc}\cos\Omega_\oplus T), \\ \delta\omega_Y &= \lambda_c + \beta_\oplus(\Lambda_{cs}\sin\Omega_\oplus T + \Lambda_{cc}\cos\Omega_\oplus T).\end{aligned} \tag{3.19}$$

The parameters λ_c, λ_s, Λ_{ss}, $\Lambda_{sc}, \ldots$ are reported in Tab. 3.1. We will use similar tables to show the details of other models.

3.2.2 The Full Non-Relativistic Theory for the ^{129}Xe/^{3}He Maser

In the previous section we studied a simplified version of the SME for a neutron at rest in a magnetic field. The relativistic Hamiltonian of the full system can be found from the Lagrangian $\mathcal{L}$ and the non-relativistic momentum-space Hamiltonian h can then be derived using Foldy-Wouthuysen techniques [42]. We keep only terms up to second order in p/m [43] :

$$\begin{aligned} h &= m + \frac{p^2}{2m} + (a_0 - mc_{00} - me_0) + \left(-b_j + md_{j0} - \tfrac{1}{2}m\varepsilon_{jkl}g_{kl0} + \tfrac{1}{2}\varepsilon_{jkl}H_{kl}\right)\sigma^j \\ &\quad + \left[-a_j + m(c_{0j} + c_{j0}) + me_j\right]\frac{p_j}{m} \\ &\quad + \left[b_0\delta_{jk} - m(d_{kj} + d_{00}\delta_{jk}) - m\varepsilon_{klm}(\tfrac{1}{2}g_{mlj} + g_{m00}\delta_{jl}) - \varepsilon_{jkl}H_{l0}\right]\frac{p_j}{m}\sigma^k \\ &\quad + \left[m(-c_{jk} - \tfrac{1}{2}c_{00}\delta_{jk})\right]\frac{p_jp_k}{m^2} \\ &\quad + \left\{\left[m(d_{0j} + d_{j0}) - \tfrac{1}{2}\left(b_j + md_{j0} + \tfrac{1}{2}m\varepsilon_{jmn}g_{mn0} + \tfrac{1}{2}\varepsilon_{jmn}H_{mn}\right)\right]\delta_{kl}\right. \\ &\quad \left. + \tfrac{1}{2}\left(b_l + \tfrac{1}{2}m\varepsilon_{lmn}g_{mn0}\right)\delta_{jk} - m\varepsilon_{jlm}(g_{m0k} + g_{mk0})\right\}\frac{p_jp_k}{m^2}\sigma^l. \end{aligned} \tag{3.20}$$

In the Schmidt nuclear model the valence neutron of ^{3}He and ^{129}Xe is in a bound $s_{1/2}$ wave,[10] for which $\langle\vec{p}\rangle = 0$. More generally, for a bound nucleon, the expectation value of any odd power of the momentum $\vec{p}$ vanishes and because of the spherical symmetry of the $s_{1/2}$ state, we have $\langle p_j^2\rangle = \langle p^2\rangle/3$. Therefore, the expectation value

[10] In this model a single nucleon is assumed to carry the entire angular momentum of the nucleus [44, 21].

$h_s = \langle s_{1/2}|h|s_{1/2}\rangle$ of the Hamiltonian above is

$$\begin{aligned} h_s &= m + \frac{\langle p^2\rangle}{2m} + \left[a_0 - mc_{00}\left(1 + \tfrac{1}{2}\frac{\langle p^2\rangle}{m^2}\right) - me_0\right] \\ &\quad - \left[\tilde{b}_j + \left(\tilde{g}_{D,j} - \tilde{d}_j\right)\frac{\langle p^2\rangle}{3m^2}\right]\sigma^j, \end{aligned} \tag{3.21}$$

where we have used the following definitions

$$\tilde{b}_j = b_j - md_{j0} + \tfrac{1}{2}m\varepsilon_{jkl}g_{kl0} - \tfrac{1}{2}\varepsilon_{jkl}H_{kl} \tag{3.22}$$

$$\tilde{d}_j = m(d_{0j} + \tfrac{1}{2}d_{j0}) - \tfrac{1}{4}\varepsilon_{jmn}H_{mn} \tag{3.23}$$

$$\tilde{g}_{D,j} = m\varepsilon_{jmn}\left(\tfrac{1}{2}g_{mn0} + g_{m0n}\right) - b_j. \tag{3.24}$$

When the two noble gases are immersed in the same magnetic field $\vec{B} = B_0\hat{j}$, h_s is simply a perturbation that shifts the Zeeman levels of both gases equally. Using the Hamiltonian $H = -\vec{\mu}_{ng}\cdot\vec{B} + h_s$ the effective Larmor precession frequency of the gases is simply:

$$\begin{aligned} \omega_{ng} &= \langle I, I_j = -\tfrac{1}{2}|H|I, I_j = -\tfrac{1}{2}\rangle - \langle I, I_j = \tfrac{1}{2}|H|I, I_j = \tfrac{1}{2}\rangle \\ &= \gamma_{ng}B_0 + 2\tilde{b}_j + 2\left(\tilde{g}_{D,j} - \tilde{d}_j\right)\frac{\langle p^2\rangle}{3m^2}. \end{aligned} \tag{3.25}$$

Notice however that the precession frequency of each noble gas is proportional to $\gamma_{ng}B_0$. Tiny sidereal modulations of the Larmor frequency of a single noble gas species would be difficult to distinguish from the instabilities caused by fluctuations on B_0. Therefore, we employ two co-located species with different γ_{ng} and use one of the two frequencies, usually ^{129}Xe, as a co-magnetometer to stabilize the magnetic field. We then look for sidereal modulations in the (angular) frequency of

the free-running species, usually ^{3}He:

$$\begin{aligned} |\delta\omega_{He}| &= \left|\omega_{He} - \frac{\gamma_{He}}{\gamma_{Xe}}\omega_{Xe}\right| \\ &= \left|2\left(1 - \frac{\gamma_{He}}{\gamma_{Xe}}\right)\left[\tilde{b}_j + \left(\tilde{g}_{D,j} - \tilde{d}_j\right)\frac{\langle p^2\rangle}{3m^2}\right]\right| \\ &= \left|3.5\tilde{b}_j + 0.012\left(\tilde{g}_{D,j} - \tilde{d}_j\right)\right|. \end{aligned} \tag{3.26}$$

In this expression we have used $\frac{\gamma_{He}}{\gamma_{Xe}} = 2.75$ and the numerical values obtained in [21] using the Schmidt model.[11] The actual frequency shift in nHz is most useful once recast in the form:

$$|\delta\nu_{He}| = k\left|\tilde{b}_j + 0.0034\left(\tilde{g}_{D,j} - \tilde{d}_j\right)\right|. \tag{3.27}$$

The definition of the constant,

$$k = \frac{3.5}{2\pi\hbar} \approx 8.46 \times 10^{32}\ \text{nHz/GeV}, \tag{3.28}$$

takes into account that the SME coefficients are usually given in GeV to provide direct comparison of the background fields' interaction energy with the nucleons' rest masses (~ 1 GeV).

Equation (3.27) can be used to obtain the time-dependent expression containing the SME parameters relative to the Sun's rest frame, with the same procedure used for the neutron in the last section. The outcome of this calculation and the experimental results of our search for sidereal modulations of the maser frequencies are reported in App. A.

[11] Notice that in Ref. [21] there is a sign error, that was subsequently corrected in Ref. [24].

3.2.3 A Lorentz Violating Model Isotropic in the CMB Frame

Here we will briefly present a model showing how a boost-symmetry test could be more sensitive than a rotation-symmetry test, despite the suppression of boost effects with respect to rotation effects by a factor β, i.e., the boost velocity (see Sect. 3.2.1). This model is briefly introduced in note [24] of our published result (see Appp. A) and mimics a set of assumptions often made in the literature dealing with Lorentz Violation [45]. We suppose that the preferred frame for the SME is that of the cosmic microwave background (CMB), not the Sun's rest frame. We also assume that the vacuum is spatially isotropic in that frame.

In order to simplify the theory as much as possible we suppose that all SME coefficients vanish, except the following:

$$(b_{CMB})_\Lambda = \begin{pmatrix} 4\,d\,m \\ 0 \\ 0 \\ 0 \end{pmatrix}, \quad (d_{CMB})_{\Lambda\Sigma} = \begin{pmatrix} 3\,d & 0 & 0 & 0 \\ 0 & d & 0 & 0 \\ 0 & 0 & d & 0 \\ 0 & 0 & 0 & d \end{pmatrix}. \tag{3.29}$$

For b_{CMB} to be spatially isotropic, the only non-vanishing component must be b_0. The structure of d_{CMB} is also completely determined if it has to be spatially isotropic and traceless.[12] Furthermore we choose $b_0 = 4\,d\,m$, where d is just a constant and m is the neutron mass.[13]

The effect of this theory on the Zeeman frequency of one of our noble gas species

[12] $d_{\mu\nu}$ must be traceless (in the Minkowski sense) for the neutron wave function to have the standard meaning.

[13] This *ad hoc* choice produces a (not-so-accidental) cancellation of the signal arising from rotation-symmetry violation.

Parameters	SME Coefficients
λ_c	$O(\beta_\oplus^2 \beta_{CMB})$
λ_s	$O(\beta_\oplus^2 \beta_{CMB})$
Λ_{cc}	$2md\beta_{CMB}^2[\cos(\eta)\ \left(1+\cos(\alpha)^2\cos(\delta)^2+5\cos(\delta)^2\sin(\alpha)^2+\sin(\delta)^2\right)$ $+4\ \cos(\delta)\ \sin(\alpha)\ \sin(\delta)\ \sin(\eta)]$
Λ_{cs}	$-4md\beta_{CMB}^2\cos(\delta)^2\ \sin(2\,\alpha)$
Λ_{ss}	$2md\beta_{CMB}^2(1+5\cos(\alpha)^2\cos(\delta)^2+\cos(\delta)^2\sin(\alpha)^2+\sin(\delta)^2)$
Λ_{sc}	$-8md\beta_{CMB}^2\cos(\alpha)\ \cos(\delta)\ (\cos(\delta)\ \cos(\eta)\ \sin(\alpha)+\sin(\delta)\ \sin(\eta))$

Table 3.2: Observable parameters of the sidereal modulations in the Zeeman frequency of a free neutron at rest on Earth as defined in Eq. (3.18). In the Lorentz violating model given in Eq. (3.29) the rotation-symmetry violating parameters λ_c and λ_s are of order $\beta_\oplus^2\beta_{CMB} \approx 10^{-11}$, while the boost-symmetry violating parameters Λ_{cc}, Λ_{cs}, Λ_{sc}, Λ_{ss} are of order $\beta_{CMB}^2 \approx 10^{-6}$. This is sufficient to more than offset the factor of $\beta_\oplus^2 \approx 10^{-4}$ that usually makes boost-symmetry tests less sensitive than rotation-symmetry tests.

is:

$$\omega_{ng} = \gamma_{ng}B_0 + 2\tilde{b}_j + O(\frac{p^2}{m^2}) \tag{3.30}$$

$$\approx \gamma_{ng}B_0 + 2(b_2 - md_{20}), \tag{3.31}$$

where we have neglected the small momentum dependent terms.

To obtain the time dependence of the above equation we must find the boost B' from the CMB-frame to the Sun-centered frame. The velocity of the CMB frame is

$$\vec{\beta}_{CMB} = \beta_{CMB}(\cos\delta\cos\alpha, \cos\delta\sin\alpha, \sin\delta), \tag{3.32}$$

where α and δ are respectively the right ascension and the declination of the CMB's velocity. Since we are interested in the terms up to the second order in $\beta_{CMB} \simeq 10^{-3}$ (as usual, we keep only the first order in $\beta_\oplus \simeq 10^{-4}$) we need to use the general boost matrix [46]:

$$B'(\vec{\beta}_{CMB}) = e^{-\hat{\beta}_{CMB}\cdot\vec{K}\tanh^{-1}\beta_{CMB}}, \tag{3.33}$$

which makes use of the boost generators:

$$K_1 = \begin{pmatrix} 0 & 1 & 0 & 0 \\ 1 & 0 & 0 & 0 \\ 0 & 0 & 0 & 0 \\ 0 & 0 & 0 & 0 \end{pmatrix}, K_2 = \begin{pmatrix} 0 & 0 & 1 & 0 \\ 0 & 0 & 0 & 0 \\ 1 & 0 & 0 & 0 \\ 0 & 0 & 0 & 0 \end{pmatrix}, K_3 = \begin{pmatrix} 0 & 0 & 0 & 1 \\ 0 & 0 & 0 & 0 \\ 0 & 0 & 0 & 0 \\ 1 & 0 & 0 & 0 \end{pmatrix}. \quad (3.34)$$

We are now able to write the Lorentz transformation $\Lambda_\alpha{}^\Sigma = (RBB')_\alpha{}^\Sigma$ that takes a vector in the CMB-frame and gives its components in the laboratory frame using the rotation R, the boost B defined in the Sect. 3.2.1, and the additional boost B' just derived.

The results of our calculation show that the rotation-symmetry violating parameters λ_c and λ_s defined in Eq. (3.18) are of order $\beta_\oplus^2 \beta_{CMB} \approx 10^{-11}$, while the boost-symmetry violating parameters Λ_{cc}, Λ_{cs}, Λ_{sc}, Λ_{ss} are of order $\beta_{CMB}^2 \approx 10^{-6}$ (see Tab. 3.2). Even if the latter are suppressed by a factor $\beta_\oplus^2 \approx 10^{-4}$, their contribution, stemming from boost-symmetry violation, will still dominate the frequency shifts.

3.3 Comparison of Lorentz Invariance Violation Bounds from the ^{129}Xe/^{3}He Maser and From Other Experiments.

Our test of boost symmetry is presented in App. A [1]. In Tab. 3.3 we show the current bounds on the SME coefficients for the fermion sector. The bounds obtained with the ^{129}Xe/^{3}He maser [1, 24, 25] (for both rotation and boost symmetry) are in bold type. The other bounds were obtained with very diverse experiments that in-

Parameter	p^+	n	e^-	Ref.
$\tilde{b}_X$, $\tilde{b}_Y$	10^{-27}	$\mathbf{10^{-31}}$	10^{-29}	[22], [24, 25], [50, 51]
$\tilde{b}_Z$	-	-	10^{-28}	[50, 51]
$\tilde{b}_T$, $\tilde{g}_T$, $\tilde{H}_{JT}$, $\tilde{d}_\pm$	-	$\mathbf{10^{-27}}$	-	[1]
$\tilde{d}_Q$, $\tilde{d}_{XY}$, $\tilde{d}_{YZ}$	-	$\mathbf{10^{-27}}$	-	[1]
$\tilde{d}_X$, $\tilde{d}_Y$	10^{-25}	$\mathbf{10^{-29}}$	10^{-22}	[21], [24, 25], [21]
$\tilde{d}_{XZ}$, $\tilde{d}_Z$	-	-	-	
$\tilde{g}_{DX}$, $\tilde{g}_{DY}$	10^{-25}	$\mathbf{10^{-29}}$	10^{-22}	[21], [24, 25], [21]
$\tilde{g}_{DZ}$, $\tilde{g}_{JK}$	-	-	-	
$\tilde{g}_c$	-	$\mathbf{10^{-27}}$	-	[1]
$\tilde{g}_-$, $\tilde{g}_Q$, $\tilde{g}_{TJ}$	-	-	-	
$\tilde{c}_Q$	10^{-22}	-	10^{-9}	[48, 49]
$\tilde{c}_X$, $\tilde{c}_Y$	10^{-24}	10^{-25}	10^{-19}	[21], [53, 47, 52]
$\tilde{c}_Z$, $\tilde{c}_-$	10^{-24}	10^{-27}	10^{-19}	[21], [53, 47, 52]
$\tilde{c}_{TJ}$	10^{-20}	-	10^{-6}	[48, 49]

Table 3.3: Orders of magnitude of present limits (in GeV) on Lorentz violating parameters in the minimal SME matter sector and corresponding references. Indeces J, K run over X, Y, Z with $J \neq K$. Limits from the $^{129}Xe/^3He$ maser are in bold type. This summary table was compiled by Peter Wolf *et al.* [54].

clude: a clock-comparison test employing a cryogenic sapphire microwave resonator and a hydrogen maser [47], doppler-shift measurements on fast $^7Li^+$ ions [48, 49], a clock-comparison test between magnetic field dependent and magnetic field independent hyperfine transitions in a Hydrogen maser [22], monitoring of a rotatable torsion balance carrying a transversely spin-polarized ferrimagnetic Dy_6Fe_{23} mass [50, 51], and a clock-comparison test between the resonance frequencies of two orthogonal cryogenic optical resonators [52].

3.3.1 Comparison with a Classical Test of Boost Symmetry in the Photon Sector

In this section we compare our test of boost invariance (presented in Appendix A) in the fermion sector with a classical boost invariance test in the photon sector: the Kennedy-Thorndike experiment (KT) [55]. This test, like the Michelson-Morley experiment (MM), has been fundamental in the history of physics and the two together condition the way most physicists understand Lorentz invariance [56]. In part, the reason why these tests are so well known is that they are communicated in a model independent way, focusing on the invariance of the velocity of light. The corresponding quantity that remains invariant in our experiment, if Lorentz symmetry is exact in the fermion sector, is the energy difference between the two Zeeman levels between which our masers oscillate.

Before we proceed, it is useful to complement the $\delta\nu_{He}$ given in Eq. (1.4) with a few terms that we had previously neglected. This enables us to compare our experiment with modern KT experiments.

When we performed a boost transformation in the derivation of Eq. (1.4), we noted that the Earth's orbital velocity $\beta_\oplus \approx 10^{-4}$ was dominant compared to the laboratory velocity $\beta_L \approx 10^{-6}$ (at the latitude of Cambridge, MA). If we include this velocity boost, Eq. (1.4) acquires three more terms. The complete expression for the predicted frequency shifts of the free-running ^{3}He maser is:

$$\begin{aligned}\delta\nu_{\rm He} &= k[(\lambda_s + \beta_\oplus(\Lambda_{ss}\sin\Omega_\oplus T + \Lambda_{sc}\cos\Omega_\oplus T))\sin\omega_\oplus T_\oplus \\ &\quad +(\lambda_c + \beta_\oplus(\Lambda_{cs}\sin\Omega_\oplus T + \Lambda_{cc}\cos\Omega_\oplus T))\cos\omega_\oplus T_\oplus \\ &\quad +\beta_L\,(\Lambda_0 + \Lambda_{c2}\cos 2\omega_\oplus T_\oplus + \Lambda_{s2}\sin 2\omega_\oplus T_\oplus)]. \qquad (3.35)\end{aligned}$$

Combinations of SME coefficients	Fit parameters
$\tilde{g}_T - 2\tilde{d}_+ \frac{1}{2}\tilde{d}_Q$	Λ_0
$\frac{1}{2}\tilde{b}_T - \frac{1}{2}\tilde{d}_- \tilde{g}_c - \frac{1}{2}\tilde{g}_T$	Λ_{c2}
$\frac{1}{2}\tilde{d}_{XY}$	Λ_{s2}

Table 3.4: This table completes the results showed in Tab. II of App. A for the ^{129}Xe/^{3}He maser. We report here the coefficients suppressed by a factor $\beta_L \approx 10^{-6}$, which had been neglected in the previous treatment. Notice that whereas Λ_{c2} and Λ_{s2} could be measured by looking for modulations of the $\delta\nu_{He}$ at twice the daily sidereal modulations, the term Λ_0 is a constant frequency shift that we are not able to measure.

The new terms, proportional to β_L, are Λ_0, Λ_{c2}, and Λ_{s2} and are combinations of the SME coefficients (see Tab. 3.4) that have not been measured. Λ_{c2} and Λ_{s2} correspond to modulations at twice the frequency of the Earth's rotation and in principle they could be measured with our experiment. Instead, we cannot measure Λ_0 since we are not able to resolve constant frequency offsets.

Kennedy-Thorndike Experiment

While the MM experiment proves that the velocity of light is isotropic in any boosted frame, the KT experiment demonstrates that the velocity of light is the same in all inertial frames irrespective of their velocity. The classic KT experiment searched for an annual modulation of the diffraction pattern of an unequal-arm interferometer. The maximum velocity change achievable in fixed laboratories on the Earth was given by twice the velocity of revolution of the Earth (2×30 km/s). However, it took 6 months to realize this major boost and stability of the apparatus was acceptable for only a few consecutive months, or sometimes a few weeks.

Current KT experiments [57, 58, 52] look for 24 h sidereal variations in the frequency of a stabilized laser compared with a laser locked to a stable cavity. The maximum velocity change happens over 12 h because of the Earth's rotation ($2 \times$

300 m/s depending on latitude). The factor of 100 smaller velocity is outweighed by the greater stability of clocks over the shorter measurement interval (24 hours, instead of months).

^{129}Xe/^{3}He Maser

Our experiment involves the comparison of a frequency defined by an H maser (no leading-order sensitivity to Lorentz violation as we saw in Ch. 1) and the precession frequency of noble gas spins in a stable magnetic field. Measuring the daily sidereal frequency modulations corresponding to λ_c and λ_s in Eq. (3.35) is equivalent to performing a MM experiment. Instead of observing a periodic shift in the interference fringes as the equal-arm interferometer is rotated, we would observe a periodic modulation of our masers' frequencies.

The SME predicts a boost effect due to the Earth's rotation, which determines the 12 h period modulations associated with the parameters Λ_{c2} and Λ_{s2}. This effect is similar to the daily sidereal modulations sought for in modern KT experiments. The sensitivity to Λ_{c2} and Λ_{s2}, however, is a factor of 100 smaller than the sensitivity to Λ_{cc}, Λ_{cs}, Λ_{ss}, and Λ_{sc}, which are simply different combinations of the same SME coefficients entering Λ_{c2} and Λ_{s2}. For this reason our best bounds on boost invariance come from the terms proportional to $\beta_\oplus$ reported in App.A. Compared to old and modern-style KT experiments, we get the best of both worlds: we profit of the larger boost provided by the Earth's orbital velocity, while our oscillators need only be very stable over a day.

3.4 Inertial Effects and Noble Gas Masers

Our noble gas masers are also NMR gyroscopes. We therefore investigate inertial effects on our masers and their impact on our Lorentz symmetry tests. Our goal is twofold. First, we want to find out whether simple inertia may produce daily or annual precession frequency modulations similar to those induced by Lorentz symmetry violation. This concern is at least in principle justified, since the laboratory frame is not inertial. Second, we want to study the frequency modulations that would arise if we rotated our experiment with the help of a rotating platform.[14] In particular we want to find out whether we should expect inertial signals with a signature similar to that of Lorentz violation and, if this were the case, how hard it would be to distinguish between the two signals.

Masers at rest in the laboratory are affected by a constant frequency shift due to the Earth's rotation (this is the same shift that makes a Focault pendulum precess at constant angular frequency), but there are no time dependent modulations. The revolution of the Earth around the Sun is not responsible for a daily frequency modulations, either. In Sect. 3.4.2 we present an erroneous line of reasoning that brought us to believe such a modulation was possible. We found quite instructive what we learned from our mistake: Analyzing the precession of orbiting gyroscopes in the context of Special Relativity (SR) alone, leads to a contradiction with Einstein's Equivalence Principle. We end Sect. 3.4.2 showing that the Equivalence Principle predicts another tiny ($\sim 10^{-14}$ Hz) constant frequency shift ascribable to the forces that keep our noble gas atoms safely inside the maser cell in the laboratory. This

[14] In principle, this could be advantageous for two reasons: (i) by reducing the rotation time we could make more measurements in the same time span, which would augment statistics and improve precision; (ii) shorter rotation times would also match the stability of our masers which, before the latest reengineering, tended to be most stable for measurement times of approximately 2 h (see Sect. 4.1).

completes the demonstration that, when our masers are fixed in the laboratory, any observation of a daily or annual sidereal modulation would be unequivocal demonstration of Lorentz symmetry violation. In Sect. 3.4.3 we describe the technical challenges to the possibility of ever operating our masers on a rotating platform for the purpose of testing Lorentz invariance.

3.4.1 NMR Gyroscopes

Traditional spinning-wheel, torque-free gyroscopes provide a maintainable reference direction in space. Conservation of angular momentum ensures that the direction around which the wheel rotates remains constant, if its moment of inertia does. An atom endowed with intrinsic nuclear angular momentum, i.e., nuclear spin, in the absence of magnetic fields behaves exactly as a spinning-wheel, hence the possibility of constructing NMR gyroscopes [59]. However, since quantum mechanics does not allow for a simultaneous measurement of the three components of angular momentum, NMR gyroscopes are uni-directional. A quantization axis must be chosen before each measurement and all slow rotation perpendicular to the quantization axis (on time-scales much longer than the spin precession period) will remain undetected. (Of course, a three dimensional gyroscope can be obtained by combining the information of three NMR gyroscopes.)

Generally, any scheme used to detect the spin state will involve the use of a magnetic field. Since the spin of a nucleon is always associated with a magnetic moment, when the atom is immersed in a magnetic field, its spin is reoriented in the direction of the field and does not provide an independent reference direction in space anymore. Nevertheless, the new system is still symmetric around the direction of quantization, and the nuclear angular momentum is still conserved in that direction.

Any rotation of the system including the atom (in our case the whole apparatus) around the quantization axis will be detected by a co-moving observer as a shift in the atom's Larmor precession frequency. Subsequent shifts will accumulate in the atom's phase, i.e., its angle of precession. For this reason the NMR gyroscope was appropriately defined as "a rate integrating single-axis rotating sensor." [59]

Inertial Frequency Shifts of Rotating Gyroscopes

A noble gas atom with nuclear spin $\vec{I}$ immersed in a magnetic field $\vec{B} = \hat{\epsilon}B_0$ precesses with frequency $\gamma_{ng}B_0$ if the magnetic field is generated in an inertial system. If the field is generated in a moving laboratory its precessional frequency is found using coordinate transformation between the laboratory frame and the local inertial frame. If this transformation involves a rotation characterized by $\vec{\omega}$, the spin's equation of motion in the laboratory frame is:

$$\left(\frac{d\vec{I}}{dt}\right)_{lab} = \left(\frac{d\vec{I}}{dt}\right)_{inertial} - \vec{\omega} \times \vec{I} \tag{3.36}$$

$$= (\gamma_{ng}\vec{B} - \vec{\omega}) \times \vec{I}. \tag{3.37}$$

The frequency shift in the laboratory is given by the projection of $\vec{\omega}$ along the direction $\hat{\epsilon}$ of $\vec{B}$ and depends on the angle α between the two:

$$\omega_{ng} = \gamma_{ng}B_0 - \vec{\omega} \cdot \hat{\epsilon} = \gamma_{ng}B_0 - \omega \cos\alpha. \tag{3.38}$$

It is important to note that the frequency $\vec{\omega}$ defined above is, in general, different from the instantaneous frequency of rotation of the atom with respect to the local inertial frame. For instance, if the atom has a circular motion of frequency ω, this

does not mean that the coordinate transformation to the atom's rest frame contains a rotation at frequency ω. This situation will be studied in detail in Sect. 3.4.2.

The "Foucault Shift"

The instantaneous Earth rotation frequency ($\omega_\oplus \approx 2\pi/24$ h $= 2\pi$ 11.6 μHz) in the laboratory is represented by a vector parallel to the Earth's axis. Using the coordinate system introduced in Sect. 3.2.1 and assuming that the magnetic field points along $\hat{\epsilon}$, the maser precession frequency shift is:

$$\delta\omega_{ng} = -\hat{\epsilon} \cdot \vec{\omega}_\oplus = -\hat{\epsilon} \cdot (-\sin\chi, 0, \cos\chi)\ \omega_\oplus. \tag{3.39}$$

We called this effect the "Foucault shift" because if we were to direct our magnetic field vertically in the laboratory (i.e., along the $\hat{z}$-axis) our masers would experience a frequency shift $\delta\omega = -\cos\chi\ \omega_\oplus$ that equals the precession frequency of a Foucault pendulum oscillating at the same co-latitude χ.

Usually we operate our masers with the magnetic field pointing along the $\hat{y}$-axis (the East-West direction) and the frequency shift of Eq. (3.39) vanishes. However, if we were to rotate the maser horizontally in the lab frame at some frequency ω_p we would expect inertial precession modulations at that frequency. We will deal with this issue in Sect. 3.4.3.

3.4.2 Inertial Effects Due to the Earth's Orbital Revolution and the Principle of Equivalence

We have seen in the last section that the rotation of the Earth leads to a shift in the precession frequency shift of our masers. The shift is constant in time (insofar as our masers are at rest in the laboratory) and this is consistent with the fact

that the Earth's angular velocity in the laboratory is a vector of fixed direction $\vec{\omega}_\oplus = \omega_\oplus(-\sin\chi, 0, \cos\chi)$.

The situation is different when we consider the revolution of the Earth around the Sun. In the Sun-centered frame the angular velocity of the Earth is a fixed vector $(\vec{\Omega}_\oplus)_J = \Omega_\oplus(0, -\sin\eta, \cos\eta)$ perpendicular to the orbit of the Earth (see Fig. 3-1) and $\Omega_\oplus \approx 2\pi$ 31.7 nHz. However, using the Lorentz transformation introduced in Sect. 3.2.1 we see daily sidereal modulations of the angular velocity in the laboratory frame:

$$\vec{\Omega}_\oplus = \Omega_\oplus \begin{pmatrix} -\cos\eta\ \sin\chi - \sin\eta\ \cos\chi\ \sin\omega_\oplus T_\oplus \\ -\sin\eta\ \cos\omega_\oplus T_\oplus \\ \cos\eta\ \cos\chi - \sin\eta\ \sin\chi\ \sin\omega_\oplus T_\oplus \end{pmatrix}. \tag{3.40}$$

Do these modulations produce frequency time dependent frequency shifts? Misapplying our atomic physics we thought so, at first.

This problem looks very similar to that of the Spin-Orbit interaction in which the electron orbits semi-classically around a nucleus, just like the Earth orbits the Sun. As in the Spin-Orbit case, if we treat the revolution of the Earth using Special Relativity (SR) we notice that the Lorentz transformation relating the Earth-centered frame to the Sun-centered frame comprises a series of boosts. In the context of the atomic spin-orbit interaction, Thomas pointed out that the combination of successive Lorentz boosts in slightly different directions cannot be written as a simple boost. A small rotation is necessary to connect the electron's and nucleus' frame over time. The rotation frequency is given by [60]:

$$\vec{\omega}_T = \frac{\gamma^2}{1+\gamma}\dot{\vec{\beta}} \times \vec{\beta}, \tag{3.41}$$

where $\dot{\vec{\beta}}$ is the electron's acceleration and $\gamma^{-1} = \sqrt{1-\beta^2}$. The same algebra applies

in the case of Earth's motion and it is straightforward to see that the Thomas precession for the Earth reduces to $\vec{\omega}_T = -\frac{1}{2}\beta_\oplus^2 \vec{\Omega}_\oplus$, in the limit of $\gamma \approx 1$. Using Eq. (3.39) for a magnetic field pointing along the $\hat{y}$-axis as usual, we find the following time dependent shift in the noble gas masers:

$$\delta\omega_{ng} = -B_0 \hat{j} \cdot \vec{\omega}_T = \tfrac{1}{2}\beta_\oplus^2 \Omega_\oplus \sin\eta \ \cos\omega_\oplus T_\oplus. \tag{3.42}$$

This tiny ($\delta\omega_{ng} \approx 10^{-16}$ Hz) daily sidereal modulation would not be observable in our masers because it is eight orders of magnitude smaller than our current sensitivity. What is disturbing though, is that with a local measurement we could, given sensitive enough masers, detect the movement of the Earth around the Sun, even if the Earth is in free fall. This would violate the Principle of Equivalence of Gravitation and Inertia, which states that in the neighborhood of a free falling body, inertia and gravity exactly compensate each other and "the laws of nature take the same form as in unaccelerated Cartesian coordinate systems in absence of gravitation" [61]. We conclude that the inertial effects on our masers must be studied in the broader context of a theory that subsumes the Equivalence Principle: we choose General Relativity (GR).

Gyroscope Precession in the Context of General Relativity

The best way to include the Principle of Equivalence, is to use the equations of motion for a moving gyroscope in GR. This approach has the drawback that GR is not a mere consequence of the Principle of Equivalence and it will be necessary to distinguish between observable inertial effects due to a combination of the Principle of Equivalence and Special Relativity and general relativistic effects, which will remain unobservable locally.

Schiff [62, 63] has studied the precession of a gyroscope subject to a non-gravitational force $\vec{F}$, immersed in the gravitational field of a homogeneous, spherical Earth of moment of inertia I, mass M and angular velocity $\vec{\omega}_{\oplus}$.

If the gyroscope's position, with respect to the center of the Earth, is indicated by $\vec{r}$, its velocity by $\vec{\beta}$ and its mass by m, the total precession of the gyroscope with respect to the fixed stars, to first order (i.e., $\gamma \approx 1$) is [62, 63]:

$$\vec{\omega}_{stars} = \frac{1}{2m}\vec{F} \times \vec{\beta} + \frac{3}{2}\frac{GM}{r^3}\vec{r} \times \vec{\beta} + \frac{GI}{r^3}\left(\frac{3(\vec{\omega}_{\oplus}\cdot\vec{r})\vec{r}}{r^2} - \vec{\omega}_{\oplus}\right). \tag{3.43}$$

The second and third terms are, respectively, the Geodetic precession and the Lense-Thirring precession. They are both consequences of GR and represent the rotation of the local inertial frame, with respect to the fixed stars. There is no way to detect these rotations by making local experiments, without actually "looking at" the fixed stars. Only the first term deals with a precession that could be detected, in principle, by a sufficiently sensitive NMR gyroscope as it gives the real precession of the gyroscope with respect to its rest frame.

A force $\vec{F}$ is applied (on average) to our noble gas atom (i.e., the gyroscope in question) to keep it confined in the maser cell. The equation of motion for the atom in the local inertial frame (for instance, an Earth-centered frame) is

$$m\dot{\vec{\beta}} = -\frac{GmM}{r^3}\vec{r} + \vec{F}. \tag{3.44}$$

The first term of Eq. (3.43), which represents the observable precession frequency, can then be written as

$$\vec{\omega}_{ng} = \frac{1}{2m}\vec{F} \times \vec{\beta} = \frac{1}{2}(\dot{\vec{\beta}} + \frac{GM}{r^3}\vec{r}) \times \vec{\beta}. \tag{3.45}$$

In the first term we recognize Eq. 3.41, e.g., the Thomas precession associated with the rotation (not the revolution!) of the Earth. This is the contribution of Special Relativity. We also see that Eq. (3.45) is consistent with the Principle of Equivalence. In fact, suppose that our maser were orbiting around the Earth. In that case the two accelerations in parenthesis would be equal and opposite, leading to no precession at all. This is consistent with the fact that a free falling gyroscope, being by definition at rest in an inertial frame, does not precess.

For an atom captured on the surface of the Earth the two accelerations do not cancel. The first term is negligible compared to the second ($\dot{\beta} = \beta_L \omega_\oplus \ll \frac{GM}{r_\oplus^2} = g$) and our conclusion is that the noble gas atom experiences a constant precession frequency shift $\omega_{ng} \approx g\beta_L/2 \approx 1.7\ 10^{-14}$ Hz, as a consequence of the non-gravitational force $\vec{F}$ appied on it. This tiny shift adds up to the shift we found in Eq. (3.39) and once again does not create any frequency modulations that may be mistaken for a Lorentz-symmetry violating signal.

3.4.3 Noble Gas Masers on a Rotating Platform

As we have noted, the prospect of higher statistics and increased frequency stability could make us wish to operate our masers on a platform rotating with a 1 to 2 h period; a number of precision experiments successfully use these devices [64, 50, 51]. In this section we analyze the constraints that arise on the detection of Lorentz violating signals from the inertial shift of Eq. (3.39). The idea would be to rotate the platform on which the ^{129}Xe/^{3}He maser rests in the horizontal $(\hat{x}-\hat{y})$ laboratory plane with a angular frequency ω_p. The rotation that we impart to the maser has two effects: (i) it changes the signature of the hypothetical Lorentz violating signal;

(ii) it introduces an inertial frequency modulation of a few μHz in the maser signals[15] at the frequency ω_p.

Lorentz Violating Signals for a Rotating ^{129}Xe/^{3}He Maser

For simplicity we will use a simplified version of Eq. (3.27), neglecting the $\tilde{g}_{D,j}$ and $\tilde{d}_j$ terms. The frequency shift for the free-running ^{3}He maser is then $\delta\nu_{He} = k\,\tilde{b}_2$ in the platform's rotating frame. In order to write $\tilde{b}_2$ in terms of the Sun's SME coefficients we must use the Lorentz transformation $\tilde{b}_\alpha = (R'RB)_\alpha{}^\Sigma\ \tilde{b}_\Sigma$ which includes the additional rotation

$$R' = \begin{pmatrix} 1 & 0 & 0 & 0 \\ 0 & \cos\omega_p T_\oplus & \sin\omega_p T_\oplus & 0 \\ 0 & -\sin\omega_p T_\oplus & \cos\omega_p T_\oplus & 0 \\ 0 & 0 & 0 & 1 \end{pmatrix}. \tag{3.46}$$

from the laboratory frame to the frame of the rotating platform. The time dependent frequency shift induced by Lorentz violation on the free running ^{3}He maser is then:

$$\begin{aligned} \delta\nu_{He} &= k\,\tilde{b}_2 \\ &= \cos\omega_p T_\oplus \left(\tilde{b}_Y \cos\omega_\oplus T_\oplus - \tilde{b}_X \sin\omega_\oplus T_\oplus\right) \\ &\quad - \sin\omega_p T_\oplus \left[-\tilde{b}_Z \sin\chi + \left(\tilde{b}_X \cos\omega_\oplus T_\oplus + \tilde{b}_Y \sin\omega_\oplus T_\oplus\right)\cos\chi\right]. \end{aligned} \tag{3.47}$$

Inertial Frequency Shifts for a Rotating ^{129}Xe/^{3}He Maser

We have seen in Sect. 3.2.1 that the Earth's angular frequency is described by the vector $\vec{\omega}_\oplus = (-\sin\chi, 0, \cos\chi)\,\omega_\oplus$ in the laboratory frame. Using Eq. (3.38) we find

[15]This is always true unless we rotate the platform around an axis parallel to the Earth's axis, which would be rather impractical at our latitudes.

the inertial shift due to the rotation of the platform on either maser:

$$\delta\omega_{ng} = -\hat{\epsilon}\cdot\vec{\omega}_{\oplus} = \hat{\jmath}\cdot R'_{ij}(-\sin\chi, 0, \cos\chi)\ \omega_{\oplus} = \sin\omega_p T_{\oplus}\ \sin\chi\ \omega_{\oplus}. \tag{3.48}$$

Taking into account the effect of co-magnetometry we obtain:

$$\begin{aligned}
\delta\nu_{He} &= \nu_{He} - \frac{\gamma_{He}}{\gamma_{Xe}}\nu_{Xe} \\
&= \left(1 - \frac{\gamma_{He}}{\gamma_{Xe}}\right)\frac{\omega_{\oplus}}{2\pi}\sin\chi\sin\omega_{\oplus}T_{\oplus} \\
&= -\nu_{in}\sin\omega_p T_{\oplus},
\end{aligned} \tag{3.49}$$

where the amplitude of the inertial frequency shift (in Cambridge, MA), $\nu_{in} = \sin\chi\,(\gamma_{He}/\gamma_{Xe} - 1)\,\omega_{\oplus}/2\pi \approx 15\ \mu$Hz, is very large compared to present limits on Lorentz violation, which are on the order of 0.1 μHz.

Combined Effects

The complete frequency shift for the combined effects of inertia and Lorentz violation is:

$$\begin{aligned}
\delta\nu_{He} &= \cos\omega_p T_{\oplus}\left(\tilde{b}_Y\cos\omega_{\oplus}T_{\oplus} - \tilde{b}_X\sin\omega_{\oplus}T_{\oplus}\right) \\
&\quad - \sin\omega_p T_{\oplus}\left[\nu_{in} - \tilde{b}_Z\sin\chi + \left(\tilde{b}_X\cos\omega_{\oplus}T_{\oplus} + \tilde{b}_Y\sin\omega_{\oplus}T_{\oplus}\right)\cos\chi\right].
\end{aligned}$$

Hence, Lorentz violation unmistakably manifests itself through the component of $\delta\nu_{He}$ which is in quadrature with the inertial effect (i.e., proportional to $\cos\omega_p T_{\oplus}$). Assuming that the table is rotated many times a day (i.e., $\omega_p \gg \omega_{\oplus}$), for every

rotation period we may use the following fit function,

$$\delta\nu_{He} = \lambda_c(T_\oplus)\cos\omega_p T_\oplus + \lambda_s(T_\oplus)\sin\omega_p T_\oplus, \tag{3.50}$$

and typically measure $\lambda_s(T_\oplus) \approx -\nu_{in}$ and $\lambda_c(T_\oplus) \approx 0$. However, establishing an experimental bound on $\lambda_c(T_\oplus)$ (i.e., establishing how close $\lambda_c(T_\oplus)$ is to zero), requires an extraordinary directional accuracy. In principle the angle of the table rotation $\omega_p T_\oplus$ is assumed to be exactly a multiple of 2π when the B_0 field points in the east-west direction. In practice the uncertainties in the determination of the east-west direction in our laboratory and on the exact direction of B_0 at the cell's site must result in a finite directional inaccuracy $\delta\theta$. Even without a Lorentz violating interaction, we would measure $\lambda_c(T_\oplus) = \nu_{in}\sin\delta\theta \approx \nu_{in}\delta\theta$. Since the current bound on $\tilde{b}_J \approx 50$ nHz, at the very least we would need to make sure that $\delta\theta \ll 50\ \text{nHz}/\nu_{in} \approx 0.2°$. Establishing such absolute accuracy, for instance making sure that $\delta\theta \leq 0.01°$, represents a substantial experimental challenge. This observation and other practical considerations,[16] seriously diminish the attractiveness of operating the ^{129}Xe/^{3}He maser on a rotating platform.

[16]Besides the difficulty and cost of installing the maser on a rotating platform, we expect that a substantial effort would be needed to screen out the periodic disturbances due to the ambient magnetic field which are static in the lab frame and therefore varying at ω_p in the table frame.

Chapter 4

Design Studies for an Optimized ^{129}Xe/^{3}He Maser

Almost a decade of intense work on the ^{129}Xe/^{3}He maser culminated in 2000 with what remains the most precise LI test for a fermion [24, 25]. This first result encouraged the construction of a new ^{129}Xe/^{3}He maser that would facilitate a systematic study of this device's properties aimed at improving frequency stability and LI testing sensitivity.

Some known limitations of the previous system provided a good point of departure for designing the new maser. The frequency stability of the previous device improved when the flow of air warming up the maser cell was decreased, suggesting that the temperature control system was not ideal. The materials used for the construction of the maser oven did not permit operation at pump bulb temperatures above 125-130° C, and yet higher temperatures increased the signal of ^{3}He, the species with worse SNR. Co-magnetometry was imperfect, but the causes of this imperfection and its effect on the masers were unclear. Stabilization of the broad-band optical pumping light from the Laser Diode Array (LDA) had been key

to maser frequency stabilization, however it was unclear whether this stabilization helped simply through maser amplitude stabilization or through other mechanisms. Would an improved light source, such as narrow-band laser, further improve the maser frequency stability? Lastly, decreasing gas pressures in the maser cells had led to better overall stability, but it was not known how much more the gas pressures could be dropped before encountering adverse effects (e.g., reduced SNR, chasing of Rb out of the pump bulb due to increased motility). An optimization of cell geometry, gas fill pressures, and operating temperatures taking into account optical pumping as well as polarization transport and losses between the two cells was required. Experimentally this optimization required extensive testing of many maser cells. Therefore, in the new system, replacing cells had to be easier than in the previous system. With these considerations in mind we carried out the studies presented in this chapter. We then designed and constructed the new maser, as we will see in the next chapter.

Our analysis begins with an assessment of the previous maser's stability and an important distinction between frequency stability and LI sensitivity. We then focus on the previous maser's blown-air temperature control system and present some improvements. The third topic, an extensive model of optical pumping (considering narrow and broad-band light sources), polarization transport, and maser dynamics in the double-bulb cell, makes up most of the chapter. Without a claim of completeness, this model illustrates some of the $^{129}Xe/^{3}He$ maser's complexity and is aimed at providing some guidance in the process of cell geometry and gas fill pressure optimization. Next, we show that different diffusion coefficients and interaction times for the two noble gas species may lead to imperfect co-magnetometry. Finally, we show that for a near-spherical maser cell maser self-interaction is negligible, allowing us to neglect this effect in the maser equations.

4.1 Previous Maser Frequency Stability and Prospects for Improvement

An in-depth analysis of the 87 days of data used for our Lorentz invariance and CPT tests ("LI tests" for short) was carried out to assess the performance of the previous maser. Here we briefly summarize our findings.

Figure 4-1 shows the average Allan deviation (full dots) for all the data available.[1] The best stability was achieved, on average, for measurement times of 1 to 2 hours. For longer times, frequency drifts and other types of non-white frequency noise dominated. If maser stability were a good indicator of LI sensitivity, an attractive way to increase sensitivity would be, for instance, to install the maser on a platform rotating with a 1 to 2 hour period. This scheme would match the period of the Lorentz violating signals with the period of best maser frequency sensitivity as well as producing higher statistics. As we have seen in Sect. 3.4.3 there are serious technical challenges to this plan. Even disregarding those, we show here using existing data that this scheme does not lead to an improved LI sensitivity essentially because the Allan deviation of the free-running maser "as is," is not a good indicator of LI sensitivity.

To obtain a good indicator we need to look closely at the procedure by which the LI violating amplitudes of daily modulations, $\delta\nu_X$ and $\delta\nu_Y$, are extracted from the raw frequency data of free-running ^{3}He. The daily fit function we use is [34]:

$$\delta\nu_{\rm He} = c_0 + c_1\, T_\oplus + c_2\, R_{He}(T_\oplus) + c_3\, R_{Xe}(T_\oplus) + \delta\nu_X \sin\,\omega_\oplus T_\oplus + \delta\nu_Y \cos\,\omega_\oplus T_\oplus. \quad (4.1)$$

This fit allows for a constant frequency offset, c_0, a linear frequency drift, $c_1\, T_\oplus$, cor-

[1] We should stress that the average stability obviously does not reflect the top performance of the previous maser, which was at times much better than the average shown in the figure [65].

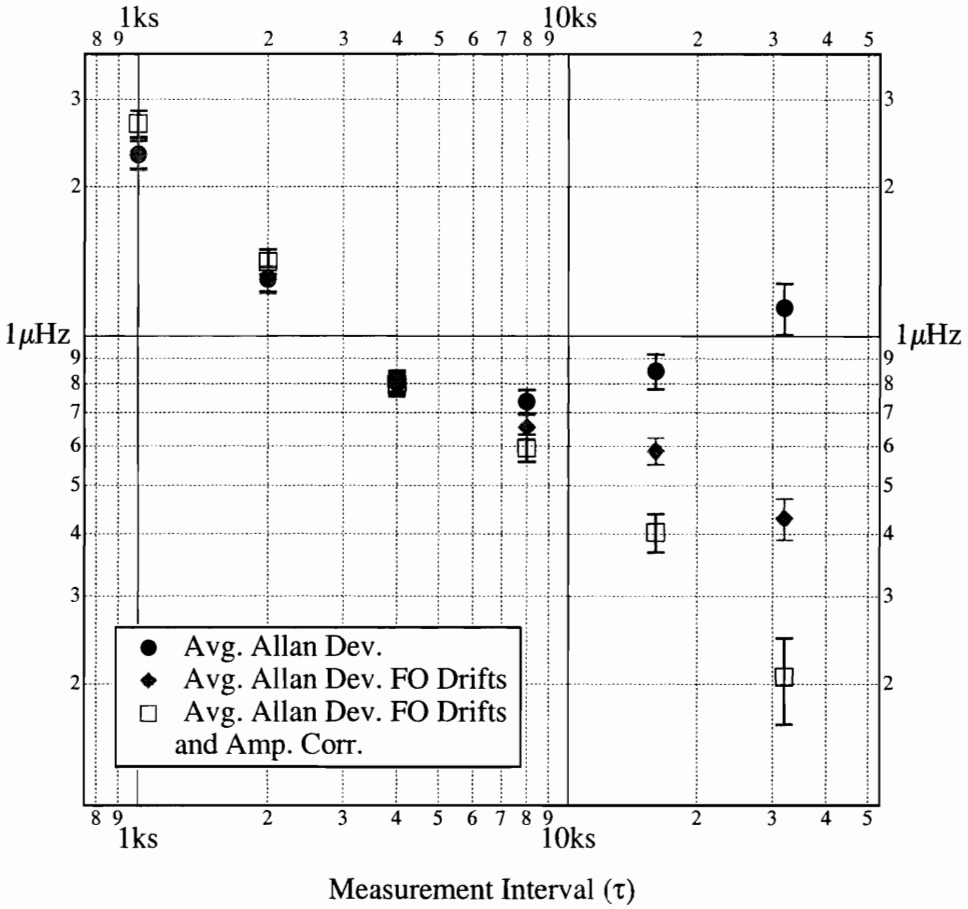

Figure 4-1: Average Allan deviation of the ^{3}He maser frequency when the ^{129}Xe is used as a co-magnetometer. The Allan deviation improves for large measurement intervals, when a daily linear frequency shift is fit out (FO) of the ^{3}He frequency. Further improvement is obtained when correlations with the maser amplitudes are subtracted out.

relations with the maser amplitudes, R_{He} and R_{Xe}, as well as the Lorentz-violating coefficients $\delta\nu_X$ and $\delta\nu_Y$ [24]. As usual, $T_\oplus$ is the time elapsed since the beginning of the sidereal day. Fitting the drifts and amplitude correlations clearly improves the sensitivity to the sidereal modulations. The Allan deviation of the residuals of a fit to the background function,

$$\delta\nu_{He}(T_\oplus) = c_0 + c_1\, T_\oplus + c_2\, R_{He}(T_\oplus) + c_3\, R_{Xe}(T_\oplus), \tag{4.2}$$

is also shown in Fig. 4-1 as well as the deviation when only an offset and a drift were fitted out. The dramatic improvement in stability at long timescales allows improved LI sensitivity to at least 32,000 s. The precision of our frequency measurements is limited only by white frequency noise and improves as the inverse square root of the measurement interval τ, therefore even the statistical advantage of obtaining more data sets does not improve the overall sensitivity. If a data set of length T is divided into T/τ samples, the statistical improvement is then proportional to $\sqrt{\tau/T}$, which makes the overall LI sensitivity independent of τ.

To verify that the LI sensitivity is independent of τ, we carried out the LI analysis on all the existing data choosing the eight fictitious rotation periods reported in Tab. 4.1, together with the total number of samples obtained. As we show in Fig. 4-2 the LI sensitivity per rotation is indeed correlated with the Allan deviation of the residual of the fit in Eq. (4.2), which is therefore a good indicator of LI sensitivity. However, the LI sensitivity obtained by averaging all samples for the 87 days of data is roughly independent of the duration of the measurement interval.

Assuming that linear frequency drifts and amplitude correlations will account for most of the long term frequency variations in our new maser, we conclude that to improve LI sensitivity we should concentrate on reducing the frequency noise (see

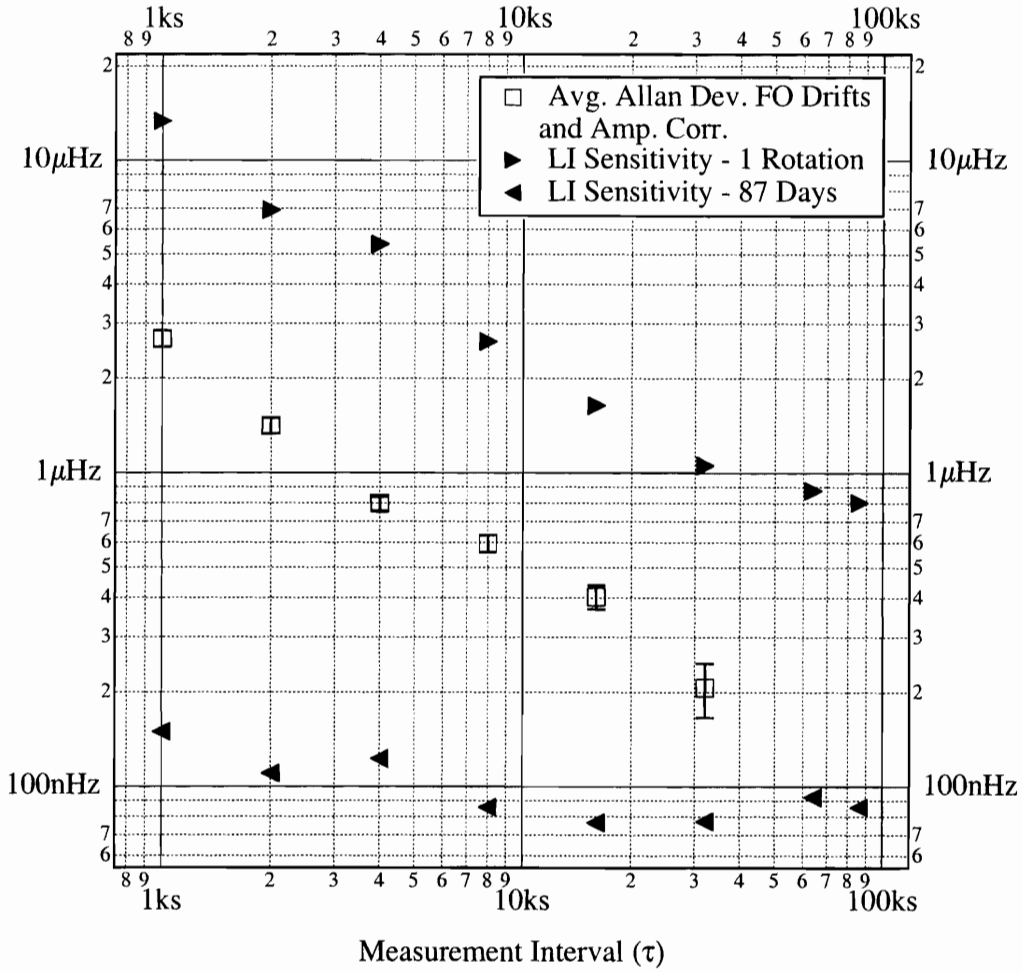

Figure 4-2: Once linear frequency drift and maser amplitude correlations have been fit out (FO) of the free-running ^{3}He frequency, the Allan deviation of its residual is a good indicator of LI sensitivity. Presently the factor of approximately 5 between the Allan deviation and the LI sensitivity is not well understood. The plot also shows that averaging over all the samples obtained for the entire data set of 87 days, leads to a flat LI sensitivity. This means that the increased statistics deriving from the shorter measurement intervals is exactly offset by the higher frequency noise that characterizes shorter frequency measurements.

Rotation Period (s)	Number of Samples
1000	7980
2000	3954
4000	1935
8000	940
16000	459
32000	186
64000	90
86163	87

Table 4.1: In order to calculate the LI sensitivity for a given rotation period we divided the 87 days of available data into samples of exactly one rotation period and performed the LI analysis on each sample.

Fig. 2-4). The rest of this chapter explores possible modifications to the system's temperature control, Rb optical pumping techniques, co-magnetometry and cell geometry, which are all thought to lead, either directly or indirectly, to a reduction of maser frequency noise. As we discussed in Sect. 2.4.2, ideally, only thermal frequency noise should limit our LI sensitivity and careful modeling should advise us in choosing a region of parameter space where the level of thermal noise is acceptable.

4.2 Temperature Control

Excellent frequency stability can only be achieved in our masers with a careful temperature control of the optical pumping and maser regions. Noble gas spatial distributions and wall relaxation rates are affected by changes in temperature, but the greatest variation occurs in the density of Rb vapor, [Rb], which depends exponentially on the temperature, T (expressed in degrees Kelvin) [66]:[2]

$$[\mathrm{Rb}] = \frac{10^{26.178-4040/T}}{T}. \tag{4.3}$$

[2]Quoted accuracy is 5%, Killian [67] does not quote accuracy.

In the pump bulb, where the temperature is kept between 90 and 150° C, an increase in the temperature by 10° C changes the Rb density by a factor 2 to 1.7. As we have seen in Sect. 2.1, the rate of spin-exchange between Rb atoms and noble gases, depends linearly on [Rb]. Temperature instabilities therefore perturb the flux of polarized atoms into the maser bulb and create amplitude instabilities that are known to perturb the maser frequencies (see Eqs. (4.1) and (2.56)).

4.2.1 Previous Maser Dependence of Temperature on Air Massflow

In the previous experiment Rb magnetization control [68, 34] was essential for achieving excellent maser frequency stability. We now think that magnetization control also compensated for pump bulb temperature fluctuations which were actually much greater than the measured 10 mK standard deviation. In testing our single bulb $^{21}Ne/^{3}He$ maser [69], which was heated with a direct flow of hot air hitting the bulb as in the original $^{129}Xe/^{3}He$ maser, similar effects were observed. As shown in Fig. 4-3 (a) the thermometer used to control the air temperature was kept at a distance from the cell. The inevitable temperature gradient between cell and thermometer was very sensitive to the airflow as shown in Fig. 4-4. We estimate that in the $^{21}Ne/^{3}He$ maser a 1% change in the air massflow led to a change of approximately 130 mK in the temperature of the gas inside the cell, even though the control thermometer downstream in the airflow was stable to a few mK. Since we only control the air massflow to a few percent, the new maser uses an indirect heating method (depicted in Fig. 4-3 (b)) that is less sensitive to air massflow fluctuations. The new design also reduces vibrations created on the cell by turbulent airflow.

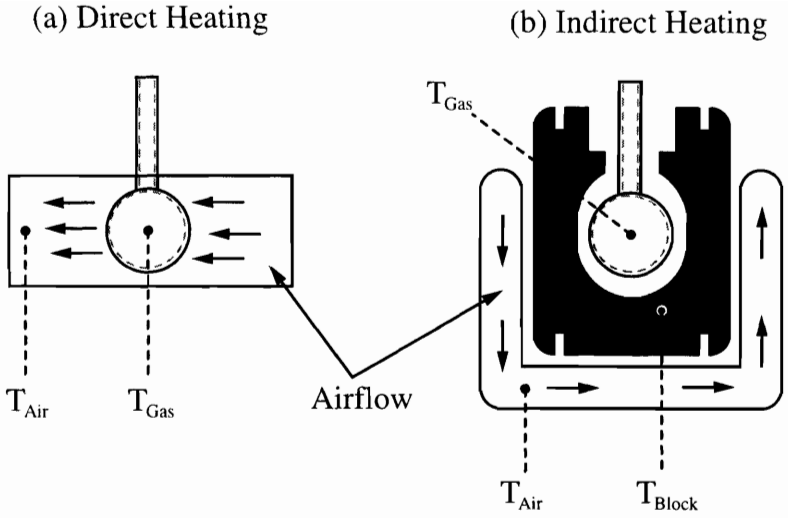

Figure 4-3: The previous maser used direct heating of the cell. In the case of the maser bulb, the thermometer is kept at a distance from the cell in order for electromagnetic fields generated by the thermometer not to interfere with the masers. The temperature gradient between the gas and the thermometer is a strong function of the airflow, as shown in Fig. 4-4. Indirect heating in the maser solves this problem (see Sect. 5.1). Airflow fluctuations are integrated out by the block's thermal capacity, while its high thermal conductivity smooths the temperature gradients across the block itself. This scheme also reduces the vibrations of the cell by removing it from the turbulent airflow.

4.2.2 Indirect Heating

Removing the cell from the airflow is not sufficient to reduce the sensitivity of the cell temperature to airflow instability. A long thermal time constant must be added to the system to further reduce fluctuations. For instance, this can be done by surrounding the cell with a block of material with a high specific heat, C, and high density, ρ. The thermal capacity of a body, such as the block in Fig. 4-5, is given by $C_{Th} = \rho\, CAL$, where A is the cross-sectional area and L is the length of the block. The material must also possess a high thermal conductivity, k, to transport heat to the cell located within the block. In analogy with an electric circuit, the flow of heat can be treated like flow of electric charge [70]. The "thermal resistance" of a good

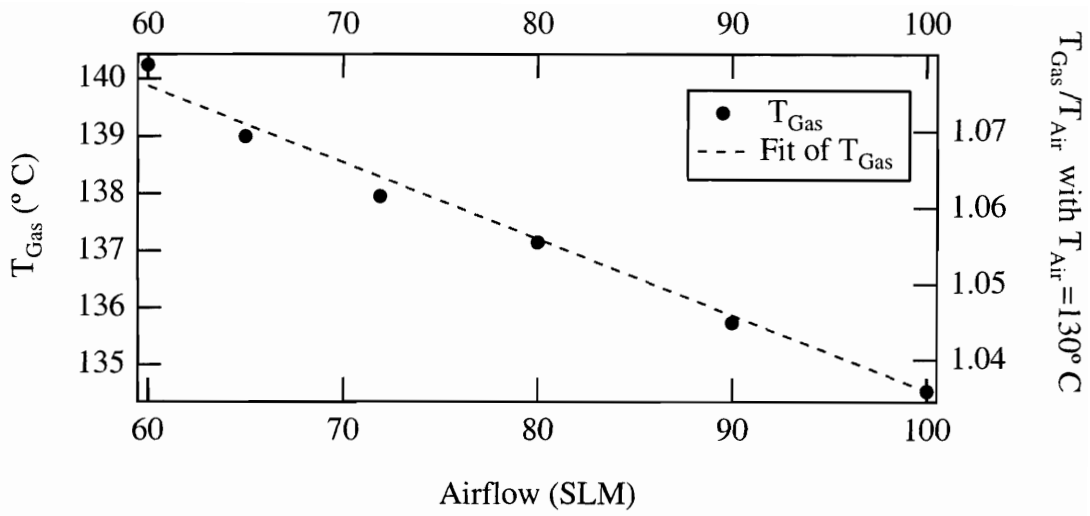

Figure 4-4: In a single-bulb $^{21}Ne/^{3}He$ maser we used a frequency shift induced by polarized Rb on the free-running ^{3}He maser to estimate the Rb density and thus its temperature. The geometry was that of "Direct Heating" shown in Fig. 4-3 (a). We were able to determine the gas temperature inside the cell, T_{Gas}, while the air temperature, $T_{Air} = 130°$ C, was kept constant by a lock loop. The temperature gradient, $T_{Gas} - T_{Air}$ was strongly dependent on the airflow (measured in standard liters per minute, SLM).

thermal conductor, $R_{Th} = L/kA$, is usually negligible compared to the resistance of the air, $R_{Th,Air} = 1/A\,h_{Air}$, used to heat it (or cool it). The air heat transfer coefficient h_{Air} varies between 15 and 150 W/m^{2}K, for still air or forced convection respectively [70].

To test improved indirect heating techniques, we used a cubic aluminum block with side length 2 cm. We warmed it up several degrees above room temperature, and let it come to equilibrium with the ambient temperature while monitoring ambient and internal temperatures (see Fig. 4-6). Air conditioning in our laboratory produces oscillations of the room temperature with a period $\tau_{Air} \approx 745$ s and amplitude of 1 K peak to peak. For this test system, the thermal time constant of the

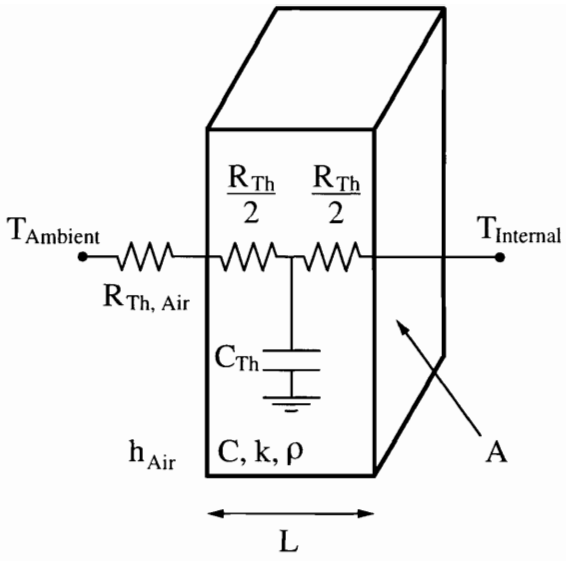

Figure 4-5: A massive block with cross-sectional area A is exposed to ambient temperature $T_{Ambient}$ on one side. Since there is a perfect analogy between heat transmission and electrical charge transmission, the internal temperature $T_{Internal}$ of the block can be assimilated to the voltage across a low pass filter, while the ambient air temperature corresponds to the driving voltage.

low pass filter in Fig. 4-5 is

$$\tau = \left(R_{Th,Air} + \frac{R_{Th}}{2} \right) C_{Th} \approx R_{Th,Air} C_{Th} = \frac{\rho C L}{h_{Air}}, \tag{4.4}$$

and it is in agreement with the observed exponential decay time of approximately 3,030 s. The ambient temperature fluctuations allow us to test our low pass filter model, for which we would predict the ratio of the amplitudes of the internal and ambient temperature fluctuations:

$$\left. \frac{\Delta T_{Internal}}{\Delta T_{Ambient}} \right|_{\omega = \frac{2\pi}{\tau_{Air}}} = \left[1 + \left(\frac{2\pi\tau}{\tau_{Air}} \right)^2 \right]^{-\frac{1}{2}} \approx 0.039 \tag{4.5}$$

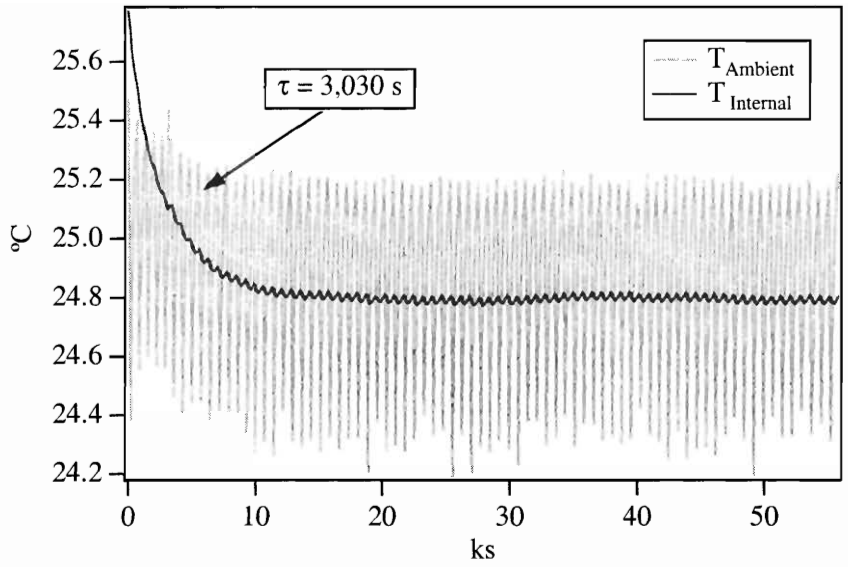

Figure 4-6: Ambient temperature and internal temperature of a small Al block in our laboratory. The block, possessing a time constant $\tau \approx 3,030$ s, slowly comes into equilibrium with the ambient temperature and follows the slow temperature fluctuations of the air conditioning cycle. The thermal capacity of the block reduces the amplitude of the ambient temperature fluctuations by a factor of 27.5.

which is consistent with the observed oscillation amplitude suppression of $1/27.5 \approx 0.036$. For forced convection, as we noted, the heat transfer coefficient, h_{Air}, increases and τ is somewhat smaller than what we observed for the case of forced heating (or cooling) of the block shown in Fig. 4-3 (b). Nevertheless, indirect heating of the cell mediated by a block with high thermal capacity and high thermal conductivity integrates out air massflow fluctuations lasting even several tens of seconds. In Sect. 5.1.1 we describe the implementation of indirect heating in the new maser oven and in Sect. 6.1 we give a first assessment of the temperature stability obtained in the new maser.

4.3 Model of Maser Behavior in a Double-Bulb Cell

In order to optimize the $^{129}Xe/^{3}He$ maser for best frequency stability we must pursue two main goals, while dealing with two major constraints. The goals are: high maser powers, needed to increase SNR, and good motional averaging, needed to improve common mode rejection of the magnetic field noise. The first constraint is the great difference in physical properties between ^{129}Xe and ^{3}He. ^{129}Xe interacts strongly with Rb and therefore it is easy to polarize, but it also relaxes rapidly due to wall-collisions and it diffuses much more slowly than ^{3}He. In our double-bulb maser, faster diffusion (obtained at lower gas densities) favors polarization transfer and motional averaging, but it also limits the interaction time of the atoms with the resonant circuit, which ultimately diminishes maser power. The second constraint is the on-resonant laser power, which is always limited. The trade-off in the choice of the laser source is that of high power, broad-band lasers, which are usually robust, but unstable. On the other end, narrow-band lasers can be stable, but also more delicate and they deliver less laser power.

In this section we develop a model that allows us to study some of the competing effects mentioned above and leads us to a quantitative prediction of the steady state maser amplitudes in the double-bulb $^{129}Xe/^{3}He$ maser. This model takes a given cell geometry, gas pressures and the intensity and spectral profile of the optical pumping laser light and produces: (i) the profile of the Rb polarization along the cell as detailed in Sect. 4.3.1; (ii) the noble gas polarization transfer rates and wall relaxation rates using the diffusion equations solved in Sect. 4.3.2; (iii) the noble gas diffusion coefficients taking into account gas inter-diffusion and self-diffusion as detailed in Sect. 4.3.3; and (iv) the noble gas steady state polarizations in presence

and absence of maser action, for which we derive, in Sect. 4.3.4, fairly transparent analytic expressions.

This section is aimed at the most easily accessible region of parameter space. Cell geometry, pick-up coil geometry, coil Qs and maser frequencies are difficult to change once the various components are built. Bulb temperatures, gas fill pressures and light sources may be varied more easily. Most of the figures in this section reflect this approach and are meant to guide the optimization of cell fill pressures for a given laser source and illustrate the interplay of competing effects.

4.3.1 Optical Pumping Optimization

Optimization of the $^{129}Xe/^{3}He$ requires maser requires careful modeling of the Rb optical pumping process for two essential reasons. First, laser power is expensive and usually limited; second, the ^{129}Xe interaction with polarized Rb is two orders of magnitude stronger than its interaction with ^{3}He. Therefore, optical pumping conditions that are optimal for one species are often unacceptable for the other. For instance, high ^{3}He polarization is usually achieved at high temperatures ($\approx 180°$ C), to exploit the high Rb density and thus high spin-exchange rate (see Sect. 2.1), and at high pressures (several atmospheres), to broaden the Rb absorption spectrum and make use of relatively cheap, high-power, broad-band lasers. On the other hand, ^{129}Xe is usually best polarized at lower temperatures and lower pressures for three reasons: (i) Rb-^{129}Xe spin rotation interactions, which limit the Rb polarization, increase linearly with the ^{129}Xe pressure; (ii) the wall coatings employed to reduce the depolarizing effect of wall-collisions can only be used at temperatures below approximately 140° C, lest they be damaged by chemical interaction with Rb; (iii) high buffer gas (N_2, He) pressures induce 3 body collisions which reduce the lifetime

of van der Waals Rb-^{129}Xe molecules thus reducing spin-exchange efficiency. Also, at high ^{129}Xe pressures ^{129}Xe-^{129}Xe interactions lead to a significant depolarization. Therefore a compromise must be found to optimize maser performance jointly.

Optical Pumping Simulation

Our optical pumping simulation for a cylindrical pump bulb is used to obtain estimates of the average Rb polarization that can be achieved with narrow- and broadband lasers. We limit our model to describe the limitations to optical pumping imposed by the finite number of resonant photons in the laser beams, as well as the effects of ^{129}Xe pressure dependent Rb relaxation, pump bulb geometry and gas temperature.

We model the absorption of an incoming, spatially homogeneous, circular beam of laser light whose Lorentian spectrum is centered at the Rb D_1 transition frequency ν_0 ($\lambda \approx 794.7$ nm in air) and has a full width at half maximum (FWHM) dependent on the laser source. The cell of length l, is divided in many (≈ 300) thin cylindrical sections of length δl in order to model the absorption of the the light as it penetrates into the cell. For the i^{th} section we calculate the optical pumping rate, $\gamma_{opt,i}$,

$$\gamma_{opt,i} = \int \Phi_{i-1}(\nu)\sigma(\nu)d\nu, \tag{4.6}$$

where $\Phi_{i-1}(\nu)$ is the photon flux density that reaches the i^{th} section and the frequency dependent absorption cross section is given by:

$$\sigma(\nu) = \frac{\sigma_0}{1 + \left(\frac{\nu-\nu_0}{\Gamma_{Pr}/2}\right)^2}. \tag{4.7}$$

The resonant cross section, $\sigma_0 = 2/\Gamma_{Pr} r_e c f$, depends on the classical electron radius,

$r_e = 2.82\ 10^{-13}$ cm, the oscillator strength, $f = 0.35$, and the speed of light, c [71]. The pressure broadened width, Γ_{Pr}, of the excited state varies with the pressure, $\mathcal{P}$, (in atmospheres) of the various gases present in the cell, as follows:

$$\Gamma_{Pr} = [18\,(\mathcal{P}_{He} + \mathcal{P}_{Xe}) + 14\,\mathcal{P}_{N_2}]\ \text{GHz}. \tag{4.8}$$

The Rb polarization for the i^{th} section is calculated using the analogue of Eq. (2.3):

$$P_{Rb,i} = \frac{\gamma_{opt,i}}{\gamma_{opt,i} + \Gamma_{sd,i}}, \tag{4.9}$$

where the Rb spin destruction rate,

$$\Gamma_{sd,i} \quad = \Gamma_{Rb} + D_{Rb}\left[\tfrac{1}{(i\,\delta l)^2} + \tfrac{1}{(l - i\,\delta l)^2}\right], \tag{4.10}$$

takes into account the spin rotation rates of Eq. (2.4) and the depolarization of the Rb atoms that diffuse to the front and the back windows of the pump bulb.[3] This effect is quite important at low pressures, when the Rb diffusion coefficient becomes larger:

$$D_{Rb} = \left(\frac{\mathcal{P}_{N_2}}{0.28} + \frac{\mathcal{P}_{He}}{1.5} + \frac{\mathcal{P}_{Xe}}{0.2}\right)^{-1} \frac{\text{cm}^2}{\text{s}}. \tag{4.11}$$

Absorption due to unpolarized Rb near the front window significantly reduces the intensity of the incoming light-beam even at high pressures. Detuning the laser can reduce losses due to depolarized Rb at the front window provided that the medium is sufficiently optically thick to absorb all the detuned light [71, 8].

An example calculated profile of incoming and outgoing laser light for a 10 W

[3]For simplicity we have considered only the lowest order diffusion modes to estimate the relaxation of Rb at the two ends of the pump bulb. This approximation is reasonable compared with the exact solution of the problem, which we solved numerically in one dimension including the effect of diffusion and using completely relaxing walls as boundary conditions.

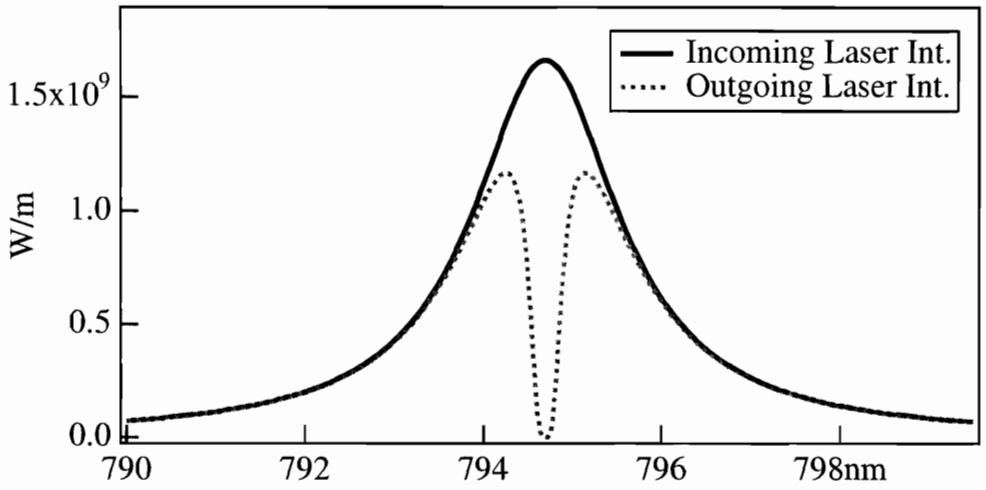

Figure 4-7: Frequency spectrum of a 10 W beam (FWHM $\approx$ 2 nm) of σ^+ light entering and exiting a cell containing $\mathcal{P}_{Xe} = 130$ Torr, $\mathcal{P}_{He} = 2,500$ Torr, $\mathcal{P}_{N_2} = 80$ Torr, at a temperature of $T_P = 140°$ C. The bulb radius and length are respectively, $r_0 = 0.83$ cm and $l = 2.8$ cm. Even for these high fill pressures, which pressure broaden significantly the Rb absorption line and make good use of the laser's broad-band light, only a fraction of the light is absorbed and the average Rb polarization is relatively low, $\langle P_{Rb} \rangle \approx 0.5$.

broad-band (FWHM $\approx$ 2 nm) laser is shown in Fig. 4-7. We chose high ^{129}Xe and ^{3}He pressures to show the depletion of resonant photons towards the end of the cell. The average Rb polarization, calculated using Eq. (4.9) for each section, amounts approximately to 50% in the case shown in Fig. 4-7.

Broad-Band vs Narrow-Band Lasers

A 30 W Coherent Laser Diode Array (LDA) whose intensity, at the entrance to the pump bulb after polarization through a beam splitter cube and various losses, has a broad, 10 W spectrum resembling that of Fig. 4-7 is often used to pump the maser. At a typical pump bulb temperature $T_P = 114°$ C, the simulation described in the

last section predicts the Rb polarization and light absorption shown in Figs. 4-8 and 4-9 as functions of noble gas fill pressure.[4]

In Fig. 4-9 we see that most of the light incident on the cell is not absorbed. The light however significantly contributes to warm up the cell and, despite the fact that the laser total power is monitored and locked to a fixed value, there is still a concern that the heat delivered could compromise the temperature stability. Diode arrays also suffer independent frequency drift of each individual diode element, which changes the amount of resonant light and destabilizes Rb optical pumping. Both concerns can be eliminated by employing a narrow-band (FWHM $\approx 10\,\mathrm{MHz} \ll \Gamma_{Pr}$) laser. For ^{129}Xe fill pressures below 50 Torr (see Fig. 4-9) 350 mW of laser power is sufficient to saturate the optical pumping transition. We present in Fig. 4-10 through Fig. 4-13 calculations of the Rb polarization and absorbed laser power for a narrow-band laser in the case of two pump bulb temperatures $T_P = 114°$ C and 140° C and various noble gas pressures. In Sect. 4.3.4 we will show the noble gas polarizations and the maser signals that can be achieved with these Rb polarizations, but before we can treat that problem we must discuss our model of polarization transfer between the two bulbs and obtain realistic estimates for the diffusion coefficients of ^{129}Xe and ^{3}He.

[4]In this section we use typical dimensions for the pump bulb: internal radius $r_0 = 0.83$ cm, internal length $l = 2.8$ cm.

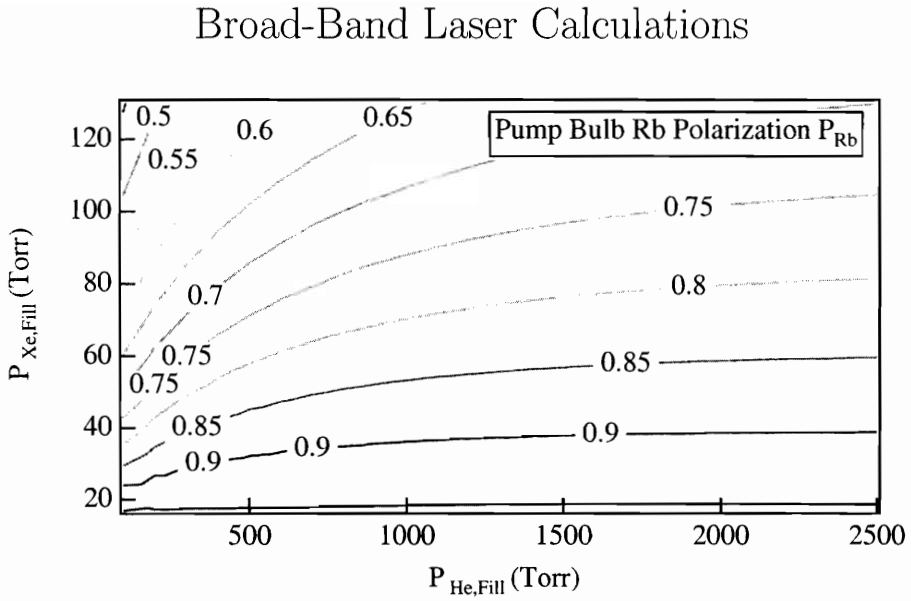

Figure 4-8: Contour plot showing the calculated mean Rb polarization, $\langle P_{Rb} \rangle$, for a range of noble gas fill pressures and fixed $\mathcal{P}_{N_2} = 80$ Torr. Optical pumping obtained with a broad-band laser (10 W, FWHM $\approx$ 2 nm) at $T_P = 114°$ C.

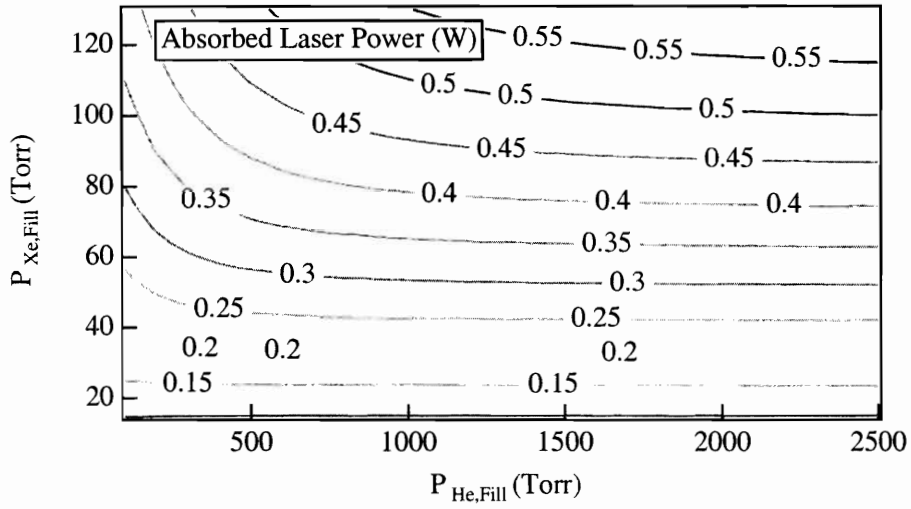

Figure 4-9: Contour plot showing the calculated absorbed laser power for a range of noble gas fill pressures and fixed $\mathcal{P}_{N_2} = 80$ Torr. Optical pumping obtained with a broad-band laser (10 W, FWHM $\approx$ 2 nm) at $T_P = 114°$ C.

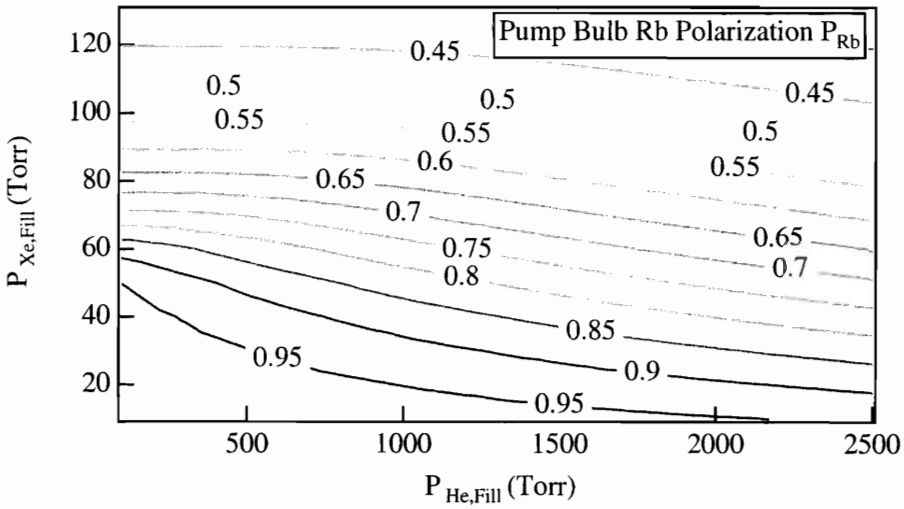

Figure 4-10: Contour plot showing the calculated mean Rb polarization, $\langle P_{Rb} \rangle$, for a range of noble gas fill pressures and fixed $\mathcal{P}_{N_2} = 80$ Torr. Optical pumping obtained with a narrowband laser (350 mW, FWHM $\approx$ 10 MHz) at $T_P = 114°$ C.

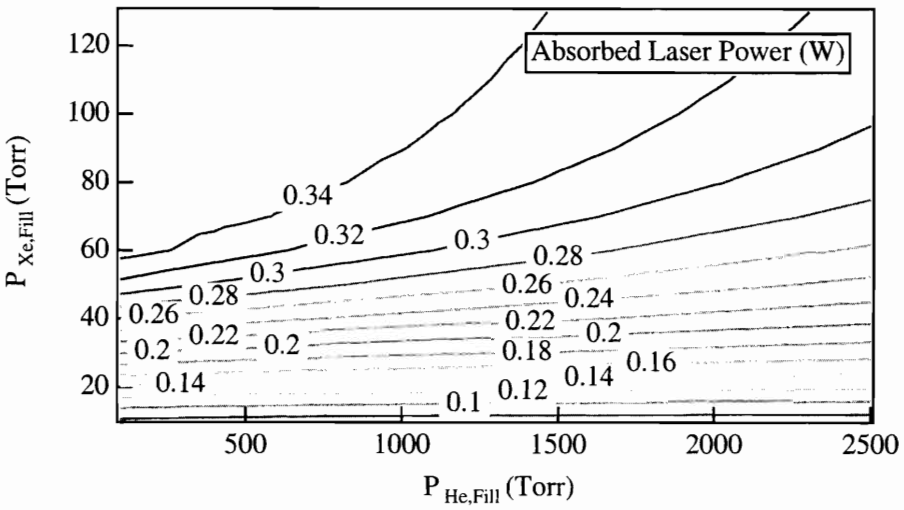

Figure 4-11: Contour plot showing the calculated absorbed laser power for a range of noble gas fill pressures and fixed $\mathcal{P}_{N_2} = 80$ Torr. Optical pumping obtained with a narrowband laser (350 mW, FWHM $\approx$ 10 MHz) at $T_P = 114°$ C.

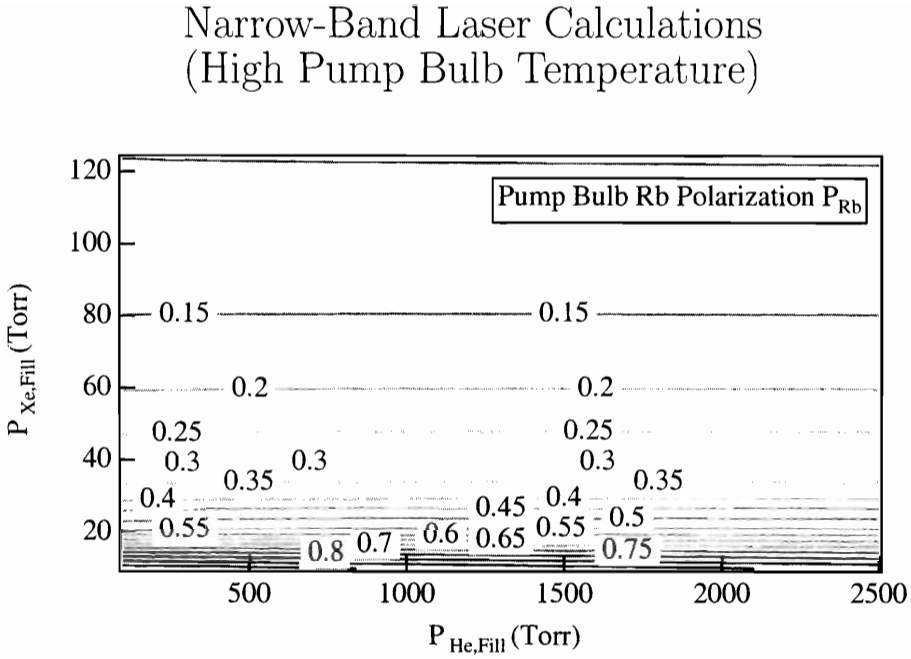

Figure 4-12: Contour plot showing the calculated mean Rb polarization, $\langle P_{Rb} \rangle$, for a range of noble gas fill pressures and fixed $\mathcal{P}_{N_2} = 80$ Torr. Optical pumping obtained with a narrowband laser (350 mW, FWHM $\approx$ 10 MHz) at $T_P = 140°$ C.

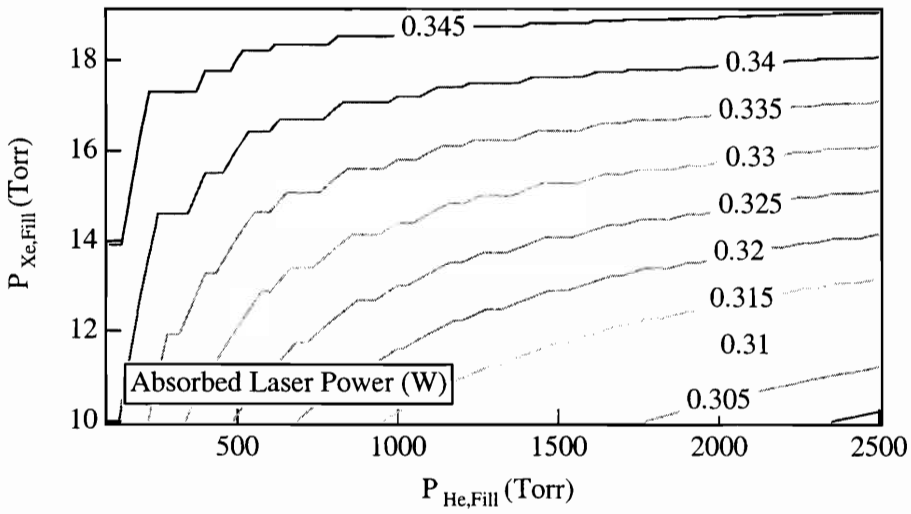

Figure 4-13: Contour plot showing the calculated absorbed laser power for a range of noble gas fill pressures and fixed $\mathcal{P}_{N_2} = 80$ Torr. Optical pumping obtained with a narrowband laser (350 mW, FWHM $\approx$ 10 MHz) at $T_P = 140°$ C.

4.3.2 Polarization Transfer

Figure 4-14 depicts a typical double-bulb cell and shows the conventions for axis directions and polarization nomenclature used in this section and in the rest of the thesis. The transfer of polarization between pump bulb and maser bulb occurs through diffusion of polarized atoms up a transfer tube of radius ρ_0 ($\approx 1-2$ mm) and length L (≈ 3 cm), which connects the two bulbs. The general diffusion equation for the polarization $\Pi(\vec{r},t)$ is:

$$\frac{\partial \Pi(\vec{r},t)}{\partial t} = D\nabla^2\Pi(\vec{r},t) - \frac{\Pi(\vec{r},t)}{T_1}, \tag{4.12}$$

where D is the diffusion coefficient and T_1 is the bulk relaxation time. Our goal is to relate the longitudinal polarization of the ensembles contained in the two bulbs. This result will be used in Sect. 4.3.4 to solve the equations of motion of spin-exchange polarization in the pump bulb and maser oscillation in the maser bulb, which are obviously interdependent. First, we will study the case of ^{3}He. We will assume that no ^{3}He polarization is lost during the diffusion up the transfer tube, thus ignoring the bulk relaxation (i.e., the second term on the right-hand side of Eq. (4.12)) as well as any losses on the transfer tube walls. This appears to be justified given that the diffusion coefficient, D_{He}, is usually greater than 1 cm^2/s, and consequently the transit time in the tube is much shorter than the relaxation time (usually a few thousands of seconds). Therefore, ^{3}He does not suffer from significant relaxation during its time in the transfer tube.

Wall relaxation is significant for ^{129}Xe and since in the transfer tube the surface to volume ratio becomes very important it is necessary to study the polarization loss in that region. We will solve Eq. (4.12) in steady state. We will neglect bulk relaxation for simplicity ($1/T_1 = 0$) and assume a wall relaxation coefficient κ. At

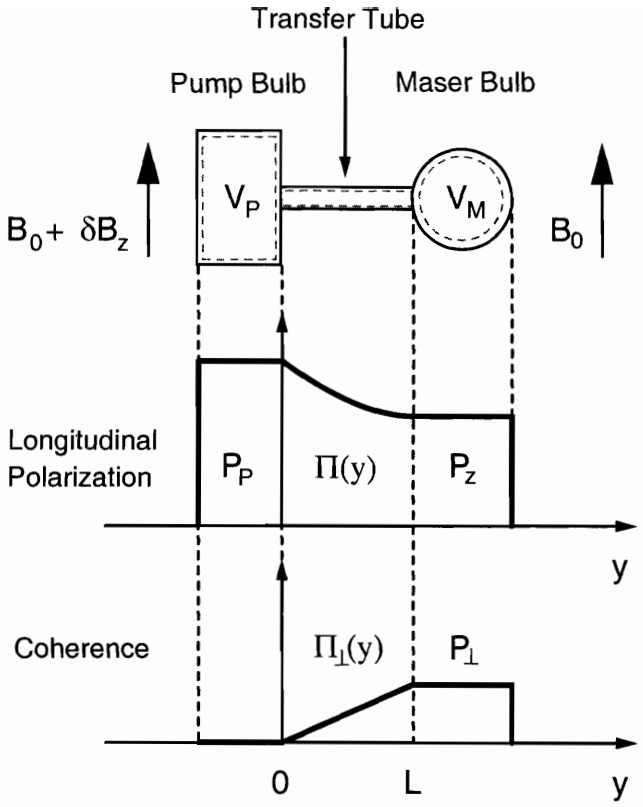

Figure 4-14: Diagram showing a typical ^{129}Xe/^{3}He maser double-bulb cell. V_P and V_M are the volumes of the pump and maser bulb, respectively. We choose the $\hat{z}$ axis along the direction of the main magnetic field, B_0, and the $\hat{y}$ axis along the direction of the transfer tube. The longitudinal polarizations (i.e., the polarizations along $\hat{z}$) of the gases in the pump bulb, P_P, and in the maser bulb, P_z, are assumed to be spatially homogeneous over the bulbs. The longitudinal polarization varies instead along the transfer tube taking the value $\Pi(y)$. Similarly, the perpendicular polarization (i.e., the coherence of the maser), which builds up homogeneously in the maser bulb, diffuses into the transfer tube, where it takes the value $\Pi_\perp(y)$. Coherence never accumulates in the pump bulb thanks to the de-phasing induced by a small longitudinal magnetic field ($\delta B_z \approx 150\,\mu$G) applied locally on the pump bulb with the help of a small coil.

the end of this section we will show how to obtain experimentally an estimate for κ.

Loss-Free Transfer Tube (^{3}He Case)

We choose the $\hat{y}$ axis to coincide with the transfer tube axis (see Fig. 4-14) and we set the origin on the side of the pump bulb so that the coordinate $y = L$ coincides with the aperture of the maser bulb. We assume homogeneous pump bulb and maser bulb longitudinal polarizations, P_P and P_z, and a spatially dependent transfer tube polarization $\Pi(y)$, with obvious boundary conditions: $\Pi(0) = P_P$ and $\Pi(L) = P_z$. The change of polarization in the pump bulb can be written:

$$\begin{aligned} \frac{d\langle P_P(\vec{r},t)\rangle}{dt} &= \frac{1}{V_P}\int_{V_P} D_P \nabla^2 P_P(\vec{r},t) d^3\vec{r} \\ &= \frac{1}{V_P}\int_{A_{tt}} D_P \vec{\nabla} P_P(\vec{r},t)\cdot \hat{n} d^2\vec{r} \\ &= \frac{D_P A_{tt}}{V_P}\,\partial_y \Pi(y,t)|_{y=0}\,, \end{aligned} \tag{4.13}$$

where we have used Eq. (4.12) and the area of the transfer tube is simply $A_{tt} = \pi\rho_0^2$. If we assume that the temperature induced variation of the diffusion coefficient along the transfer tube is compensated by a corresponding temperature induced change in gas density, we find that the requirement of negligible losses in the transfer tube leads to a steady-state solution of Eq. (4.12) with the following linear polarization profile:

$$\Pi(y) = P_P - \frac{y}{L}(P_P - P_z). \tag{4.14}$$

Note that plugging this expression into Eq. (4.13) we find that the net loss rate of polarization from the pump bulb is:

$$G_P = \frac{D_P A_{tt}}{V_P L}. \tag{4.15}$$

We can interpret G_P as the rate at which polarized atoms escape from the pump bulb. An analogous escape rate, G_M, can be defined for the maser bulb.

Relaxing Transfer Tube (^{129}Xe Case)

To take into account wall relaxation, the diffusion equation must be solved with the appropriate boundary conditions:

$$\nabla^2\Pi(\rho,y)=0 \qquad \text{with} \qquad \begin{cases} \Pi(\rho,0)=P_P \\ \Pi(\rho,L)=P_z \\ D\nabla_\perp\Pi(\rho_0,y)=-\kappa\Pi(\rho_0,y) \end{cases} \tag{4.16}$$

Because of the cylindrical symmetry we can solve the problem in two dimensions. We choose $P(\rho,y)=R(\rho)Y(y)$ and substituting the trial solution $Y(y)=e^{\pm\delta y}$ into the Laplace equation above, we obtain a radial differential equation,

$$\ddot{R}(\rho)+\frac{1}{\rho}\dot{R}(\rho)+\delta^2R(\rho)=0, \tag{4.17}$$

whose general solution is the sum of two Bessel functions:

$$R(\rho)=c_1J_0(\delta\rho)+c_2Y_0(\delta\rho). \tag{4.18}$$

Only $J_0(\delta\rho)$ does not diverge for $\rho\to 0$, thus the general solution has the form:

$$\Pi(\rho,y)=\sum_{m=0}^{\infty}J_0(\delta_m\rho)(A_me^{\delta_m y}+B_me^{-\delta_m y}). \tag{4.19}$$

Using this equation, the boundary condition on the surface of the transfer tube becomes:

$$-D\delta_m J_1(\delta_m \rho_0) = -\kappa J_0(\delta_m \rho_0), \tag{4.20}$$

which determines the value of δ_m for all m. We are not aware of an analytic solution to this equation, but we can find an approximate solution for $m = 0$ and then show that for ^{129}Xe this term is dominant. For simplicity we define $x = \rho_0 \delta_0$ and a large quantity $w = D/\rho_0\kappa \approx 2,000$, for typical values $D = 0.165$ cm^2/s, $\rho_0 = 0.2$ cm and $\kappa = 4 \times 10^{-4}$ cm/s. Assuming that $x \ll 1$ we develop the Bessel functions in Eq. (4.20) keeping terms to the second order in x and we obtain the simple equation $wx^2/2 = 1 - x^2/4$, which is self-consistent with our assumption $x \approx \sqrt{2/w} \ll 1$. To lowest order, the solution for the diffusion equation is therefore

$$\Pi(\rho, y) = \left[1 - \frac{1}{2w}\left(\frac{\rho}{\rho_0}\right)^2\right](A_0 e^{\delta_0 y} + B_0 e^{-\delta_0 y}) \tag{4.21}$$

where $\delta_0 = \sqrt{2\kappa/D\rho_0} \approx 0.16$ cm^{-1} in a typical situation. Notice that the radial parabola is very shallow. If, for a moment, we slightly modify the radial profile of the two boundary conditions in the following way:

$$\Pi(\rho, 0) = P_P\left[1 - \frac{1}{2w}\left(\frac{\rho}{\rho_0}\right)^2\right] \quad , \quad \Pi(\rho, L) = P_z\left[1 - \frac{1}{2w}\left(\frac{\rho}{\rho_0}\right)^2\right], \tag{4.22}$$

we find that $A_m = B_m = 0$ for all $m \neq 0$. This shows that even if we keep the original boundary conditions, all terms with $m \neq 0$ will have very small coefficients A_m, B_m. In fact, the extra terms of the sum in Eq. (4.19) are needed only to transform the shallow parabolas given by the $m = 0$ term at the $y = 0$ and $y = L$

boundaries into straight lines. Clearly we can neglect these terms[5] and write simply:

$$\Pi(y) = P_P \left(\cosh \delta y + \eta \sinh \delta y\right) \quad \text{with} \quad \begin{cases} \Pi(L) = P_z \\ \delta = \sqrt{\frac{2\kappa}{D\rho_0}} \end{cases} \tag{4.23}$$

where the boundary condition at $y = L$ determines η and for convenience we have dropped the subscript of ρ.

Following the procedure at the end of the last section we can find the rates of escape from the two bulbs using the following expressions,

$$\begin{aligned} \partial_y \Pi|_{y=0} &= -\delta \frac{P_P \cosh \delta L - P_z}{\sinh \delta L}, \\ \partial_y \Pi|_{y=L} &= -\delta \frac{P_P - P_z \cosh \delta L}{\sinh \delta L}, \end{aligned} \tag{4.24}$$

in conjunction with Eq. (4.13). Notice however that the correction to the escape rates when δ is small, is only quadratic in δL:

$$G_P L\delta \coth \delta L = G_P \left[1 - \frac{(\delta L)^2}{3} + O(\delta^4 L^4)\right]. \tag{4.25}$$

Determination of κ from Relaxation in a Single Bulb

If wall collisions are the dominant mechanism for polarization relaxation in a spherical bulb, it is possible to relate the wall relaxation coefficient κ to an effective bulk relaxation rate $1/T_{1,Wall}$ In practice we substitute the first term on the right-hand

[5]We actually solved the problem completely noting that, since κ is very small, to a good approximation $\delta_m \rho_0$ are the zeros of J_1. Equation 4.19 can be differentiated and evaluated at the boundaries. The coefficients A_m and B_m can be found using the orthogonality conditions for the Bessel functions. The result, as we mentioned in the text, is that the longitudinal profile of the solution is basically unaffected because the terms with big δ_m have small A_m and B_m coefficients and die out rapidly along y. Of course, this solution assumes a straight radial profile of the polarization even at the entrance of the maser bulb. If this approximation is not valid, due to high wall relaxation and negligible polarization reaching the maser bulb, neither is our solution. In that case however we would not have a ^{129}Xe maser.

side of Eq. (4.12) with a term that looks like the second, i.e.,

$$-\frac{P_z(\vec{r},t)}{T_{1,Wall}} = D\nabla^2 P_z(\vec{r},t). \tag{4.26}$$

Since we measure $T_{1,Wall}$ for the whole ensemble, we must integrate Eq. (4.26) over the bulb volume,

$$\begin{aligned} -\frac{\langle P_z(t)\rangle}{T_{1,Wall}} &= \frac{1}{V_{Bulb}}\int_{V_{Bulb}} D\nabla^2 P_z(\vec{r},t)d^3\vec{r} & (4.27)\\ &= \frac{1}{V_{Bulb}}\int_{S_{Bulb}} D\vec{\nabla}P_z(\vec{r},t)\cdot\hat{n}\ d^2\vec{r} & (4.28)\\ &= \frac{S_{Bulb}}{V_{Bulb}}(-\kappa P_z(r_0,t)). & (4.29) \end{aligned}$$

In the so-called "clean-wall limit", in which many wall collision are necessary to depolarize the atom, $\langle P_z(t)\rangle \cong P_z(r_0,t)$, and for a spherical bulb of radius r_0 we obtain

$$\kappa = \frac{r_0}{3T_{1,Wall}}. \tag{4.30}$$

Note that the coefficient κ can be related to α, the spin flip probability per wall collision. In a spherical bulb, simple kinetic theory considerations lead to the identity $\kappa = \alpha v_{th}/4$, where v_{th} is the atom's thermal velocity. This could be interesting because it yields the temperature dependence of κ if one assumes that α is temperature independent. Unfortunately, this simple theory does not work well because binding mechanisms prolong the atom's residency times on the surface at lower temperatures [72]. Nevertheless, at a specific temperature Eq. (4.30) gives a good order-of-magnitude estimate of the wall relaxation coefficient and was used in the past to estimate the ^{129}Xe wall relaxation in the pump bulb $\kappa = 1.4 \times 10^{-4}$ cm/s for $T_P = 120°$ C and in the maser bulb $\kappa = 2.8 \times 10^{-4}$ cm/s for $T_P = 45°$ C [37].

In Sect. 6.4 we will show that in our cells the relaxation coefficients are about three times bigger.

4.3.3 Inter-Diffusion and Self-Diffusion

Before solving the maser equations of motion for our noble gas masers we estimate the diffusion coefficients of ^{129}Xe and ^{3}He in the two bulbs. In doing so we take into account that the maser bulb and the pump bulb are kept at different temperatures, T_M and T_P respectively. This affects the local noble gas densities n_M and $n_P = n_M \frac{T_M}{T_P}$, which are related to each other because the partial pressure $\mathcal{P}$ of the gas is the same in the two connected bulbs. Assuming that the transfer tube volume is negligible compared to the volumes of the two bulbs, V_M and V_P, and knowing that the cell was filled initially with partial pressure $\mathcal{P}_{Fill}$ at temperature T_{Fill} (see Sect. 5.2.2) we find the common partial pressure to be

$$\mathcal{P}(\mathcal{P}_{Fill}, T_{Fill}, \frac{T_M}{T_P}, \frac{V_M}{V_P}) = \mathcal{P}_M = n_M k_B T_M = \mathcal{P}_{Fill} \frac{T_M}{T_{Fill}} \frac{V_M + V_P}{V_M + \frac{T_M}{T_P} V_P} \tag{4.31}$$

Once the partial pressure $\mathcal{P}_B$ of gas species B is known, the diffusion coefficient for inter-diffusion with species A is given by [41]

$$D_{A,B}(\mathcal{P}_B, T_{Bulb}) = \alpha_{AB} \frac{760 \text{ Torr}}{\mathcal{P}_B} \left(\frac{T_{Bulb}}{T_0} \right)^{\beta_{AB}} \tag{4.32}$$

where we have assumed that the partial pressures $\mathcal{P}$ are expressed in Torr (1 atm $\approx$ 760 Torr), the coefficients α_{AB} and β_{AB} are presented in Tab. 4.2, and self-diffusion is simply given by the special case in which $B = A$. Finally, the coefficients of self-diffusion and inter-diffusion through all the gases present in the bulb must be

A	B	α_{AB}	β_{AB}
He	He	1.62	1.71
He	Xe	0.496	1.644
He	N_2	0.613	1.524
Xe	Xe	0.048	1.9
Xe	He	0.496	1.644
Xe	N_2	0.106	1.789

Table 4.2: Coefficients describing the inter-diffusion of gas species A into gas species B according to Eq. (4.32). The coefficients are from Refs. [41, 73].

combined. For instance, the diffusion coefficient for ^{3}He is given by

$$\frac{1}{D_{He}} = \frac{1}{D_{He,He}} + \frac{1}{D_{He,Xe}} + \frac{1}{D_{He,N_2}} \tag{4.33}$$

and an analogous expression holds for ^{129}Xe. Notice that we considered also the significant density of N_2, used in our cells to quench the radiative decays of Rb and prevent radiation trapping during the optical pumping process (see Sect. 2.1). In Figs. 4-15 and 4-16 we show the diffusion coefficients for ^{129}Xe, and ^{3}He for a typical range of the noble gases fill pressures.

Bulb Escape Times

In Sect. 4.3.2 we have found the rates G_P and G_M at which polarized atoms escape the pump and maser bulb respectively. Now that we know the diffusion coefficients for the noble gases we can show the maser bulb escape times ($1/G_M$) for ^{3}He (see Fig. 4-17) and ^{129}Xe (see Fig. 4-18) in a typical range of fill pressures for a typical cell.

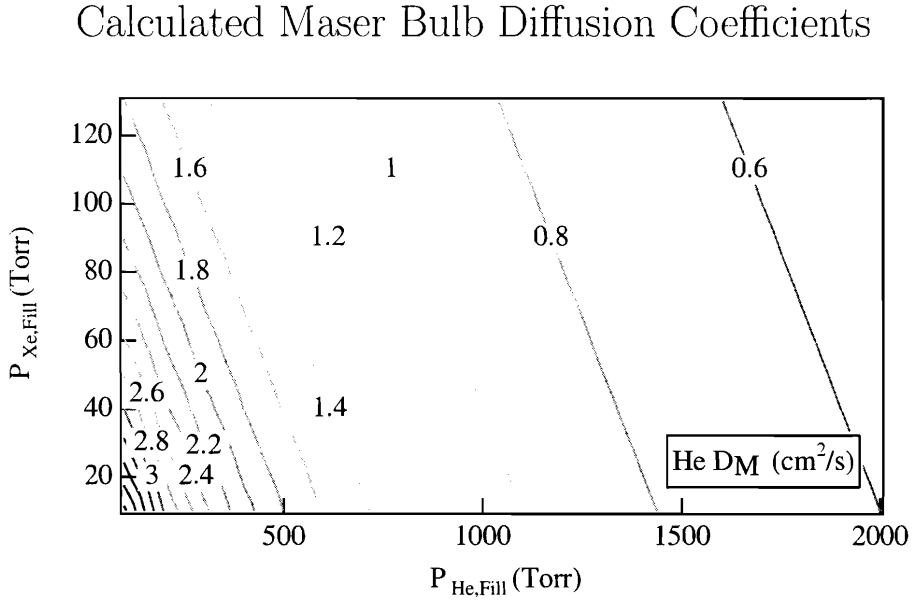

Figure 4-15: Contour plot showing the calculated diffusion coefficient, D_M, of ^{3}He in the maser bulb for a range of noble gas fill pressures, fixed $\mathcal{P}_{N_2} = 80$ Torr and temperature $T_M = 50°$ C.

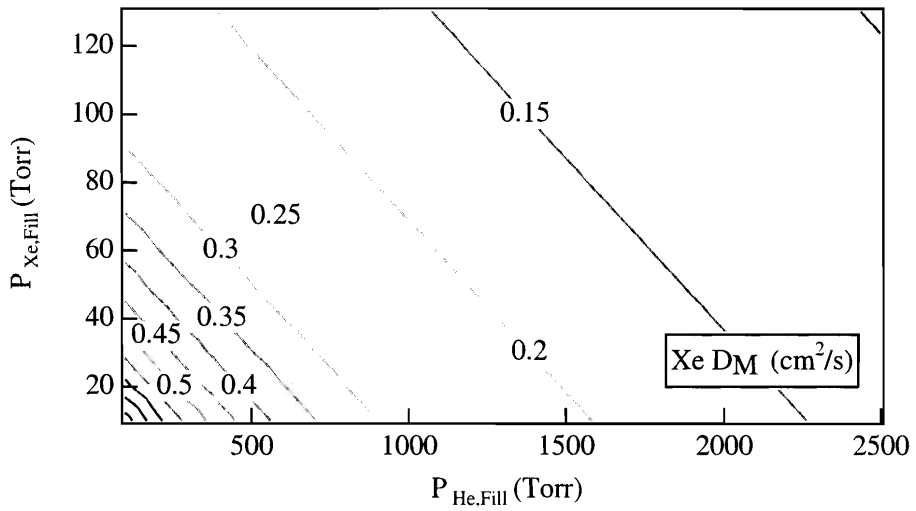

Figure 4-16: Contour plot showing the calculated diffusion coefficient, D_M, of ^{129}Xe in the maser bulb for a range of noble gas fill pressures, fixed $\mathcal{P}_{N_2} = 80$ Torr and temperature $T_M = 50°$ C.

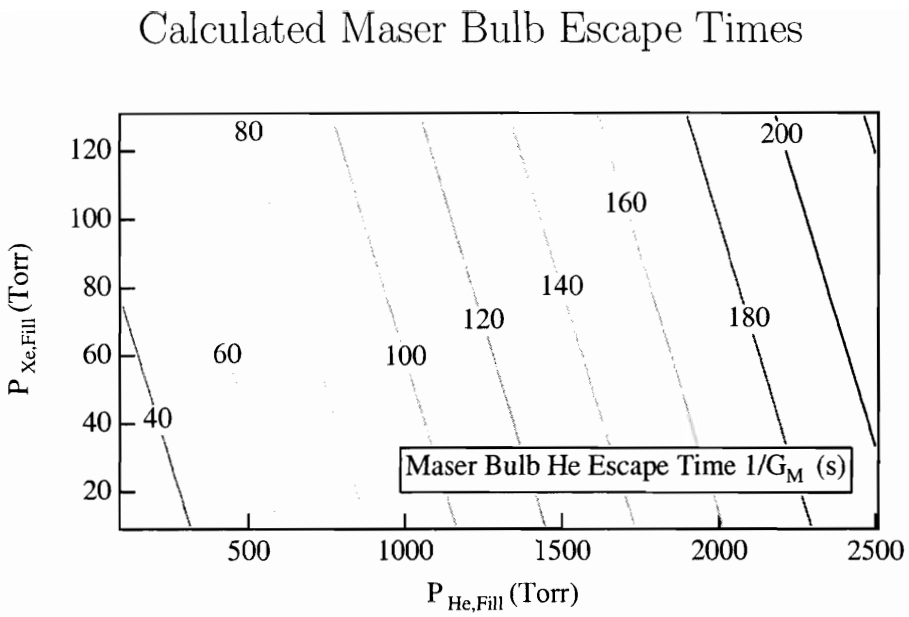

Figure 4-17: Contour plot showing ^{3}He maser bulb escape time for a range of noble gas fill pressures, fixed $\mathcal{P}_{N_2} = 80$ Torr at $T_M = 50°$ C.

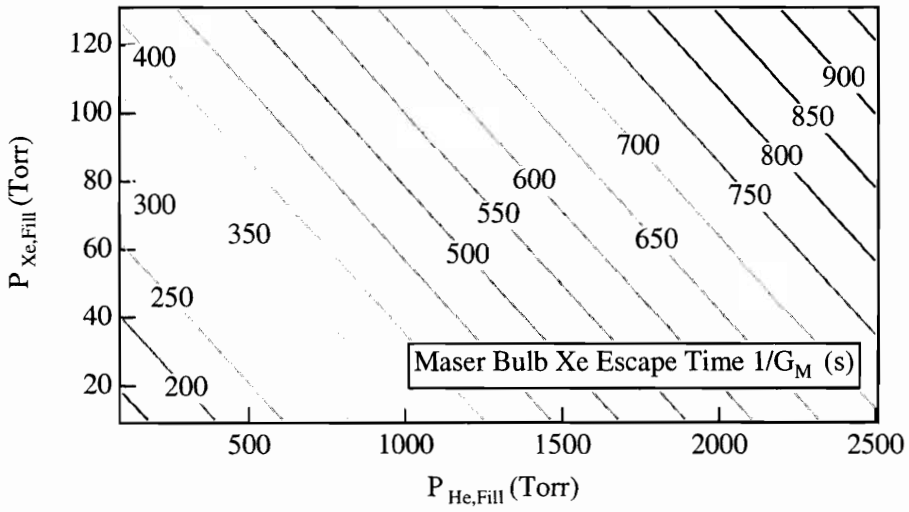

Figure 4-18: Contour plot showing ^{129}Xe maser bulb escape time for a range of noble gas fill pressures, fixed $\mathcal{P}_{N_2} = 80$ Torr at $T_M = 50°$ C.

4.3.4 Modified Bloch Equations and Steady State Polarizations

In Sect. 2.3 we presented the general theory for a spin-1/2 Zeeman maser bulb receiving a constant flux of polarized atoms from an outside source and whose feedback resonant circuit was in general detuned from the Zeeman frequency. In this section we solve the realistic problem of the double-bulb maser, in which the noble gas atoms are polarized in the pump bulb through spin-exchange collisions with optically pumped Rb and then diffuse into the maser bulb, where the maser oscillation takes place. For simplicity we will assume that the tuned circuit is exactly on resonance at the Zeeman frequency (i.e., $\alpha = \pi/2$).

The process of spin-exchange polarization was discussed in Sect. 2.1. For convenience we define a source term, S, and a pump bulb lifetime T, which take into account the effects of the spin-exchange interaction:

$$S = P_{Rb}\gamma_{se}, \tag{4.34}$$

$$\frac{1}{T} = \frac{1}{T_{1,P}} + \gamma_{se}. \tag{4.35}$$

The feedback of the resonant circuit was discussed in Sect. 2.3.1 and is characterized by the Rabi frequency, ω_R (defined in Eq. (2.31)), and the radiation damping time, τ_{RD} (defined in Eq. (2.32)):

$$\omega_R = \frac{P_\perp}{\tau_{RD} P_{z,0}} = \frac{P_\perp}{\tau}, \tag{4.36}$$

$$\tau_{RD}^{-1} = \frac{\hbar\gamma_{ng}^2}{4}\frac{\xi_o^2 Q V_M}{L_{pu}}[ng]P_{z,0}. \tag{4.37}$$

As usual, $P_{z,0}$ is the equilibrium polarization that would be achieved in the maser

bulb in absence of masing. We also introduced a characteristic feedback time $\tau = \tau_{RD}\, P_{z,0}$, which depends on the geometry of cell and pickup coil, as well as the noble gas density and gyromagnetic ratio, but is independent of polarization and polarization transfer efficiency.

The gas polarization profile in the transfer tube, $\Pi(y)$, was discussed in Sect. 4.3.2, where for each bulb we also introduced the bulb escape rate,

$$G_{Bulb} = \frac{A_{tt} D_{Bulb}}{V_{Bulb} L}, \tag{4.38}$$

which depends on the gas diffusion coefficient D_{Bulb}, the cross section of the tube A_{tt}, its length L, and the bulb volume V_{Bulb}.

Taking into account diffusion into and out of the transfer tube, we can now write the time variation of the pump bulb longitudinal polarization, P_P, and the analogue of the maser Eqs. (2.34) and (2.36) for the noble gas longitudinal and perpendicular polarizations, P_z and $P_\perp$, in the maser bulb (see also Fig. 4-14):

$$\dot{P}_P = S - \frac{P_P}{T} + G_P L\, \partial_y \Pi|_{y=0}\,, \tag{4.39}$$

$$\dot{P}_z = -\frac{P_z}{T_1} - \omega_R P_\perp - G_M L\, \partial_y \Pi|_{y=L}\,, \tag{4.40}$$

$$\dot{P}_\perp = -\frac{P_\perp}{T_2} + \omega_R P_z - G_M L\, \partial_y \Pi_\perp|_{y=L}\,. \tag{4.41}$$

Analytical solutions for the steady state polarizations can be found both in the case of polarization transfer with no losses, which applies to ^{3}He, and in the case of ^{129}Xe, where losses are not negligible. We will discuss the two cases separately in the next two sections, in a third section we will compare maser signals, powers and the expected thermal frequency noise.

^{3}He Equilibrium Solutions

In Sect. 4.3.2 we discussed the transfer of polarization without losses. For longitudinal and perpendicular polarization, we choose the following functions:

$$\Pi(y) = P_P - \frac{y}{L}(P_P - P_z), \tag{4.42}$$

$$\Pi_\perp(y) = \frac{y}{L}P_\perp. \tag{4.43}$$

While the boundary conditions that $\Pi(y)$ has to meet were clear, the conditions for the perpendicular polarization diffusing out of the maser bulb needed further assumptions. We chose boundary conditions that imposed continuity at the entrance of the maser bulb ($\Pi_\perp(L) = P_\perp$) and a vanishing perpendicular polarization at the entrance of the pump bulb ($\Pi_\perp(0) = 0$) . As we will see in Sect. 5.4.5, whatever perpendicular polarization there may be in the pump bulb, it can easily be destroyed by applying a small, localized, longitudinal magnetic field. When we use such a field, Eq. (4.43) appears justified. Notice that we have neglected coherence losses due to magnetic field gradient-induced dephasing in the transfer tube. This approximation is good when the ^{3}He T_2^* has been maximized making use of a dedicated set of gradient trim coils (see Sect. 5.4.2).

In writing our solutions it is convenient to use the following definitions:

$$\begin{aligned}
\frac{1}{T^*} &= G_P + \frac{1}{T} = G_P + \frac{1}{T_{1,P}} + \gamma_{se}, \qquad (4.44)\\
\frac{1}{T_1^*} &= G_M + \frac{1}{T_1},\\
\frac{1}{T_2^*} &= G_M + \frac{1}{T_2},\\
\lambda &= G_P T^* G_M T_1^* = \left(\frac{G_P}{G_P + \frac{1}{T_{1,P}} + \gamma_{se}}\right)\left(\frac{G_M}{G_M + \frac{1}{T_1}}\right) < 1.
\end{aligned}$$

The first three equations simply modify the polarization lifetime and coherence time taking into account the escape times from the two bulbs. The dimensionless quantity λ approaches unity when bulb escape rates dominate over other relaxations rates and optical pumping rates, which is usually the case for ^{3}He.

The steady state solutions for the longitudinal polarizations when the feedback system is turned off are:

$$P_{P,0} = \frac{S\,T^*}{1-\lambda}, \tag{4.45}$$

$$P_{z,0} = \frac{S\,\lambda}{G_P(1-\lambda)} = G_M T_1^* P_{P,0}. \tag{4.46}$$

Notice that when λ approaches 1, $P_{P,0} \approx ST/(1 + TG_P/T_1G_M))$, where ST is the polarization that would be achieved in a single (pump) bulb cell. In this limit, since $G_M T_1^* \approx 1$ we have roughly the same polarization in both bulbs, $P_{P,0} \approx P_{z,0}$.

When we connect the feedback circuit, the polarizations in the two bulbs reach the following equilibrium values:

$$\frac{P_{P,eq}}{P_{P,0}} = 1 - \lambda(1 - \frac{\tau_{RD}}{T_2^*}), \tag{4.47}$$

$$\frac{P_{z,eq}}{P_{z,0}} = \frac{\tau_{RD}}{T_2^*}, \tag{4.48}$$

$$\frac{P_{\perp,eq}}{P_{z,0}} = \sqrt{(1-\lambda)\frac{\tau_{RD}}{T_1^*}(1 - \frac{\tau_{RD}}{T_2^*})}. \tag{4.49}$$

The last two equations strongly resemble Eqs. (2.37) and (2.38) thanks to our definitions in Eqs. (4.44). Again, when λ approaches 1 we see that the longitudinal polarization is roughly the same in the two bulbs, $P_P \approx P_z = P_{P,0}\tau_{RD}/T_2^* \approx \tau/T_2^*$. In this limit, the threshold condition, $\tau_{RD} < T_2^*$, becomes $\tau < T_2^* P_{P,0}$.

In Tab. 4.3 we list the typical values of the quantities that enter our equations

of motion. Choosing the fill pressures $\mathcal{P}_{He,Fill} = 600$ Torr, $\mathcal{P}_{Xe,Fill} = 30$ Torr, and using the Rb polarization obtained with our numeric optical pumping simulation (see Sect. 4.3.1 and in particular Fig. 4-10) for a narrow-band laser at $T_P = 114°$ C, we obtain the results listed in Tab. 4.4.

Once the geometry of the cell and the laser source have been chosen, the most easily adjustable operating parameters are the gas fill pressures. We therefore show contour plots for the ^{3}He equilibrium polarizations in Figs. 4-19 through 4-23 for a wide range of fill pressures. We also show the predicted values for τ_{RD} in Fig. 4-24.

^{129}Xe Equilibrium Solutions

In Sect. 4.3.2 we solved the problem of wall-collision-induced polarization relaxation in the transfer tube. For longitudinal and perpendicular polarizations, we choose the following profiles:

$$\Pi(y) = \cosh \delta y \; P_P + \frac{\sinh \delta y}{\sinh \delta L} \; (P_z - P_P \cosh \delta L), \tag{4.50}$$

$$\Pi_\perp(y) = \frac{\sinh \delta y}{\sinh \delta L} \; P_\perp, \tag{4.51}$$

where $1/\delta = 1/\sqrt{2\kappa/D\rho_0}$ is the characteristic wall relaxation length. The first of these equations is simply the solution to the boundary-value problem in Eq. (4.23). The second equation, represents the perpendicular polarization which diffuses out of the maser bulb. As in the last section we choose the perpendicular polarization to vanish at the entrance of the pump bulb. In the case of ^{129}Xe this condition is certainly met even without the application of an additional magnetic field to the pump bulb region. In fact, the interaction with polarized Rb in the illuminated region sufficiently detunes the ^{129}Xe frequency away from the maser frequency that it is no longer part of the masing ensemble (see Sect. 6.7.1). Again, we have neglected

Description	Parameter	^{3}He	^{129}Xe	Units
Quality factor	Q	16.4	15.6	-
Gyromagnetic ratio	γ	2π 3243.72	2π 1177.79	Hz/G
Operating maser frequency	ω_M	4710	1710	Hz
Velocity averaged SE cross-section	k_{se}	6.7×10^{-20}	1.75×10^{-16}	cm^3/s
Polarization lifetime (pump)	$T_{1,P}$	6000	500	s
Polarization lifetime (maser)	T_1	6000	500	s
Coherence time (maser)	T_2	200	300	s
Wall loss parameter	κ	0	0.0006	cm/s
^{3}He fill pressure	$\mathcal{P}_{He,Fill}$	600		Torr
^{129}Xe fill pressure	$\mathcal{P}_{Xe,Fill}$	30		Torr
N_2 fill pressure	$\mathcal{P}_{N_2,Fill}$	80		Torr
Pump bulb temperature	T_P	114		° C
Maser bulb temperature	T_M	50		° C
Fill temperature	T_{Fill}	22		° C
Pump bulb Rb density	[Rb]	1.4×10^{13}		cm^{-3}
Static magnetic field	B_0	1.51		G
Pick-up coil mean field	ξ_0	444		G/A
Pump bulb length	l	2.8		cm
Pump bulb radius		0.83		cm
Transfer tube length	L	3		cm
Transfer tube cross-section	$A_{tt} = \pi\rho_0^2$	$\pi\ 0.2^2 = 0.13$		cm^2
Pump bulb volume	V_P	6		cm^3
Maser bulb volume	V_M	4		cm^3
Preamplifier gain	G	5,000		-
Pick-up coil inductance	L_{pu}	92		mH
Laser power		350		mW
Laser spectrum FWHM		10		MHz

Table 4.3: The 27 input parameters needed to calculate the steady state values of maser polarizations, maser powers and expected levels of thermal frequency noise given in Tab. 4.4.

Description	Parameter	^{3}He	^{129}Xe	Units
Effective spin-exchange rate	$S = P_{Rb}\gamma_{se}$	8.9×10^{-7}	0.0023	1/s
Effective polarization lifetime (pump)	T^*	71	130	s
Effective polarization lifetime (maser)	T_1^*	64	180	s
Effective coherence time (maser)	T_2^*	48	145	s
Characteristic feedback time	$\tau = \tau_{RD} P_{z,0}$	0.030	4.8	s
Pump bulb escape time	$1/G_P$	72	323	s
Maser bulb escape time	$1/G_M$	65	294	s
Diffusion coefficient (pump)	D_P	2.0	0.45	cm^2/s
Diffusion coefficient (maser)	D_M	1.5	0.32	cm^2/s
Polarization transfer efficiency	λ	0.98	0.23	-
Wall relaxation length	$1/\delta$	–	8.3	cm
Rb Polarization	P_{Rb}	0.94		-
Absorbed laser light		191		mW
In absence of masing				
Longitudinal polarization (pump)	$P_{P,0}$	0.0028	0.39	-
Longitudinal polarization (maser)	$P_{z,0}$	0.0028	0.23	-
While masing				
Longitudinal polarization (pump)	P_P	0.0007	0.32	-
Longitudinal polarization (maser)	P_z	0.00061	0.033	-
Precessing polarization	$P_\perp$	0.00015	0.063	-
Radiation damping time	τ_{RD}	11	21	s
Maser amplitude	R	11	29	mV
Maser power	W	1.1×10^{-9}	2.1×10^{-8}	erg/s
Frequency noise at 24 h	$\Delta\nu_{wf}$	101	8	nHz
Static magnetic field induced by M_z	$8\pi M_z/3$	1.2	1.2	μG

Table 4.4: Steady state parameters calculated using the input parameters in Tab. 4.3 and the equations introduced throughout Sect. 4.3. Note that the numerical values specifically refer to a cell with $\mathcal{P}_{He,Fill} = 600$ Torr, $\mathcal{P}_{Xe,Fill} = 30$ Torr, illuminated with the low power, narrow-band laser. Most of the parameters listed here are displayed in the contour plots in the rest of this section for a range of noble gas fill pressures.

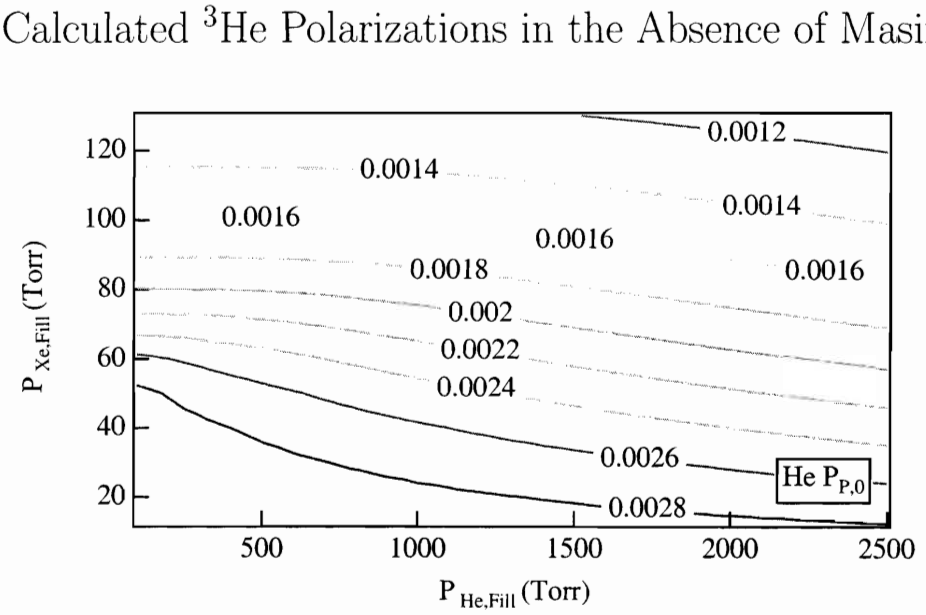

Figure 4-19: Contour plot showing the calculated ^{3}He longitudinal polarization, $P_{P,0}$, in the pump bulb in the absence of masing for a range of noble gas fill pressures. $T_P = 114°$ C, narrow-band laser used for optical pumping, other input parameters as in Tab. 4.3.

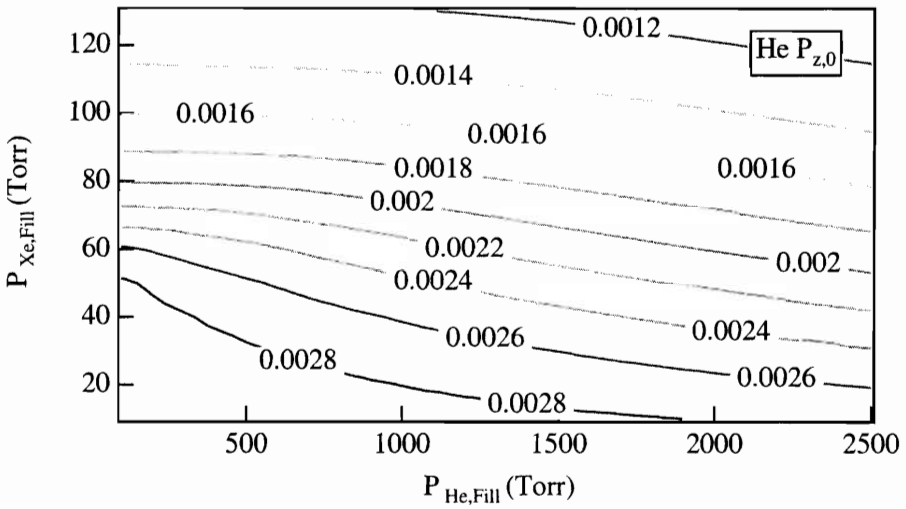

Figure 4-20: Contour plot showing the calculated ^{3}He longitudinal polarization, $P_{z,0}$, in the maser bulb in the absence of masing for a range of noble gas fill pressures. $T_P = 114°$ C, narrow-band laser used for optical pumping, other input parameters as in Tab. 4.3.

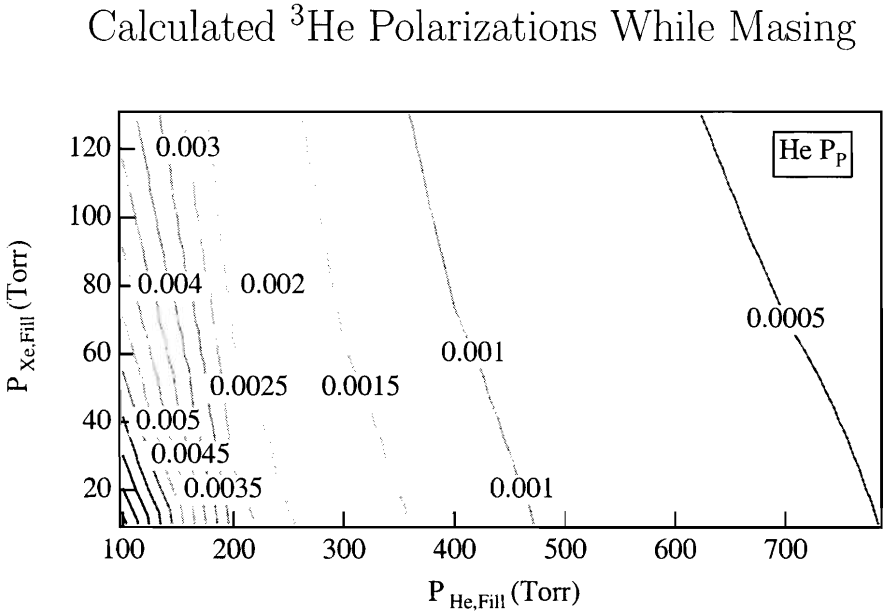

Figure 4-21: Contour plot showing the calculated ^{3}He longitudinal polarization, P_P, in the pump bulb while masing for a range of noble gas fill pressures. $T_P = 114°$ C, narrow-band laser used for optical pumping, other input parameters as in Tab. 4.3.

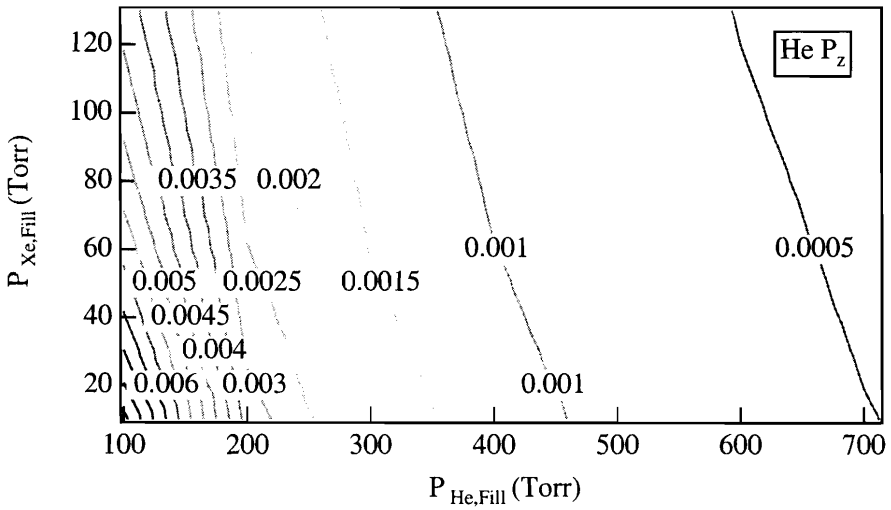

Figure 4-22: Contour plot showing the calculated ^{3}He longitudinal polarization, P_z, in the maser bulb while masing for a range of noble gas fill pressures. $T_P = 114°$ C, narrow-band laser used for optical pumping, other input parameters as in Tab. 4.3.

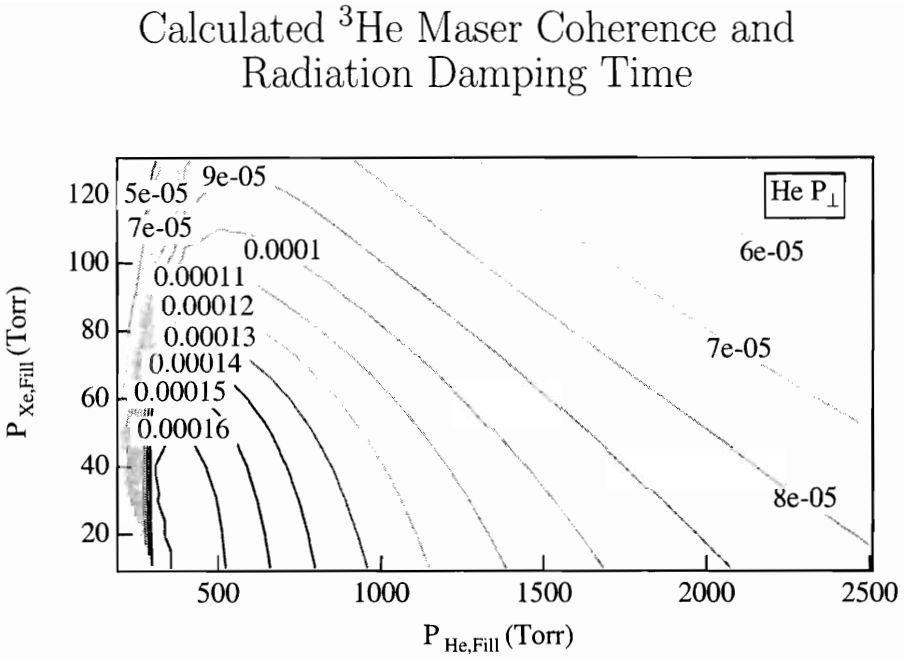

Figure 4-23: Contour plot showing the calculated ^{3}He perpendicular polarization, $P_\perp$, in the maser bulb while masing for a range of noble gas fill pressures. $T_P = 114°$ C, narrow-band laser used for optical pumping, other input parameters as in Tab. 4.3.

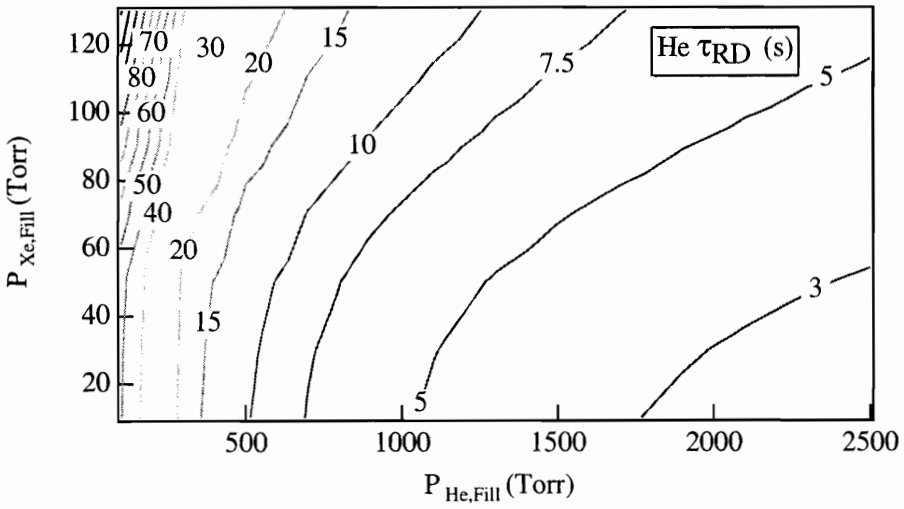

Figure 4-24: Contour plot showing the calculated ^{3}He radiation damping time, τ_{RD}, for a range of noble gas fill pressures. $T_P = 114°$ C, narrow-band laser used for optical pumping, other input parameters as in Tab. 4.3.

the coherence loss rate, $1/T_{2,tt}$, due to magnetic field gradients in the transfer tube, because we assumed optimal trimming of our gradient coils. These losses can be taken into account by replacing δ in Eq. (4.51), with $\delta' = \sqrt{2\kappa/D\rho_0 + 1/DT_{2,tt}}$.

It is convenient to modify Eqs. (4.44) in the following way:

$$\begin{aligned}
\frac{1}{T^*} &= G_P\ \delta L \coth \delta L + \frac{1}{T} = G_P\ \delta L \coth \delta L + \frac{1}{T_{1,P}} + \gamma_{se}, \qquad (4.52)\\
\frac{1}{T_1^*} &= G_M\ \delta L \coth \delta L + \frac{1}{T_1},\\
\frac{1}{T_2^*} &= G_M\ \delta L \coth \delta L + \frac{1}{T_2},\\
\lambda &= G_P T^* G_M T_1^* \left(\frac{\delta L}{\sinh \delta L}\right)^2 < 1.
\end{aligned}$$

These definitions are equivalent to the previous ones in the limit of negligible wall relaxation ($\delta L \to 0$). The efficiency of polarization transfer, λ, is manifestly worsened by wall relaxation (typically $\delta^2 L^2/\sinh^2 \delta L \approx 0.95$).

With the changes in the definitions above, the analytic solutions for the steady state polarizations are exactly equal to those found in the previous section, with the exception of

$$P_{z,0} = G_M T_1^* P_{P,0}\ \frac{\delta L}{\sinh \delta L}, \qquad (4.53)$$

which also converges to Eq. (4.46) for $\delta L \to 0$.

Since the diffusion coefficient is usually much smaller for ^{129}Xe than for ^{3}He, the effective times in Eqs. (4.52) are not dominated by bulb escape, even when we neglect wall relaxation. As a result, the polarization transfer for ^{129}Xe is less efficient than for ^{3}He and typically $\lambda \approx 0.1 - 0.3$.

For the parameters listed in Tab. 4.3 and using the Rb polarization values obtained with our numeric optical pumping simulation of a narrow-band laser at

$T_P = 114°$ C, we obtain the polarization contour plots shown in Figs. 4-25 through 4-29. We also show in Fig. 4-30 the predicted values for τ_{RD}.

Maser Signals, Maser Powers and Expected Thermal Frequency Noise

Of the quantities presented in the last two sections, only the radiation damping times and the T_2^* are observable. Another quantity that we can accurately measure is the maser signal, V_{ab}, from which we can calculate the maser power, W_{ng}, and subsequently the level of expected frequency noise, $\Delta\nu_{fw}$. For convenience we reproduce here Eqs. (2.45), (2.43), and (2.70) derived in Ch. 2:

$$V_{ab} = G\sqrt{\omega_M L_{pu} Q W}, \tag{4.54}$$

$$W_{ng} = \frac{\hbar\omega_M}{2}[ng]V_M \frac{P_{\perp,eq}^2}{\tau_{RD} P_{z,0}}, \tag{4.55}$$

$$\Delta\nu_{fw}(\tau) = \frac{1}{\pi T_2^*}\sqrt{\frac{k_B T_M}{2W_{ng}\tau}}. \tag{4.56}$$

Figures 4-31 and 4-32 show the contour plots of the expected signals for the two masers, while Figs. 4-33 and 4-34 show the maser powers. We have used the parameters listed in Tab. 4.3, a pump bulb temperature $T_P = 114°$ C and a narrow-band laser. The curves of equal power for ^{3}He clearly show that the region of lowest ^{129}Xe pressure and highest ^{3}He pressure is optimal for the ^{3}He maser. Instead, the highest ^{129}Xe maser power is obtained in absence of ^{3}He with approximately 60 Torr of ^{129}Xe. Higher ^{129}Xe pressures lead to poor Rb polarization (see Fig. 4-10) and complete absorption of laser light (see Fig. 4-11) due to high Rb-^{129}Xe spin-destruction.

For ^{129}Xe fill pressures below 60 Torr, both the ^{3}He and ^{129}Xe pressures can be decreased, leaving maser powers and signals unchanged. This shows that there is a tradeoff between the decrease in number density, which drops with fill pressures, and

Calculated ^{129}Xe Polarizations in the Absence of Masing

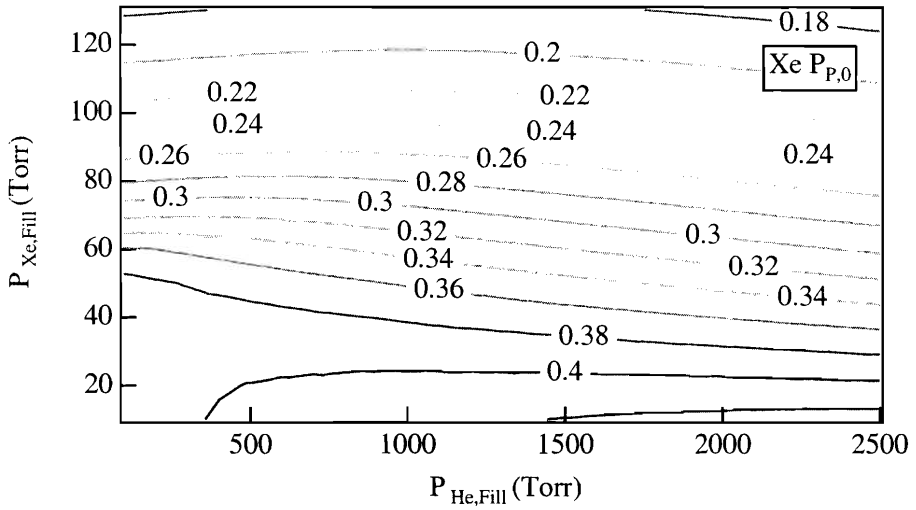

Figure 4-25: Contour plot showing the calculated ^{129}Xe longitudinal polarization, $P_{P,0}$, in the pump bulb in the absence of masing for a range of noble gas fill pressures. $T_P = 114°$ C, narrow-band laser used for optical pumping, other input parameters as in Tab. 4.3.

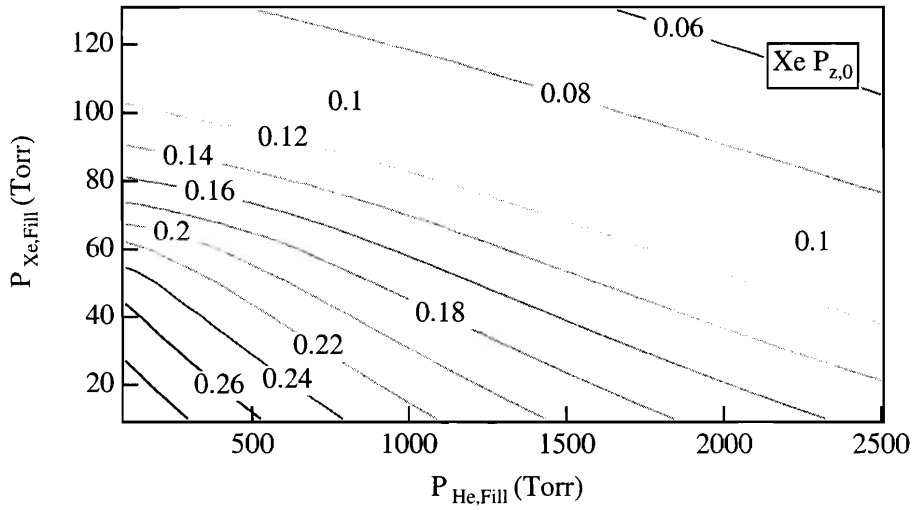

Figure 4-26: Contour plot showing the calculated ^{129}Xe longitudinal polarization, $P_{z,0}$, in the maser bulb in the absence of masing for a range of noble gas fill pressures. $T_P = 114°$ C, narrow-band laser used for optical pumping, other input parameters as in Tab. 4.3.

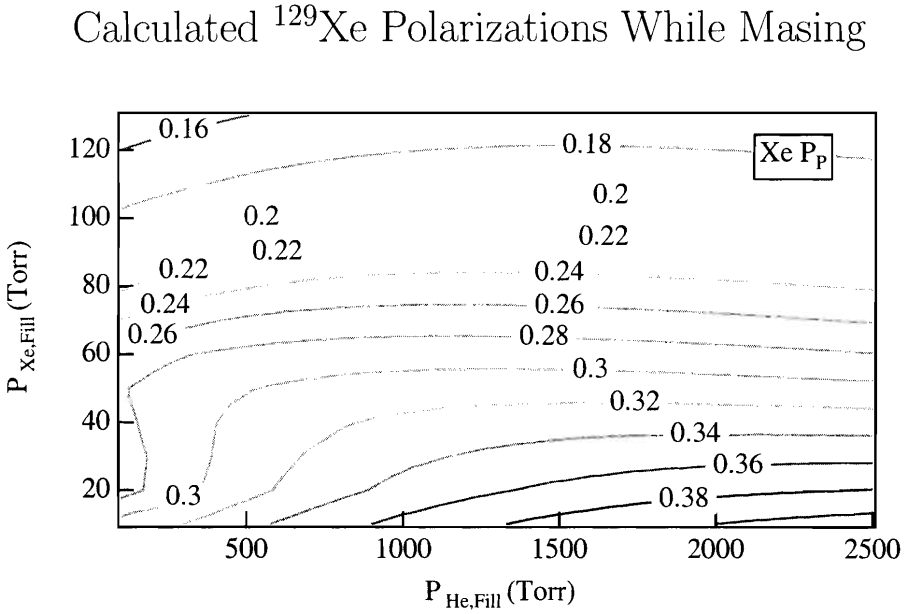

Figure 4-27: Contour plot showing the calculated ^{129}Xe longitudinal polarization, P_P, in the pump bulb while masing for a range of noble gas fill pressures. $T_P = 114°$ C, narrow-band laser used for optical pumping, other input parameters as in Tab. 4.3.

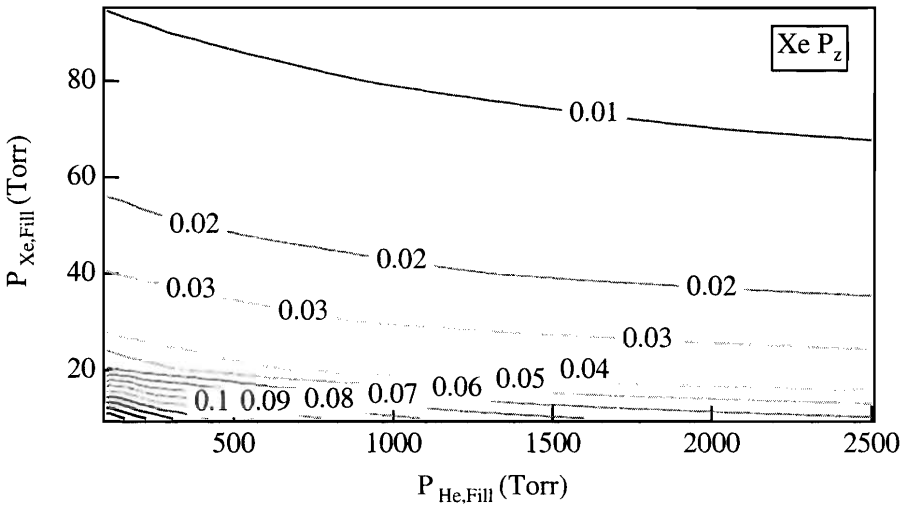

Figure 4-28: Contour plot showing the calculated ^{129}Xe longitudinal polarization, P_z, in the maser bulb while masing for a range of noble gas fill pressures. $T_P = 114°$ C, narrow-band laser used for optical pumping, other input parameters as in Tab. 4.3.

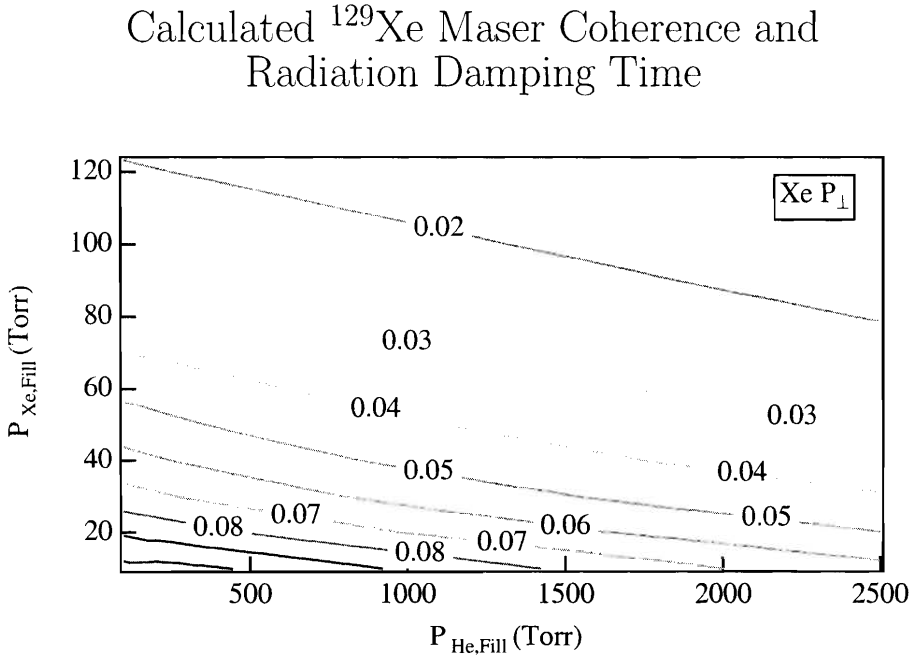

Figure 4-29: Contour plot showing the calculated ^{129}Xe perpendicular polarization, $P_\perp$, in the maser bulb while masing for a range of noble gas fill pressures. $T_P = 114°$ C, narrow-band laser used for optical pumping, other input parameters as in Tab. 4.3.

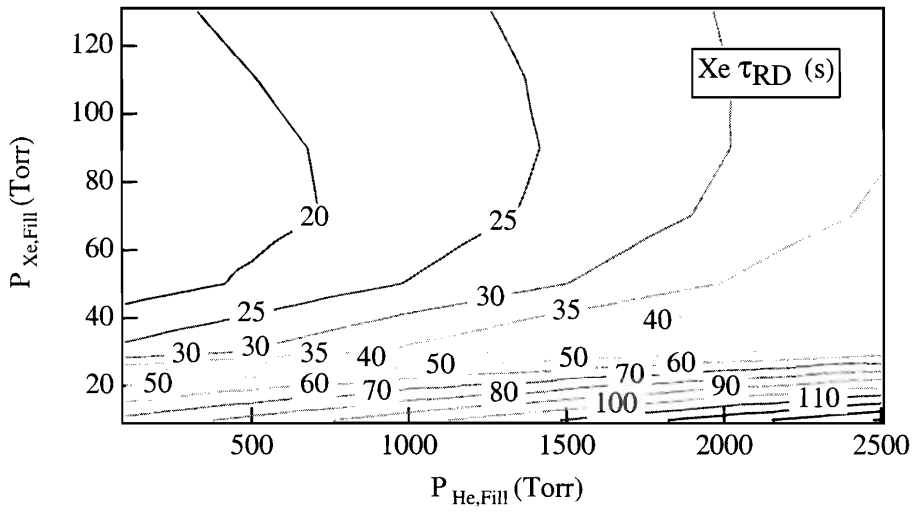

Figure 4-30: Contour plot showing the calculated ^{129}Xe radiation damping time, τ_{RD}, for a range of noble gas fill pressures. $T_P = 114°$ C, narrow-band laser used for optical pumping, other input parameters as in Tab. 4.3.

an increase in polarization transport efficiency due to higher diffusion coefficients at lower pressures. For fixed maser power, operating the masers with higher diffusion coefficients and lower densities has several advantages, and a major disadvantage. At high densities the magnetic induction created by the static magnetization of one gas species deteriorates the magnetic environment of the other species, shortening the other species' coherence time [34]. Thus low densities are advantageous. Higher diffusion coefficients obtained at low fill pressures also improve spatial averaging of residual magnetic field gradients as well as pickup coil field inhomogeneity. Moreover, in the next section we will argue that higher diffusion coefficients are likely to improve co-magnetometry.

The disadvantage that comes with low fill pressures is that bulb escape time decreases and this worsens the thermal frequency noise as shown in Eq. (4.56). Since the ^{3}He maser power is always one or two orders of magnitude smaller than the ^{129}Xe power, ^{3}He is the species most affected by thermal noise. As Fig. 4-35 shows, the curves of equal thermal noise for ^{3}He are not quite as steep as the curves of equal power. Faster diffusion shortens the ^{3}He bulb escape time. As the interaction time, T_2^*, decreases so does the line Q and this worsens the level of thermal frequency noise.

A straightforward way to increase the ^{3}He power is to increase the pump bulb temperature. This induces an exponential increase in the Rb density and a corresponding increase in spin-exchange rate (provided that there is enough light to keep the Rb polarization sufficiently high). In Fig. 4-37 through 4-40 we show maser signal and thermal frequency noise for both masers at a pump bulb temperature $T_P = 140°$ C. In Sect. 4.3.1 we computed the level of Rb polarization that can be attained at this temperature in theory[6] (see Fig. 4-12 and 4-13). Figure 4-39 shows

[6]In practice at these higher temperatures our simulations seem to overestimate the flux of ^{129}Xe

that at low ^{3}He and ^{129}Xe pressures, the thermal frequency noise remains substantial, whereas for ^{3}He pressures above $1,400$ Torr and ^{129}Xe pressures below 40 Torr the level of noise is much smaller.

4.4 Co-Magnetometry

The oscillation frequencies of our Zeeman masers depend to first order on the magnetic field created by the main solenoid. Since the stability of our power supply varies between 10 and 100 ppm, a single-species noble gas maser would not be a very sensitive tool for LI tests. As we have already noted, maser frequency stability is drastically improved by employing a second co-located maser as a co-magnetometer. Evidence for imperfect co-magnetometry was obtained by applying small magnetic field gradients across the cell and observing sizable maser frequency shifts whereas perfect co-magnetometry would have yielded no effect. Preliminary experimental tests of co-magnetometry are reported in Sect. 6.8.

In this section we study theoretically the spatial distribution of the two noble gas species. We try to understand how co-located they really are and whether this matters at all. Considering that the polarized atoms reach the maser bulb through a small opening, there is a legitimate concern that the different diffusion coefficients for the two species (see Sect. 4.3.3) and different wall relaxation rates may lead to a different mean distribution of the two masing species.

---

polarization that reaches the maser bulb. We suspect that when the pump bulb temperature is increased a substantial density of unpolarized Rb vapor in the transfer tube depolarizes the ^{129}Xe atoms, thus reducing the flux into the maser bulb. This effect has not been included in the models presented in this chapter and will be studied in Ch. 6.

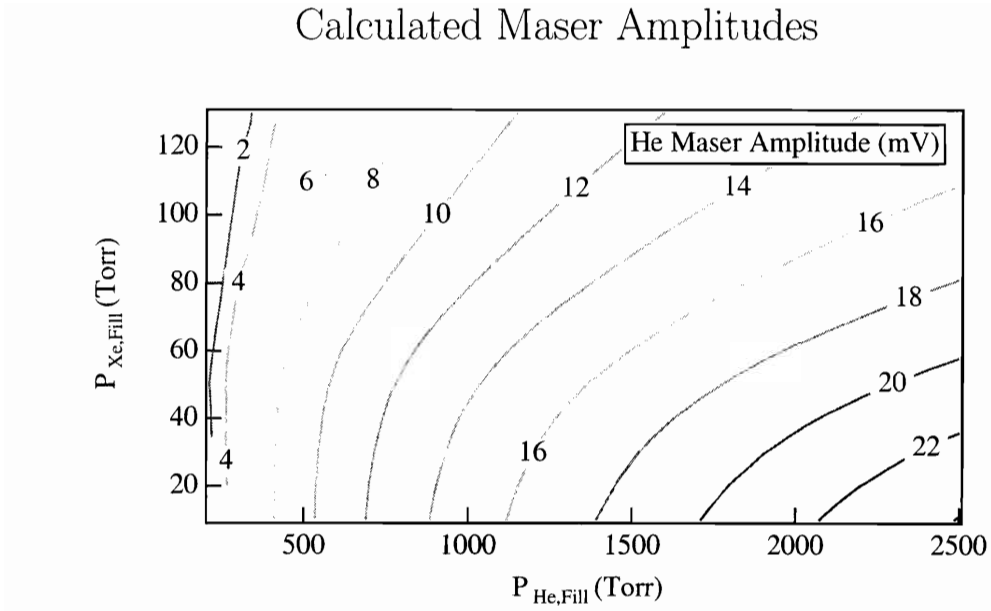

Figure 4-31: Contour plot showing the calculated ^{3}He maser output voltage for a range of noble gas fill pressures. $T_P = 114°$ C, narrow-band laser used for optical pumping, other input parameters as in Tab. 4.3.

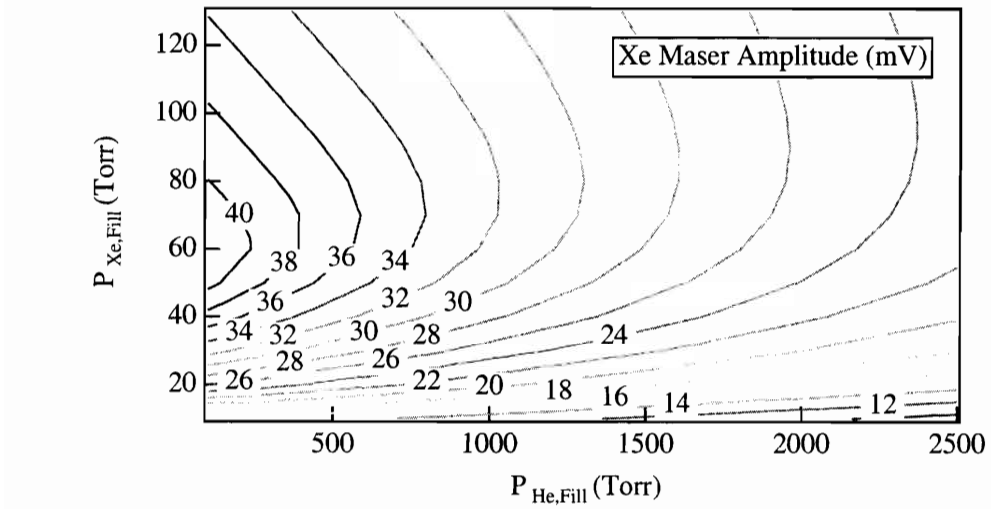

Figure 4-32: Contour plot showing the calculated ^{129}Xe maser output voltage for a range of noble gas fill pressures. $T_P = 114°$ C, narrow-band laser used for optical pumping, other input parameters as in Tab. 4.3.

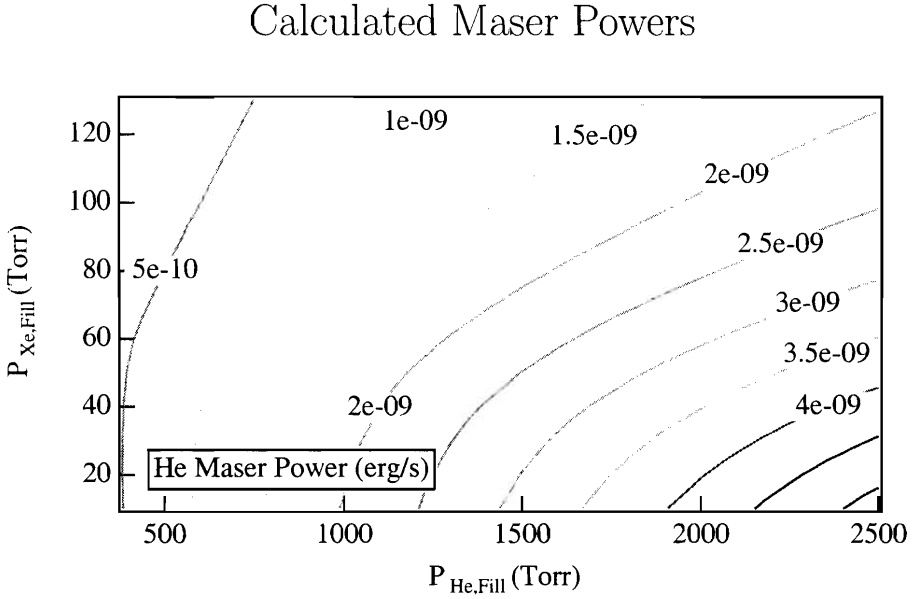

Figure 4-33: Contour plot showing the calculated ^{3}He maser power for a range of noble gas fill pressures. T_P = 114° C, narrow-band laser used for optical pumping, other input parameters as in Tab. 4.3.

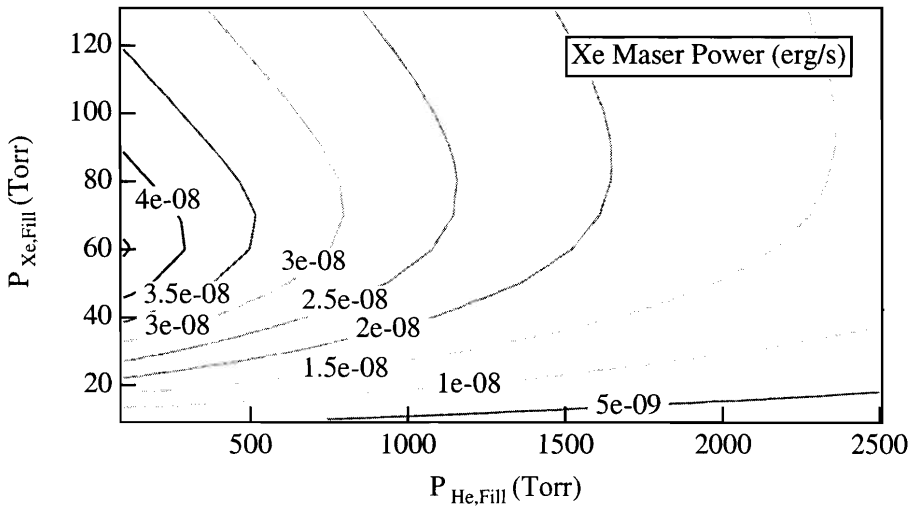

Figure 4-34: Contour plot showing the calculated ^{129}Xe maser power for a range of noble gas fill pressures. T_P = 114° C, narrow-band laser used for optical pumping, other input parameters as in Tab. 4.3.

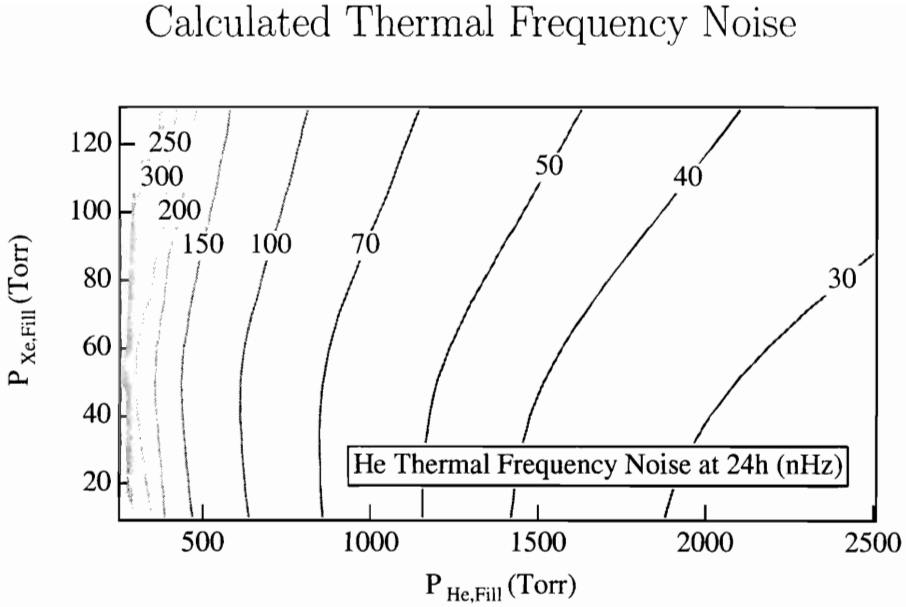

Figure 4-35: Contour plot showing the calculated ^{3}He thermal frequency noise for a range of noble gas fill pressures. T_P = 114° C, narrow-band laser used for optical pumping, other input parameters as in Tab. 4.3.

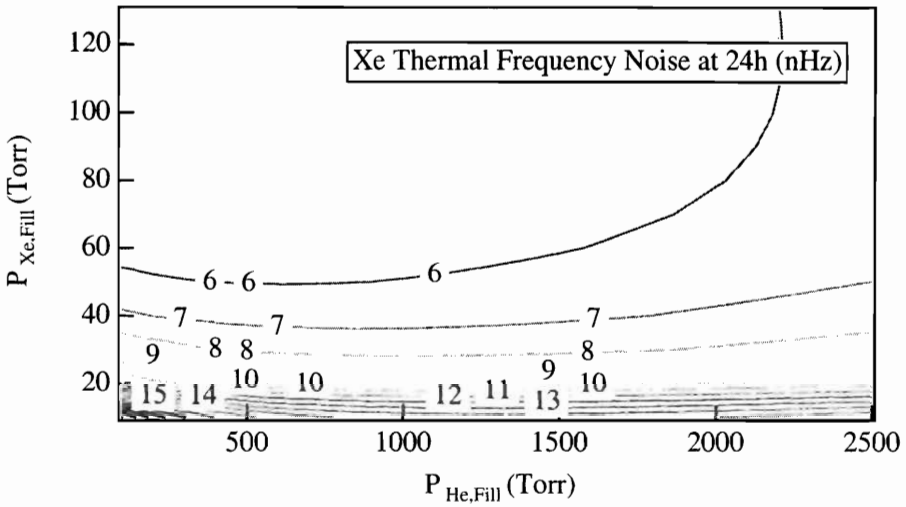

Figure 4-36: Contour plot showing the calculated ^{129}Xe thermal frequency noise for a range of noble gas fill pressures. T_P = 114° C, narrow-band laser used for optical pumping, other input parameters as in Tab. 4.3.

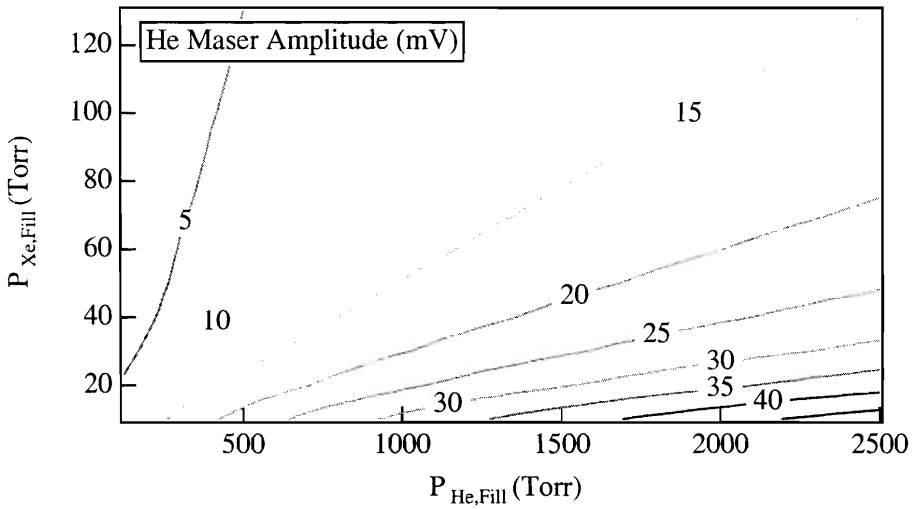

Figure 4-37: Contour plot showing the calculated ^{3}He maser output voltage for a range of noble gas fill pressures. T_P = 140° C, narrow-band laser used for optical pumping, other input parameters as in Tab. 4.3.

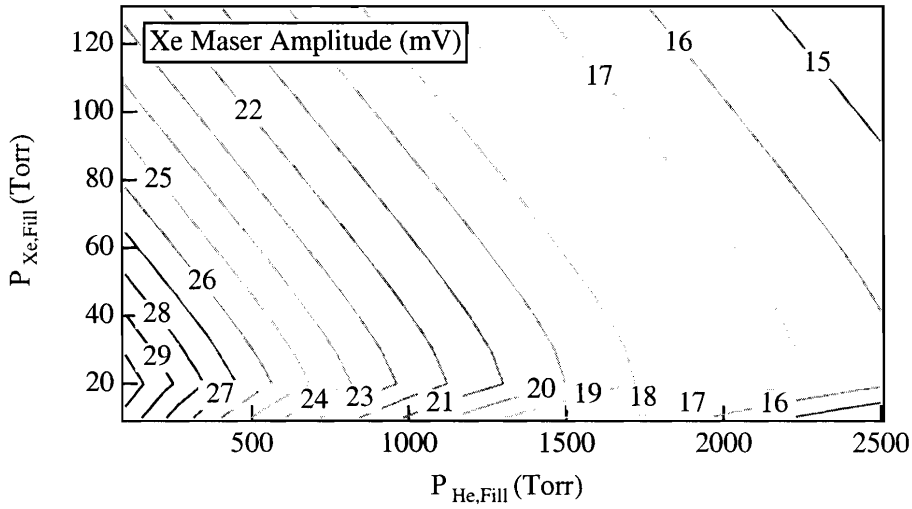

Figure 4-38: Contour plot showing the calculated ^{129}Xe maser output voltage for a range of noble gas fill pressures. T_P = 140° C, narrow-band laser used for optical pumping, other input parameters as in Tab. 4.3.

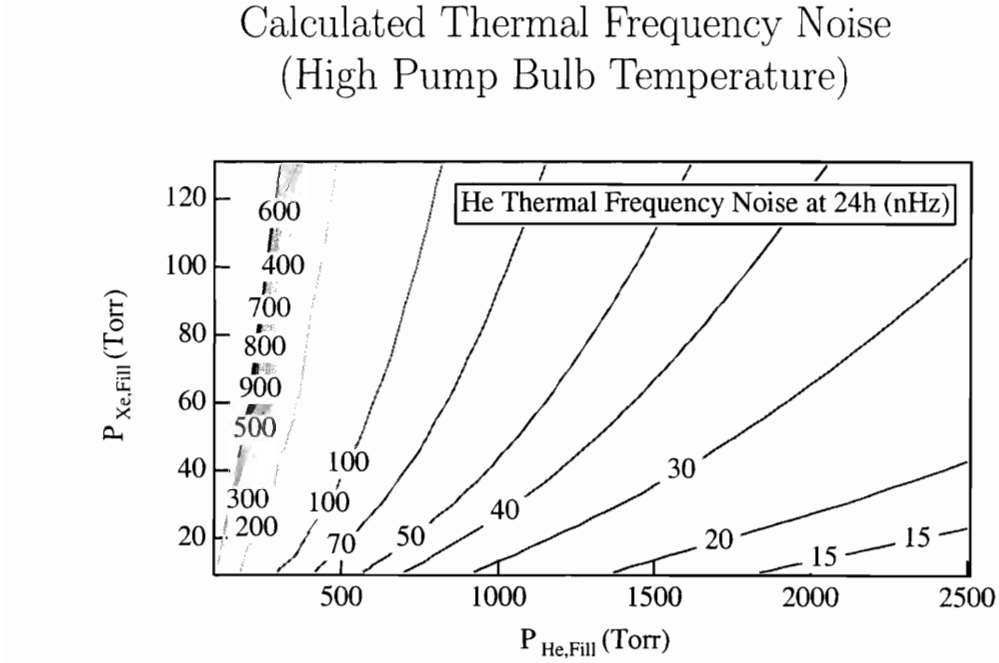

Figure 4-39: Contour plot showing the calculated ^{3}He thermal frequency noise for a range of noble gas fill pressures. T_P = 140° C, narrow-band laser used for optical pumping, other input parameters as in Tab. 4.3.

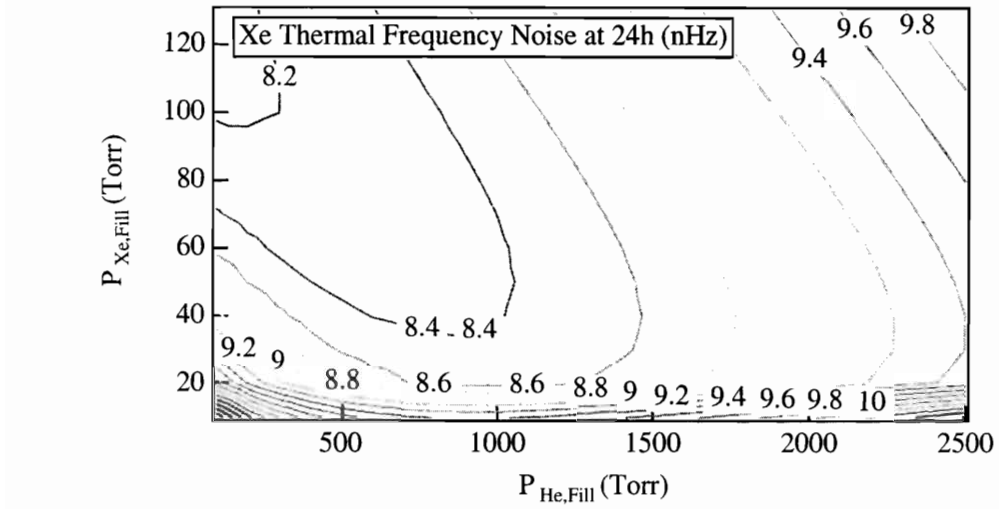

Figure 4-40: Contour plot showing the calculated ^{129}Xe thermal frequency noise for a range of noble gas fill pressures. T_P = 140° C, narrow-band laser used for optical pumping, other input parameters as in Tab. 4.3.

4.4.1 Imperfect Overlap of ^{129}Xe and ^{3}He Ensembles

In Sect. 4.3 we have solved the equations of motion for our Zeeman masers implicitly assuming the spatial homogeneity over the maser bulb of three quantities: (i) the main magnetic field B_0; (ii) the perpendicular polarization $P_{\perp,ng}$; and (iii) the pick-up coil field B_1. In this section we wish to look at what happens to maser co-magnetometry when we relax the first two assumptions. In Sect. 6.8.2 we will briefly explore the possible effects of departing from (iii).

The equations of motion for a spatially extended masing ensemble, in which $B_0(\vec{r})$ and $P_{\perp,ng}(\vec{r})$ have a spatial dependence and B_1 is homogeneous, yield the following mean value for the maser frequency [37]:

$$\omega_{ng} = \gamma_{ng} \frac{\int_{V_M} B_0(\vec{r}) P_{\perp,ng}(\vec{r}) d^3\vec{r}}{\int_{V_M} P_{\perp,ng}(\vec{r}) d^3\vec{r}}. \tag{4.57}$$

At present we are unable to solve the maser equations of motion for an extended masing ensemble in a double-bulb cell and find an analytic expression for the steady state distribution of $P_{\perp,ng}(\vec{r})$. Nevertheless, we may use Eq. (4.57) to study the effects of magnetic field gradients on the maser frequencies.

In the presence of linear magnetic field gradients across the maser bulb we can write the longitudinal magnetic field as: $B_0(\vec{r}) = B_0(\vec{0}) + \vec{\nabla} B_0(\vec{0}) \cdot \vec{r}$, where $\vec{r} = \vec{0}$ is defined to be the center of the maser bulb. Using Eq. (4.57) the maser frequency becomes

$$\omega_{ng} = \gamma_{ng} B_0(\vec{0}) + \gamma_{ng} \vec{\nabla} B_0(\vec{0}) \cdot \langle \vec{r}_{ng} \rangle, \tag{4.58}$$

where we have defined the noble gas center of (perpendicular) polarization as:

$$\langle \vec{r}_{ng} \rangle = \frac{\int_{V_M} \vec{r} P_{\perp,ng}(\vec{r}) d^3\vec{r}}{\int_{V_M} P_{\perp,ng}(\vec{r}) d^3\vec{r}}. \tag{4.59}$$

The ^{129}Xe maser frequency is usually locked to the frequency of a reference oscillator ω_{Xe}^{ref} by adjusting the correction B_z^{corr} to the main magnetic field. B_z^{corr} must then satisfy the following equation:

$$\omega_{Xe} - \omega_{Xe}^{ref} = \gamma_{Xe}\left(B_z^{corr} + \vec{\nabla}B_0(\vec{0}) \cdot \langle \vec{r}_{ng} \rangle\right) = 0. \tag{4.60}$$

The frequency shift of the free-running ^{3}He maser with respect to the expected frequency $\gamma_{He}\omega_{Xe}^{ref}/\gamma_{Xe}$ is:

$$\begin{aligned} \delta\omega_{He} &= \gamma_{He}\omega_{He} - \frac{\gamma_{He}}{\gamma_{Xe}}\omega_{Xe}^{ref} \\ &= \gamma_{He}\vec{\nabla}B_0(\vec{0}) \cdot (\langle \vec{r}_{He} \rangle - \langle \vec{r}_{Xe} \rangle). \end{aligned} \tag{4.61}$$

A linear dependence of the frequency shift implied by Eq. (4.61) on the intensity of small gradients was indeed observed, suggesting a displacement of the ^{129}Xe and ^{3}He polarization centers by a few tens of μm, both along the direction of the transfer tube, $\hat{y}$, and along the axis of the cylindrical maser bulbs previously in use [34].

As we noted, a direct attempt to evaluate Eq. (4.59) immediately meets the problem that we are unable to obtain the equilibrium spatial distribution $P_{\perp,eq}(\vec{r})$ from the set of non-linear equations of motion seen in Sect. 4.3.4. In the next section we show that we can find the centers of polarization if we assume that the polarized atoms after reaching the maser bulb spend an average time τ radiating. We assume that then they leave the masing ensemble, either because field gradients and wall collisions make them de-cohere, or simply because they escape from the maser bulb.

Even if we do not have a quantitative estimate for τ, the solution presented in the next section leads to two interesting conclusions: (i) the centers of polarizations $\langle \vec{r}_{ng} \rangle$ do not depend on the flux of incoming polarized atoms; and (ii) both finite lifetime

and wall relaxation lead to $\langle \vec{r}_{ng} \rangle \propto 1/D$ in the limit of large D. The importance of (i) is clear: Instabilities in the optical pumping spin-exchange process, or temperature instability in the pump bulb will not move the center of polarization and they will not create time dependent frequency shifts in the masers (i.e., frequency noise) by moving the center of polarization across the inevitable residual magnetic field gradients. (ii) confirms that larger diffusion coefficients would help bring the centers of polarization closer together, regardless of the process that is responsible for their separation.

A plausible choice for τ is, for instance, the effective bulb escape time for the coherences: T_2^*. Plugging this characteristic time and the other relevant parameters listed in Tabs. 4.3 and 4.4 into the formulae that we derive in the next section, yields the polarization centers shown in Figs. 4-41 and 4-42. From the plots we conclude that the distance between the centers should be on the order of few tens of μm and it is expected to decrease with the fill pressures.

4.4.2 Calculation: Polarization Distribution in a Spherical Bulb with Disk-Like Source, Bulk and Wall Relaxation

We calculate the center of polarization of a gas with diffusion coefficient D that enters a spherical maser bulb of radius r_0, through a hole subtending an angle $2\theta_0$ from the center of the bulb. The atoms have a bulk relaxation time τ and undergo wall-collisions characterized by a coefficient κ (see also Sect. 4.3.2). We solve the

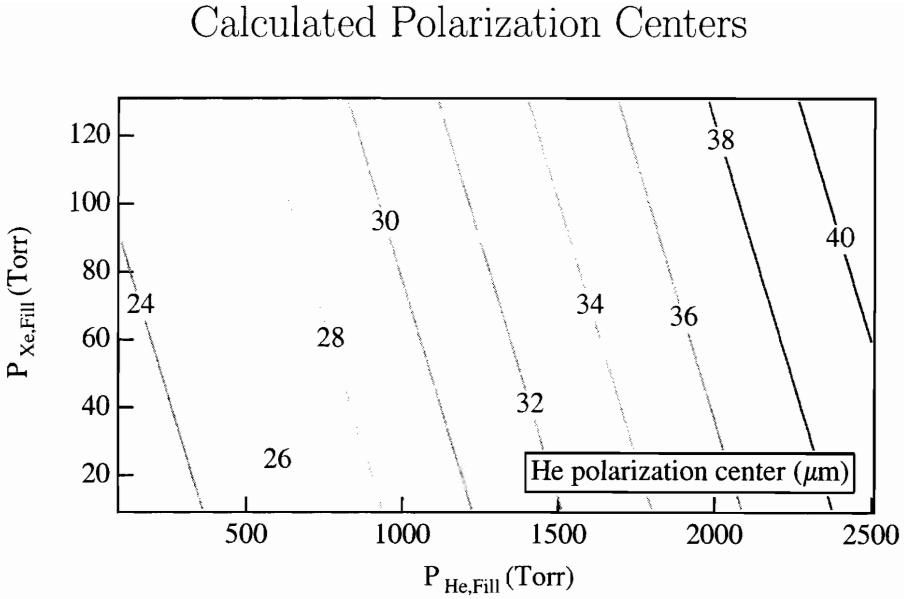

Figure 4-41: Contour plot showing the calculated polarization center, $\langle y \rangle_{He}$, for a range of noble gas fill pressures. $T_P = 114°$ C, narrow-band laser used for optical pumping, and other input parameters as in Tab. 4.3.

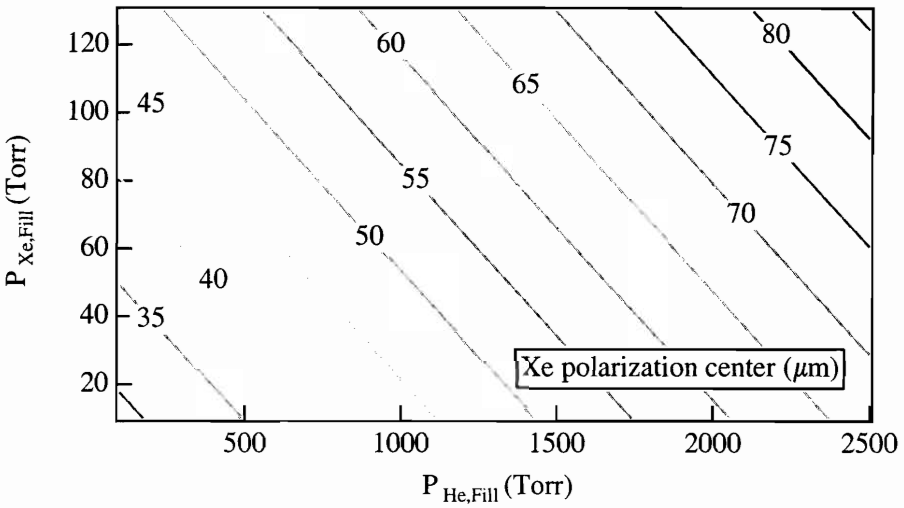

Figure 4-42: Contour plot showing the calculated polarization center, $\langle y \rangle_{Xe}$, for a range of noble gas fill pressures. $T_P = 114°$ C, narrow-band laser used for optical pumping, and other input parameters as in Tab. 4.3.

diffusion Eq. (4.12) in steady state and impose the appropriate boundary conditions,

$$D\nabla^2 P = \frac{1}{\tau}P \qquad \text{with} \qquad D\nabla_\perp P = \begin{cases} \phi & \text{for } \theta \leqslant \theta_0 \\ -\kappa P & \text{for } \theta > \theta_0 \end{cases} \tag{4.62}$$

describing a flux, ϕ, of polarized atoms per unit surface area per unit density entering the bulb through a circular aperture and a homogeneously relaxing bulb surface. Slightly modified boundary conditions greatly simplify our task:

$$\nabla^2 P = \frac{1}{\tau D}P = a^2 P \qquad \text{with} \qquad D\nabla_\perp P + \kappa P = \begin{cases} \phi & \text{for } \theta \leqslant \theta_0 \\ 0 & \text{for } \theta > \theta_0 \end{cases} \tag{4.63}$$

where we defined $a^{-1} = \sqrt{\tau D}$ and the symbol $\nabla_\perp$ indicates the variation along the normal to the bulb's surface. We therefore work in the approximation that wall relaxation takes place at the source too, but since the source is usually quite small this approximation is very good.

The symmetry around the $\hat{y}$ axis allows us to treat the problem in two dimensions: the distance from the center of the bulb, r, and the angle θ, between the atom's position vector $\vec{r}$ and the $\hat{y}$ axis. The center of the source is located at $\theta = 0$ and the source extends to $\pm\theta_0$. We will use the following trial solution:

$$P(r,\theta) = \sum_{l=0}^{\infty} \alpha_l R_l(r) P_l(\cos\theta), \tag{4.64}$$

which makes use of the Lagrange polynomials, $P_l(\cos\theta)$. The boundary condition

in Eq. (4.63) can also be defined in terms of these polynomials as follows:

$$\begin{aligned} f(\theta) &= \sum_{l=0}^{\infty} \beta_l P_l(\cos\theta) = \begin{cases} \phi & \text{for } \theta \leqslant \theta_0 \\ 0 & \text{for } \theta > \theta_0 \end{cases} \\ \beta_l &= \tfrac{1}{2}\left(P_{l-1}(\cos\theta_0) - P_{l+1}(\cos\theta_0)\right). \end{aligned} \tag{4.65}$$

Substituting Eq. (4.64) into Eq. (4.63), we find that the radial function $R(r)$ must satisfy the following differential equation:

$$\ddot{R}(r) + \frac{2}{r}\dot{R}(r) - \left(a^2 + \frac{l(l+1)}{r^2}\right) R(\rho) = 0. \tag{4.66}$$

This equation admits two solutions, expressed in terms of hyperbolic I and K Bessel functions [74]:

$$R_l(r) = c_1 \frac{1}{\sqrt{r}} K_{1/2+l}(ar) + c_2 \frac{1}{a^{1/2+l}\sqrt{r}} I_{1/2+l}(ar). \tag{4.67}$$

Only $I_{1/2+l}(ar)$ is acceptable in our case, since it does not diverge at the origin. We therefore choose $c_1 = 0$ and $c_2 = 1$. The determination of the α_l coefficients is now straightforward; using Eq. (4.63), Eq. (4.66), as well as the trial solution in Eq. (4.64), we find:

$$\alpha_l = \frac{\phi\beta_l}{D\dot{R}_l(r_0) + \kappa R_l(r_0)}. \tag{4.68}$$

Having completely solved Eq. (4.63) we can now determine two quantities of interest: The mean polarization in the bulb $\langle P \rangle$ and the polarization center $\langle \vec{r} \rangle$.

Apart from numeric coefficients, we find that $\langle P \rangle$ is proportional to α_0:

$$\begin{aligned}
\langle P \rangle &= \frac{1}{V}\int_V P(r,\theta)d^3\vec{r} \\
&= \frac{2\pi}{V}\sum_{l=0}^{\infty}\alpha_l \int_0^{\pi}\sin\theta P_l(\cos\theta)d\theta \int_0^{r_0} r^2 R_l(r)dr \\
&= \frac{2\pi}{V}\sum_{l=0}^{\infty} 2\alpha_l\delta_{l0}\int_0^{r_0} r^2 R_l(r)dr \\
&= \frac{3\alpha_0}{r_0^3}\int_0^{r_0} r^2 R_0(r)dr \propto \alpha_0.
\end{aligned} \tag{4.69}$$

We also find that the center of polarization is displaced from the center of the bulb in the direction of the source, it lies on the symmetry axis $\hat{y}$ (see Fig. 4-14) and it depends only on α_1 and α_0:

$$\begin{aligned}
\langle y \rangle &= \frac{1}{V\langle P\rangle}\int_V yP(r,\theta)d^3\vec{r} \\
&= \frac{2\pi}{V\langle P\rangle}\sum_{l=0}^{\infty}\alpha_l \int_0^{\pi}\sin\theta\cos\theta P_l(\cos\theta)d\theta \int_0^{r_0} r^3 R_l(r)dr \\
&= \frac{2\pi}{V\langle P\rangle}\sum_{l=0}^{\infty}\frac{2}{3}\alpha_l\delta_{l1}\int_0^{r_0} r^3 R_l(r)dr \\
&= \frac{\alpha_1}{r_0^3\langle P\rangle}\int_0^{r_0} r^3 R_1(r)dr \propto \alpha_1/\alpha_0.
\end{aligned} \tag{4.70}$$

The general solutions are better expressed in terms of the dimensionless quantities $t(ar_0) = \tanh(ar_0)/ar_0$ and $k = \kappa r_0/D$:

$$\langle P \rangle = \frac{3\phi\sin^2\frac{\theta_0}{2}\left(1 - t(ar_0)\right)}{a^2 r_0 D\left[1-(1-k)t(ar_0)\right]}, \tag{4.71}$$

$$\langle y \rangle = \frac{3r_0\cos^2\frac{\theta_0}{2}\left[1-(1-k)\ t(ar_0)\right]\left[1-(1+\frac{1}{3}a^2r_0^2)\ t(ar_0)\right]}{(2-k)\left(1-t(ar_0)\right)\left[1-\frac{2-k+a^2r_0^2}{(2-k)}\ t(ar_0)\right]}. \tag{4.72}$$

As we anticipated at the end of last section, $\langle y \rangle$ does not depend on ϕ.

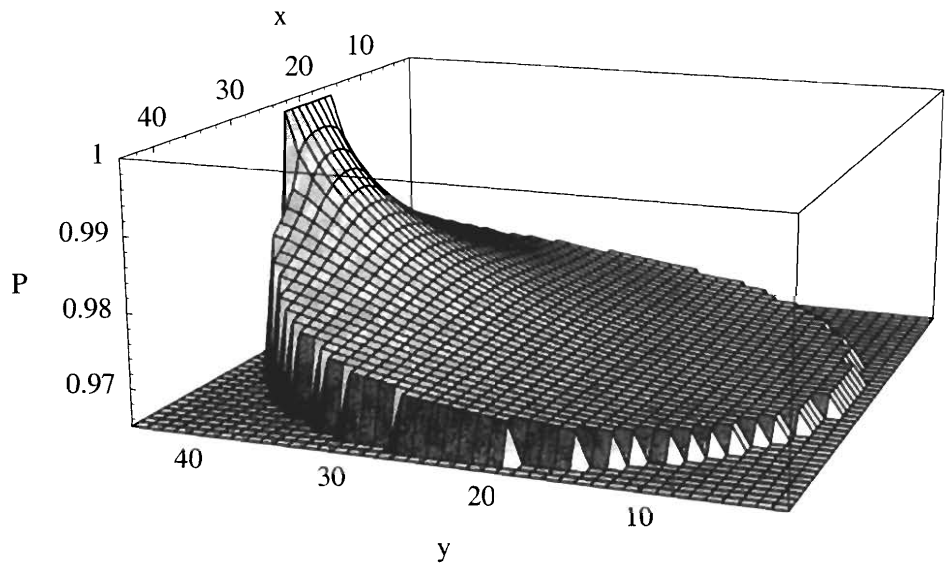

Figure 4-43: Calculated equilibrium polarization distribution in 2D for a circular cell with 1 cm radius. The polarized atoms (i.e., $P = 1$) enter from an arc of approximately 23° corresponding to a transfer tube diameter of 4 mm. The atoms diffuse to the loss-free walls with diffusion coefficient $D = 0.3$ cm/s^2 and we chose a bulk relaxation time $\tau = 300$ s. Using this distribution we obtain that the center of polarization is displaced towards the source by $\langle y \rangle \approx 26$ μm. The distribution was obtained using a mesh of 44×44 points, with mesh spacing $\Delta = 0.05$ cm and using the method of successive overrelaxation (SOR) [75] to solve the diffusion equation, $u_{j+1,l} + u_{j-1,l} + u_{j,l+1} + u_{j,l-1} - (4 + \Delta^2/\tau D)u_{j,l} = 0$, with the boundary conditions mentioned above.

We will evaluate the equations above in the limits in which one relaxation mechanism dominates over the other. The limiting expressions in which bulk relaxation vanishes, $a = 1/\sqrt{D\tau} \rightarrow 0$, is

$$\langle P \rangle = \frac{\phi \sin^2 \frac{\theta_0}{2}}{\kappa}, \qquad \langle y \rangle = \frac{3\kappa r_0^2 \cos^2 \frac{\theta_0}{2}}{5(D + \kappa r_0)}. \tag{4.73}$$

When wall relaxation is negligible, $k = \kappa r_0/D \rightarrow 0$, then

$$\langle P \rangle = \frac{3\phi\tau \sin^2 \frac{\theta_0}{2}}{r_0}, \tag{4.74}$$

$$\langle y \rangle = \frac{3r_0 \cos^2 \frac{\theta_0}{2} \left[1 - (1 + \frac{1}{3}a^2 r_0^2)\, t(ar_0)\right]}{2\left[1 - \left(1 + \frac{1}{2}a^2 r_0^2\right) t(ar_0)\right]} \tag{4.75}$$

$$= \frac{1}{5}\frac{r_0^3 \cos^2 \frac{\theta_0}{2}}{\tau D} - \frac{8}{175}\frac{r_0^5 \cos^2 \frac{\theta_0}{2}}{(\tau D)^2} + O[r_0^6 (\tau D)^{-\frac{5}{2}}]. \tag{4.76}$$

In Eq. (4.76) we have assumed $a\, r_0 = r_0/\sqrt{\tau D}$ is small.[7] As we anticipated at the end of the last section, in the appropriate limit both Eq. (4.73) and Eq. (4.76) show that $\langle y \rangle \propto 1/D$.

In Fig. 4-43 we show the steady polarization distribution obtained solving Eq. (4.63) numerically, in two dimensions, using the method of successive overrelaxation (SOR) [75]. The centers of polarization calculated with this alternative method agree very well with the analytical solution just presented.

4.5 Maser Bulb Geometry and Self-Interaction

The first incarnation of the dual noble gas maser was also designed for electric dipole moment searches [34]. Because of this, previous maser bulbs where cylindrical in shape and molybdenum plates were attached at each end of the cylinder and used as electrodes. We have since abandoned the cylindrical maser bulb. That shape had two disadvantages: (i) the pickup coil field was not homogeneous on the bulb reducing the effectiveness of the co-magnetometry along the cylinder axis, and (ii) the cylindrical shape induced magnetization self-interaction, which causes the maser frequency to depend on the longitudinal magnetization. The purpose of this section is to show that a spherical maser bulb eliminates self-interaction, under the approximation of homogeneous magnetization, which is approximately correct, as

[7] Notice that equating $\langle P \rangle$ in Eq. (4.73) and in Eq. (4.74) we obtain again a result already derived in Sect. 4.3.2, which gives the wall relaxation coefficient $\kappa = \frac{r_0}{3\tau}$ in terms of the mean observed lifetime.

we saw in the previous section.

Here we follow the theory of spin maser self-interaction worked out by Romalis and Happer (RH)[8] [76]. However, we will make the simplifying assumption that the magnetization of our gases is homogeneous in the maser bulb. As we have already seen in Sect. 2.3, the time evolution of the magnetization is given by

$$\partial_t \vec{M} = \gamma \vec{B}^e \times \vec{M}. \tag{4.77}$$

RH show that $\vec{B}^e$, the ensemble-averaged magnetic induction, is different from Maxwell's macroscopically averaged field $\vec{B}$. In particular, in Gaussian units,

$$\vec{B} = \vec{H} + 4\pi\vec{M}, \tag{4.78}$$

$$\vec{B}^e = \vec{H} + \frac{4\pi}{3}\vec{M}. \tag{4.79}$$

The difference between the two comes from "having excluded the magnetization of the core of the atoms." In other words, since a small portion of magnetization produces a magnetic induction at its own location equal to $8\pi\vec{M}/3$ (see the last term of Eq. (2.5)) and we know that a magnetization does not interact with the field it produces, we conclude that the magnetic induction that the magnetization interacts with is precisely given by $\vec{B}^e = \vec{B} - 8\pi\vec{M}/3$. For definiteness we define three magnetic fields that make up the total magnetic field $\vec{H}$: $\vec{H}_E$, the externally applied magnetic field, $\vec{H}_C$, the magnetic field produced by the maser coil, and $\vec{H}_M$, the magnetic field produced by the surrounding magnetization.

Instead of solving the problem for a cylindrical bulb, we will consider the problem

[8]RH were interested in large samples of polarized ^{3}He and the possibility of small masing regions ($\approx$ 3 mm) in which the conditions for masing were locally met (for instance, when a strong magnetic field gradient was applied perpendicularly to the B_0 field).

of self-interaction in a symmetric ellipsoidal bulb with semi-major axis length a, which is along the axis of symmetry, and semi-minor axis length b. In [77] we find that the homogeneously magnetized ellipsoid produces a homogeneous magnetic field which, in general, is not collinear with the magnetization and can be written in the following way:

$$\vec{H}_M = 4\pi \left(\beta_\perp M_x \, \beta_\perp M_y, \beta_z M_z\right), \tag{4.80}$$

where

$$\begin{aligned} \beta_\perp &= -\frac{ab^2}{2} \int_0^\infty \frac{ds}{(s+b^2)^2 \sqrt{(s+a^2)}}, \\ \beta_z &= -\frac{ab^2}{2} \int_0^\infty \frac{ds}{(s+a^2)^{3/2}(s+b^2)}. \end{aligned} \tag{4.81}$$

In the special case that the ellipsoid degenerates into a sphere ($a = b$), we have $\beta = \beta_\perp = \beta_z = -\frac{1}{3}$. Combining Eq. (4.79) and Eq. (4.80), we find:

$$\vec{B}^e = \vec{H}_E + \vec{H}_C + 4\pi\beta\vec{M} + \frac{4\pi}{3}\vec{M} = \vec{H}_E + \vec{H}_C, \tag{4.82}$$

which indeed shows how, for a spherical magnetization, $\vec{H}_M$ drops out of the maser dynamics described by Eq. (4.77).

In the general case though we have,

$$\vec{B}^e = (0, 0, B_0) + 4\pi \left(\beta_\perp M_x \, \beta_\perp M_y, \beta_z M_z\right) + \frac{4\pi}{3}\vec{M}, \tag{4.83}$$

and Eq. (4.77) yields a maser frequency ω_M proportional to the the longitudinal

magnetization M_z and to the difference $\beta_z - \beta_\perp$,

$$\gamma \vec{B}^e \times \vec{M} = \omega_M \left(-M_y, M_x, 0\right) \tag{4.84}$$

$$\omega_M = \gamma B_0 + 4\pi\gamma M_z \left(\beta_z - \beta_\perp\right). \tag{4.85}$$

By integrating Eqs. (4.81), we obtain for instance that $\beta_z - \beta_\perp = 0.1$ for $b/a = 0.77$, which is roughly the ratio of the previous maser bulb's length and diameter. Self-interaction is suppressed much more strongly (i.e., $\beta_z - \beta_\perp = 0.001$) when $b/a = 0.975$, so that an imperfection of $2 - 3\%$ in the sphericity of our bulbs, will make self-interaction negligible compared to the interaction with the other co-located magnetized species.

4.6 Conclusions on Design Studies and Open Questions

Most of the studies presented in this chapter were carried out before the construction of the new maser. We concentrated on four main areas of investigation: (i) the previous maser's limitations to LI sensitivity; (ii) the prospects of improving the temperature stabilization of the maser cell; (iii) the gas pressure optimization; and (iv) the co-magnetometry limitations ascribable to imperfect motional averaging and diffusion. We summarize here our conclusions for each point in turn:

(i) Although the best frequency stability in the previous maser was obtained for measurement intervals of approximately 2 hours, the sensitivity to slow frequency modulations of period T kept improving all the way to the desired $T = 1$ day. From this we concluded that the factor limiting the LI sensitivity was the level of medium term frequency noise and not the long term phase meander, which in

the previous system could be accounted for using maser amplitude correlations and a constant linear frequency drift. As a result of this new understanding a search for the sources of medium term frequency noise became the main focus of the new experiment. Thermal frequency noise, magnetic noise affecting the maser because of imperfect co-magnetometry, and noise induced by optical pumping light instabilities are currently being investigated, as we shall see in Ch. 6.

(ii) We concluded that the limitations of the previous maser's temperature stabilization system were probably caused by the instability of the airflow. We also argued that indirect heating should solve this problem while also reducing the vibrations induced on the cell by direct exposure to the airflow.

(iii) Modeling the interplay of optical pumping, polarization transport and maser action helped describe a number of competing effects. For instance, we found that in certain conditions, as we expected, it is conceivable to decrease the noble gas pressures (in specific proportions) without affecting the intensity of the maser signals. In fact, lower gas pressures yield higher polarization mobility, which increases the flux of polarized atoms in the maser cell, but at the same time decreases the interaction time with the cavity. In the optical pumping process, pressure broadening of the Rb absorption line allows for a better use of the broad-band light. On the other hand, at lower gas pressures the Rb polarization can be kept closer to saturation where spin-exchange optical pumping is probably more stable.

As a practical example, we predict that if we intend to use a narrow-band laser delivering at the cell approximately 350 mW of light, we should keep the ^{129}Xe pressure below 50 Torr. For excessively low ^{3}He pressures, the ^{3}He maser becomes sensitive to thermal frequency noise because of the short interaction time with the cavity. Hence, gas pressures above 1,000 Torr are needed. A similar reasoning helps selecting operating temperatures and gas pressures based on the amount of light

available. The underlying rationale for decreasing the gas pressures is that better motional averaging should improve co-magnetometry. This brings us to our last point.

(iv) Our diffusion model basically confirms that imperfect co-magnetometry could be due to a lack of spatial overlap of the two masing species. The order of magnitude of the frequency shifts observed when applying magnetic field gradients is consistent with the co-magnetometer limitations arising from the slight inhomogeneities in the calculated noble gas polarization distributions. However, our theory needs further input from experiment since it is not clear at this moment what physical quantity should be used as the characteristic time in the diffusion model.

Open Questions

We close this chapter with a number of open questions that need more theoretical and experimental work to be answered. The first question was stated in the paragraph above: What is the characteristic time needed to find the correct polarization center?

Second question: Are there other mechanisms that may lead to imperfect co-magnetometry? Recent experiments suggest that the spatial inhomogeneity of the pick-up coil field and the fact that this field extends well beyond the maser bulb may provide alternative mechanisms.

Third question: Is the thermal noise a limiting factor? In the previous system simple estimates indicated that the thermal frequency limit had not been reached. Our simulations instead clearly indicate that we may be close to the thermal frequency noise limit. Only experiment can resolve this issue.

Fourth question: Is there a way to model the loss of ^{129}Xe polarization due to

the interaction with unpolarized Rb in the transfer tube?

Fifth question: Why is there a factor of approximately 5 between the Allan deviation and the LI sensitivity (see Fig. 4-2)? Preliminary numerical simulations indicate that the two should differ only by a factor of $\sqrt{2}$.

Chapter 5

Experimental Realization

In this chapter we describe the design and construction of the new $^{129}Xe/^{3}He$ maser. We concentrate our attention on the components that recently have been entirely rebuilt, or added to the experiment. We begin by reviewing the new oven design, the blown air temperature control of the maser, and the procedure for making $^{129}Xe/^{3}He$ maser cells. We then discuss the characteristics and stabilization scheme of a new narrow-band laser used for Rb optical-pumping. This laser is now under test and its performance is being compared to the laser diode array (LDA) formerly used. Next, we provide an overview of the magnetic field environment: magnetic shielding, main field characteristics, field stabilization, and various attempts to confine the maser action to the maser bulb region. We conclude by describing the signal detection system.

5.1 A New Oven Design to Improve Temperature Control and Accessibility

In Sect. 4.2.1 we discussed the advantages of a temperature control system based on indirect heating of the maser cell. As Fig. 5-1 shows, hot and cold air circulate in 2.5" and 3" deep air ducts cut into the oven, surrounding high thermal conductivity pump and maser blocks, whose thermal capacity integrate out fast thermal fluctuations, providing stable heating of the maser cell.

Table 5.1 presents the physical characteristics of various materials used in the experiment. Ultem[1] was chosen for the heated-air-carrying portion of the oven because it is an excellent non-magnetic thermal insulator and can withstand temperatures twice as high as the Nylatron plastics formerly used.

The design was also changed to improve access to the cell. In the previous system, separate maser and pump ovens were assembled around the cell and needed to be taken apart when the maser cell had to be replaced: this procedure required several hours. The new oven design shown in Figs. 5-4 and 5-5 is geometrically more stable because the housing of the cell is machined into a single block of Ultem. The replacement of the cell is now a matter of just a few minutes. It is sufficient to pull the oven towards the open end of the solenoid, remove the oven lid, pull out the previous cell and insert the new one, which was previously installed on a spare cell holder. In addition, the 1/4" ID, insulated, semirigid Teflon tubing that bring hot and cold air and most of the wiring are connected to the back of the oven and do not need to be removed when replacing a cell.

[1]Available from Quadrant Engineering Plastic Products.

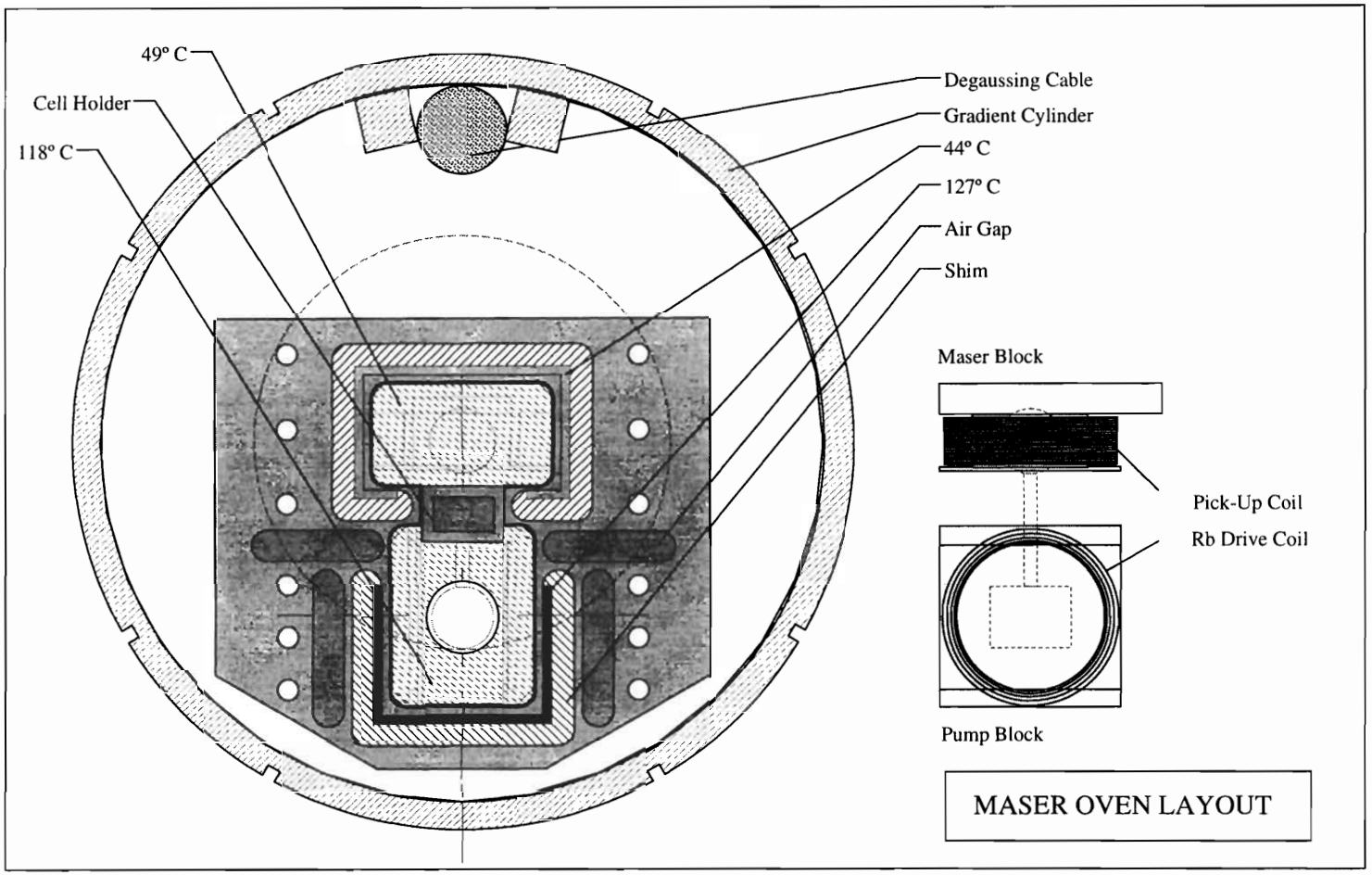

Figure 5-1: Section of the maser oven installed in the gradient cylinder. The maser bulb is centered on the axis of the cylinder. The pump bulb is located entirely within the circular aperture of the shields marked by the inner dashed circle. Hot and cold air circulates inside deep air ducts surrounding the pump and the maser blocks. Air gaps thermally separate the hot and cold regions. Twelve plastic screws keep in place the Ultem lid (not shown) that insulates the front end. A side view of the blocks shows the coils wound on them and the cell position.

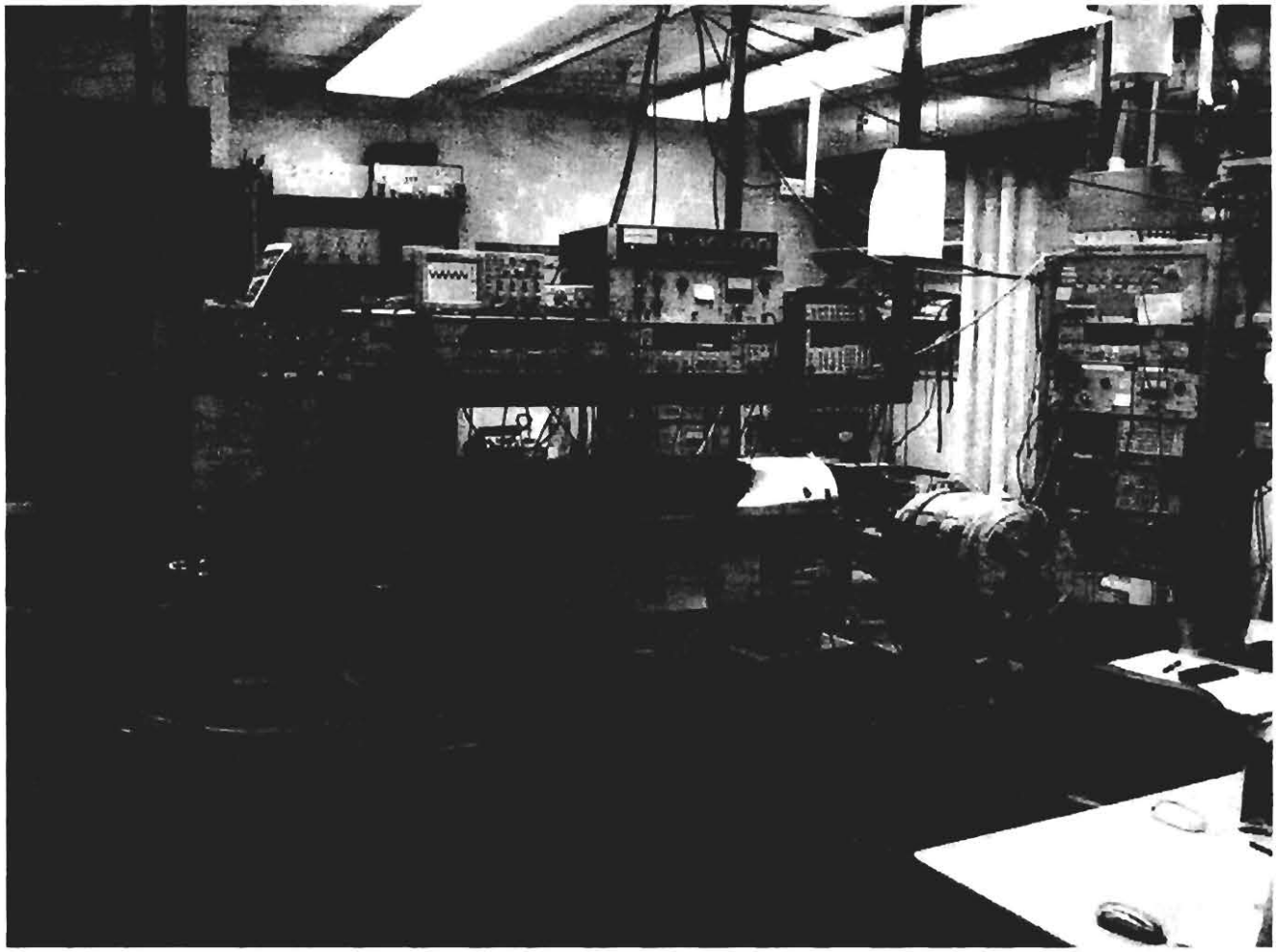

Figure 5-2: A photograph of the ^{129}Xe/^{3}He maser laboratory. From left to right we see on a floating table the Toptica TA 100 laser, the μ-metal shields (in which main solenoid and oven are installed) surmounted by a cloud carrying some of the lock-in amplifiers, function generators, and PID controllers used in the experiment. Finally, we see a barrel-shaped smaller set of μ-metal shields covered in thermally insulating fiberglass containing the resonator coil and the main circuit board.

Material	**Density** ($g\ cm^{-3}$)	**Specific Heat** ($J\ Kg^{-1}K^{-1}$)	**Thermal Conductivity** ($W\ m^{-1}\ K^{-1}$)	**Coefficient of Thermal Exp.** (K^{-1})	**Continuous Service in Air** (Max ° C)	**Uses**
Ultem 1,000, unfilled, extruded	1.28	-	0.12	56×10^{-6}	171	Oven, air duct shims, cell holder
Nylatron GS, MoS2 filled, extruded	1.16	-	0.24	72×10^{-6}	104	Gradient cylinder
Boron nitride, unbound, Grade AX05	1.85	800	78 (130)*	1 (0.3)* $\times 10^{-6}$	$> 2,000$	Pump and maser blocks
Copper magnet wire, SL Polyimide-ML insulation	8.92	380	401	16.5×10^{-6}	240	Pick-up and Rb drive coils
Silicone RTV	1.09	-	0.21	270×10^{-6}	204	Maser bulb cast
TFE Teflon	2.15	1,172	0.25	-	260	Tubing
Air	1×10^{-3}	720	0.028	-	-	

Table 5.1: Physical characteristics of the materials used in the $^{129}Xe/^{3}He$ maser. *The boron nitride is a pressed ceramics with anisotropic thermal properties. Coefficients referring to the direction perpendicular to the pressing direction are given in brackets.

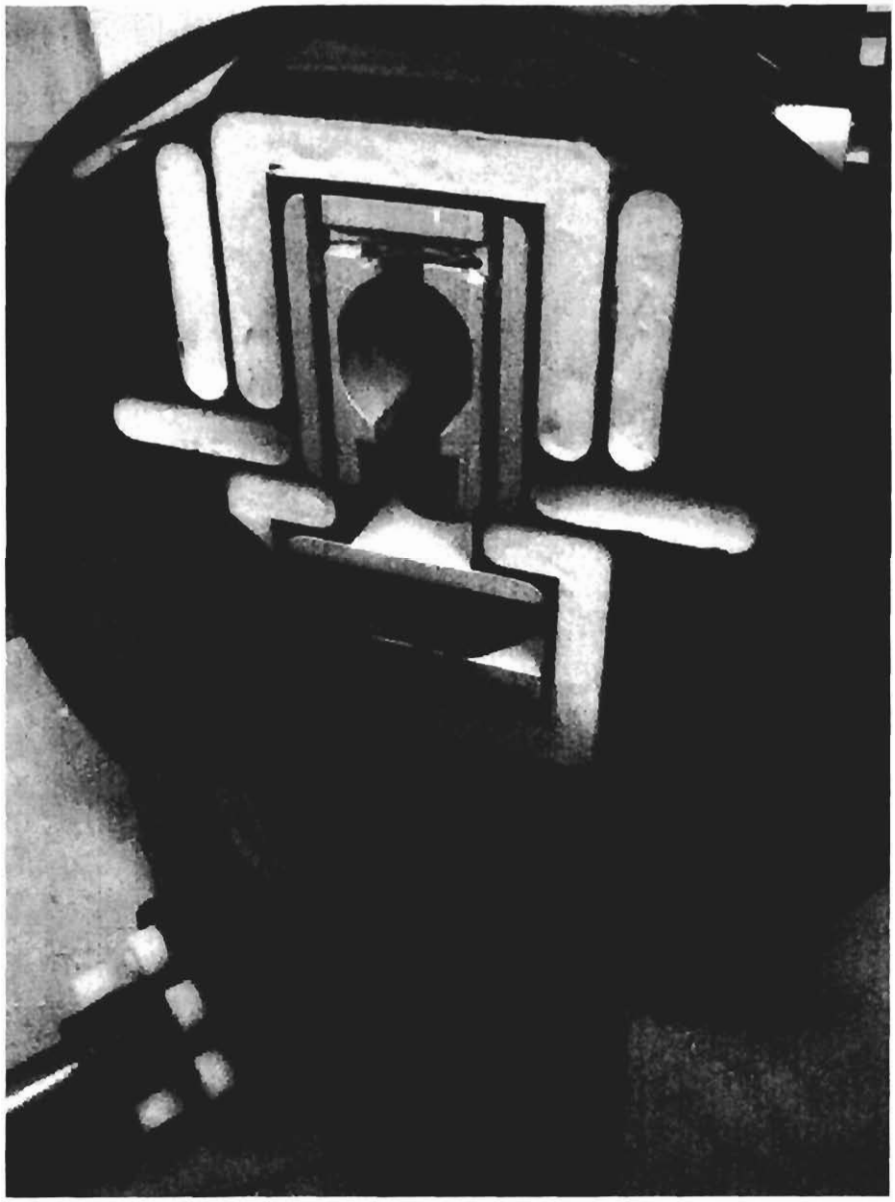

Figure 5-3: The new maser oven. Air circulates in narrow air ducts machined out of a single block of Ultem 1,000 and located beneath the white silicone RTV profiles, warming up and cooling down the boron nitride pump and maser blocks, respectively. The cell, mounted on its cell holder (see Fig. 5-14) fits into the aperture in the middle of the oven. Visible on the maser block (bottom) is the 1,600 turn pick-up coil, which is part of a double-tuned circuit and acts as maser cavity (see Sect. 5.5.1). On the pump block (top) the picture shows two coils in a quasi-Helmholtz configuration, used for resonantly driving the Rb Zeeman transitions in the Rb magnetization detection scheme [34]. The oven is held within a Nylatron frame that fits within a Nylatron cylinder on which are wound magnetic field gradient correction coils.

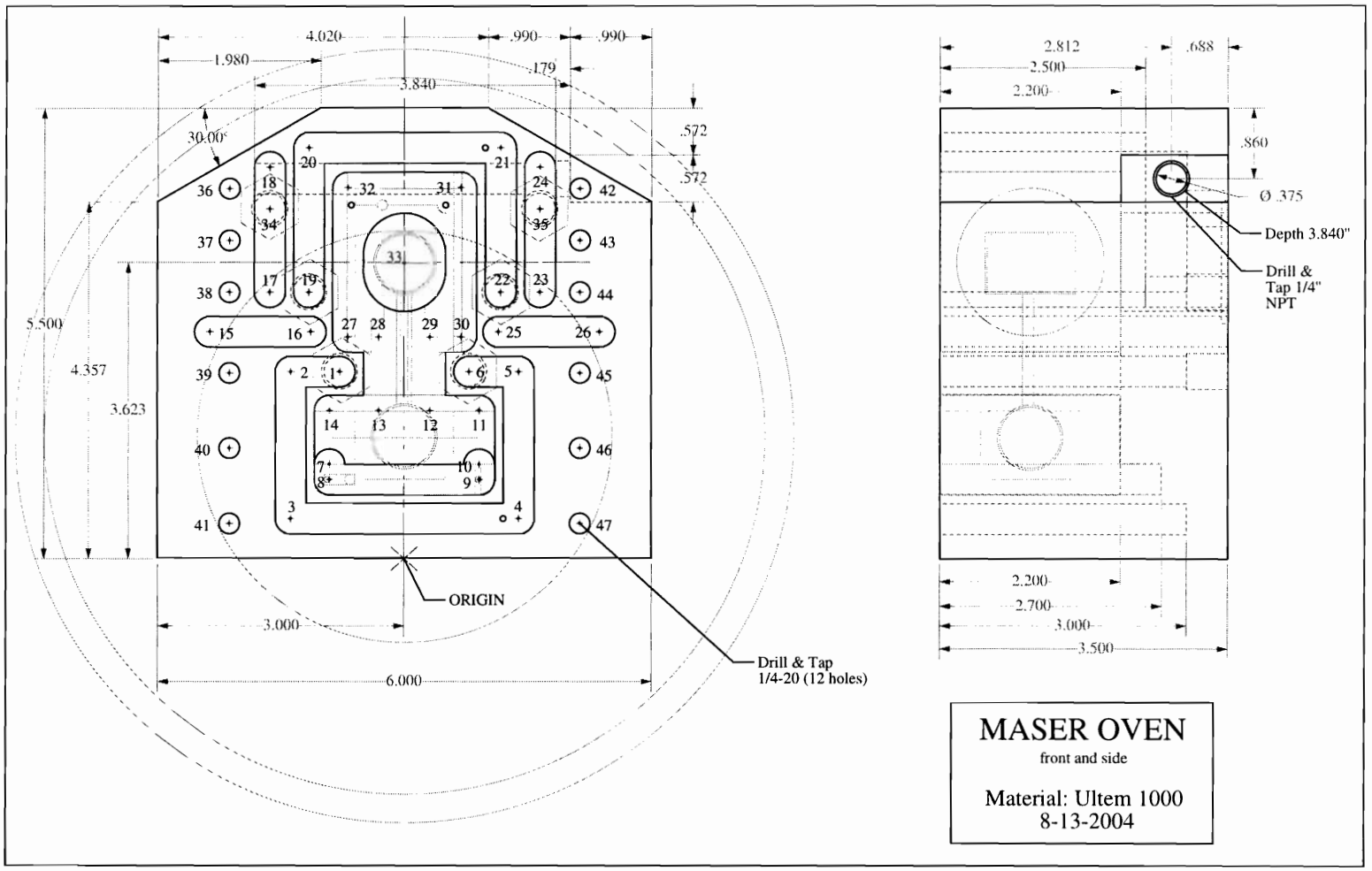

Figure 5-4: Machine drawing of the maser oven fabricated from a single block of Ultem 1,000 – front and side view. All dimensions are in inches.

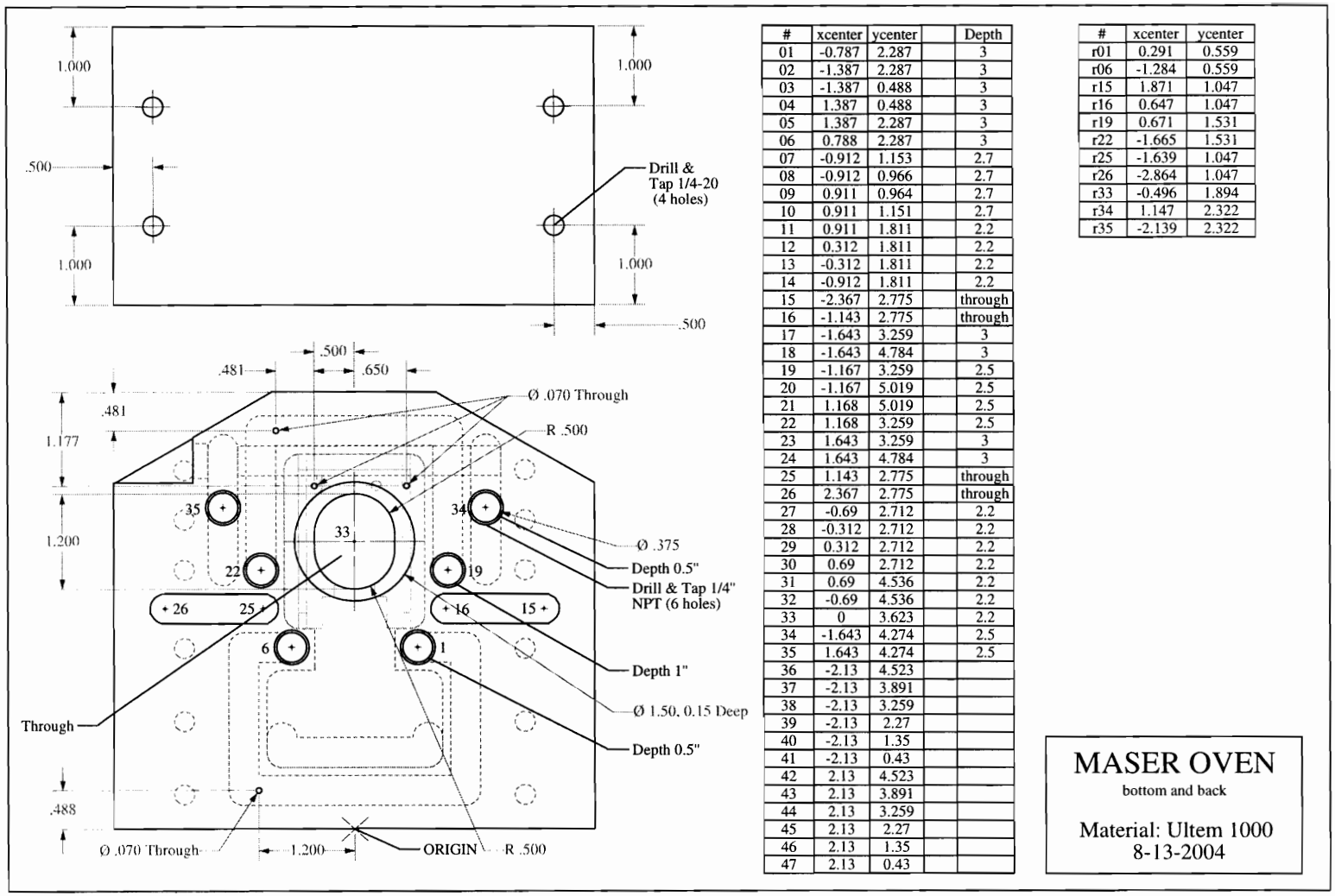

#	xcenter	ycenter		Depth
01	-0.787	2.287		3
02	-1.387	2.287		3
03	-1.387	0.488		3
04	1.387	0.488		3
05	1.387	2.287		3
06	0.788	2.287		3
07	-0.912	1.153		2.7
08	-0.912	0.966		2.7
09	0.911	0.964		2.7
10	0.911	1.151		2.7
11	0.911	1.811		2.2
12	0.312	1.811		2.2
13	-0.312	1.811		2.2
14	-0.912	1.811		2.2
15	-2.367	2.775		through
16	-1.143	2.775		through
17	-1.643	3.259		3
18	-1.643	4.784		3
19	-1.167	3.259		2.5
20	-1.167	5.019		2.5
21	1.168	5.019		2.5
22	1.168	3.259		2.5
23	1.643	3.259		3
24	1.643	4.784		3
25	1.143	2.775		through
26	2.367	2.775		through
27	-0.69	2.712		2.2
28	-0.312	2.712		2.2
29	0.312	2.712		2.2
30	0.69	2.712		2.2
31	0.69	4.536		2.2
32	-0.69	4.536		2.2
33	0	3.623		2.2
34	-1.643	4.274		2.5
35	1.643	4.274		2.5
36	-2.13	4.523		
37	-2.13	3.891		
38	-2.13	3.259		
39	-2.13	2.27		
40	-2.13	1.35		
41	-2.13	0.43		
42	2.13	4.523		
43	2.13	3.891		
44	2.13	3.259		
45	2.13	2.27		
46	2.13	1.35		
47	2.13	0.43		

#	xcenter	ycenter
r01	0.291	0.559
r06	-1.284	0.559
r15	1.871	1.047
r16	0.647	1.047
r19	0.671	1.531
r22	-1.665	1.531
r25	-1.639	1.047
r26	-2.864	1.047
r33	-0.496	1.894
r34	1.147	2.322
r35	-2.139	2.322

MASER OVEN
bottom and back

Material: Ultem 1000
8-13-2004

Figure 5-5: Machine drawing of the maser oven fabricated from a single block of Ultem 1,000 – bottom and back view. All dimensions are in inches.

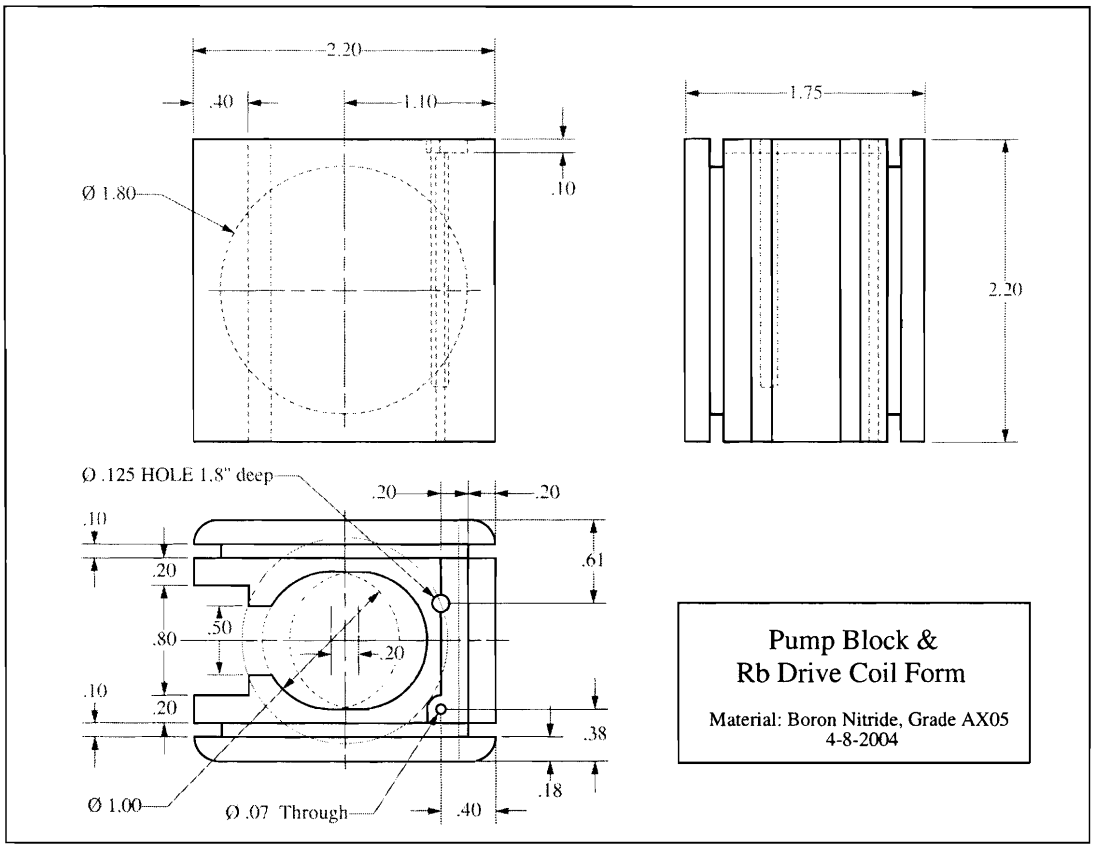

Figure 5-6: Machine drawing of the pump block. All dimensions are in inches.

The oven is installed on a cylindrical support that tightly slides inside a fixed Nylatron cylinder on which we installed a set of gradient coils (see Sect. 5.4.2). The support is keyed and slides on a rail screwed at the top of the gradient cylinder allowing only longitudinal, but no rotational movement of the oven. Figure 5-3 shows the oven installed on its support. Pump and maser blocks are in place. The top of the air ducts are sealed off with one-part silicone RTV[2] to prevent hot and cold air from entering the cell housing. Early testing showed that inserting Ultem shims into the air ducts and reducing their volume by approximately 80%, significantly improved the temperature control providing better insulation from ambient temper-

[2]GE Company, RTV162.

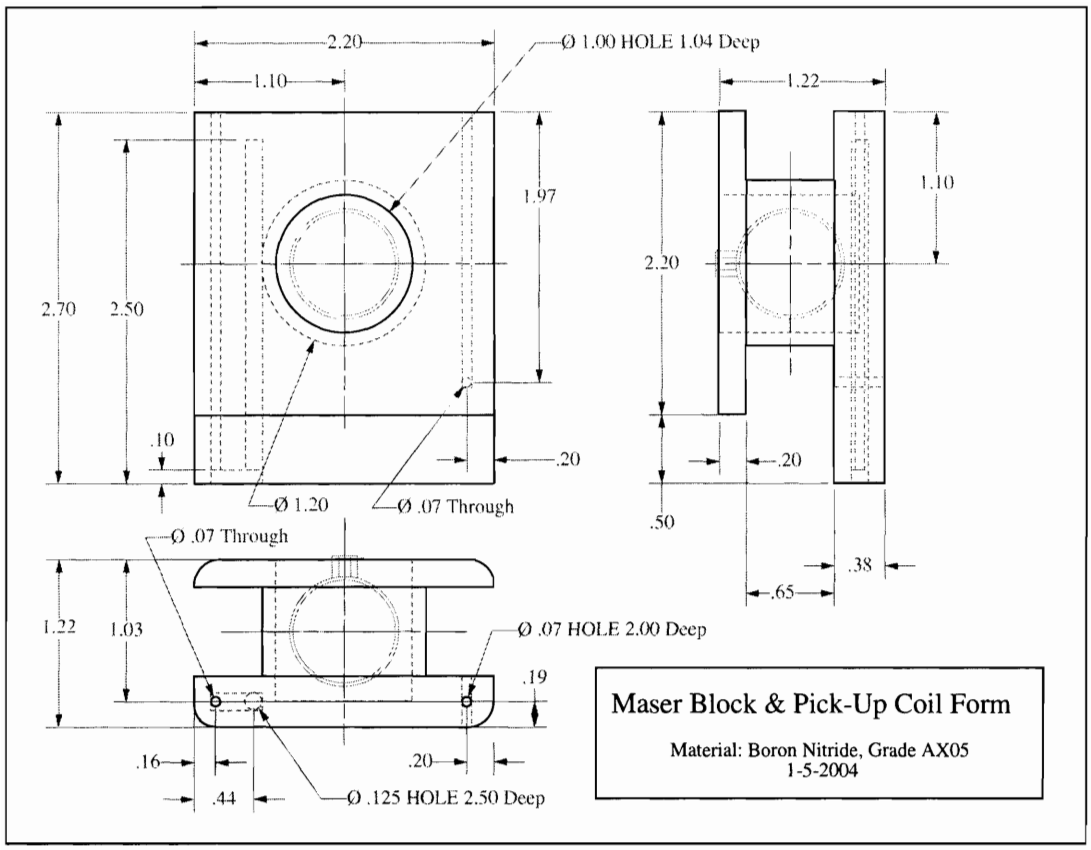

Figure 5-7: Machine drawing of the maser block. All dimensions are in inches.

ature fluctuations. In each air duct we installed thermometers for controlling the temperature of the air (see Sect. 5.1.1).

The maser and pump blocks are built out of boron nitride.[3] This is the ceramics with the highest thermal conductivity on the market, which can still be machined with ordinary cutting tools. The drawings in Figs. 5-6 and 5-7 show that the maser and pump blocks, besides providing a thermal buffer for the heating and cooling of the cell, are designed to accommodate respectively the pick-up coil (see Sect. 5.5.1) and a quasi-Helmholtz coil[4] used to drive the Rb Zeeman transitions and monitor or lock the Rb magnetization (see Sect. 5.3.2). In both blocks, 2" deep holes provide

[3]Grade AX05, available from Saint-Gobain Ceramics.

[4]Two 200 turn coils are wound into the circular grooves cut in the pump block shown in Fig. 5-6.

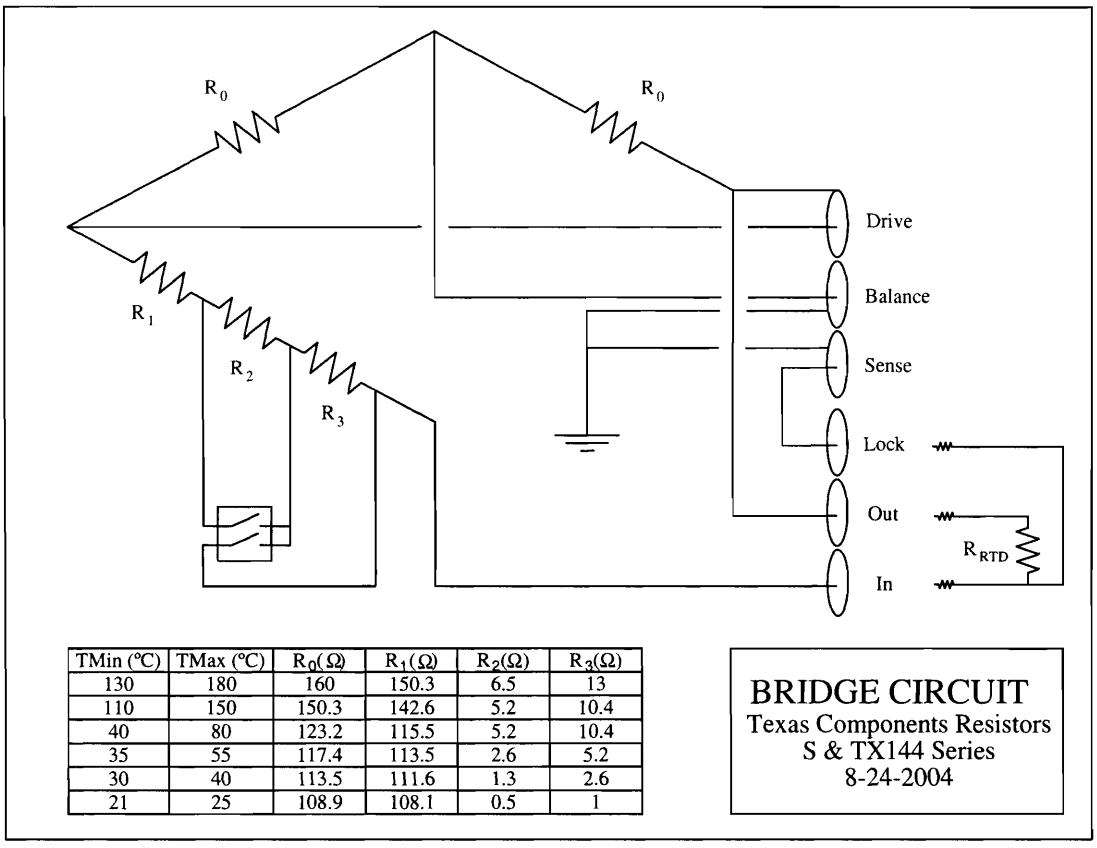

TMin (°C)	TMax (°C)	$R_0(\Omega)$	$R_1(\Omega)$	$R_2(\Omega)$	$R_3(\Omega)$
130	180	160	150.3	6.5	13
110	150	150.3	142.6	5.2	10.4
40	80	123.2	115.5	5.2	10.4
35	55	117.4	113.5	2.6	5.2
30	40	113.5	111.6	1.3	2.6
21	25	108.9	108.1	0.5	1

BRIDGE CIRCUIT
Texas Components Resistors
S & TX144 Series
8-24-2004

Figure 5-8: Circuit schematic of one of the six, three wire, balanced bridges used for sensitive temperature detection and lock. In equilibrium, $R_{Set}(R_1, R_2, R_3) = R_{RTD} = (100 + 0.385\ T)\ \Omega$ where T is expressed in degrees Celsius. The double-switch allows us to select four set temperatures evenly distributed in the range between TMin and TMax.

housing for the thermometers used to stabilize the block temperatures.

5.1.1 Temperature Control

The ambient temperature of the $^{129}Xe/^{3}He$ maser laboratory is maintained at approximately 21° C with characteristic oscillations of 0.1-1° C in amplitude (depending on the measurement position in the lab) and a period of approximately 500 s, due to the cycling of the air conditioning unit. Most components in our experiment need further temperature stabilization. Less thermally sensitive components, such as

photodiodes, are stabilized using independent, homemade temperature controllers. The external resonator and most of the double-resonant circuit (see Sect. 5.5) are contained in a separate thermally, electrically, and magnetically isolated enclosure which has an independent blown air temperature control system. The enclosure is heated slightly above room temperature, typically 30° C (see Sect. 6.1).

Since our Zeeman masers are sensitive to magnetic disturbances we use throughout the experiment non-magnetic, wire wound, 100 Ω, three lead, platinum RTD elements covered in a ceramic enclosure for robustness.[5] In order to obtain sensitive temperature resolution ($\approx$ 0.1 mK) with small currents (to limit both noise and self-heating), the RTDs are in a balanced bridge driven by a lock-in amplifier.[6] The bridge output signal measured with the lock-in amplifier is fed to a PID temperature controller driving an air process heater.[7] In Fig. 5-8 we show the schematic of the bridge circuits. One arm of the bridge acts as a voltage divider, while different combinations of the resistances[8] R_1, R_2 and R_3, can be selected using two switches to give four possible set resistor values. In equilibrium, R_{RTD} matches the set resistance.

Figure 5-9 shows the temperature control scheme used for locking the temperature of maser and pump blocks. A regulated flow of air through the heater and into the air channel delivers heat to the oven and then to the block via conduction. As we argued in Sect. 4.2.1, the amount of heat delivered to the block depends not only on the temperature measured by RTD 2 located in the airflow, but also on the air mass flow that sets the temperature gradient along the air channel (the gradient becomes smaller as the flow increases). The high thermal conductivity of the

[5]Available from Omega Engineering Inc., series 1PT100KN.

[6]Standard Research System (SRS) lock-in amplifiers, models 830 and 850.

[7]LR-130 PID controllers, once produced by Linear Research Inc.

[8]The resistors used for the bridge have very low nominal temperature coefficient of resistance ($\approx$ 0.3 ppm/° C) and are available from Texas Components, series S and TX144.

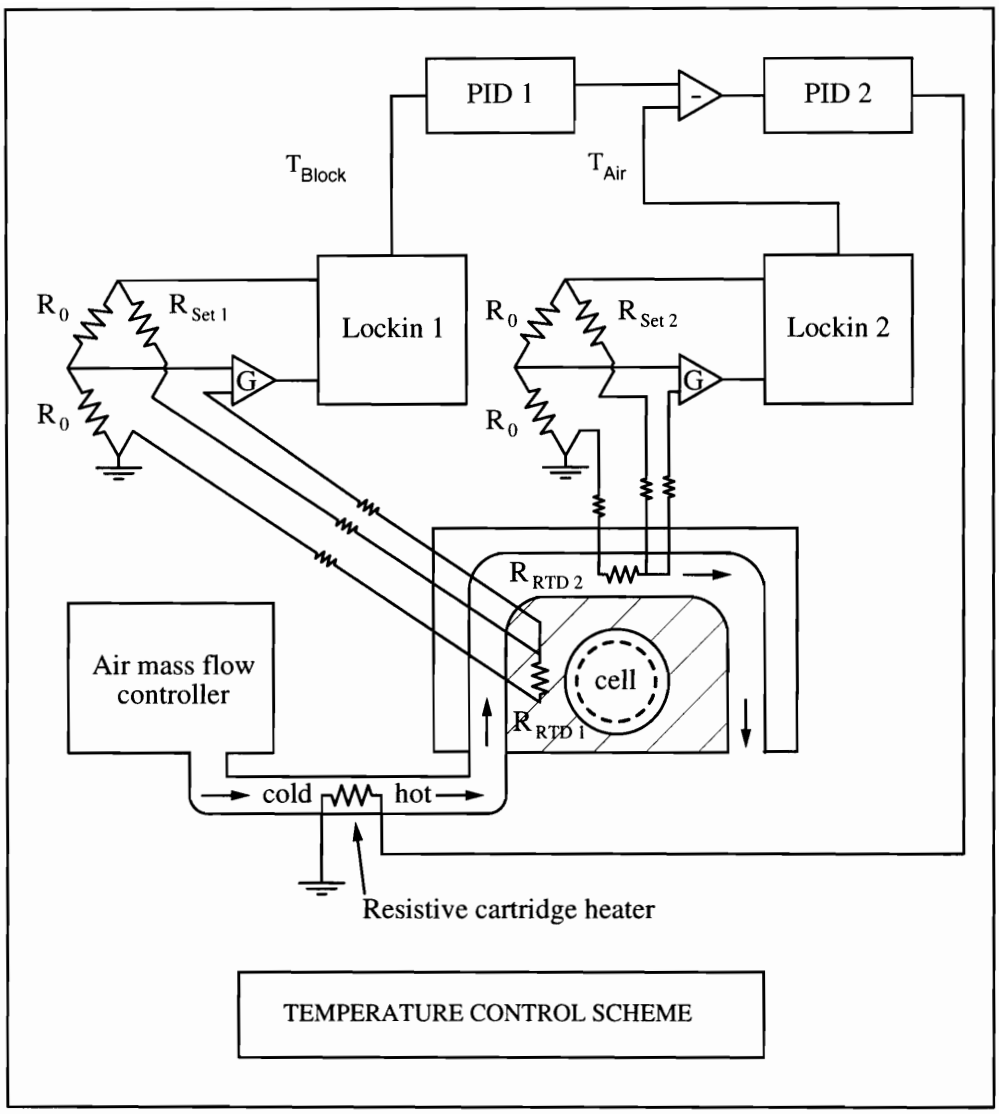

Figure 5-9: Schematic of the double-lock blown air temperature control system used for locking the temperatures of the pump and maser bulbs.

boron nitride helps diminish the effects of this gradient on the block temperature. The thermal capacity of the block helps to integrate out the temperature fluctuations in the block as measured by RTD 1, located in a hole inside the block. The double-lock stabilizes the block in two stages: first, a short time constant (tens of seconds) feedback loop locks $T_{RTD,1}$ to some reasonable T' which brings the block temperature close to the desired value. Then, more slowly (hundreds of seconds), a second feedback loop controls the gain of the first feed-back loop, and thus adjusts T' to be exactly the air temperature needed to make $R_{RTD,1} = R_{Set,1}$. This double-lock yields a temperature stability of a few mK in a day, as we will see in the experimental tests detailed in Sect. 6.1. This lock allows for easy capture and lock stability is excellent, whereas in a single lock to RTD 1 capture is hard and even small perturbations break the lock.

5.2 Double-Bulb Maser Cells

The mixture of ^{129}Xe, ^{3}He, N_2, and Rb used[9] in the ^{129}Xe/^{3}He maser is contained in a Pyrex cell with a blown spherical (maser) bulb joined by a straight transfer tube to a cylindrical (pump) bulb whose flat ends allow for a homogeneous illumination of the gas. In Fig. 5-10 we show the cell drawing.

In order to reduce the rate of nuclear spin relaxation caused by the interaction of ^{129}Xe nuclei with magnetic impurities on the glass walls, the cells are coated with a self-assembling silane compound called octadecyltrichlorosilane (CH_3-$(CH_2)_{17}$-$SiCl_3$, available from Sigma-Aldrich[10]), known as OTS. This compound consists of long hydrocarbon chains each with a trichlorosilane group at one end. In the coating

[9]We typically use 90% enriched ^{129}Xe (chemical purity 99.999%) and 99.9% enriched ^{3}He, available from Spectra Gases, Alpha, NJ.

[10]This compound is stable, reacts violently with water, it is incompatible with strong acids, strong bases, strong oxidizing agents. Air-sensitive. Combustible.

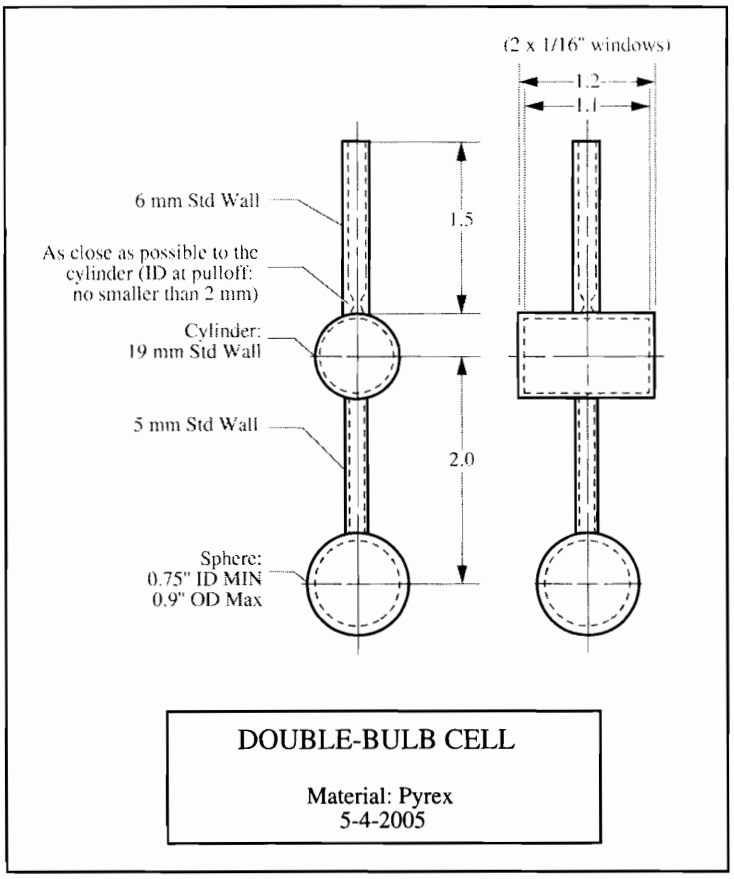

Figure 5-10: Typical double-bulb glass cell before pull-off. All dimensions are in inches unless otherwise specified.

process this group binds to the silicates in the glass, relinquishing the chlorine atoms. The result is a carpet of hydrocarbon chains lining the cell walls. As ^{129}Xe atoms approach the cell walls they bounce off the hydrocarbon chains, keeping at a distance from the depolarizing magnetic impurities always present on the cell walls.

As Fig. 5-11 shows, initially the cell is connected to a glass manifold that typically carries two cells. The manifold is designed to be connected to a gas filling station (providing vacuum to approximately 10^{-9} Torr) with the help of a 1/2" Ultra-Torr seal. Two open tubes in the manifold allow pipet-access to the cells during

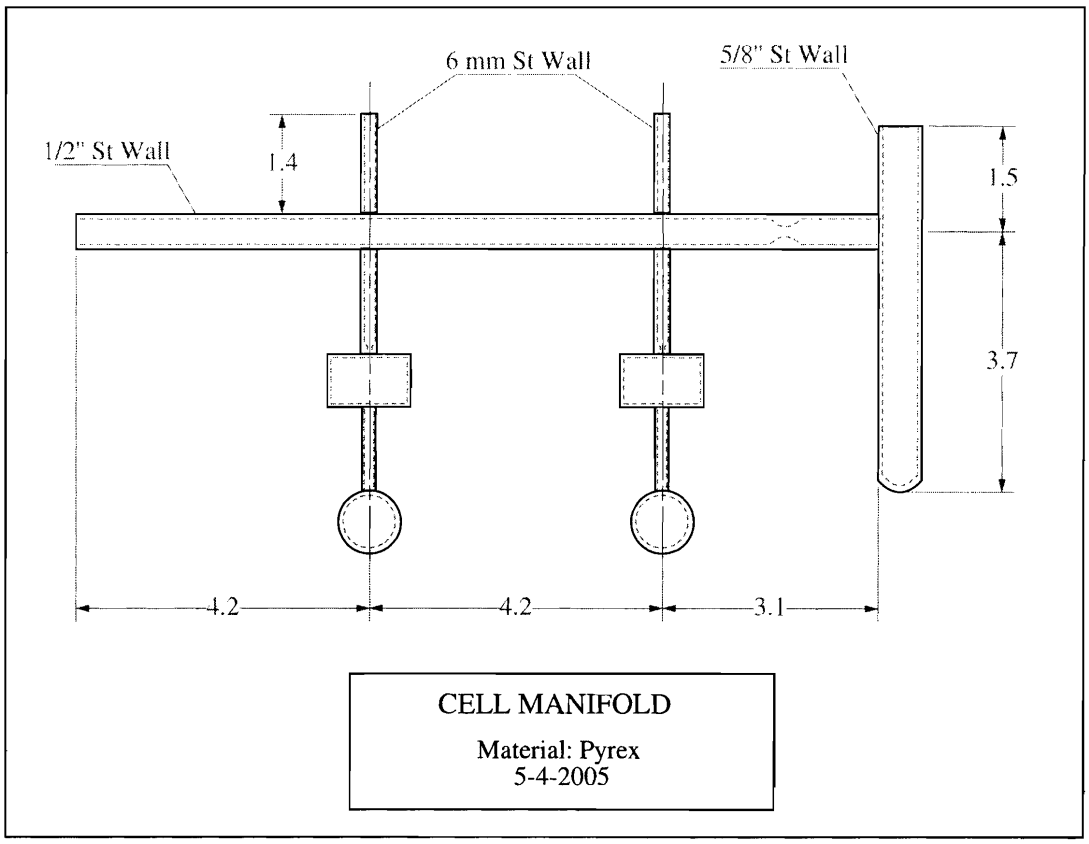

Figure 5-11: Typical glass manifold used to make two maser cells. All dimensions are in inches unless otherwise specified.

the cleaning and coating processes described in the next section, and a side arm accommodates a Rb ampoule.

5.2.1 Cell Cleaning and Coating

In this section we give a brief summary of our cleaning and coating procedures. More details can be found in Refs. [78] and [79].

Before the cells are coated, surface contaminants are removed from the glass using "piranha" solution, which consists of 3 parts of 30% H_2O_2 (hydrogen peroxide) and 7 parts of 97% H_2SO_4 (sulfuric acid) by volume. The piranha solution is prepared

Figure 5-12: DI water inside an uncoated (left) and a coated (right) pump bulb. Clearly the water does not stick to the coated surface and the shape of the water surface is dramatically affected.

inside a fume hood by pouring H_2SO_4 into 30% H_2O_2 (the acid should be added last). The solution, which is initially bubbling, hot, and viscous, is poured into the whole manifold and left there for about three hours. During this time the cells are inspected periodically to eliminate gas bubbles that may form and prevent homogeneous cleaning of the cell inner surface. The whole manifold is then rinsed three times with de-ionized (DI) water, three times with methanol, and again three times with DI water. After rinsing, the manifold is dried for about an hour in a rough-vacuum oven at room temperature, after which air is allowed back in, and the manifold is left to rest overnight.

A 2 millimolar OTS coating solution is prepared by adding 0.788 ml of OTS (with the help of an Eppendorf reference pipette) to every liter of a solution containing 80% of hexane (C_6H_{14}), 12% of carbontetrachloride (CCl_4), and 8% of chloroform ($CHCl_3$). This coating solution is left inside the cells for about five minutes. Par-

ticular care is used while pipetting the solution into and out of the cells, so that the solution never touches the inner walls of the tubes at the height of the pull-offs. This is important because during the pull-off procedure burned coating could fall into the cells, contaminating them. The cells are then rinsed three times with chloroform, put in a vacuum oven whose temperature is slowly increased to approximately 200° C and left to polymerize at this high temperature for about a day.

The quality of the coating can be tested by pouring DI water in the cell and observing that the water does not wet the surface (see Fig. 5-12) and rolls around in the cells much like mercury on a Teflon surface. After this test it is necessary to dry the manifold again by putting it in the vacuum oven at 200° C for a few hours.

5.2.2 Cell Filling

After coating, the manifold is attached to the gas filling station. The access tubes are sealed off by carefully melting the glass with an oxygen-propane torch. A sealed 1 gram, natural abundance Rb ampoule is opened, dropped into the manifold sidearm and the top of the sidearm is quickly sealed off with the torch.[11] The manifold is placed under vacuum and baked-out[12] at 140° C for about a day, until the glass has out-gassed most impurities and the vacuum pressure has dropped to about 10^{-8} Torr and looks stable.

Cell filling begins with the fairly slow process of chasing Rb from the sidearm into the pump bulbs. This is done using a heat-gun to warm the manifold near the opened Rb ampoule and observing Rb vaporize and condense on the colder parts of the manifold. Particular attention is paid not to overheat the cells with the heat-

[11] Rb oxidizes rapidly and exposure to air should be minimized.

[12] A simple makeshift oven is made by wrapping the cells in aluminum foil, winding heat tape on the top and then covering the tape with more aluminum foil. The heat tape should be kept away from the sidearm containing the Rb ampoule to prevent spreading Rb during the bake-out.

gun to avoid damaging the coating (we avoid temperatures higher than 140° C). Rb chasing ends when the pump bulb contains one or two drops of Rb metal. The glass sidearm is then pulled off using the torch to reduce the manifold volume that would waste ^{3}He later on during cell filling.

As shown in Fig. 5-13, we identify three distinct regions when the manifold is connected to the cell filling station, each with a well defined volume: the load volume, V_{Load}, where the gases are loaded one at a time, the volume V_{Tube} that comprises the glass manifold (excluding the cell to be filled) as well as other interstitial spaces on the cell filling station, and the cell volume $V_{Cell} = V_M + V_P$, which is made up by the maser and pump bulb volumes (we neglect for simplicity the volume of the transfer tube). V_{Load} and V_{Tube} are usually not known exactly, whereas V_{Cell}, V_M, and V_P are measured ahead of time, by weighing the water needed to fill the various parts of the cell. For convenience we define $r = V_M/V_{Cell}$, the fractional volume of the cell occupied by the maser bulb.

Before filling the cell it is necessary to run a calibration procedure, which is equivalent to measuring V_{Load} and V_{Tube}. This is easily done by loading N_2 in V_{Load} with pressure $\mathcal{P}_1$, then measuring the equilibrium pressure $\mathcal{P}_2$, once N_2 has been allowed to expand in the whole manifold by opening valve 1. Again, leaving valve 1 open, we measure the slightly smaller equilibrium pressure $\mathcal{P}_3$ when the maser bulb has been cooled from ambient temperature, T_{Amb}, to liquid N_2 temperature, $T_{N_2} = 77$ K. Equating the number of atoms and molecules in the various volumes, we get the following equations:

$$\mathcal{P}_1 V_{Load} = \mathcal{P}_2 \left(V_{Load} + V_{Tube} + V_{Cell}\right), \tag{5.1}$$

$$\mathcal{P}_1 V_{Load} = \mathcal{P}_2 \left[V_{Load} + V_{Tube} + V_{Cell}\left(1 - r + \frac{T_{Amb}}{T_{N_2}} r\right)\right] \tag{5.2}$$

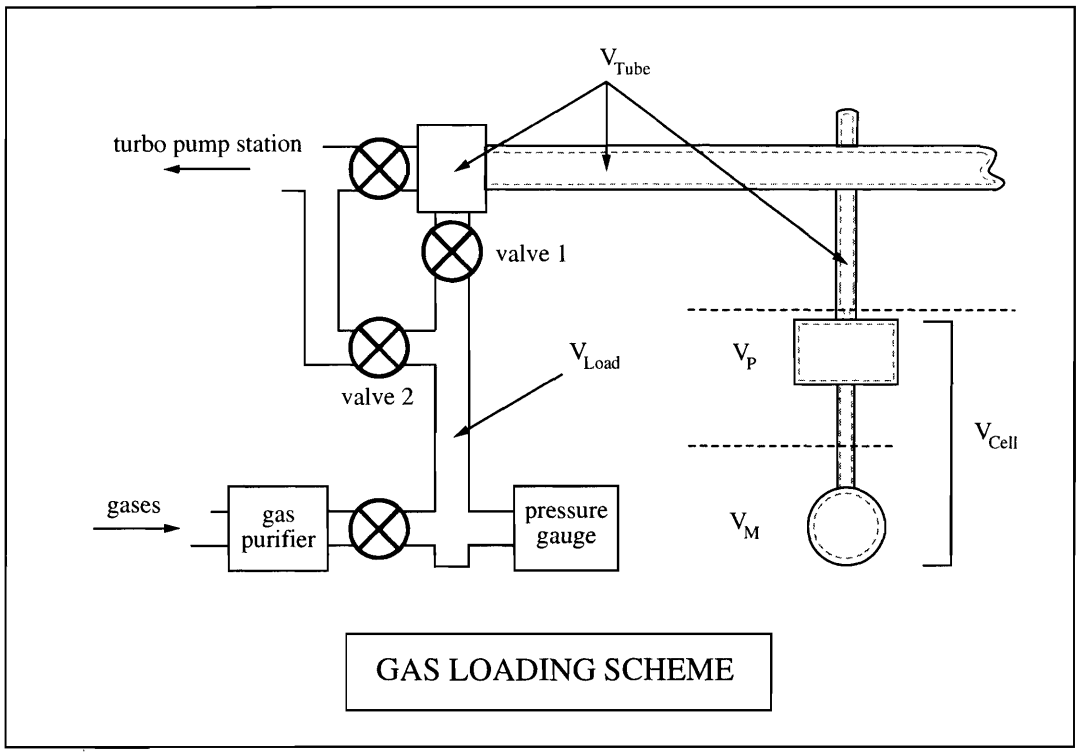

Figure 5-13: Cell filling diagram. The cell manifold is attached to the gas filling station using a 1/2" Ultra-Torr seal. Valve 1 separates the load volume, V_{Load}, from the volume of the manifold, comprising the volume of the cell itself, V_{Cell}, and the rest of the volume, V_{Tube}.

which yield the volume ratios

$$\frac{V_{Cell}}{V_{Load}} = \frac{\mathcal{P}_1(\mathcal{P}_2 - \mathcal{P}_3)}{\mathcal{P}_2\mathcal{P}_3} \frac{T_{N_2}}{r(T_{Amb} - T_{N_2})}, \tag{5.3}$$

$$\frac{V_{Tube}}{V_{Load}} = \frac{\mathcal{P}_1 - \mathcal{P}_2}{\mathcal{P}_2} - \frac{V_{Cell}}{V_{Load}}. \tag{5.4}$$

Once the calibration above has been carried out, the manifold and the load region are evacuated.

Our goal is to fill the cell with gas pressures $\mathcal{P}_{Xe}$, $\mathcal{P}_{N_2}$ and $\mathcal{P}_{He}$ at ambient temperature. The maser bulb is immersed in liquid N_2 for all the duration of the cell

filling procedure. ^{129}Xe is loaded first. Since this gas is liquid at T_{N_2}, cryopumping ensures that all the gas will liquefy in the maser bulb. The desired ^{129}Xe load pressure is then simply $\mathcal{P}_{Xe,Load} = \mathcal{P}_{Xe} V_{Cell}/V_{Load}$. Quickly after valve 1 is opened the pressure gauge will reach a pressure very close to zero, indicating that ^{129}Xe has found its way to the cold maser bulb and condensed there. N_2 is loaded next, there is no risk of N_2 condensing in the maser bulb because the pressure inside the manifold is below 1 atm. With some algebra we find that the V_{Load} should be loaded with pressure:

$$\mathcal{P}_{N_2,Load} = \frac{T_{N_2}}{r(T_{Amb} - T_{N_2}) + T_{N_2}} \frac{\mathcal{P}_1}{\mathcal{P}_3} \mathcal{P}_{N_2}. \tag{5.5}$$

N_2 is allowed to expand in the glass manifold, then valve 1 is closed and the load volume is evacuated using valve 2. V_{Load} is then loaded with ^{3}He at a pressure

$$\mathcal{P}_{He,Load} = \frac{T_{N_2}}{r(T_{Amb} - T_{N_2}) + T_{N_2}} \left(\frac{\mathcal{P}_1}{\mathcal{P}_3} \mathcal{P}_{He} + \mathcal{P}_{N_2} \right), \tag{5.6}$$

Our calculation assumes that initially $\mathcal{P}_{He,Load}$ is greater that the N_2 pressure from the previous load. If this is the case, when valve 1 is opened ^{3}He flows in the glass manifold. Attention must be paid to close valve 1 as soon as the pressure has stabilized in order to prevent N_2 from diffusing back into the load volume and mixing with ^{3}He. If the pressure $\mathcal{P}_{He,Load}$ is higher than the pressure in the ^{3}He bottle, one can can load ^{3}He in n rounds, each time loading with the following pressure:

$$\mathcal{P}_{He,Load} = \frac{T_{N_2}}{r(T_{Amb} - T_{N_2}) + T_{N_2}} \left[\frac{1}{1 - \left(1 - \frac{\mathcal{P}_3}{\mathcal{P}_1}\right)^n} \mathcal{P}_{He} + \mathcal{P}_{N_2} \right]. \tag{5.7}$$

Clearly there is no need to evacuate the load volume between one load and the next. This method was used several times with n = 2 or 3, to use ^{3}He bottles with low

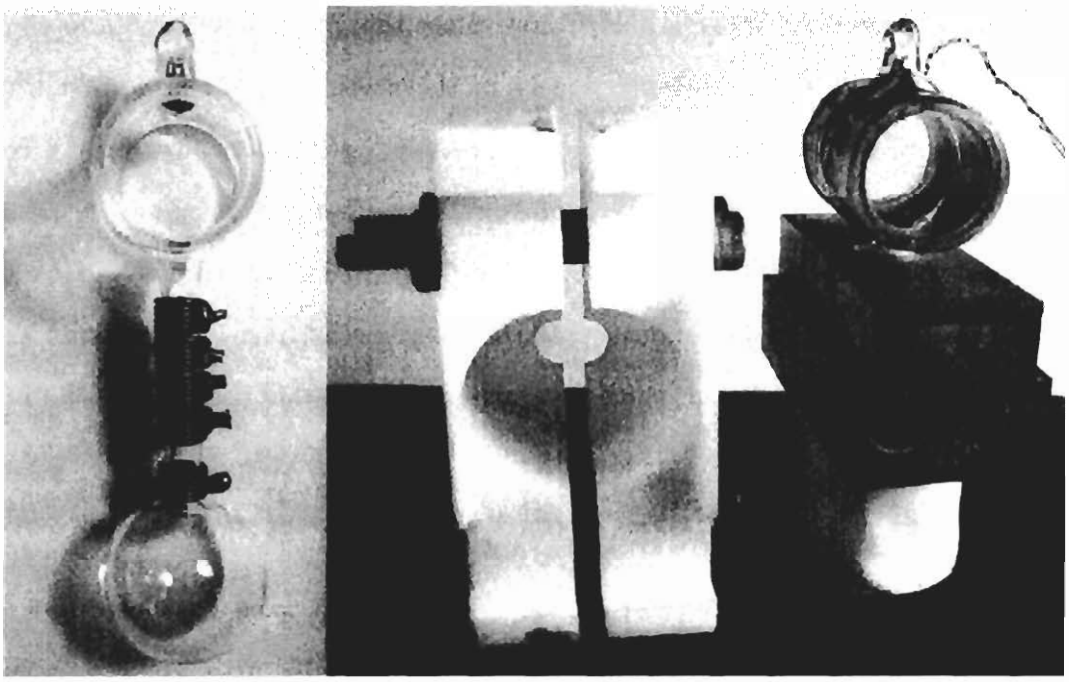

Figure 5-14: A maser cell before (left) and after (right) being mounted on the cell holder. A large drop of Rb metal is visible at the top of the pump bulb in the pull-off tip. The cell holder is mostly empty to provide better thermal insulation between pump and maser region. Two holes at the bottom of the cell holder allow cooling of the transfer tube. The silicone RTV that covers the maser bulb helps improve the thermal connection with the maser block and is installed using a Teflon mold (center).

residual pressures. While making especially high pressure cells it may be necessary to cool the whole cell and not just the maser cell. In those cases the formulae above are still valid if we choose r = 1. In all circumstances it is important that the final pressure inside the (cold) cell is kept below one atmosphere. This ensures proper sealing of the melted glass during pull-off.

5.2.3 Cell Preparation

As Figure 5-14 shows, after the cell has been pulled off, the liquid Rb is accumulated in the pull-off tip (typical volume is approximately 10 mm^3), where it provides Rb atoms for optical pumping. The choke coils are wound (see Sect. 5.4.4) and the cell is installed on the cell holder, which is made out of two small Ultem pieces held together with one-part silicone RTV.[13] To provide good thermal insulation between pump and maser regions, the inside of the cell holders is emptied to leave an air gap. Recently cell holders have been machined in such a way that cold air can be circulated around the transfer tube, in a small volume of approximately 2 cm^3.

The maser bulb is then dipped into a mold full of liquid, two-parts silicone RTV,[14] which is left to dry overnight. The mold is machined out of two Teflon blocks and its cylindrical hole with 1" diameter is identical to the maser bulb receptacle in the pick-up coil (see Figs. 5-7 and 5-14). We found that even though silicone RTV is not a good thermal conductor (see Tab. 5.1), it still significantly improves the thermal connection between the maser cell and the maser block and decreases the maser bulb temperature by about 10° C, in typical operating conditions.

5.3 Optical Pumping System

High-power broad-band lasers satisfy the needs of most hyper-polarized noble gas NMR applications: medium or long term stability of spin-exchange optical pumping is rarely required and high gas pressures (severals atmospheres) are often desirable. On the other hand, in the $^{129}Xe/^3He$ maser the gas pressures are relatively low and the instability of spin-exchange optical pumping directly translates into maser fre-

[13] GE Company, RTV162.
[14] GE Company, RTV11.

quency instability. Hence, it is worth investigating the advantages of using narrow-band lasers, which can be more stable and easier to control. As we pointed out in Sect. 4.3.1, the main drawback of such lasers (besides the cost) is the relatively low laser power, which translates into weaker maser signals more susceptible to thermal frequency noise. Given the complexity of our system and the uncertainties in the quantitative predictions of Rb optical pumping, discussed in Sect. 4.3.1, the trade-off between lower laser power and higher stability of narrow-band lasers can only be studied experimentally. The design studies presented in Ch. 4 provide some guidance, but only a direct comparison of the maser performance with the two types of lasers, trying out many different cells, will ultimately decide which laser will be used for the next LI test.

The narrow-band laser currently employed is the Toptica TA 100 shown in Fig. 5-15. In the next section we review its characteristics and the methods used to stabilize laser power and frequency. Characteristics and stabilization methods for the Coherent Laser Diode Array (LDA) system used as broad-band optical pumping source are described in [68, 34]. Below we limit ourselves to a brief description.

5.3.1 Narrow-Band Laser Characteristics and Stabilization

The Toptica TA 100 is a laser system in which a tapered amplifier serves as the output amplifier for the Toptica Laser Head DL 100, in the following referred to as "master oscillator." The master oscillator is a 35 mW, 1 MHz linewidth, external-cavity diode laser, whose frequency can be tuned by adjusting a grating in a "Littrow" setup (i.e., the first diffraction order of the grating is reflected back into the laser diode) with the help of a piezo actuator. The output beam of the master oscillator provides the seed for the tapered amplifier, whose output is a coherent

beam of approximately 500 mW.[15] In Fig. 5-15 we show our setup. A test beam from the master oscillator emerges from the back of the laser (lower left corner) and is directed toward a photodiode after passing through a vacuum Rb cell kept at approximately 80° C in a small oven. The transmission profile in Fig. 5-16 shows the characteristic spectrum of the Rb D_1 line. Laser frequency locking is usually realized by modulating the grating angle in the proximity of one of the main absorption lines and using phase sensitive detection of the transmitted light at the piezo modulation frequency. The signal is proportional to the distance from the center of the absorption and is used, with the help of a homemade PID controller, to lock the laser frequency by properly adjusting the grating angle. After amplification, the laser light is circularly polarized by a $\lambda/4$ plate and directed towards the maser cell for optical pumping.

In the presence of high noble gas pressures, the absorption line of Rb is both broadened and shifted. In Fig. 5-16 we show the transmission profile (dashed) for a cell containing 700 Torr of ^{129}Xe. The vacuum and pressure broadened profiles overlap, but clearly it is optimal to lock the laser to the Rb line which is closest to the center of the pressure broadened profile. In our maser cells, ^{3}He is usually the gas with the highest density. The shift for ^{3}He has the opposite sign as that for ^{129}Xe. At 114° C, the pressure shift amounts to approximately 6.2 GHz/amg and pressure broadening is approximately 18.7 GHz/amg [80]. Hence, locking to the Rb vacuum dips is feasible for ^{3}He densities below 2 amg. Figure 5-16 also shows a linear decrease in laser intensity as the laser frequency is increased. This feature is due to the "feed forward application" of the Toptica laser, which adjusts

[15]Unfortunately, in the first year of operation we have twice noticed a substantial reduction of laser power over time. After a few months of intensive use, the tapered amplifier had to be replaced. Degradation of the new amplifier appears to be occurring again at the time of this writing. Ultimately, the Toptica TA 100 may prove to be too delicate to perform the next LI tests, which should last for several months.

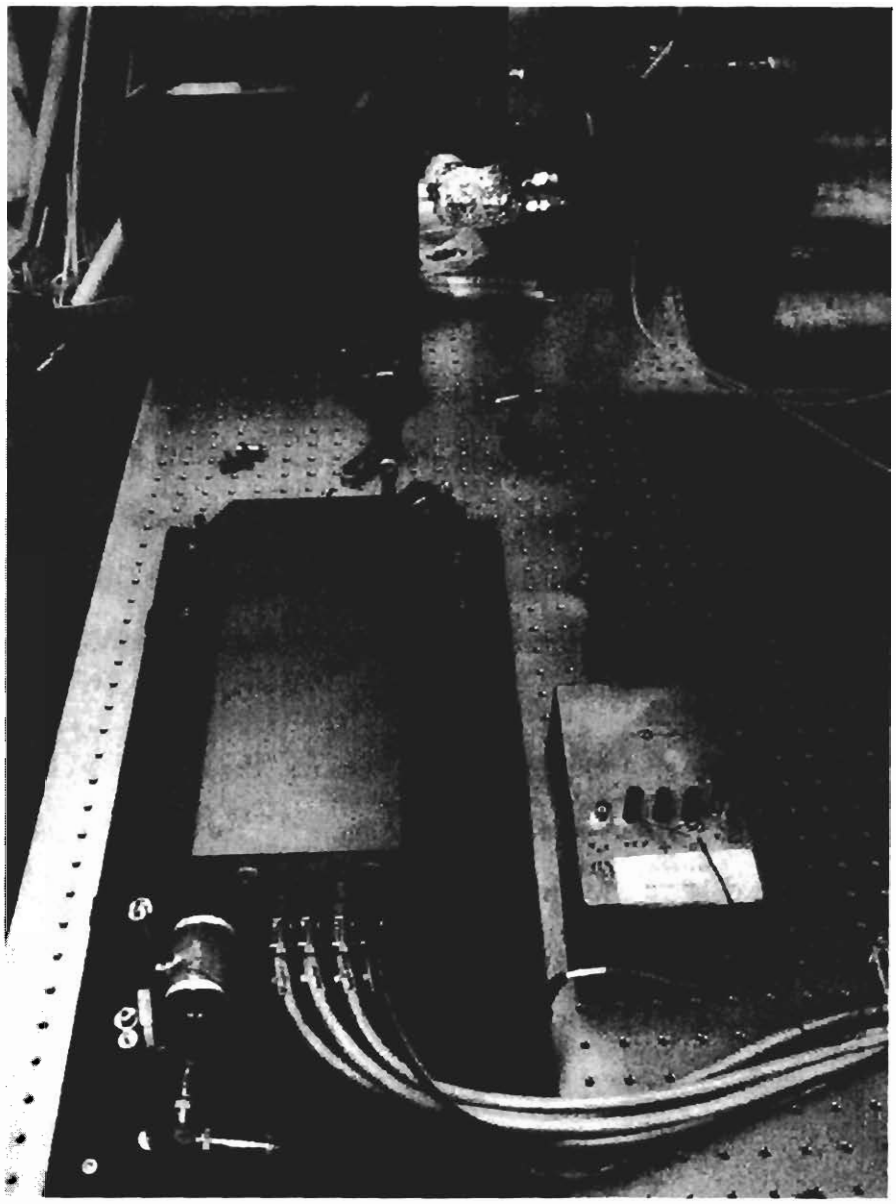

Figure 5-15: The new narrow-band Toptica laser ($\approx$ 10 MHz width) is tuned to the Rb D_1 line ($\approx$ 795 nm) and is employed for Rb optical pumping. A small portion of the light from the laser diode is transmitted through a semi-reflecting mirror and reaches a vacuum cell containing Rb vapor (lower left in the picture). Absorption spectroscopy of this light and small adjustments of the laser's grating allow for precise wavelength stabilization. The bulk of the light from the laser diode provides the seed for a tapered amplifier emitting approximately 500 mW of light, part of which is monitored (lower right in the picture) and used to stabilize the laser total power by adjusting the amplifier current. The laser beam is expanded, circularly polarized and directed towards the pump bulb.

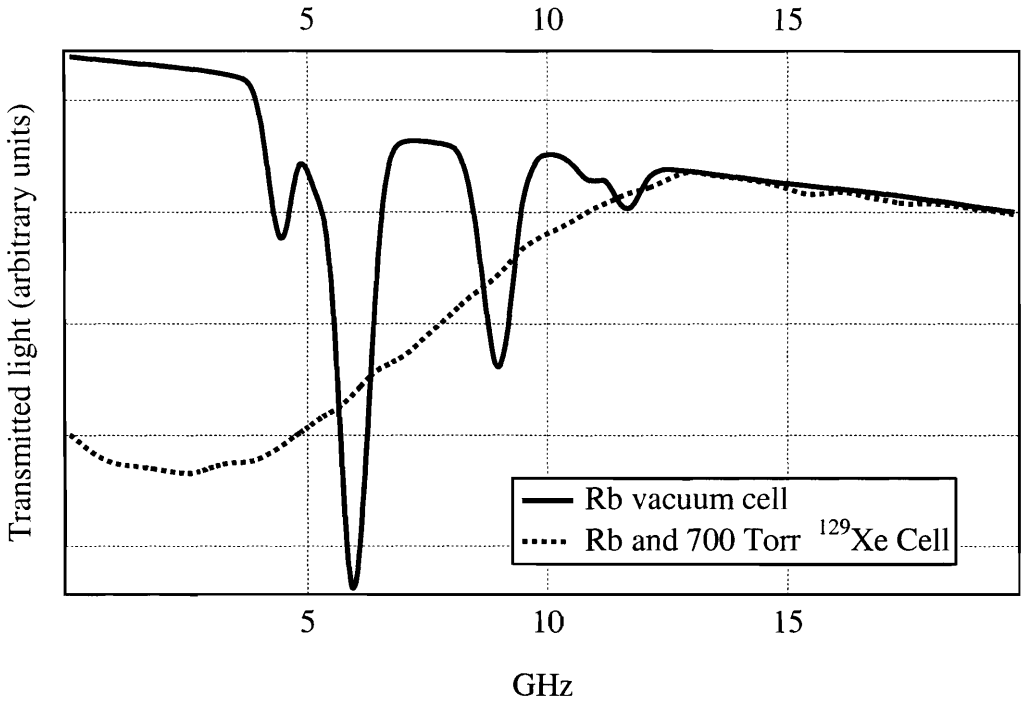

Figure 5-16: Transmission spectrum of master oscillator light through a vacuum Rb Cell compared to the transmission spectrum of the amplified light detected after a cell containing also 700 Torr of ^{129}Xe. ^{129}Xe shifts and broadens the Rb absorption profile. The laser "feed forward" feature is responsible for the linear decrease of light intensity with laser frequency (see text).

the master oscillator current proportionately to the amplitude of the piezo scan in order to suppress mode hops. The mode hop free range is usually limited to 20 GHz as shown in the figure.

The laser power is locked by adjusting the tapered amplifier current and stabilizing the intensity of a few mW of light picked up from the main output beam with the help of a semi-reflecting mirror (see Fig. 5-15 on the right-hand side of the laser). In order to make the laser intensity lock independent of slow photodiode current drifts, we use a chopper to obtain an AC signal at approximately 80 Hz and then we proceed with phase sensitive detection of the photodiode current.

Both photodiodes used for the laser stabilization are temperature stabilized using homemade temperature controllers.

5.3.2 Broad-Band Laser (LDA) Characteristics and Stabilization

The Coherent[16] Fiber Array Integrated Package (FAP-I) is a laser diode array emitting 30 W of unpolarized light with spectral width of approximately 2 nm and tunable to the Rb D_1 line ($\approx$ 794.7 nm). The line-shape and total power of the LDA are controlled by adjusting the injected current and the operating temperature of the diode bar. The light from the diode array is coupled to an optical fiber bundle and then passed through a collimator producing a spot size roughly equal to the diameter of the pump bulb. The beam is linearly polarized with a beam-splitter cube and then circularly polarized with a Meadowlark[17] liquid crystal variable retarder (LCVR) acting as $\lambda/4$ plate. The amplitude of a square voltage fed to the LCVR dynamically controls the angle of rotation of its axis[18] and thus regulates the number of σ^+ polarized photons in the beam.

Figure 5-17 presents a schematic of the two feedback loops used for the LDA stabilization. The stabilization technique is described in detail elsewhere [68, 34]. Here, we provide only a brief summary.

A small portion of the laser beam is picked off using a microscope slide, passed through a diffuser, a chopper, and then sent to a photo-diode. The amplitude of the voltage across the photo-diode is detected at the chopper frequency using a lock-in amplifier whose signal is then sent to a PID controller regulating the LDA's diode

[16]Coherent, Inc., 5100 Patrick Henry Drive, Santa Clara, California 95054.

[17]Meadowlark Optics, Inc,, 5964 Iris Parkway, Frederick, CO 80530.

[18]The voltage actually controls the relative optical length between fast and slow axis of the liquid crystal.

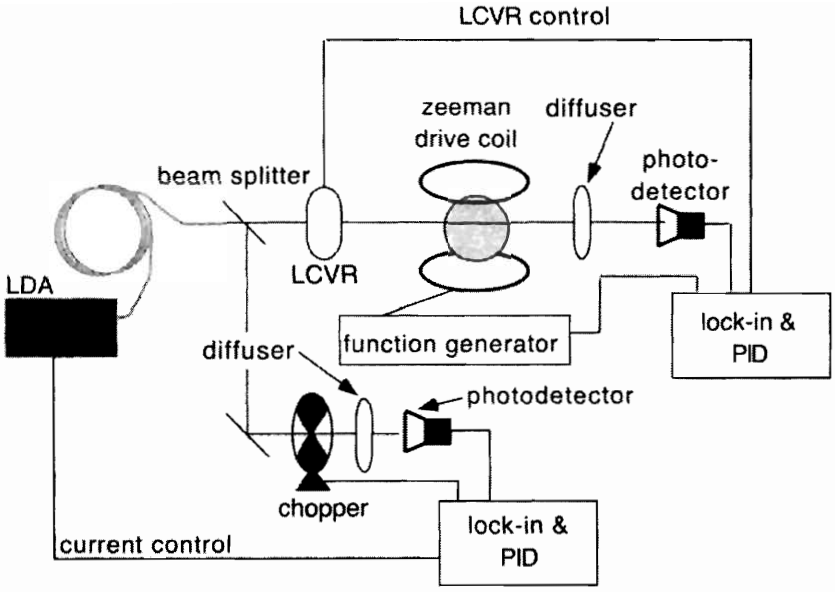

Figure 5-17: Schematic of the two feedback loops used for the LDA stabilization of laser total power and Rb magnetization in the pump bulb [68, 34].

bar current. This first feedback loop controls the laser total power to a few parts in 10^4 as we will show in Sect. 6.2.

A second feedback loop is used to stabilize the Rb magnetization since the frequency of the broad-band laser cannot be controlled directly, as it was done with the Toptica laser. The Rb polarization in the pump bulb is slowly modulated ($\sim$ 400 Hz) using a weak Zeeman drive applied to the pump bulb region with a set of coils installed on the pump block (see Fig. 5-6). The polarization modulation induces a modulation on the intensity of the light transmitted through the pump bulb, which is then measured with a photodiode. The amplitude of the voltage modulation across the photodiode, $V_{M_{Rb}}$, is detected using a lock-in amplifier. Since $V_{M_{Rb}} \propto P_{Rb}^2$[Rb], near saturation (i.e., $P_{Rb} \approx 1$), $V_{M_{Rb}}$ is roughly proportional to the Rb magnetization, P_{Rb}[Rb]. Control of the Rb magnetization in achieved by adjusting the voltage amplitude of the LCVR square voltage, which regulates the polarization of the light

so that $V_{M_{Rb}}$ is held constant (to a few parts per thousand, see Sect. 6.2).

5.4 Magnetic Field Environment

In this section we describe the various components of the experiment dedicated to controlling the magnetic field environment, which is clearly vital since our Zeeman masers depend to first order on the magnetic field. We begin by describing the magnetic shields used to isolate the atoms from ambient magnetic noise. We then review the design of the main solenoid and the set of shim coils used to render the DC magnetic field more homogeneous. Next we describe the magnetic field stabilization scheme depicted schematically in Fig. 1-1.

In addition, the oscillating magnetic field produced by the pick up coil during maser action can extend sufficiently far to stimulate emission in the transfer tube and in the pump bulb. There are a number of reasons why this is undesirable, as we will see in Sect. 6.7. To prevent masing outside of the maser bulb we currently use two different strategies: (i) we install choke coils around the transfer tube to dephase and screen out the pick-up field in that region (Sect. 5.4.4); (ii) we install a small longitudinal coil around the pump bulb to detune the atoms in the pump bulb away from resonance (Sect. 5.4.5).

5.4.1 Magnetic Shielding

The main solenoid is placed inside three concentric, cylindrical magnetic shields, as Fig. 5-18 shows. The innermost shield provides a protected return path for the field produced by the solenoid. All three shields provide isolation from ambient magnetic field noise, which in our laboratory has known drifts on the order of 200 μG/h and shows occasional sudden changes as big as 500 μG. We also measured an upper

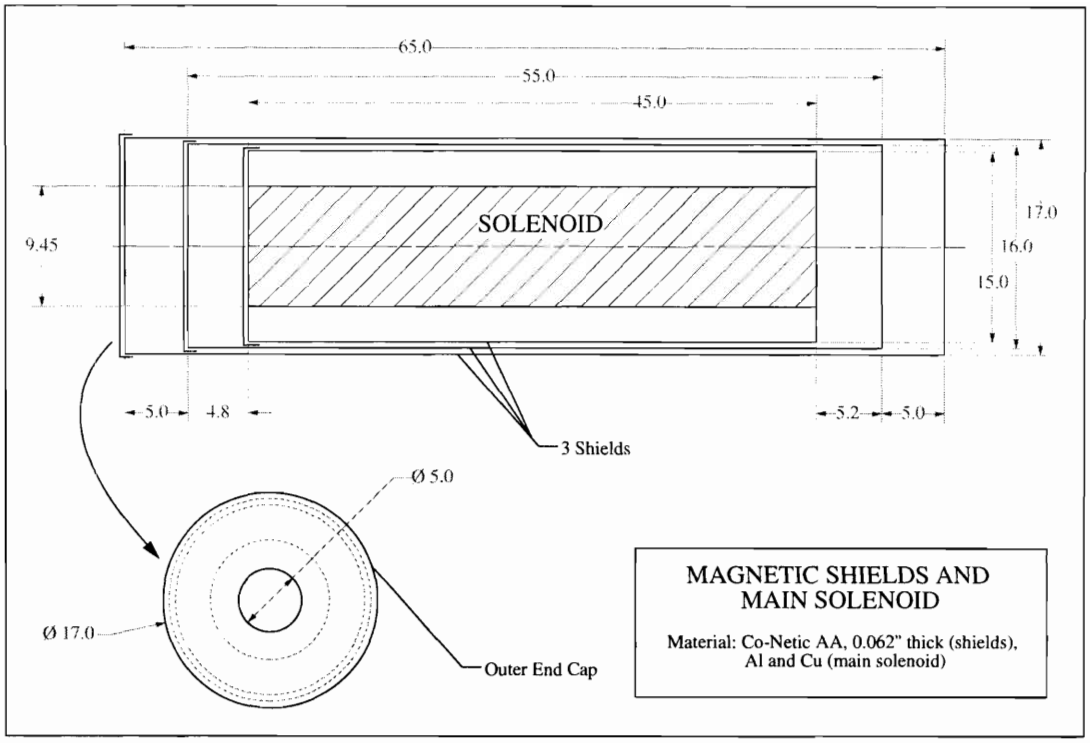

Figure 5-18: Main solenoid and three nested μ-metal magnetic shields used in the ^{129}Xe/^{3}He maser. The shields are oriented east-west in the laboratory when performing an LI test. Removable end-caps on one side of the shields allow installation of the maser oven. The ends of each shield feature a 5" diameter access hole to provide optical, electrical, and blown air access to maser oven and gradient cylinder. All dimensions are in inches.

bound for the magnetic gradient noise in our laboratory: $|\vec{\nabla}B| < 4/\sqrt{Hz}\ \mu$G/cm.

The effectiveness of the transverse shielding was measured in 1999 by applying an external magnetic field and measuring the shift with a magnetometer located inside the shields [34]. The transverse shielding factor, defined as the ratio of the magnetic field induced by the coil without and with the shields, was found to be approximately 20,000. In a similar way, we recently measured the longitudinal screening factor[19] to

[19]We used a single, 2 m diameter, circular coil. We located the coil at one end of the cylindrical μ-metal shields, thus applying an inhomogeneous magnetic field of a few Gauss along the $\hat{z}$ axis and we measured the field inside the shields. The longitudinal shielding ratio quoted is the ratio between the expected field at the maser bulb site and the field intensity measured there with a magnetometer. We note however that the notion of longitudinal and transverse shielding

Main Solenoid Parameter	Value
Diameter	9.375"
Length	44.5"
Wall thickness	0.060"
Turns density	50/inch
DC resistance	182.2 Ω
Field at center	24.3 G/A

Table 5.2: Characteristics of the solenoid used in the ^{129}Xe/^{3}He experiment [34].

be approximately 280. In the longitudinal direction the screening factor is expected to be worse, since the cylindrical shields have large access holes at the two ends.

The residual magnetization of the shields and solenoid's aluminum support are typically responsible for longitudinal magnetic field gradients of approximately 3 μG/cm, which are about 10 times smaller than the longitudinal inhomogeneity of the electromagnet's field in the central region. Linear gradients can be corrected for with the help of shim coils, but the same is not true for more irregular residual fields. To make sure that the residual magnetization is as homogeneous as possible, we employ a degaussing system which consists of a 60 wire cable, 5 m long, installed on the gradient cylinder (see Fig. 1-1) through which a bipolar power supply can drive a current of approximately 8 A per wire, or 480 A total. The sign and intensity of the current can be varied to saturate the shields (at least the innermost ones) and progressively drive the shields' residual magnetization through a series of hysteresis cycles of decreasing amplitude, until it is reduced adiabatically to zero. The period of one hysteresis cycle is usually chosen to be on the order of few seconds to have large skin-depth so that the shield suffers minimal eddy current screening. The amplitude of the oscillations' envelope is brought to zero in about 300 s. So far, this degaussing procedure has produced only minor improvements on the overall maser

is somewhat misleading because the small residual fields induced inside the shield by external, inhomogeneous magnetic fields, in general, are not collinear with them.

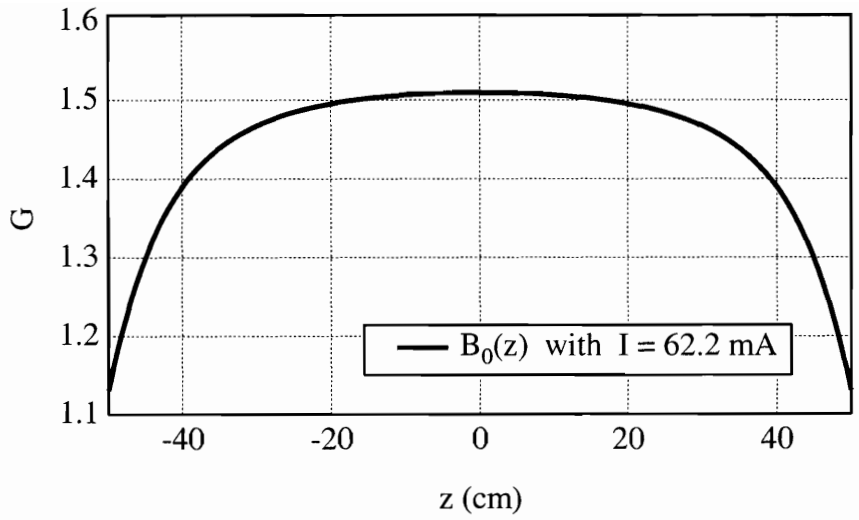

Figure 5-19: Calculated profile of the magnetic field produced by the main solenoid along its symmetry axis, $\hat{z}$. An homogeneous field of approximately 1.5 G is obtained with a solenoid current of approximately 62.2 mA.

performance. Probably over the size of the maser cell ($\approx$ 2 cm diameter) the fields produced by the residual magnetization are fairly linear and can be shimmed out with proper tuning of the gradient coils.

5.4.2 Main Solenoid and Gradient Coils

The main solenoid was carefully wound by David Bear and Rick Stoner in 1999 from 25 AWG copper wire[20] on a hollow aluminum cylinder [34]. Although a two layer configuration was tried out, a single layer winding was found to produce the best field homogeneity. The completed layer was painted with marine spar varnish to prevent small excursions of the windings due to vibrations and mechanical stress. Table 5.2 summarizes salient properties of the main solenoid. Based on these specifications the magnetic field can be easily calculated. Figure 5-19 shows the profile of the main

[20] 25 HAPT polyester-amide wire

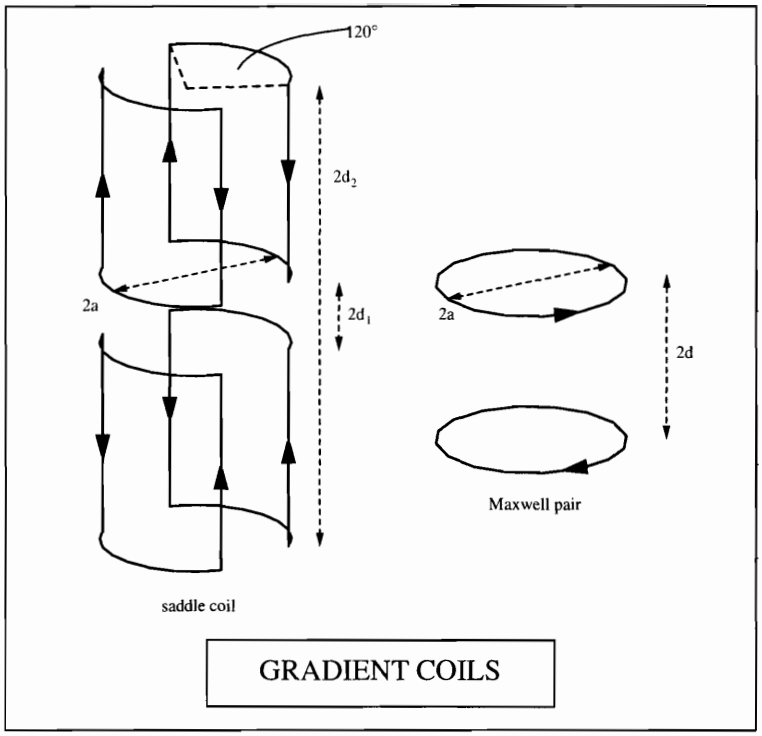

Figure 5-20: Design of the coils installed on the gradient cylinder (see Fig. 5-23). The best linearity in the central region is achieved by choosing $d_1 = 0.38\ a$ and $d_2 = 2.55\ a$ for the saddle coil and $d = \sqrt{3}/2\ a$ for the Maxwell pair [81].

magnetic field along the $\hat{z}$ axis, $B_0(z)$, for a typical applied current of approximately 62.2 mA.

In the previous maser, the gradient coils were inlaid on a 8" long cylindrical shroud containing the whole maser. That layout had the disadvantage that the gradients coils were fairly small and not very homogeneous. Moreover, reproducing a particular shimming configuration to compare the properties of different cells was difficult because the shroud had to be entirely removed from the solenoid when a maser cell was replaced.

The new set of gradient coils is now wound on a gradient cylinder designed to remain permanently located inside the main solenoid. This ensures that a certain

shimming configuration can be preserved. The larger dimensions of the cylinder also accommodates larger gradient coils producing magnetic field gradients that are linear over many centimeters. Figure 5-23 shows the machine drawing of the gradient cylinder.

In the special grooves cut into the outer surface of the cylinder we wound three gradient coils. For all coils we used a single winding. Two saddle coils like that shown in Fig. 5-20 and rotated by 90° with respect to each other, produce the linear dB_z/dy and dB_z/dx gradients shown in Fig. 5-21. A Maxwell pair, like that depicted in Fig. 5-20, produces the linear dB_z/dz gradient shown in Fig. 5-22. The dimensions of the gradient coils were chosen to give the best linearity [81]. The coil radius $a = 11.65$ cm determines $d_1 = 0.38\ a$ and $d_2 = 2.55\ a$ for the saddle coils and $d = \sqrt{3}/2\ a$ for the Maxwell pair. For better stability, after winding the coils the grooves were filled with non-corrosive, one-part silicone RTV.

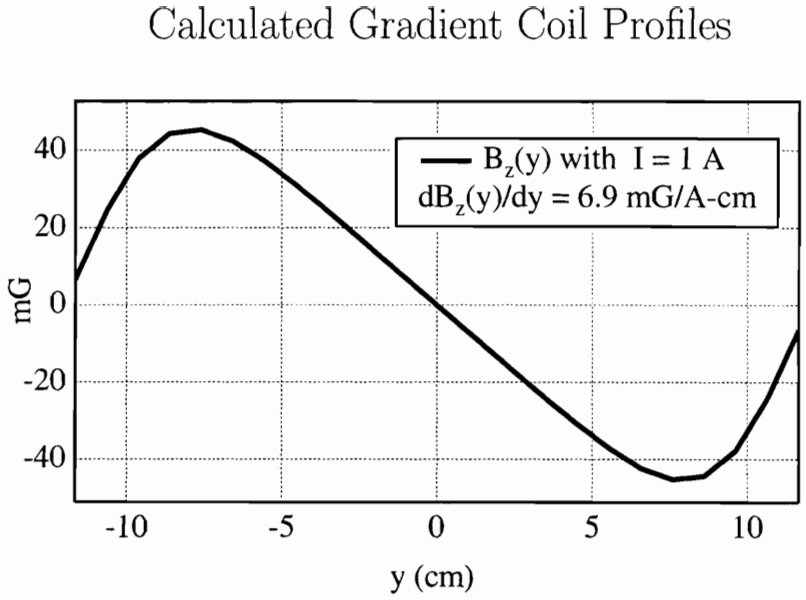

Figure 5-21: Calculated profile of the longitudinal magnetic field gradient along the $\hat{y}$ direction produced by flowing 1 A through a saddle coil like that shown in Fig. 5-20. The same gradient is obtained in the $\hat{x}$ direction by using another saddle coil rotated by $\pi/2$.

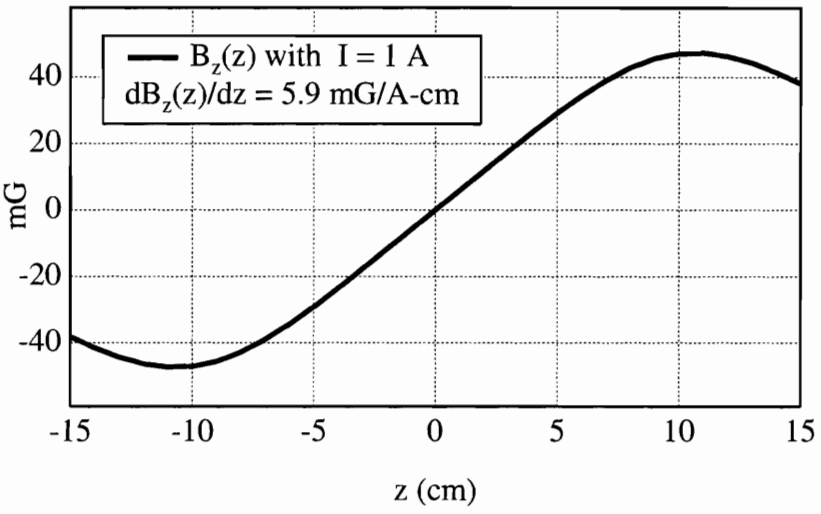

Figure 5-22: Calculated profile of the longitudinal magnetic field gradient along the $\hat{z}$ direction produced by flowing 1 A through a Maxwell pair (see Fig. 5-20). The best linearity in the central region is achieved by choosing $d = \sqrt{3}/2\ a$ [81].

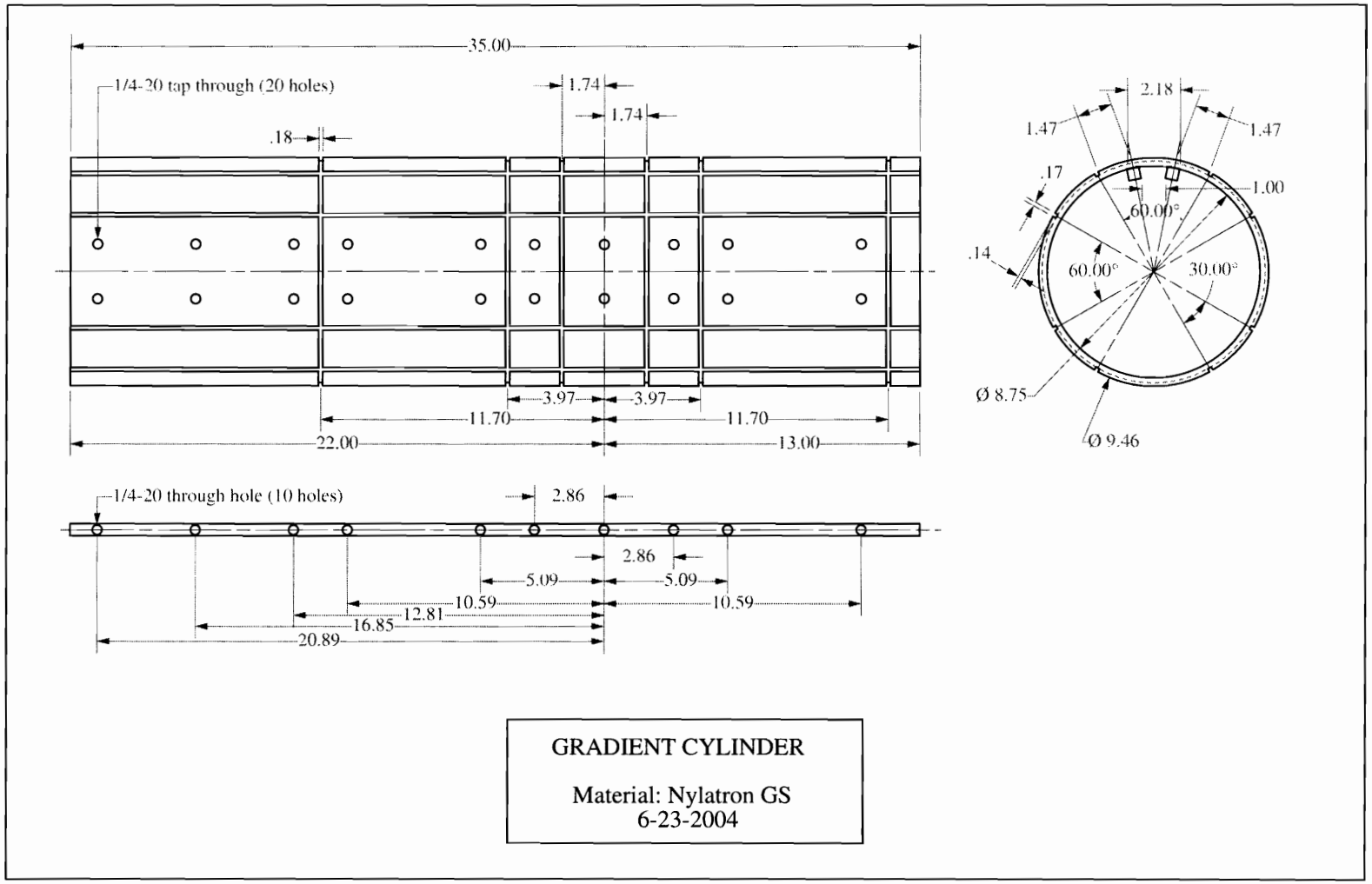

Figure 5-23: Machine drawing of the gradient cylinder and one of the two square rods screwed on the inside of the cylinder to support the degaussing cable, as shown in Fig. 5-1. All dimensions are in inches.

5.4.3 Magnetic Field Stabilization

The solenoid and gradient trim coils are driven by a four-channel, homemade current controller box. The output current on each channel is stable to approximately 10 ppm when free-running. In order to further stabilize the magnetic field environment and provide real-time comagnetometry, the solenoid field is controlled by phaselocking the ^{129}Xe maser to an ultra-stable, LI violation insensitive H maser, as shown in Fig. 1-1. Section 5.5 describes in detail the signal detection system in the ^{129}Xe/^{3}He maser. Here we focus on the operation of the phase-lock loop.

The maser signals are measured across a capacitance and multiplied 5,000 times using a low noise preamplifier. The highest SNR ^{129}Xe maser signal is sent to a lock-in amplifier referenced to the H maser. The lock-in serves as a low-pass filter as well as a phase-sensitive detector. The output signal from the lock-in is processed by a PID circuit controlling the solenoid current. The loop's time constants are optimized by minimizing the phase noise of the locked species in the short term ($\approx$ 200 s).

A series of experiments carried out with the previous apparatus, comparing the long term stability of the ^{129}Xe/^{3}He maser with many different magnetic field lock settings, failed to demonstrate a direct connection between the noisiness of the magnetic field lock and the frequency noise that limits the masers' medium term stability. Although this may seem puzzling at first, if we assume perfect comagnetometry, the noisiness of magnetic field corrections only induces phase noise in the free-running species, not frequency noise. If this were not the case, the frequency noise would also manifest itself as a random walk of the phase of the locked species, which certainly is not present since that species is phase locked.

The optimization of the magnetic field lock mentioned above, if not fundamen-

tal, remains nevertheless useful. Minimizing the phase noise of both masers makes the onset of other more damaging types of noise obvious for shorter measurement intervals. The optimization is particularly important when using the LDA, because the Rb magnetization lock scheme requires a stable magnetic field.

5.4.4 Choke Coils

A simple technique was introduced by Rick Stoner and David Bear to enhance the spatial uniformity of the masing ensembles, thereby improving the noble gas coherence times (T_2) and the effectiveness of the ^{129}Xe comagnetometer. The transfer tube of each ^{129}Xe/^{3}He cell is wrapped with a series of five adjacent "choke coils," each consisting of six turns of 22 AWG copper magnet wire wound in a single layer, as shown in Fig. 5-14.

Reactive back-currents (due to Lenz's Law) are induced in the choke coils by the time varying magnetic fields produced by the (co-axial) pick-up coil and also by the precessing noble gas magnetizations. The magnetic field produced by these back-currents reduces and dephases both the net transverse field in the transfer tube and the contribution of noble gas atoms in the transfer tube to the mean magnetization signal sensed by the detection coil. The segmented design of the choke coils allows the reactive magnetic fields to adopt a profiled spatial dependence, thus providing more effective flux exclusion.

5.4.5 Pump Bulb Solenoid

A 60 turn solenoid is wound on the cylindrical pump bulb (see Fig. 5-14) with the purpose of applying a small longitudinal field, $\delta B_z \approx 150\,\mu$G, to the pump bulb region as shown in Fig. 4-14. This field does not need to be homogeneous. Its

purpose is simply to shift the ^{3}He Zeeman frequency in the pump bulb away from the maser frequency, so that the pick-up coil peripheral field reaching the pump bulb does not excite ^{3}He transition there. This solenoid was added when we realized that peripheral field effects can seriously compromise co-magnetometry as we will see in Sect. 6.7 and in particular can convert optical pumping light instability into maser frequency instability, as argued in Sect. 6.7.2.

5.5 Signal Detection System

Figure 5-24 shows the layout and the schematic of the ^{129}Xe/^{3}He maser double-resonant circuit. Time-varying magnetic fields produced by precessing noble gas magnetizations are detected by an inductive pick-up coil (L_2, R_2) surrounding the maser bulb.[21] When running the maser, switch S_2 is shorted and S_1 is switched to the lower position. Positive feedback to both noble gas species is provided via a dual-resonance tank circuit, formed by an external resonator coil (L_1, R_1) and ultra-stable tuning capacitors (C_1, C_2, C_{2+}). The maser signals are measured as sinusoidally varying voltages across the capacitor $C_2 + C_{2+}$.

When doing free induction decay (FID) measurements (see Sect. 6.5), the system is operated with switch S_1 in the upper position. In this configuration the resonator is disengaged and C_3 is sufficiently small that the single resonant frequency is well above the operating frequencies of either maser. The so called "pulse box" is plugged into S_2 and transverse Rabi pulses can be applied to the atoms by inductively driving the main circuit with a secondary circuit connected to a programmable function generator. The original design of this circuit is due to Rick Stoner and is discussed

[21] Formerly, two separate resonant circuits were used, one for each species. Even if those circuits had better quality factors, the single pick-up coil configuration with a double-resonant circuit turned out to be preferable. A single pick-up coil guarantees the same magnetic field distribution for both noble gas species and as we saw in Sect. 4.4 this is crucial for co-magnetometer effectiveness.

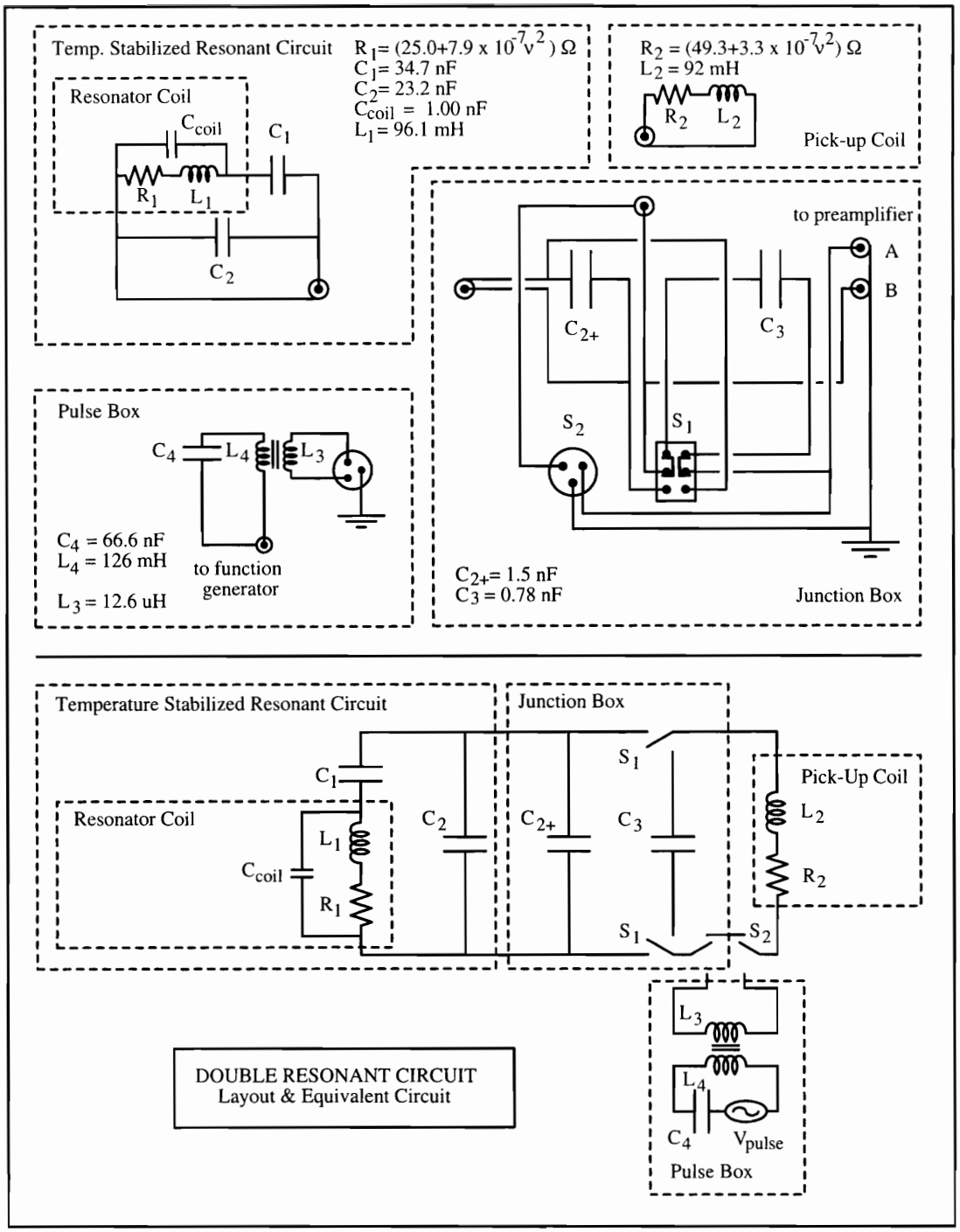

Figure 5-24: Layout (top) and equivalent circuit (bottom) of the double-resonant circuit. The values of the circuit components reflect our latest in situ tuning.

further in [37]. The following sections describe in detail the design and operation of the components of the $^{129}Xe/^{3}He$ maser signal detection system.

5.5.1 Pick-up and Resonator Coils

Design of the $^{129}Xe/^{3}He$ maser resonant circuit begins with the pick-up coil, whose dimensions are dictated by the cell size. The wire gauge must be determined balancing competing effects. Smaller gauge wire wound on a form of fixed size results in a larger number of turns and larger inductance. Unfortunately, more turns and smaller wire diameter yield also larger resistance, which in turn decreases the Q of any resonant circuit making use of that inductance and induces larger Johnson noise. Moreover, smaller wire gauge has a larger fractional content of AC resistance. This is important because the AC resistance appears to be more temperature sensitive than the DC resistance, potentially affecting the $^{129}Xe/^{3}He$ maser's long-term frequency stability [34].

Based of these stability considerations, we wound our new pick-up coil (see Figs. 5-7 and 5-3) with 1,600 turns of 28 AWG insulated magnet wire,[22] a wire gauge significantly larger than the 32 AWG employed in the previous experiment. This enabled us to decrease the coil resistance by a factor of 2.9, while reducing the inductance only by a factor 1.6. Because of the larger wire diameter, the temperature sensitive AC resistance was also greatly reduced.

We employ the same resonator coil that was previously in use:[23] a multilayer coil wound with 28 AWG insulated magnet wire on a Nylatron cylinder with 2.4" diameter and 5.4" length [34]. In the next section we explain in some detail how the pick-up and resonator coils are characterized.

[22]Single layer Polyimide-ML insulation (thermal class 240° C) available from MWS Wire Indus-

Description	Parameter	Pick-up coil	External resonator	Units
Wire gauge		28	25	AWG
Inductance	L	92.1	96.1	mH
DC resistance	R_{DC}	48.6	25.0	Ω
AC resistance coeff.	k_{AC}	3.3×10^{-7}	7.9×10^{-7}	Ω/Hz^2
Stray capacitance	C_{coil}	0.1	1.0	nF
Resistance at 1.7 kHz	R	49.6	27.3	Ω
Resistance at 4.7 kHz	R	55.9	42.5	Ω

Table 5.3: Room-temperature characteristics of the pick-up and external resonator coils presently used in the ^{129}Xe/^{3}He maser.

Coil Characterization

Here we describe the procedure used to measure the inductance and AC resistance of our coils. Consider a simple RLC series circuit, where L is the inductance of the coil, R is its resistance, and $C = C_{coil} + C_i$ has two components: C_{coil}, the stray capacitance of the coil and C_i, a low-loss capacitor whose value is known with good precision. An AC voltage is induced across L by bringing in its proximity a coil driven by a variable frequency function generator. By measuring with a lock-in amplifier the voltage V_r across a small resistor $r \ll R$, it is easy to find the resonant frequency $\omega = (LC - R^2C^2/2)^{-1/2} \approx 1/\sqrt{LC}$ at which the detected voltage reaches the maximum, V_r^{Max}. The approximation reflects the fact that in our coils the impedance of L is large and the impedance of C is usually small. L and C_{coil} are found by measuring ω_i for several capacitor values C_i, and performing a linear fit of the function $1/\omega_i^2 = C_{coil}L + LC_i$.

In order to obtain the frequency-dependent AC resistance, it is necessary to measure the width at half power $\Delta\omega_i$ of the resonant curve (i.e., the frequency distance between the points where $V_r = V_r^{Max}/\sqrt{2}$) for each capacitor value C_i. For

tries.

[23]Note that for realizing a double-resonant circuit at least two inductances are needed.

a generic series RLC circuit it is well known that $Q = \omega/\Delta\omega = \omega L/R$, hence we have that $R_i = \Delta\omega_i L$. The right hand side of this equation is known and yields the total resistance of the coil at frequency ω_i. In the relevant frequency regime for our masers, when ω_i is between 0 and 2π 10 kHz, in addition to the DC resistance the coil resistances exhibit a quadratic behaviour: $R_i = R_{DC} + k_{AC}\nu^2$. The fit parameters for the two coils are summarized in Tab. 5.3.

5.5.2 Resonant Circuit Tuning

In this section we outline the procedure for the tuning of the double-resonant circuit, which is done in two stages: an initial coarse tuning in which we assume that $C_{2+} = 0$ and a fine tuning procedure in which the appropriate value of C_{2+} is found.

We assume that both inductances have been built at this point. L_1, R_1, L_2, R_2, and C_{coil} are henceforth treated as constants[24] and tuning basically consists in picking the capacitances C_1 and C_2. These two degrees of freedom are used to select the operating frequency of the ^{129}Xe maser, ω_{Xe}^{Set}, and to make sure that $\omega_{He}/\omega_{Xe} = \gamma_{He}/\gamma_{Xe} = \gamma_{HX} \approx 2.75408$. Both maser frequencies should be chosen away from the noisy harmonics of 60 Hz.

The part of the double-resonant circuit which is located in a temperature stabilized environment (see dashed box at the lower left hand side in Fig. 5-24) has the following equivalent impedance:

$$\frac{1}{Z_{Res}} = i\omega C_2 + \frac{1}{\frac{1}{i\omega C_1} + \left(i\omega C_{coil} + \frac{1}{R_1 + i\omega L_1}\right)^{-1}}. \tag{5.8}$$

A generalization of the frequency-dependent quality factor $\rho_c(\omega)$ and dephasing $\alpha(\omega)$

[24] For simplicity we consider only the stray capacitance of the resonator coil, C_{coil}, and we neglect the stray capacitance of the resonator coil which is ten times smaller.

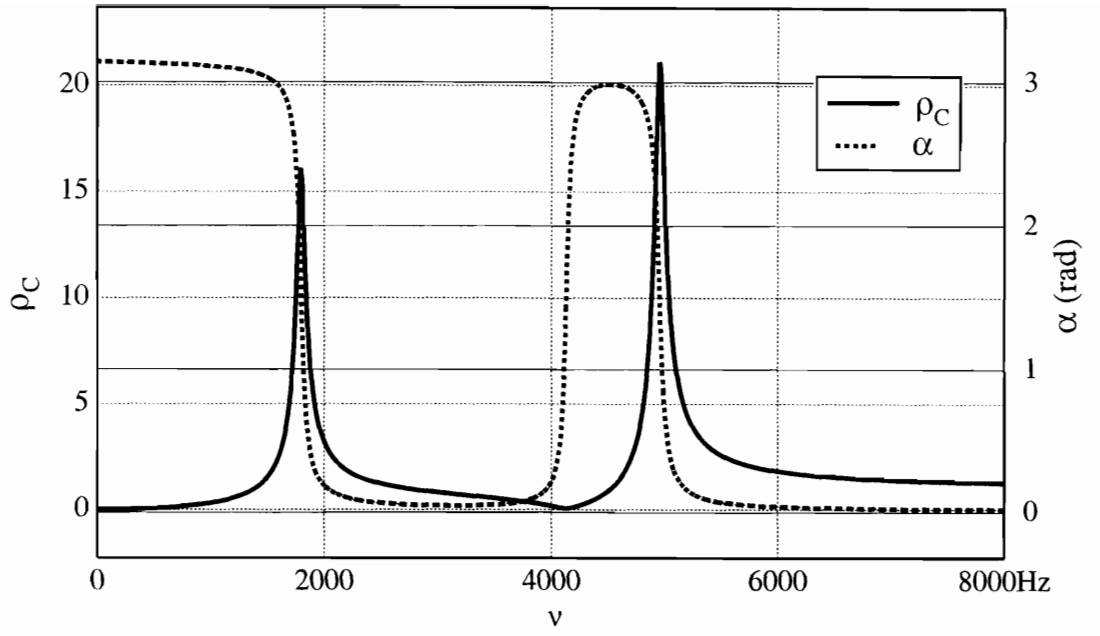

Figure 5-25: Examples of calculated frequency-dependent quality factor $\rho_c(\omega)$ and dephasing $\alpha(\omega)$ for the double-resonant circuit. These functions replace and generalize to the double-resonant case the definitions introduced in Sect.2.3.1 and fully characterize the feed-back of our tank circuit.

introduced in Eq. (2.26) is easily obtained by replacing $Z_C = 1/i\omega C$ with Z_{Res}:

$$\rho_c(\omega)e^{i\alpha(\omega)} = \frac{i\omega L_2}{i\omega L_2 + Z_{Res} + R_2}. \tag{5.9}$$

The two maxima of $\rho_c(\omega)$ are the generalized quality factors Q_{Xe} and Q_{He} for the two species and they are located at the resonant frequencies ω_{Xe} and ω_{He} (see Fig. 5-25). Since the maxima positions depend only weakly on the coil resistances, approximate, analytic expressions for the resonant frequencies can be found by setting $R_1 = R_2 = 0$,

$$\omega^2_{Xe}(C_1, C_2) = \frac{b - \sqrt{b^2 - 4a}}{2a} \quad , \quad \omega^2_{He}(C_1, C_2) = \frac{b + \sqrt{b^2 - 4a}}{2a}, \tag{5.10}$$

where we have used the following definitions:

$$a = ((C_1 + C_{coil})C_2 + C_1 C_{coil})L_1 L_2, \tag{5.11}$$

$$b = (C_1 + C_{coil})L_1 + (C_1 + C_2)L_2. \tag{5.12}$$

Equations (5.10) are then used to find the desired capacitor values as a function of the chosen operating ^{129}Xe frequency and the frequencies' ratio: hence $C_i = C_i(\omega_{Xe}^{Set}, \gamma_{HX})$, with $i = 1, 2$. Note that there is some flexibility for the choice of ω_{Xe}^{Set}, since the magnetic field can be adjusted so that $B_0 = \omega_{Xe}^{Set}/\gamma_{Xe}$, but there is no tunability of the frequencies' ratio, which is given by nature.

Once the optimal values of C_1 and C_2 are determined, the capacitors are soldered to the main circuit board, which is then screwed on the top of the resonator coil. The resonator coil and main circuit board are then installed in a temperature stabilized container located inside a three layer μ-metal shield which prevents the resonator coil from picking up ambient magnetic field. The maser oven is put inside the shields in the position and at the temperature at which maser operation is expected. The signals from the resonant circuit and the pick-up coil reach the junction box through homemade, rigid triax conductors, as Fig. 5-26 shows. Installation of the pick-up coils in their final shielding environment is necessary because the shields modify significantly the free space inductance of the coil measured in the last section. Similarly, changes in pick-up coil temperature affect its resistance and probably also its geometry.

In order to fine tune the resonator when all components are in situ the capacitor C_2 installed on the main circuit board is purposefully chosen approximately 2 nF below its theoretical optimal value. C_2 can be subsequently increased by soldering one or more capacitors C_{2+} in parallel on the junction box circuit. However, since

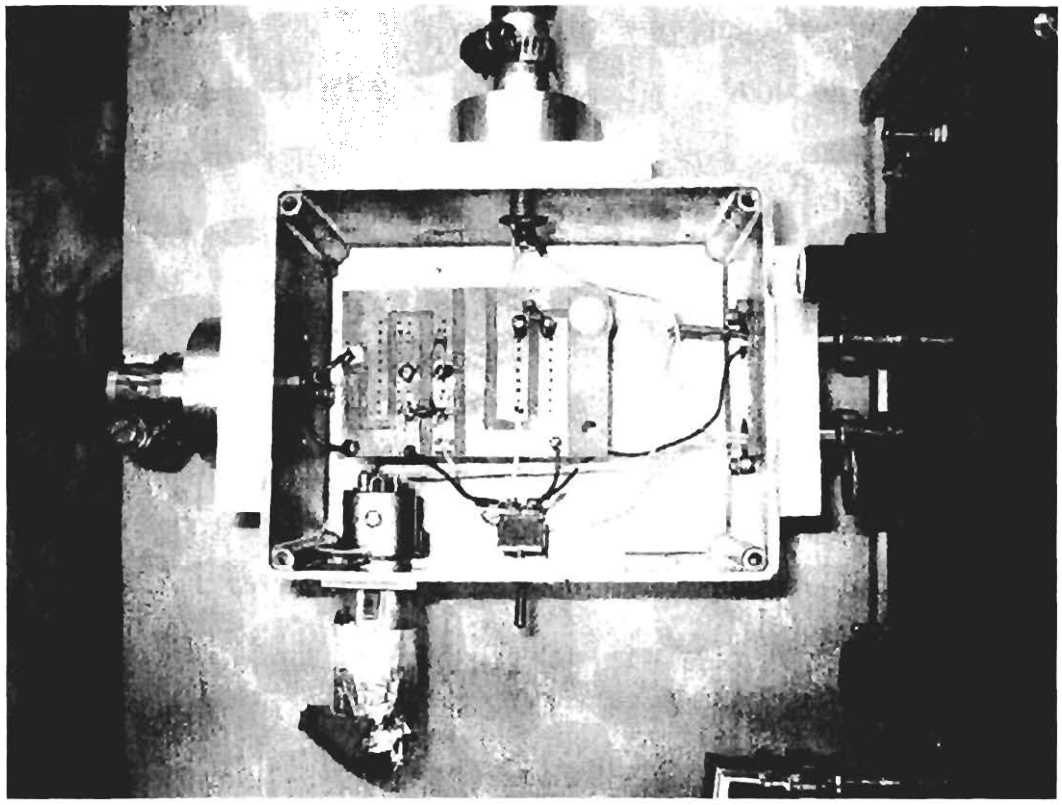

Figure 5-26: Top view of the junction box with lid temporarily removed. Pick-up coil and external resonant circuit are connected to each other on the board carrying the capacitors C_{2+} and C_3. The signals reach the box through long, rigid, tirax cables. The maser signal is amplified by a low-noise preamplifier, visible on the right-hand side.

the box is not ovenized, C_{2+} should be as small as possible. The next section explains how we select the right value for C_{2+}.

Fine-Tuning

Fine-tuning of the dual resonant circuit is an iterative process which consists of measuring the two resonant frequencies, selecting a capacitor value C_{2+}, then measuring again the resonant frequencies, modifying further C_{2+}, and so on. Thanks to the careful characterization of the coils outlined in Sect. 5.5.1, fine-tuning requires

typically only one or two iterative steps.

To measure the resonant frequencies the plug that shorts S_2 (see Fig. 5-24) is removed and the short is replaced with a small resistor, r $\approx 1\ \Omega$. The voltage across this resistor, V_r, is monitored with a lock-in amplifier while the resonant circuit is inductively excited with the help of a small coil permanently installed in proximity of the pick-up coil, driven by a function generator with constant voltage V_{Drive}, but varying frequency, ω. Since the oscillating voltage induced in the resonant circuit is proportional to ωV_{Drive}, $V_r(\omega) = rI \propto r|\omega/(R_2 + r + i\omega L_2 + Z_{Res})|$. For $r \ll R_2$ this expression is exactly proportional to $\rho_c(\omega)$ in Eq. (5.9). Hence, this procedure enables us to measure $\rho_c(\omega)$,[25] apart from an overall constant which can be easily found.[26] A suboptimal C_2 leads to an observed ratio $\omega_{He}^{Obs}/\omega_{Xe}^{Obs} > \gamma_{HX}$. A simple way to find the optimal value of C_{2+} is to develop numerically the ratio of the resonant frequencies given in Eq. (5.10) to second order

$$\frac{\omega_{He}(C_1, C_2 + C_{2+})}{\omega_{Xe}(C_1, C_2 + C_{2+})} = \frac{\omega_{He}(C_1, C_2)}{\omega_{Xe}(C_1, C_2)} + \kappa_1(C_1, C_2)\ C_{2+} + \kappa_2(C_1, C_2)\ C_{2+}^2 \qquad (5.13)$$

and then solve the quadratic equation

$$\frac{\omega_{He}^{Obs}}{\omega_{Xe}^{Obs}} + \kappa_1(C_1, C_2)\ C_{2+} + \kappa_2(C_1, C_2)\ C_{2+}^2 = \gamma_{HX} \qquad (5.14)$$

for C_{2+}. After soldering a capacitor with this value on the junction box circuit board, the ratio of the resonant frequencies is measured again and Eq. (5.14) is employed once more to find a further correction. This iterative process stops when the uncertainty on $\omega_{He}^{Obs}/\omega_{Xe}^{Obs}$ is on the same order of magnitude of the difference

[25]Note that $\rho_c(\omega)$ cannot be directly measured, since measuring the voltage across the pick-up coil does not simply give the voltage across the inductance L_2. It rather gives the voltage across L_2, R_2 and the induced drive voltage, all connected in series.

[26]The asymptotic value of $V_r(\omega)$ for high frequencies corresponds to $\rho_c = 1$.

between this ratio and γ_{HX}. Typically with one or two iterations we achieve the desired precision of a few parts in a thousand.

5.5.3 Cabling and Grounding

The $^{129}Xe/^{3}He$ maser cabling and grounding schemes follow standard principles discussed in the literature [82]. Electronic instruments used in the $^{129}Xe/^{3}He$ maser experiment are powered by a 110 VAC Ferrups Uninterruptable Power Supply (UPS) to whose ground the equipment racks are also connected. All maser signals are measured differentially and are carried by homemade rigid triax consisting of a low capacitance, semi-rigid coaxial cable, housed inside 5/8" inner diameter hollow copper tubing, which provides electrical shielding. Teflon tubing is used to insulate the coaxial cable from the copper tubing.

The signal from the the maser pick-up coil reaches a homemade aluminum junction box located just outside of the $^{129}Xe/^{3}He$ maser's magnetic shields. The junction box (shown in Figure 5-26) houses the tuning capacitors, C_{2+} and C_3. The A and B differential inputs on a low-noise voltage preamplifier[27] mate directly to BNC bulkhead fittings on the junction box, while the cables from the external resonator and pick-up coil are attached to the junction box via standard bulkhead SMA fittings. The magnetic shields housing the $^{129}Xe/^{3}He$ maser oven and solenoid are connected to signal ground, as are the junction box case and the shielding on all signal-carrying cables including the copper tubing, and the resonator shields.

[27]Ithaco 1201 Low Noise Voltage Preamplifier.

5.5.4 Signal Processing and Data Storage

The detected maser signals are read as sinusoidally varying voltages across the capacitor $C_2 + C_{2+}$. Typical raw signal levels are 2-10 μV. The signals are buffered and pre-processed by the low-noise voltage preamplifier. The amplifier is typically set with a wide frequency passband (300 Hz - 10 kHz) and a gain of 5,000.

The amplified signals are sent to three separate SRS digital lock-in amplifiers. An SRS-830 lock-in serves as a prefilter and phase-sensitive detector for the magnetic field phase-lock loop (Sect. 5.4.3). Two SRS-850 lock-ins monitor and record the phase and amplitude of the ^{129}Xe and ^{3}He masers. The data are typically sampled at 1/2 Hz, as triggered by an ultra-stable signal derived from a reference hydrogen maser. The SRS-850 digital low-pass filters are set with bandwidth equal to 78 mHz and 24 dB/octave roll-off. All timebase and reference signals used in the ^{129}Xe/^{3}He maser experiment are derived from the same hydrogen maser clock, thus eliminating concerns about unstable phase and frequency differences between the reference oscillators. Finally, data stored in the lock-in buffers are continuously downloaded via a GPIB interface to a computer for analysis and archiving.

Chapter 6

Current System Performance

This final chapter provides an overview of the system's current status. We report here the operational details of the temperature control system and the laser stabilization schemes, and we assess their performance. We describe the methods used for measuring the primary parameters of the $^{129}Xe/^{3}He$ maser, such as polarization lifetimes, decoherence times, and radiation damping times, and we compare our observations with the predictions of our modified Bloch theory. We then introduce a new topic: a study of the effects of peripheral pick-up coil fields on the maser frequency. We also show preliminary experimental tests on co-magnetometry. Finally, we present an assessment of maser frequency stability and the maser's current sensitivity to Lorentz invariance violation.

6.1 Performance of Temperature Control System

We previously discussed the importance of temperature control in our experiment (Sect. 4.2) and the design of the temperature locking schemes of the most delicate components: the pump and maser bulbs (Sect. 5.1.1). In this section we report on

the details of the temperature locks and the temperature stability achieved to date.

Table 6.1 shows the range of operational temperatures for each lock and typical root mean squares (RMS) of the locked signals. Maser and pump bulbs are temperature stabilized using indirect heating and the double-lock depicted in Fig. 5-9. Typical settings for the lock-in amplifiers and PID controllers used for the temperature locks are given in Tab. 6.2 and Tab. 6.3, respectively.

Since long-term stability is crucial in our experiment, we have extensively studied the temperature stability of our locks and of the environment. Figure 6-1 shows the power spectrum (introduced in Sect. 2.4) of the ambient temperature in our laboratory for ten consecutive days. The air-conditioning cycle is responsible for the most prominent peak corresponding to a period of approximately 500 s. $1/f$ noise is also present and is responsible for the long term instability shown in Fig. 6-2. The typical ambient temperature stability of approximately 0.1° C in a day is achieved by using an air-conditioning apparatus dedicated to the ^{129}Xe/^{3}He maser room and scrupulously making use of a double-door air-lock for accessing the room.

The low temperature coefficient of the resistors used in the bridges (see Fig. 5-8) should make the measurements fairly insensitive to ambient temperature fluctuations and drifts. To assess the bridges' stability we temporarily replaced the RTDs with temperature stable resistors of the same kind used in the bridges and we monitored their resistance for ten days. Figure 6-3 shows the power spectrum of the measured resistance for one of the bridges, given in terms of the equivalent temperature corresponding to the measured resistance. The power spectrum is very flat and the 500 s period oscillations of the ambient temperature do not appear to affect the measurement. Figure 6-4 shows that the bridges' intrinsic stability is adequate to measure relative temperature changes of approximately 1 mK in a day, which is

Description	Temperature Range (° C)	Typical RMS (mK)
Maser Air	36-44	18
Maser Block	43-49	5
Pump Air	135-180	60
Pump Block	115-140	6
Resonator Air	30-32	9

Table 6.1: Typical range of operational temperatures for various components and root mean squares (RMS) of the locked temperatures. The averaging time for each data point is approximately 4 s.

Description	FS (mV)	TC (s)	ν_{ref} (Hz)	Airflow (SLM)
Maser Air	20	1	509	60
Maser Block	10	1	449	-
Pump Air	10	0.3	331	80
Pump Block	1	1	389	-
Resonator Air	20	1	569	40

Table 6.2: Settings of the lock-in amplifiers driving and sensing the bridge circuits depicted in Fig. 5-8 and used for temperature control of maser cell and resonator. All filters slopes are set to 24 dB/Oct. We report full scale values (FS), time constants (TC), the prime numbers chosen as reference frequencies (ν_{ref}) and the airflow rate used for each lock in standard liters per minute (SLM).

Description	Gain	T_{Int} (s)	T_{Diff} (s)	T_{HF} (s)	R_{Out} (kΩ)
Maser Air	1	100	30	0.03	0
Maser Block	3	300	0	0	1
Pump Air	0.3	22	10.01	0.03	0.062
Pump Block	1	300	0	0	1
Resonator	1	220	100	0	0.062

Table 6.3: Settings of the PID controllers used for temperature control of maser cell and resonator. T_{HF} is the high frequency cutoff and R_{Out} is the output resistance of the voltage controller.

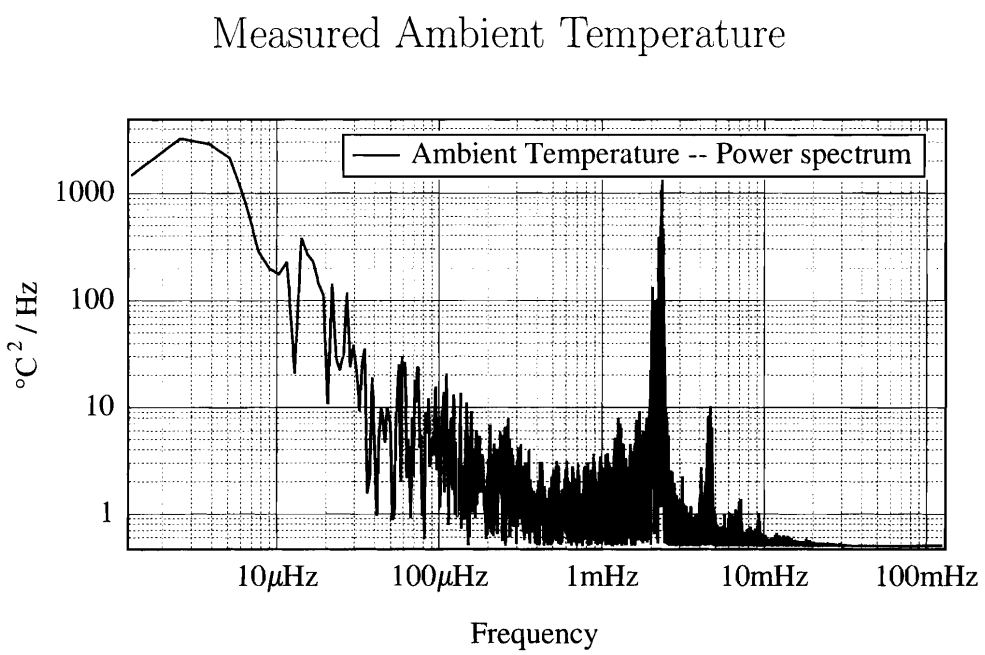

Figure 6-1: Power spectrum of the ambient temperature measured in our laboratory for ten consecutive days. The noise corresponding to the 500 s air-conditioning cycle makes up approximately 40% of the temperature's noise. The first few harmonics of this signal are visible. $1/f$ noise is also present and is responsible for the long term instability illustrated in Fig. 6-2.

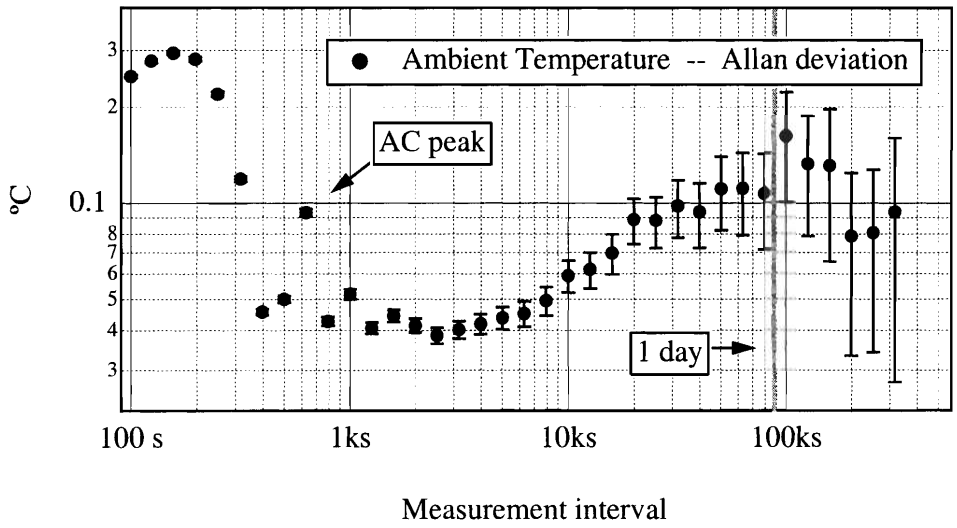

Figure 6-2: Allan deviation of the ambient temperature for a data set 10 days long.

our sensitivity goal.[1]

Finally, in order to assess the temperature stability of the gas inside the maser and pump bulb we prepared a mock cell containing an RTD in each bulb. The temperature stability of these free-running thermometers is shown in Figs. 6-5 and 6-6. The pump bulb stability is slightly worse than the maser bulb stability, probably because the pump bulb is kept at higher temperature (114° C instead of 50° C for the maser bulb). The overall temperature stability is better then 1 mK in a day. These measurements do not take into account the heat load of the laser light used for optical pumping. Unstable laser power will result in unstable gas temperatures. This is of particular concern when we make use of the broad-band laser source, whose power ($\approx$ 10 W) provides significant heating. In the next section we deal with the stabilization of the total laser power, which should help stabilize the heat deposited on the pump bulb. Presently we believe that heating by the laser is the main source of cell temperature instability.

6.2 Performance of Optical Pumping System

In Sect. 5.3 we discussed the characteristics and stabilization schemes used for the Toptica TA 100 narrow-band laser and for the broad-band Coherent Laser Diode Array (LDA). In Tab. 6.4 we report the typical operating range of each parameter and the root mean squares of the locked signals. Tables 6.5 and 6.6 list the typical settings of lock-in amplifiers and PID controllers. Figures 6-7 through 6-10 present

[1]Both our modified Bloch theory in Sect. 4.3.4 and the data presented later in this chapter (Sect. 6.6.3) show that a 1 mK change in the pump bulb temperature leads to a fractional change in maser amplitudes of a few parts in 10^5. Assuming a worst case scenario in which the same fractional variation applies to the longitudinal magnetizations in the maser bulb (estimated to be at most few μG), we find that the shifts induced in the masers are on the order of few tens of nHz in a day, i.e., compatible with our stability goals. In Sect. 6.8.3 we analyze the correlations between maser amplitudes and frequencies in more detail.

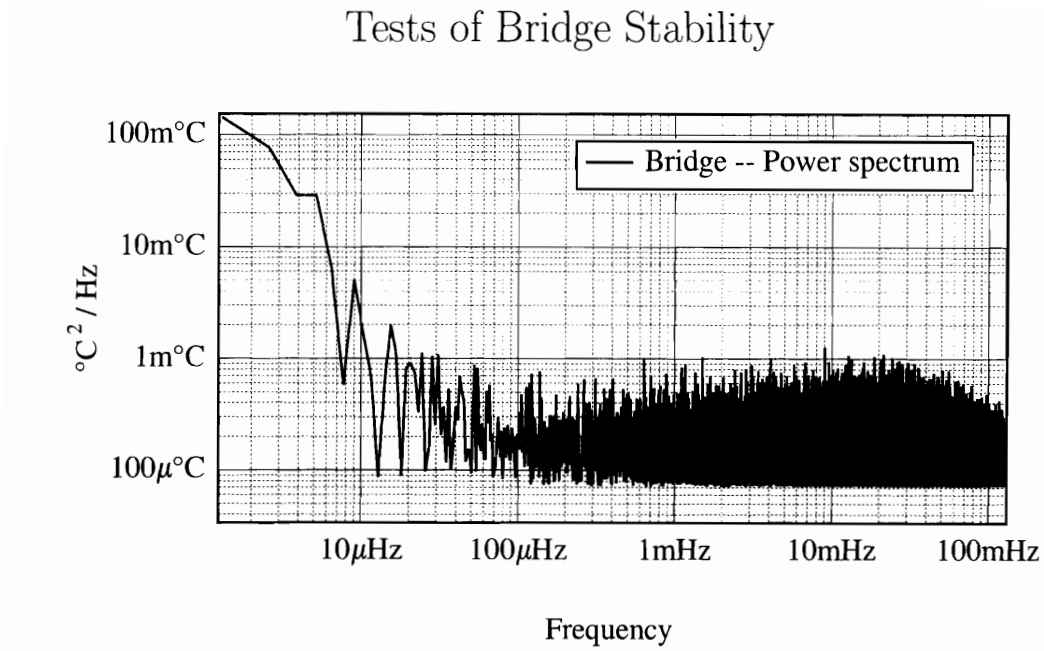

Figure 6-3: Power spectrum of a resistance measurement carried out monitoring a stable resistor with one of the balanced bridge circuits depicted in Fig. 5-8 for about 10 days. The result of this measurement is given in terms of the equivalent temperature uncertainty that would correspond to the resistance uncertainty. Note that the density of points at higher frequency is due to the log scale of the $\hat{x}$ axis.

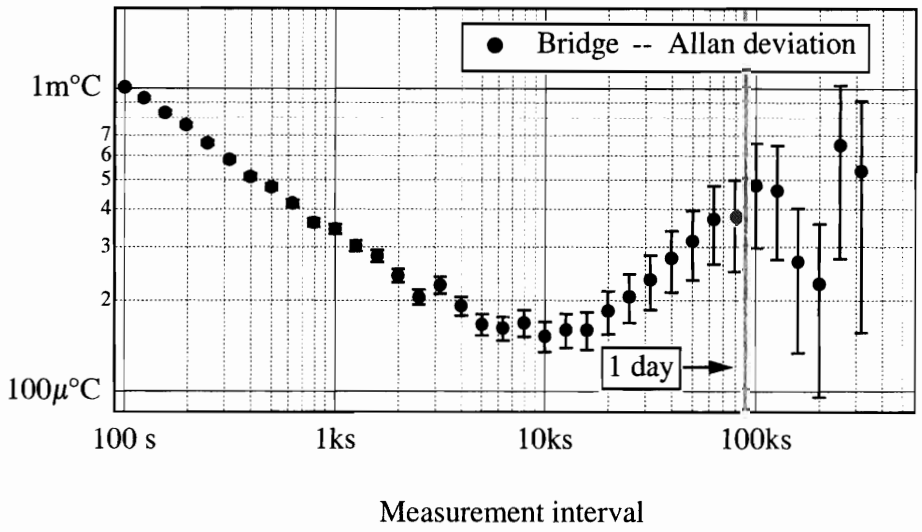

Figure 6-4: Allan deviation of a resistance measurement carried out monitoring a stable resistor with one of the balanced bridge circuits depicted in Fig. 5-8 for about 10 days. The result of this measurement is given in terms of the equivalent temperature uncertainty that would correspond to the resistance uncertainty.

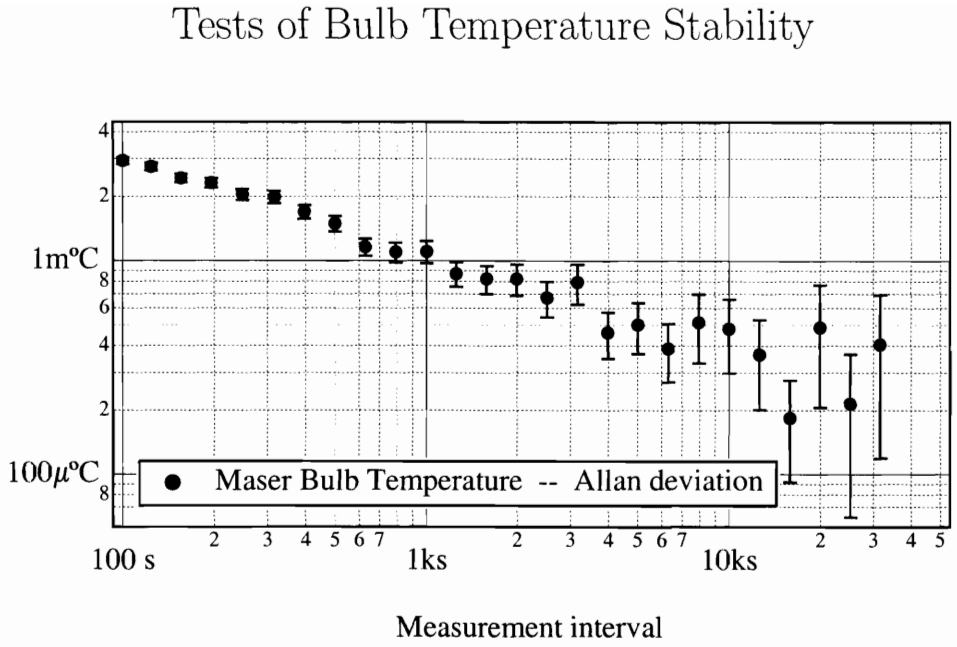

Figure 6-5: Allan deviation of the temperature measured for a day by a thermometer placed in the maser bulb of a mock glass cell. The bulb temperature was temperature stabilized at approximately 50° C.

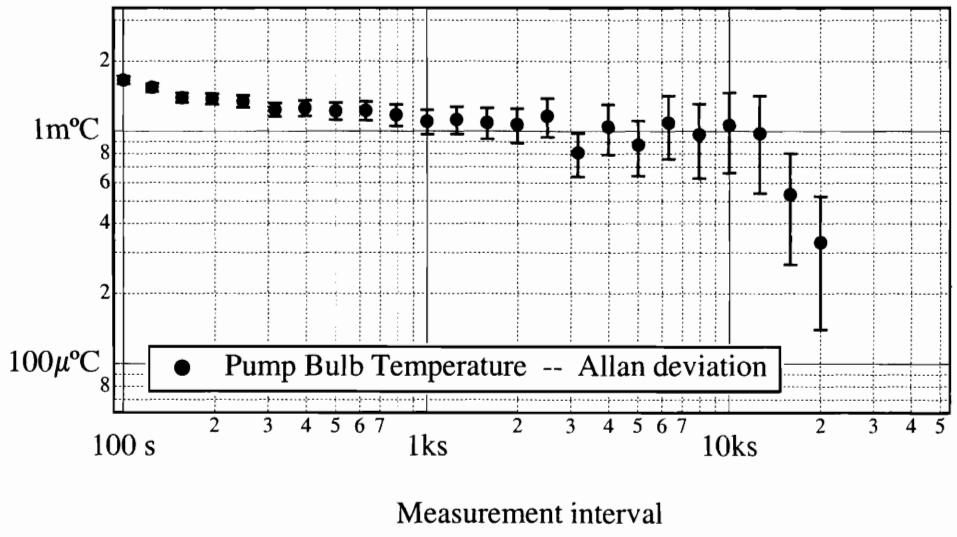

Figure 6-6: Allan deviation of the temperature measured for a day by a thermometer placed in the pump bulb of a mock glass cell. The bulb temperature was temperature stabilized at approximately 114° C.

Description	Operating Range	Typical RMS
Toptica Power	350-280 mW	20 μW
Toptica Frequency	794.7 nm	2 MHz
LDA Power	10 W	1 mW
$V_{M_{Rb}}$	450 μV	0.4 μV

Table 6.4: Typical range of operational parameters for narrow and broad-band lasers now being tested. The averaging time for each data point is approximately 4 s.

Description	FS (mV)	TC (s)	ν_{ref} (Hz)	Slope (dB/oct)
Toptica Power	200	0.3	73	24
Toptica Frequency	2	0.1	30	18
LDA Power	200	0.3	73	18
$V_{M_{Rb}}$	1	3	400	12

Table 6.5: Settings of the lock-in amplifiers used for stabilizing laser power, frequency, and Rb magnetization signal. We report full scale values (FS), time constants (TC), the reference frequencies (ν_{ref}), and slopes of the filters used. Note that various filter slopes are chosen not because of noise rejection requirements, but because they introduce optimal phase shifts in the lock loops.

Description	Gain	T_{Int} (s)	T_{Diff} (s)	T_{HF} (s)	R_{Out} (kΩ)
Toptica Power	0.1	0.1	0	0	10
Toptica Frequency	0.3	0.3	0	0	100
LDA Power	3	1	0.3	0.03	1
$V_{M_{Rb}}$	10	10	3	0.3	100

Table 6.6: Settings of the PID controllers used for stabilizing laser power, frequency, and Rb magnetization signal. T_{HF} is the high frequency cutoff and R_{Out} is the output resistance of the voltage controller.

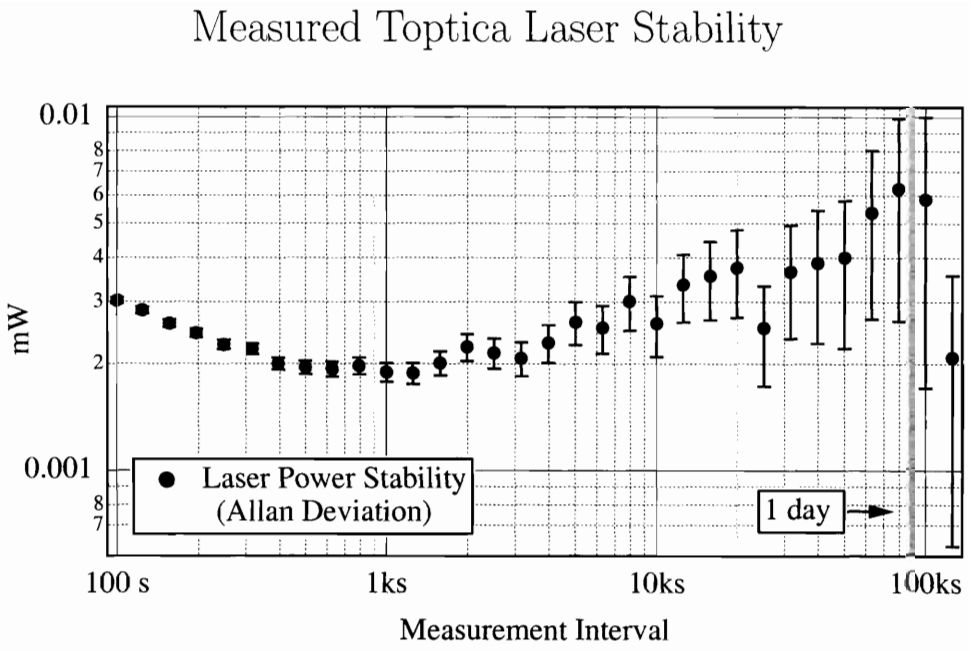

Figure 6-7: Allan deviation of the locked Toptica TA 100 laser power.

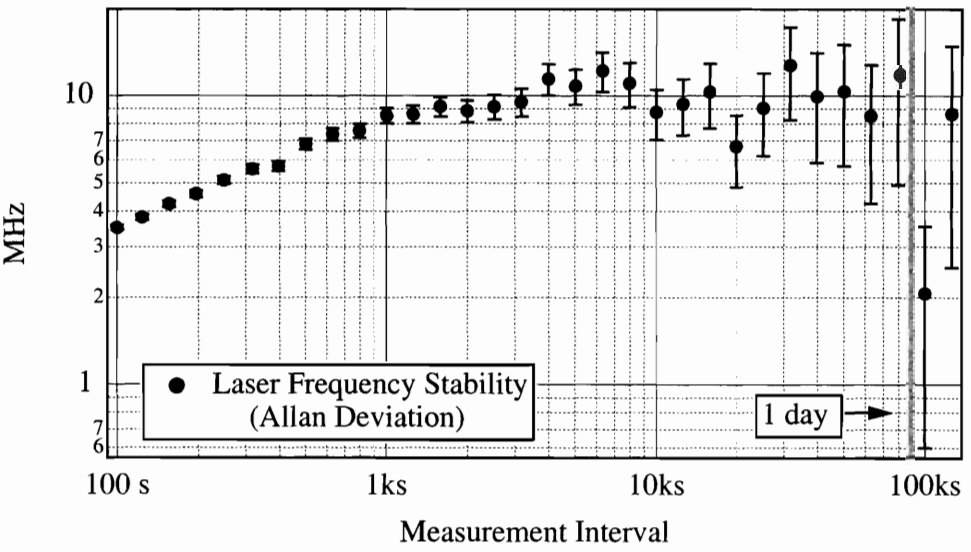

Figure 6-8: Allan deviation of the locked Toptica TA 100 laser frequency.

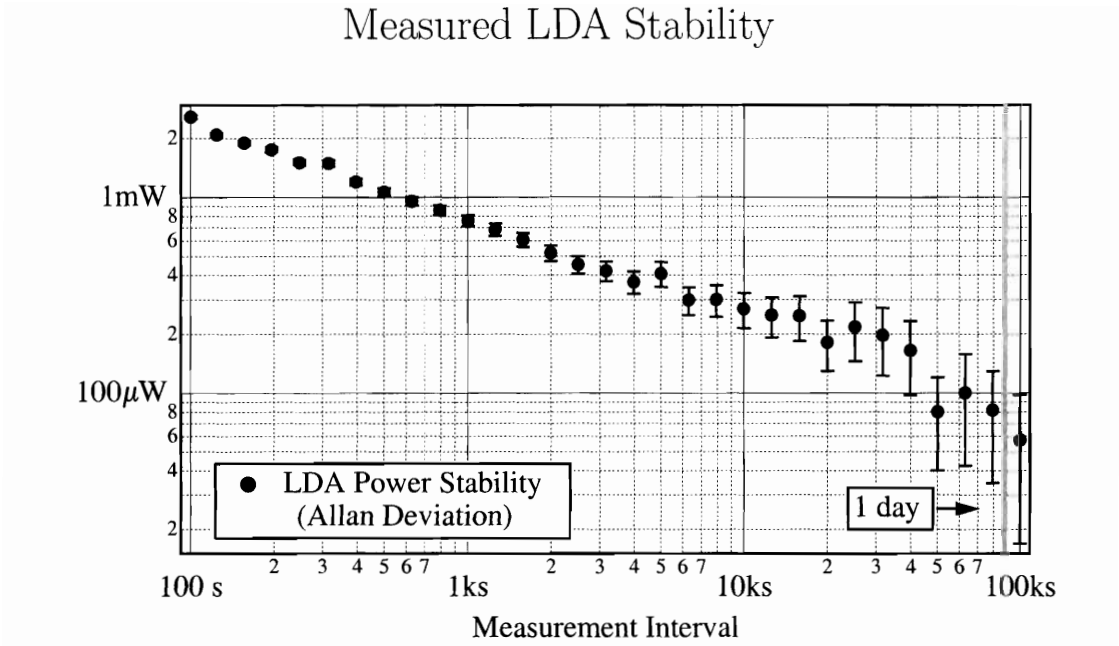

Figure 6-9: Allan deviation of the locked LDA laser power. The average power was 15 W.

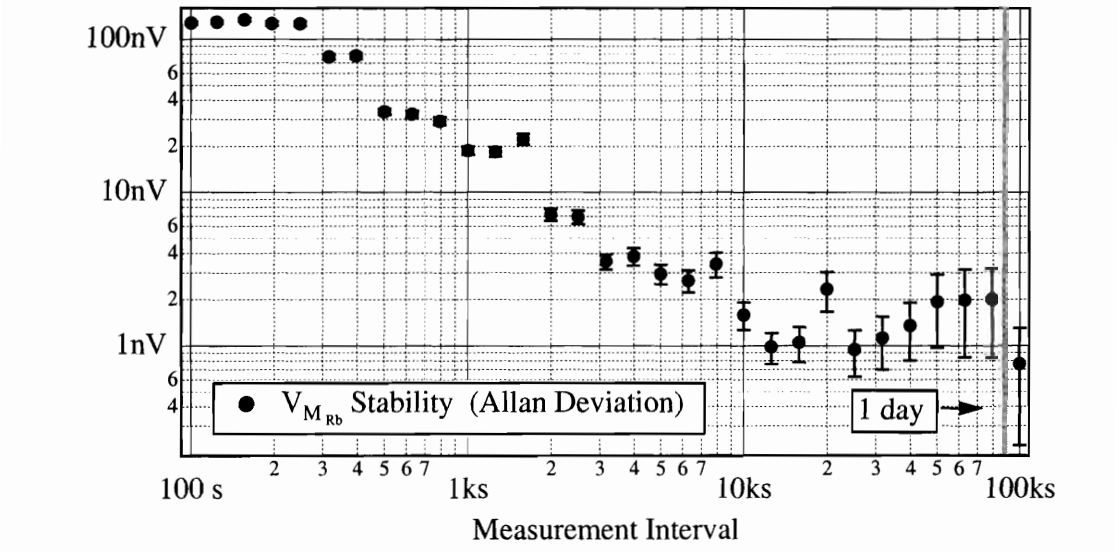

Figure 6-10: Allan deviation of the locked Rb magnetization signal $V_{M_{Rb}}$. The average signal was $\langle V_{M_{Rb}} \rangle \approx 453\,\mu$V.

the stability of the laser powers, as well as the stability of the laser frequency for the Toptica laser and the stability of the locked Rb magnetization signal used to control the LDA.

6.3 Cell Details

Experimental work has focused on making and testing maser cells. Our most recent cell making procedure, described in Sect. 5.2, is the result of trial and error process which lasted several months. Table 6.7 reports the gas fill pressures for 5 of the cells made to date. Initially we used cells like those in Fig. 5-10 but with transfer tube ID of approximately 2 mm instead of 4 mm. The names of the first-generation cells begin with the letter A, while the names of the cells with geometry like that in Fig. 5-10 begin with by the letter B. A-type cells were optimized for very low gas pressures. A narrow transfer tube diameter was used to increase the ^{3}He interaction time with the cavity at low pressures. However, the narrow tubing used for the transfer tube had very thick walls (the only standard tubing available had a 9 mm OD), which created a strong thermal connection between maser and pump bulbs and prevented proper cooling of the maser bulb. Also, the amount of Rb traditionally deposited in the pump bulb (a thin coating in part of the pump bulb) turned out to be insufficient for the low pressure cells as Rb was more rapidly chased into the maser bulb by the temperature gradient. We solved this problem by depositing macroscopic amounts of Rb (1 or 2 droplets) in the cells. Table 6.7 also lists other cell characteristics, whose definitions and measurement techniques will be discussed in the next sections.

Cell name	A_1	B_1	B_2	B_3	B_4	Units
$\mathcal{P}_{He,Fill}$	240	600	800	1600	1400	Torr
$\mathcal{P}_{Xe,Fill}$	13	30	40	40	25	Torr
$\mathcal{P}_{N_2,Fill}$	35	85	85	85	85	Torr
^{3}He T_1	13	1.5	-	4	-	h
^{129}Xe T_L	300	-	-	200 (370)	-	s
^{3}He T_2^*	61	100	-	130	-	s
^{129}Xe T_2^*	120	200	-	185	-	s
Pol. Center $\langle y \rangle$	-	16	-	200	-	μm
Rb amount	coating	droplet	droplet	droplet	droplet	-
Choke coils	no	no	no	yes	-	-
Pump solenoid	no	yes	no	yes	-	-

Table 6.7: Characteristics of the maser cells made since October 2004. The fill pressures refer to an ambient temperature of 21° C. The polarization and coherence lifetimes were measured at $T_M = 50°$ C and $T_P = 114°$ C except for the value within brackets, which was measured for $T_P = 90°$ C.

6.4 Time Evolution of Noble Gas Longitudinal Polarization Below Threshold

The time evolution of the longitudinal polarization in the maser bulb, P_z, when the resonator is disengaged (i.e., no feed-back) and the laser is turned off (at $t = 0$) is monitored as follows. A transverse Rabi field is applied to the maser bulb with the pick-up coil, thus creating a transverse noble gas magnetization that undergoes free induction decay (FID) [83]. Further tips are applied to the atoms at fixed time intervals ($\sim 2,000$ s for ^{3}He, 60 s for ^{129}Xe) and the initial signal amplitude, which is proportional to P_z, is recorded. As Fig. 6-11 shows, these initial amplitudes decrease exponentially over time. Each tip is of the same size and sufficiently small ($\theta_{tip} \leq 5°$) that pulsing does not contribute significantly to the rate of longitudinal polarization depletion. Theoretically, the time evolution of $P_z(t)$ is obtained from the modified Bloch Eqs. (4.39) and (4.40), assuming $S = \omega_R = 0$. For simplicity, here we find approximate expressions for the characteristic relaxation rates, neglecting, in the

case of ^{129}Xe, the relaxation in the transfer tube and using a single bulb escape rate $G_P \sim G_M \sim G$. Both approximations are quite good and do not alter the two most important features of the model: (i) the transfer of polarization between the two bulbs; and (ii) the different relaxation rates in the two bulbs, due to spin-exchange with unpolarized Rb in the hot pump bulb. The equations of motion for the longitudinal polarizations are:

$$\begin{pmatrix} \dot{P}_P(t) \\ \dot{P}_z(t) \end{pmatrix} = \begin{pmatrix} -\frac{1}{T_1} - \gamma_{se} - G & G \\ G & -\frac{1}{T_1} - G \end{pmatrix} \begin{pmatrix} P_P(t) \\ P_z(t) \end{pmatrix}. \tag{6.1}$$

We assume that initially the spins are prepared in their equilibrium polarizations $P_{P,0}$ and $P_{z,0}$ given by Eqs. (4.45) and (4.46) respectively. The time evolution of the polarizations when the light is turned off evolves through a combination of two characteristic rates,

$$\frac{1}{T_S} \approx \left(\frac{1}{T_1} + \frac{\gamma_{se}}{2} + G + \sqrt{G^2 + \frac{\gamma_{se}^2}{4}} \right), \tag{6.2}$$

$$\frac{1}{T_L} \approx \left(\frac{1}{T_1} + \frac{\gamma_{se}}{2} + G - \sqrt{G^2 + \frac{\gamma_{se}^2}{4}} \right), \tag{6.3}$$

which are the eigenvalues of the 2×2 matrix in Eq. (6.1). We have seen in Sect. 4.3 that ^{3}He diffuses quickly between the two bulbs compared to its intrinsic relaxation and spin-exchange rates, which are both very small (i.e., $G \gg \gamma_{se}, 1/T_1$). Hence, for ^{3}He we have $T_S \approx 1/2G$ and $T_L \approx T_1$. This means that we can confidently identify the long decay time T_L of the longitudinal polarization (see Fig. 6-11) with the ^{3}He intrinsic lifetime T_1. The observed ^{3}He T_1 times are on the order of a few hours and vary greatly from cell to cell. The first cell we made, A_1, had a ^{3}He $T_1 \approx 13$ h, but more recently we have obtained much shorter lifetimes (see Tab. 6.7) and we

suspect that a surface contaminant may be responsible for this effect (see below).

For ^{129}Xe the approximations above are not valid. In fact, using the values given in Tabs. 4.3 and 4.4, we obtain that the "short" and the "long" characteristic times are on the same order of magnitude: $T_S \approx 105$ s and $T_L \approx 340$ s. In particular, the longest decay time $T_L \neq T_1 = 500$ s. T_L was measured for ^{129}Xe, and strongly depends on the temperature of the pump bulb, since it depends on γ_{se} as Eq. (6.3) indicates. This was verified in cell B_3, for which we measured $T_L \approx 200$ s for $T_P = 114°$ C and $T_L \approx 370$ s for $T_P = 90°$ C.

In the lower temperature measurement γ_{se} should be negligible, so that probably $T_1 \approx T_L = 370$ s, which is somewhat lower than expected. If we assume that wall relaxation dominates and that we can use Eq. (4.30) even for the double-bulb cell (after all the 2 bulbs have roughly the same size), we obtain a wall relaxation coefficient $\kappa = r_0/3\,T_{1,Wall} = 9 \times 10^{-4}$ cm/s, which is about three times larger than the value of $\kappa = 2.8 \times 10^{-4}$ cm/s quoted in Ref. [37]. This may indicate that wall relaxation for cell B_3 is stronger than in the previous maser cells due to a surface contaminant (which relaxes also ^{3}He), or to an ineffective coating.

Comparing the high and low temperature measurement above we can also estimate γ_{se} for ^{129}Xe. Again, we assume that $T_1 \approx T_L = 370$ and we solve the Eq. (6.3) for γ_{se}, using $T_L = 200$ and the theoretical estimate for $G = 1/310$ s^{-1}. We obtain $\gamma_{se} \approx 0.01$ s^{-1}, which is about 2.5 times larger than the theoretical prediction at $T_P = 114°$ C using the model introduced in Sect. 4.3. Given the uncertainties involved in the theoretical estimates (spin exchange coefficients, diffusion coefficients from tabulated values, pump bulb temperature, etc.) the observed disagreement between theory and experiment is not surprising.

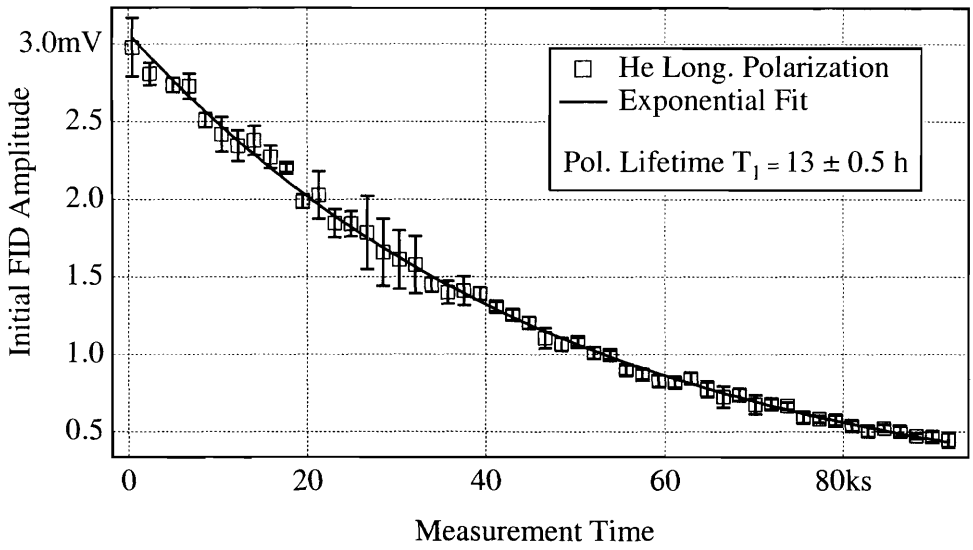

Figure 6-11: Measurement of ^{3}He longitudinal polarization lifetime, T_1, in the maser cell A_1 obtained by applying small tips to the ^{3}He polarization ensemble at fixed time intervals . Each tip is of the same size and sufficiently small that pulsing does not contribute significantly to the rate of longitudinal polarization depletion. The exponential time constant of the polarization decay is the longitudinal polarization lifetime.

6.5 Measurement of Noble Gas Decoherence Times Below Threshold

In the last section we noted that applying a transverse Rabi field to the maser bulb creates a transverse noble gas magnetization that undergoes free induction decay [83]. Figures 6-12 and 6-13 show typical FID ringdowns for ^{3}He and ^{129}Xe after application of brief resonant Rabi pulses.[2] Curve-fitting the signal amplitude with a function of the form

$$R_{ng}(t) = c_0 + c_1 \cos(c_2\, t + c_3)\, e^{-c_4\, t}, \tag{6.4}$$

[2]As we saw in Sect. 5.5, Rabi pulses can be applied to the atoms by inductively driving the main circuit (after disengaging the resonator) with a secondary circuit connected to a programmable function generator.

yields the noble gas ensemble effective decoherence time $T_2^* = 1/c_4$, defined in Eqs. (4.44) and (4.52) for ^{3}He and ^{129}Xe respectively, and $c_2/2\pi$ yields the beat frequency, ν_b.

A series of such measurements are used to trim the gradient coils (described in Sect. 5.4.2) with the purpose of achieving the best magnetic field homogeneity. Figure 6-14, for instance, shows the rate of de-coherence, c_4, as the current in the dB_z/dz gradient coil is varied. The parabolic shape of the curve is consistent with the quadratic dependence on magnetic gradients given in Eq. (2.9). The gradient coil current maximizing T_2^* is chosen and the procedure is repeated for the dB_z/dx and dB_z/dy coils.

We recently measured ^{129}Xe and ^{3}He decoherence times for three different B_0 intensities in cell B_3 after proper trimming of the gradient coils. Figure 6-15 shows only a weak dependence on the non-linear field inhomogeneities created by the main solenoid.[3] Other significant factors limiting the decoherence times are bulb escape and wall interaction, as we saw in Sects. 2.2.2 and 4.3.4. Bulb escape probably accounts for the short effective decoherence times observed in the lowest pressure cell A_1 (see Tab. 6.7). In the past, a sizable increase of the decoherence times was observed after installing the choke coils [34], but a systematic study of this effect has not been carried out in the new apparatus.

6.6 Preliminary Tests of Modified Bloch Theory

Our current understanding of the ^{129}Xe/^{3}He maser theory was amply discussed in Sects. 2.3 and 4.3.4. At present, only a small portion of the predictions made by that theory have been tested. The reason is threefold. First, the new maser has

[3] These inhomogeneities should increase with the main field and cannot be compensated using the shim coils' linear corrections.

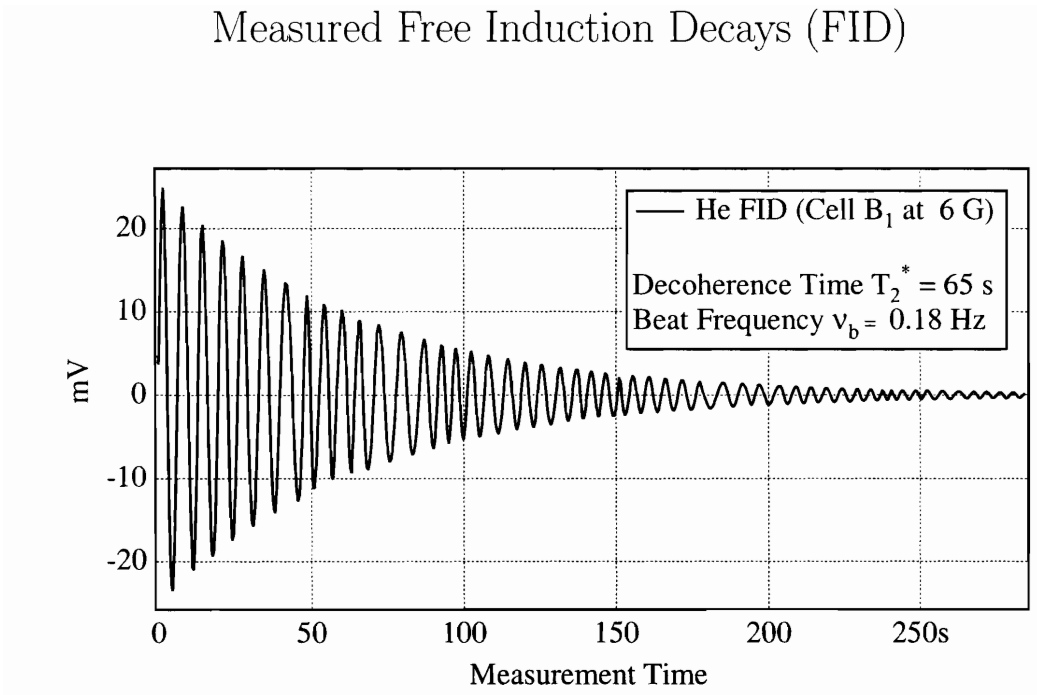

Figure 6-12: Typical ^{3}He free induction decay (FID) ring-down. The exponential decay time is identified with the decoherence time T_2^* introduced in Sect. 4.3.4.

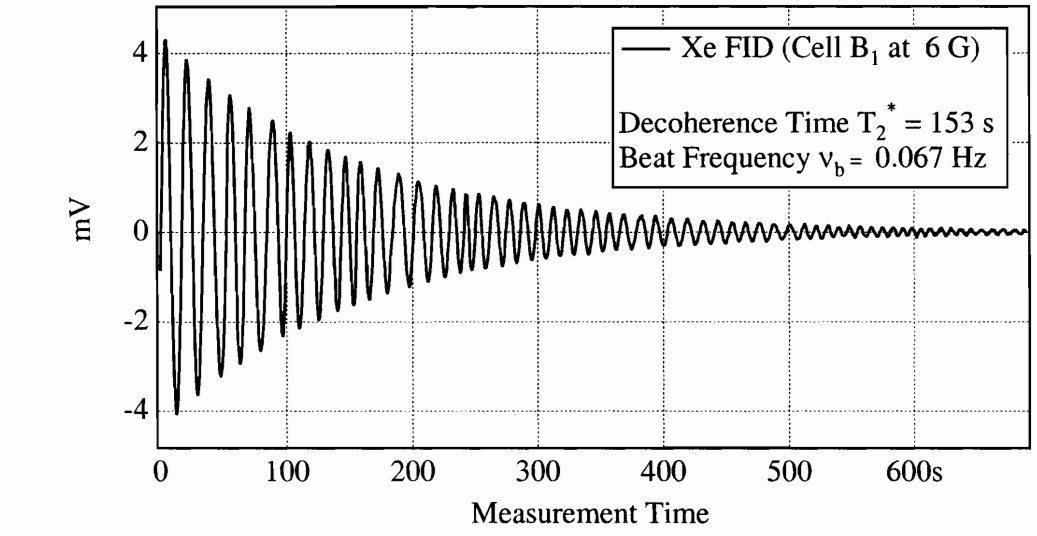

Figure 6-13: Typical ^{129}Xe free induction decay (FID) ring-down. The exponential decay time is identified with the decoherence time T_2^* introduced in Sect. 4.3.4.

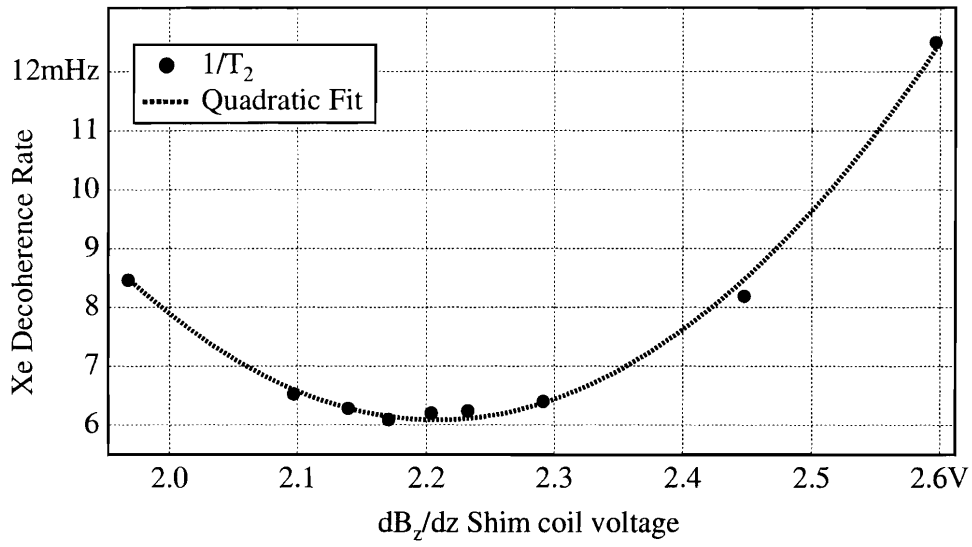

Figure 6-14: Trimming of the dB_z/dz gradient coil aimed at achieving the best field homogeneity. The decoherence rate $1/T_2^*$ is measured for various coil currents, until the current minimizing this rate is found. The parabolic fit is consistent with the quadratic dependence on magnetic gradients given by Eq. (2.9).

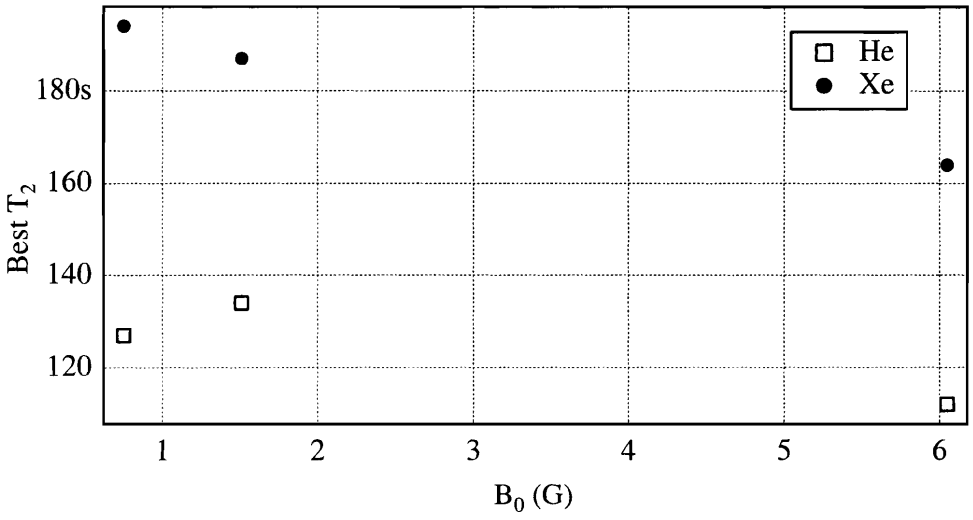

Figure 6-15: Noble gas decoherence times for three different B_0 fields in cell B_3, after careful trimming of the gradient coils.

been fully operational for only few months at the time of this writing. Second, more diagnostic tools would be needed to carry out proper testing.[4] Third, testing the maser theory is very time consuming and presently most of the time on the apparatus is dedicated to optimizing the stability of its many components.

With these considerations in mind we show some preliminary comparisons of experimental results and theoretical predictions. We begin with an observation of the radiation damping times, we continue with the detection of underdamped oscillations in the maser amplitudes, and we conclude with a measurement of the maser amplitudes for various pump bulb temperatures in cells B_1 and B_2.

6.6.1 Measurement of the Radiation Damping Times

In Sect. 2.3.2 we noted that the effective radiation damping time can be directly measured by pumping the atoms in the low energy state and measuring the FID rates, $1/T_{2,On}$ and $1/T_{2,Off}$, of the perpendicular polarization when the resonator is turned on and off. The effective radiation damping time is given by $\tau_{RD} = (1/T_{2,On} - 1/T_{2,Off})^{-1}$.

In Sect. 2.3.1 we defined the radiation damping rate as

$$\frac{1}{\tau_{RD}} = \frac{\hbar\gamma_{ng}^2}{4}\frac{\xi_o^2 Q V_M}{L_{pu}}[ng]P_{z,0}. \tag{6.5}$$

The modified Bloch theory gives specific predictions for $P_{z,0}$ as indicated in Eqs. (4.46) and (4.53).

Since $P_{z,0}$ strongly depends on the pump bulb temperature, T_P, through the

[4]For instance, installing a pick-up coil around the pump bulb would be very helpful. This would allow: (i) measurement of the polarization of ^{129}Xe before transport losses; (ii) optimization of the laser settings for best optical pumping; (iii) measurement of the noble gas decoherence times in the pump bulb; and (iv) accurate measure of the pump bulb temperature by detecting the frequency shifts induced by Rb on the precession frequency of the noble gases.

Measured Free Induction Decays (FID)

Temperatures (° C)		^{3}He times (s)			^{129}Xe times (s)		
T_{Block}	T_P	$T_{2,On}$	$T_{2,Off}$	τ_{RD}	$T_{2,On}$	$T_{2,Off}$	τ_{RD}
124	116	73	175	6.5	41	7	54
111	103	73	169	8.4	34	9.5	42.5
97	89	76	183	13	39	15.7	50

Figure 6-16: For three pump block temperatures we list the estimated pump bulb temperature, T_P, and the measured transverse decoherence times, $1/T_{2,On}$ and $1/T_{2,Off}$, for cell B_1. The effective radiation damping time τ_{RD} is calculated using Eq. (2.40).

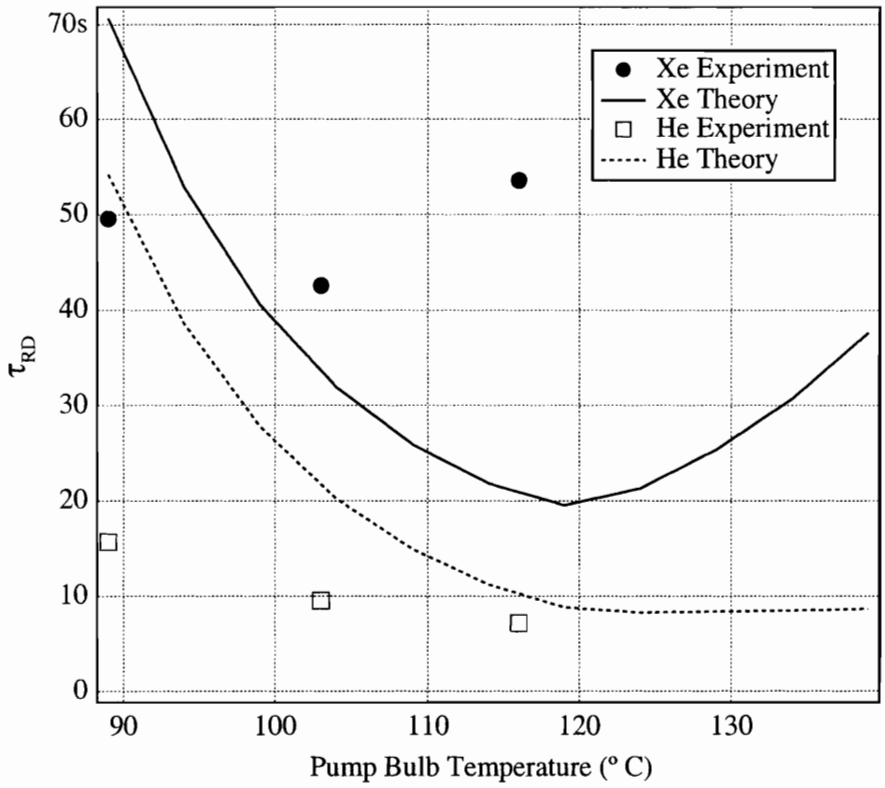

Figure 6-17: Radiation damping times measured in cell B_1 for the two noble gases and theoretical predictions using the set of input parameters given in Tab. 4.3. Above $T_P = 120°$ C the theoretical τ_{RD} increases because the ^{129}Xe flux of polarized atoms in the maser bulb decreases. This is due to the depletion of resonant light in the pump bulb and the consequent Rb depolarization as T_P is increased. The polarized ^{129}Xe flux is further reduced by spin-exchange relaxation with unpolarized Rb in the transfer tube. This relaxation mechanism is not included in our theoretical estimates and may help explain the discrepancy with the experimental data.

Rb density and thus the rate of spin-exchange optical pumping, we have measured τ_{RD} as T_P changes. These measurements are reported in Tab. 6-16 and plotted in Fig. 6-17 where we also show the theoretical predictions for a narrow-band laser with delivered power of approximately 250 mW. Our theoretical predictions are not very satisfactory. Presently we believe that the the main uncertainties limiting the comparison of experiment and theory are: (i) T_P was not directly measured for lack of a temperature sensor on the pump bulb, but was deduced from T_{Block} using a fixed temperature difference[5] of 8° C; (ii) there are great uncertainties in the simulation of spin-exchange optical pumping (see Sects. 2.1 and 4.3.1); and (iii) so far we have not found a convenient way to take into account the ^{129}Xe relaxation due to spin-exchange with unpolarized Rb vapor in the warmest section of the transfer tube. The latter mechanism is likely to be the main source of reduction of the ^{129}Xe flux in the transfer tube, which by reducing $P_{z,0}$ lengthens τ_{RD}, as Eq. (6.5) shows.

6.6.2 Observation of Underdamped Oscillations

In Sect. 2.3.4 we saw that above threshold the maser amplitude may experience underdamped oscillations of frequency $\nu_{Osc} = 1/\pi\sqrt{2T_1\tau_{RD}}$. Using the quantities listed in Tabs. 4.3 and 4.4, we obtain the theoretical frequencies $\nu^{Th}_{Osc,Xe} \approx 2.2$ mHz and $\nu^{Th}_{Osc,He} \approx 0.9$ mHz.

In Figs. 6-18 and 6-19 we show the maser amplitudes observed with cell B_1 in a three day run for which most of the experimental settings were roughly those reported in Tab. 4.3. The underdamped oscillations are not obvious in the noisy maser amplitudes, but their power spectrums in Figs. 6-20 and 6-21 show that small oscillations are present and have roughly the expected frequencies.

[5]This is only a very crude approximation based on a measurement (performed using a mock cell) of the gradient between pump block and pump bulb (see Sect. 6.1).

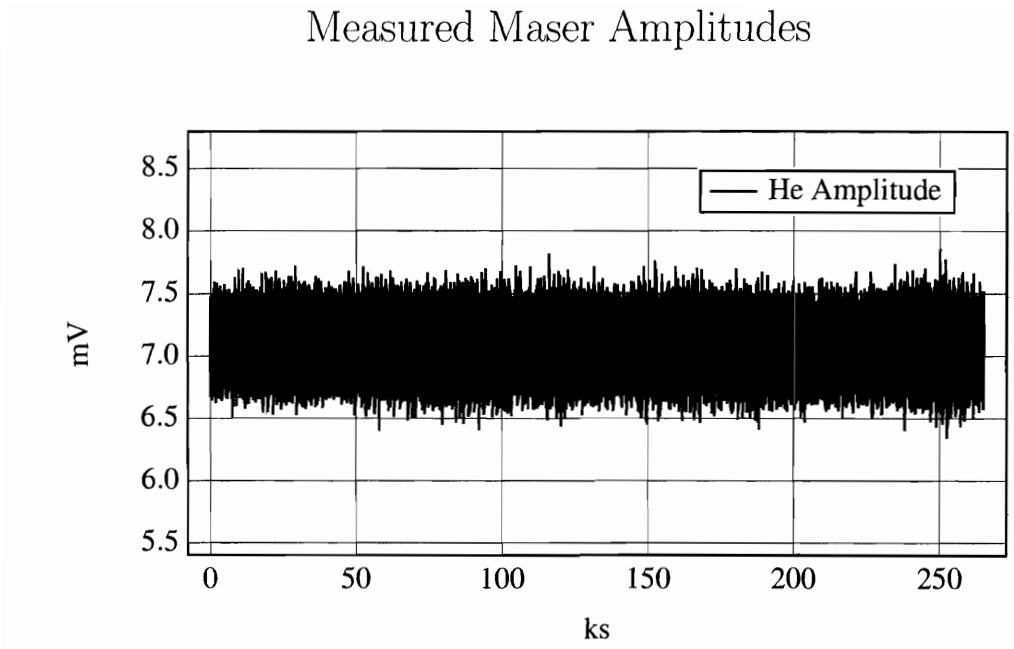

Figure 6-18: ^{3}He maser amplitude in a three day data set collected with cell B_1 and the narrow-band Toptica TA 100 laser. To the best of our knowledge the experimental setup parameters are those given in Tab. 4.3.

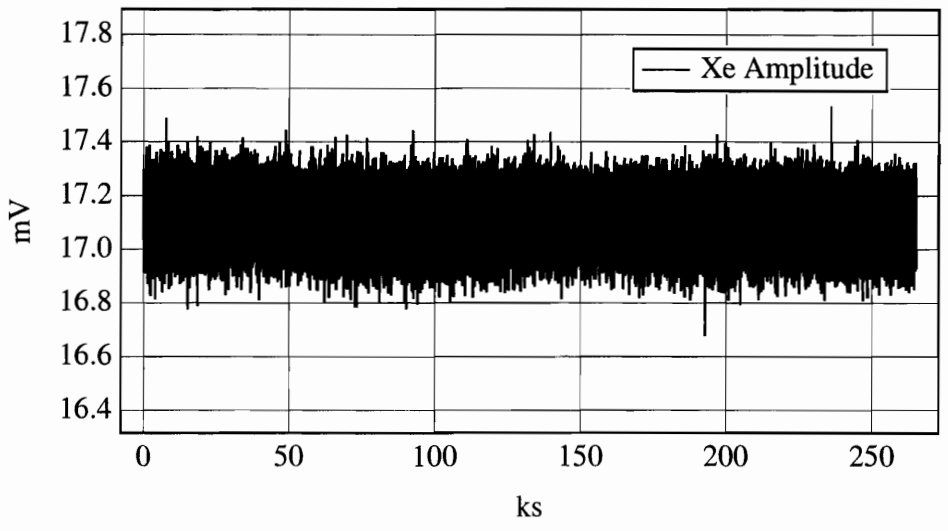

Figure 6-19: ^{129}Xe maser amplitude in a three day data set collected with cell B_1 and the narrow-band Toptica TA 100 laser. To the best of our knowledge the experimental setup parameters are those given in Tab. 4.3.

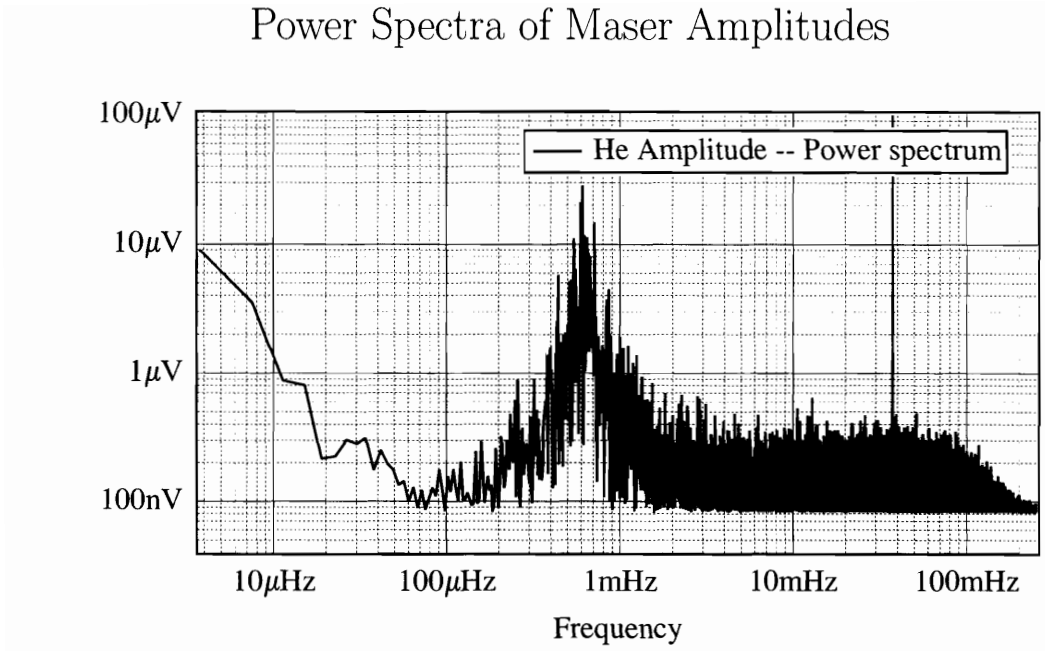

Figure 6-20: Power spectrum of the ^{3}He maser amplitude in Fig. 6-18. The peak at approximately 0.7 mHz is due to small underdamped oscillations of the ^{3}He maser amplitude.

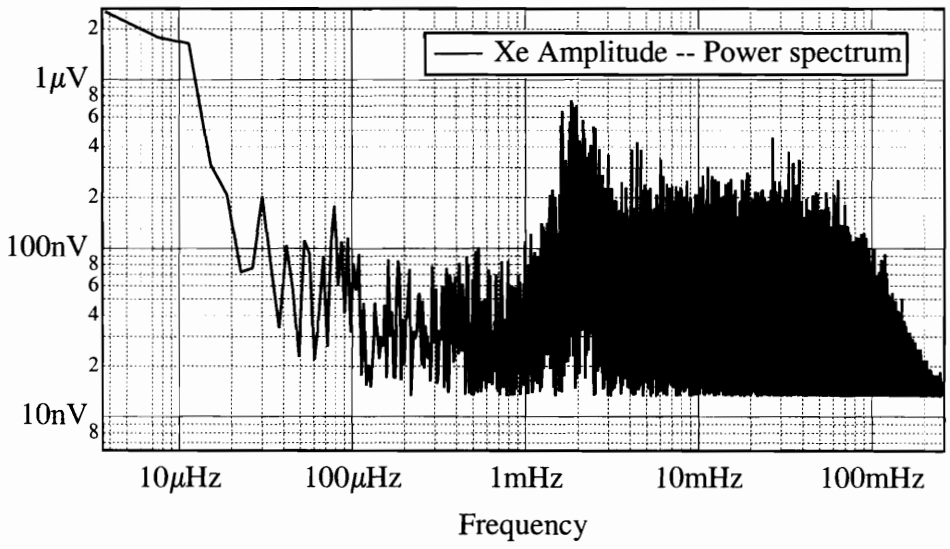

Figure 6-21: Power spectrum of the ^{129}Xe maser amplitude in Fig. 6-19. The peak at approximately 2 mHz is due to small underdamped oscillations of the ^{129}Xe maser amplitude.

6.6.3 Measurement of Maser Amplitudes vs Pump Bulb Temperature

A practical way to test the modified Bloch theory presented in Sect. 4.3.4 is to vary the pump bulb temperature, T_P, and measure the steady state maser amplitudes. We have done this for cells B_1 and B_2. The results are reported in Tabs. 6-22 and 6-24. Figures 6-23 and 6-25 show the experimental values and the theoretical predictions, calculated using the modified Bloch theory with input parameters as in Tab. 4.3, except for the narrow-band laser intensity for which we used the value of 250 mW. Whereas the ^{3}He maser amplitudes are fairly well described by the theory, the ^{129}Xe amplitudes are not. The three caveats mentioned at the end of Sect. 6.6.1 apply to this preliminary measurement. In particular, ^{129}Xe relaxation due to the interaction with unpolarized Rb in the warmest part of the transfer tube induces major losses when the pump bulb temperature is increased and the temperature of the transfer tube rises. We demonstrated that it is possible to recover a higher ^{129}Xe flux into the maser bulb (and consequently higher ^{129}Xe maser amplitudes) by cooling the transfer tube with compressed air. The problem with this scheme though, is that cooling the transfer tube perturbs the overall cell temperature stability. Any scheme using such cooling during normal maser operation should include an additional temperature lock of the air used for cooling. However, this scheme will probably have the shortcomings of direct cooling that we tried to avoid with the redesign of the ^{129}Xe/^{3}He maser.

Measured Maser Amplitudes vs T_P

(Cell B_1)

T_{Block} (° C)	T_P (° C)	^{129}Xe Ampl. (mV)	^{3}He Ampl. (mV)
111	103	19.6	6.1
118	110	19.5	7.3
124	116	18	8
131	123	15.5	8.7
138	130	12.7	8.9
144	136	9.3	8.7

Figure 6-22: For six pump block temperatures we list the estimated pump bulb temperatures, T_P, and the measured maser amplitudes of the two noble gas masers, using cell B_1.

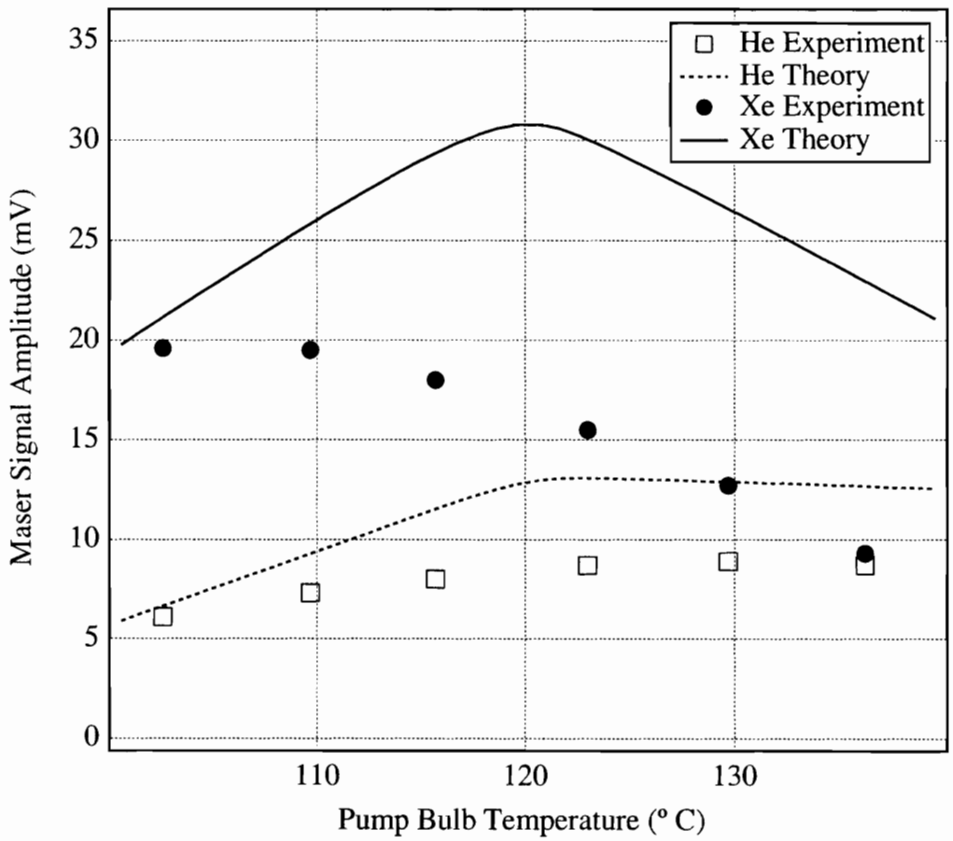

Figure 6-23: Maser amplitudes of the two noble gas masers in cell B_1 as a function of the pump bulb temperature, T_P. The theoretical amplitudes are calculated using the modified Bloch theory with input parameters as in Tab. 4.3 except for the narrow-band laser intensity, which is here 250 mW.

Measured Maser Amplitudes vs T_P

(Cell B_2)

T_{Block} (° C)	T_P (° C)	^{129}Xe Ampl. (mV)	^{3}He Ampl. (mV)
104	96	25.7	6.1
111	103	25.4	7.2
118	110	23.9	8.4
124	116	22	9.2
131	123	19.5	10
138	130	16.7	10.4
144	136	14.3	10.8

Figure 6-24: For seven pump block temperatures we list the estimated pump bulb temperatures, T_P, and the measured maser amplitudes of the two noble gas masers, using cell B_2.

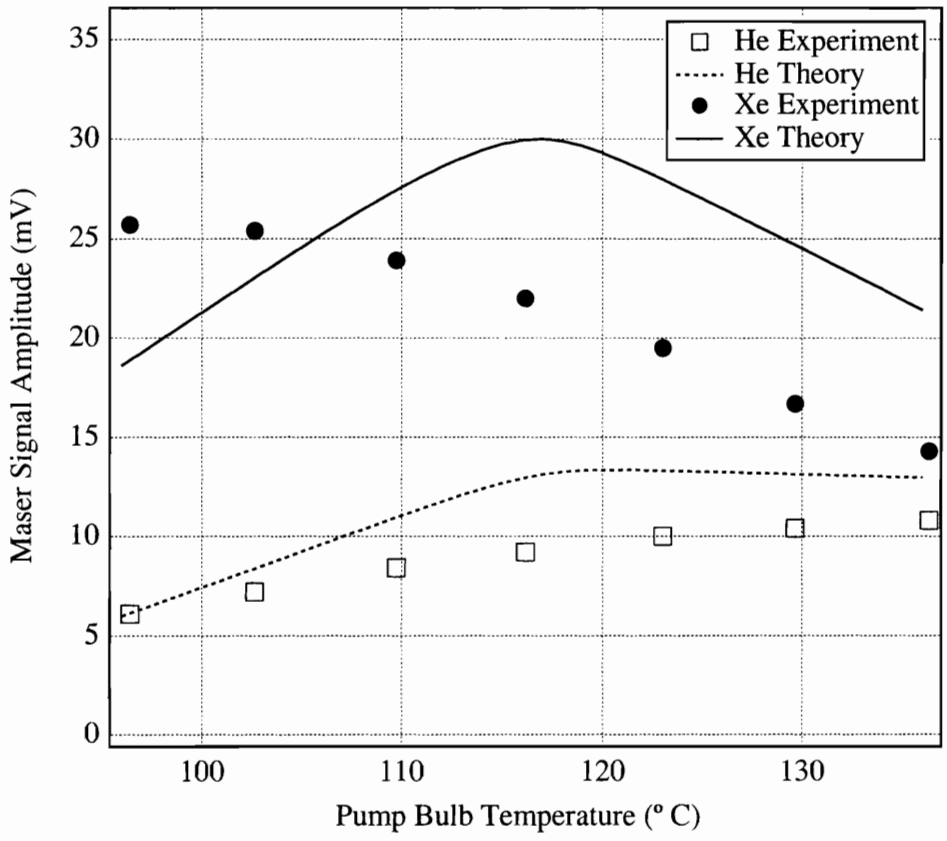

Figure 6-25: Maser amplitudes of the two noble gas masers in cell B_2 as a function of the pump bulb temperature, T_P. The theoretical amplitudes are calculated using the modified Bloch theory with input parameters as in Tab. 4.3 except for the narrow-band laser intensity, which is here 250 mW.

6.7 Peripheral Pick-Up Coil Field Effects

In this section we deal with a maser frequency shift mechanism that was first observed when we began our co-magnetometry investigations.[6] Our first attempt to measure the distance between the centers of polarization of the two masing species along $\hat{y}$ (the direction of the transfer tube as shown in Fig. 6-28) by applying a dB_z/dy gradient yielded the ^{3}He frequency shift data shown in Fig. 6-26. Besides the linear slope that had been observed in the past, we found a surprising resonant feature, a narrow region in which a change in magnetic field gradient as little as few μG/cm induces a maser frequency shift of almost a mHz: an enormous shift by ^{129}Xe/^{3}He maser standards. This region of hypersensitivity to magnetic gradient fluctuations is also the region, as Fig. 6-26 shows, in which the noble gas decoherence times are longest and it is there that the ^{129}Xe/^{3}He maser is most effectively operated.

The dispersive-like frequency shift is due to the fringe field of the pick-up coil, which in the pump bulb is still intense enough to tip the ^{3}He atoms and make them participate in the maser action. When ^{3}He atoms in the pump bulb are immersed in a magnetic field slightly different from that of the maser bulb they pull the maser frequency towards their local Zeeman frequency. In the next section we develop a simple model that captures the essential features of this frequency shift mechanism. We then discuss the possibility that, through this mechanism, optical pumping light instabilities may be converted directly into maser frequency instabilities. Since this is to be avoided at all costs, we have installed a small longitudinal coil on the pump bulb. This coil locally shifts the Zeeman frequency of ^{3}He in the pump bulb sufficiently far from the Zeeman frequency of ^{3}He in the maser bulb that the fringe

[6] We introduced co-magnetometry in Sect. 4.4 and we relate our experimental findings on that topic in Sect. 6.8.

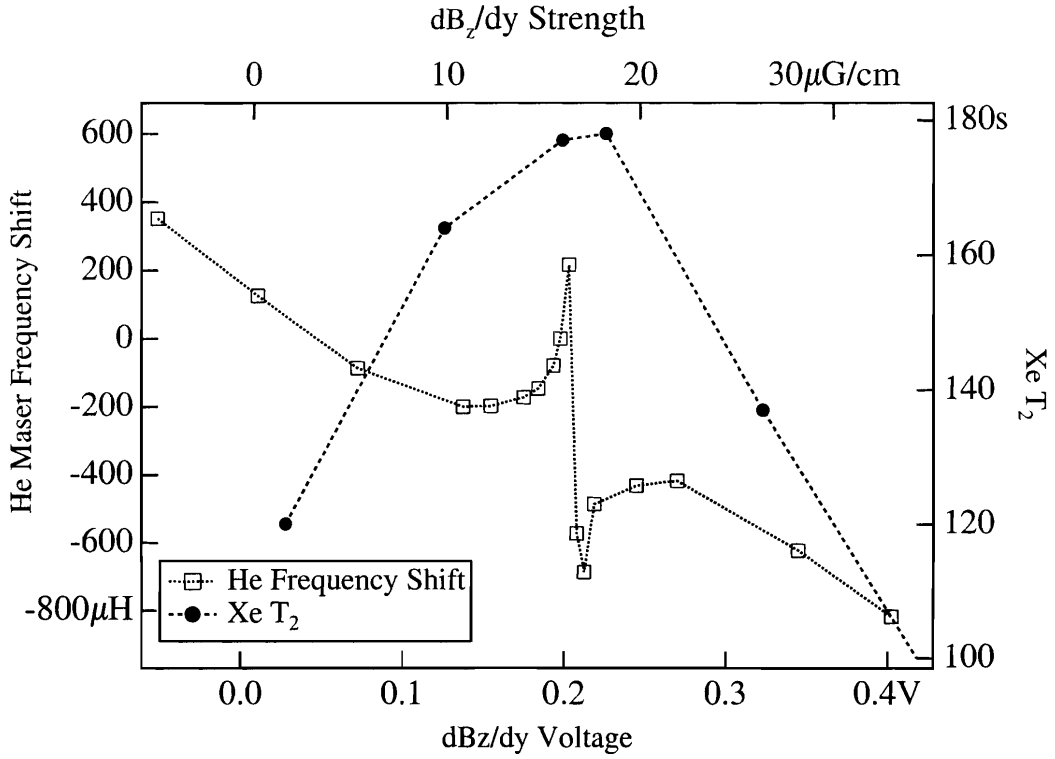

Figure 6-26: ^{3}He maser frequency shift as a function of the dB_z/dy gradient applied on the maser cell when the ^{129}Xe maser is phase-locked. In the central region, where the shim coil creates a very homogeneous magnetic field (as the maximization of the ^{129}Xe T_2 indicates), a sharp, dispersive-like shift is encountered. This frequency shift arises because the fringe field of the pick-up coil excites ^{3}He coherence in the pump bulb.

pick-up coil field becomes ineffective in exciting pump bulb coherence. We have not mentioned ^{129}Xe because, as we will argue in Sect. 6.7.2, the interactions of ^{129}Xe with polarized Rb sufficiently shift the ^{129}Xe frequency in the pump bulb away from the ^{129}Xe maser frequency.

6.7.1 Masing of Two Spatially Separated Ensembles in Slightly Different Magnetic Fields

In this section we study the behavior of a maser made up of two spatially separated, spherical ensembles of atoms of the same species. In our model the two ensembles interact with each other only indirectly, via feed-back from the pick-up coil. We choose the $\hat{y}$ axis along the axis of the pick-up coil and we assume that the centers of the two ensembles $\vec{P}$ and $\vec{p}$ lie on $\hat{y}$: $\vec{P}$ is located at y_1 and $\vec{p}$ is located at y_2. As we saw in Eq. (2.21) of Sect. 2.3, in the frame rotating at the maser frequency, ω_M, the equations of motion for the two polarizations can be written as follows:

$$\dot{\vec{P}} = (0, \omega_{R1}, \omega_1 - \omega_M)) \times \vec{P} + \frac{P_{z,0}\hat{z} - \vec{P}}{\{T_2, T_2, T_1\}}, \tag{6.6}$$
$$\dot{\vec{p}} = (0, \omega_{R2}, \omega_2 - \omega_M)) \times \vec{p} + \frac{p_{z,0}\hat{z} - \vec{p}}{\{T_2, T_2, T_1\}}.$$

The two ensembles lie in slightly different magnetic fields B_{01} and B_{02}. We define $\omega_i = \gamma B_{0i}$ and $\omega_2 = \omega_1 + \Delta$. The Rabi frequencies ω_{R1} and ω_{R2} for the two ensembles are different. The two species occupy volumes V_1 and V_2 and the field of the pick-up coil defined in Eq. (2.22) has two distinct average strengths per unit current ξ_1 and ξ_2:

$$\xi_i = \frac{1}{V_i} \int_{V_i} d^3\vec{r}\, \xi\,(\vec{r}). \tag{6.7}$$

The radiation damping times, defined in Eq. (2.32), are proportional to each other:

$$\frac{\tau_{RD1}}{\tau_{RD2}} = \frac{\xi_2^2 V_2 p_{z,0}}{\xi_1^2 V_1 P_{z,0}} = \alpha^2 v \frac{p_{z,0}}{P_{z,0}}. \tag{6.8}$$

We have defined $\alpha = \xi_2/\xi_1$, $v = V_2/V_1$, and we have assumed equal number density for the two ensembles. Following the derivation presented in Sect. 2.3.1, one can

Region	Volume (cm^3)	ξ_i (G/A)	$\langle y \rangle$ (cm)
Maser Bulb	4	444	~ 0
Transfer Tube	0.3	153	2.5
Pump Bulb	6	27.8	5

Table 6.8: The three regions in which the noble gas atoms reside have different volumes, average pick-up field intensity ξ_i, and average distance $\langle y \rangle$, from the center of the pick-up coil.

show that the two Rabi frequencies differ by a factor α:

$$\omega_{R1} = \frac{1}{\tau_{RD1}} \frac{P_x + \alpha v p_x}{P_{z,0}}, \tag{6.9}$$

$$\omega_{R2} = \frac{1}{\tau_{RD2}} \frac{p_x + \frac{1}{\alpha v} P_x}{p_{z,0}} = \alpha \omega_{R1}. \tag{6.10}$$

As in Sect. 2.3.2 we have chosen the $\hat{x}$ axis along the perpendicular polarization, which gives the additional constraint $P_y + \alpha v p_y = 0$ and determines the maser frequency shift $\delta = \omega_M - \omega_1$. In steady state the left-hand side of Eqs. (6.6) vanishes. After eliminating the other 5 variables from the 6 equations, we are left with the following fourth-order equation

$$\begin{aligned} v\alpha^2 \frac{p_{z,0}}{P_{z,0}} \frac{\Delta}{\delta} (\Delta - \delta) &= \alpha^2 \Delta + \left(1 - \alpha^2\right) \frac{\tau_{RD1}}{T_2} (\Delta - \delta) \\ &\quad + \tau_{RD1} T_2 (\Delta - \delta) \left[(\Delta - \delta)^2 - \alpha^2 \delta^2\right], \end{aligned} \tag{6.11}$$

from which we learn that the maser frequency shift depends only on the ratio of the volumes v and on the relative magnitude of $p_{z,0}$ and $P_{z,0}$, and not on T_1.

A maser cell can be divided into three regions: maser bulb, pump bulb, and transfer tube. Volumes, average distance $\langle y \rangle$ from the geometric center of the maser bulb, and average pick-up field intensity for the three regions are given in Table 6.8. Since the pick-up field is strongest in the maser bulb, the contributions of the pump

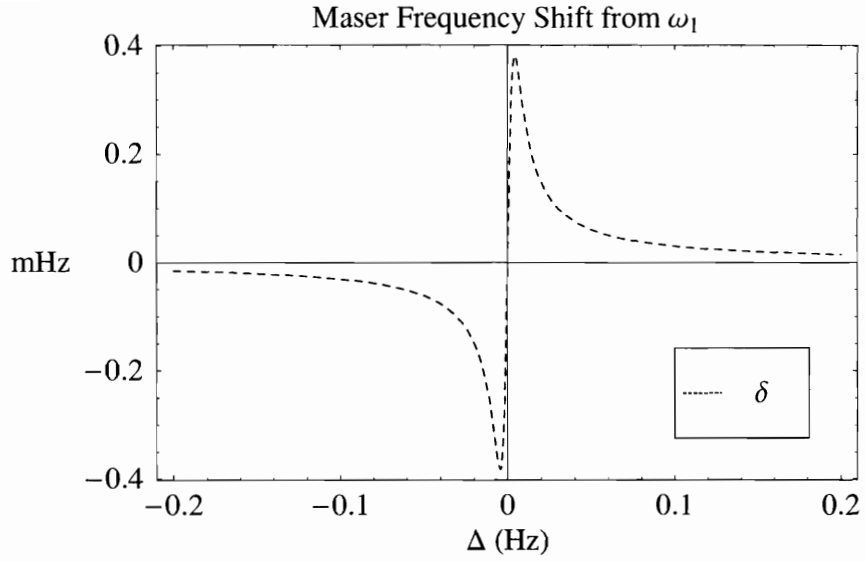

Figure 6-27: Numerical solution of Eq. (6.11) for the maser frequency shift δ as a function of Δ. We used the following realistic parameters: $\alpha = 27.8/444$, $v = 6/4$, $p_{z,0}/P_{z,0} = 1.2$, $\tau_{RD} = 10$ s, $T_2 = 240$ s.

and transfer tube produce only small perturbations to the maser frequency. We solve Eq. (6.11) for $\delta \ll \Delta$ and then check that our treatment is self-consistent. Neglecting all quadratic and higher terms in δ, we obtain the following approximate expression for the maser frequency shift (from the nominal frequency of the ensemble 1):

$$\delta(\Delta) \approx v\frac{p_{z,0}}{P_{z,0}}\frac{\Delta}{1 + v\frac{p_{z,0}}{P_{z,0}} + (1-\alpha^2)\frac{\tau_{RD1}}{T_2\alpha^2} + \frac{\tau_{RD1}T_2}{\alpha^2}\Delta^2}. \tag{6.12}$$

For self-consistency, this approximation is valid only when $\frac{1}{v}\frac{P_{z,0}}{p_{z,0}} + (1-\alpha^2)\frac{\tau_{RD2}}{T_2} \gg 1$, which is a condition usually met in our masers when we consider either the pump bulb ensemble (for which $\alpha = 27.8/444 \ll 1$, $v \sim 1$, and $\tau_{RD2}/T_2 \approx 10$) or the transfer tube ensemble (for which $v = 0.3/4 \ll 1$, $\alpha \sim 1$, and $P_{z,0}/p_{z,0}v \approx 10$) perturbations to the maser bulb ensemble.

Equation (6.12) shows that when the detuning Δ is small enough that we can

neglect the quadratic term in the denominator, there is a significant perturbation to the maser frequency (see Fig. 6-27). This perturbation slowly dies out as we increase the detuning. The maximum maser shift, δ_{Max}, and the value of detuning for which it occurs, Δ^*, are:

$$\delta_{Max} = \tfrac{1}{2} v \frac{p_{z,0}}{P_{z,0}} \frac{\alpha^2}{\tau_{RD1}} \sqrt{1 + \alpha^2 \left[\left(1 + v \frac{p_{z,0}}{P_{z,0}} \right) \frac{T_2}{\tau_{RD1}} - 1 \right]}, \tag{6.13}$$

$$\Delta^* = \frac{1}{T_2} \sqrt{1 + \alpha^2 \left[\left(1 + v \frac{p_{z,0}}{P_{z,0}} \right) \frac{T_2}{\tau_{RD1}} - 1 \right]}. \tag{6.14}$$

Hence, to a good approximation the peak-to-peak amplitude of the dispersive feature in the maser frequency is roughly $v \frac{p_{z,0}}{P_{z,0}} \frac{\alpha^2}{\tau_{RD1}} = \frac{1}{\tau_{RD2}}$ and the peaks are $2/T_2$ apart.

As we saw already in Fig. 6-26 such a feature was first observed in our experiment by applying dB_z/dy gradients that would increase both pump bulb and transfer tube average field, $B_z(y)$, proportionately to their respective distance y_{tt} and y_P from the center of the applied shim-gradient (see Fig. 6-28). Figure 6-26 shows that the perturbation to the maser frequency is maximum for gradient intensities that maximize the ^{129}Xe decoherence time and remains significant for all desirable T_2 values. This means that the standard shimming configuration in which the maser is commonly operated is also the configuration in which atoms in the pump bulb and in the transfer tube couple best to the oscillation in the maser bulb. Any mechanism that perturbs the atoms' precession frequency in the pump bulb and in the transfer tube will efficiently pull the maser frequency.

In order to verify our theory, we wound a coil around the pump bulb (see Fig. 5.4.5) and scanned the resonance, this time applying a local B_z field to the atoms in the pump bulb instead of a gradient on the whole cell. The result, reported in Fig. 6-29, shows that our theory captures very well the shape of the

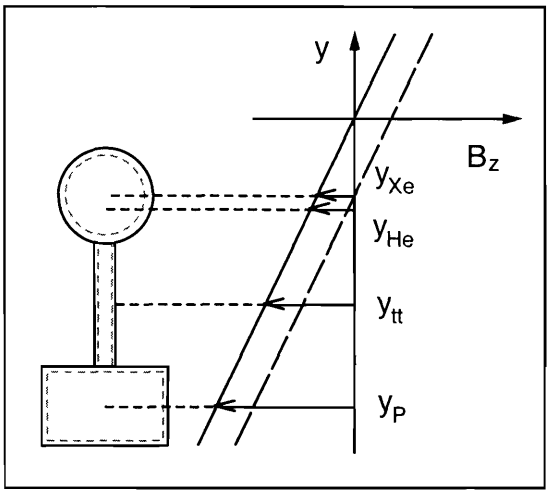

Figure 6-28: Longitudinal magnetic field applied to the maser cell. When the dB_z/dy (continuous line) is applied, the center of polarization of the ^{129}Xe maser (see Eq. (4.59)) detects a net change in the longitudinal magnetic field. The ^{129}Xe phase lock adjusts the main solenoid field to compensate for this offset. The resulting profile of B_z along $\hat{y}$ is given by the diagonal dashed line.

resonance. The theoretical curve was obtained for the realistic values $\alpha = 27.8/444$, $v = 6/4$, $p_{z,0}/P_{z,0} = 1.2$, $\tau_{RD} = 10$ s and assuming that only ^{3}He is affected by the shift. The only parameter used that is not realistic is $T_2 = 240$ s, which is a factor of two bigger than the observed ^{3}He effective decoherence time. This large value of T_2 may be correcting for our simplistic model of two ensembles localized at two points in space, as a representation of a maser occupying an extended region.

We shall also see that Eq. (6.12) directly couples the Rb induced shifts, which may be caused by light instabilities, into maser frequency shifts: a mechanism that could seriously compromise the maser performance. Before exploring this issue further, we provide a simple interpretation of the maser frequency shift derived in this section.

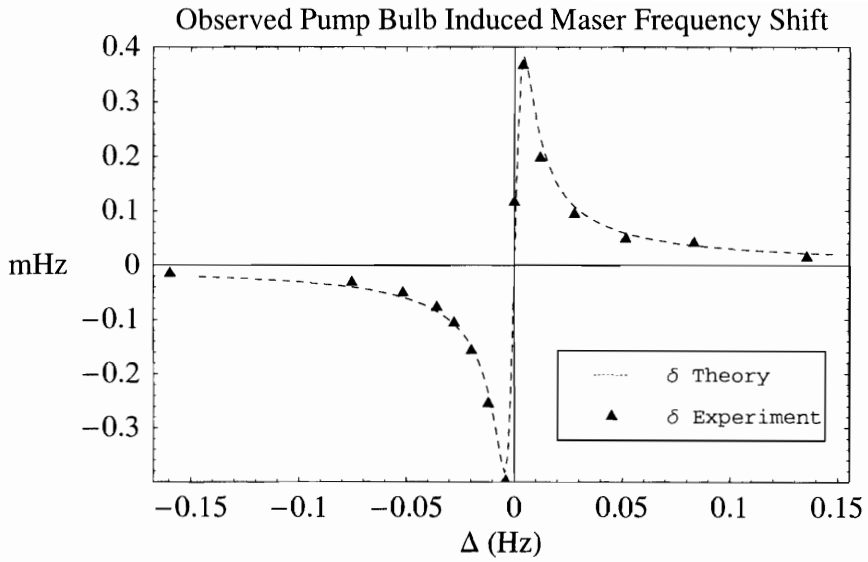

Figure 6-29: Observed ^{3}He maser frequency shift due the Zeeman frequency shift Δ induced on the ^{3}He atoms in the pump bulb with the help of a small solenoid installed on the pump bulb itself. The theoretical curve is the numerical solution of Eq. (6.11) for which we used the following realistic parameters: $\alpha = 27.8/444$, $v = 6/4$, $p_{z,0}/P_{z,0} = 1.2$, $\tau_{RD} = 10$ s, $T_2 = 240$ s.

A Simple Interpretation

The maser frequency shift in Eq. (6.11) may seem surprising at first. In order to understand this frequency shift mechanism, we return to Eqs. (6.6) and solve the two equations $\dot{p}_y = 0$ and $\dot{P}_y = 0$ for the maser frequency, ω_M. We find that ω_M is an average of the two Zeeman frequencies ω_1 and ω_2, weighted by the in-phase components of the perpendicular magnetizations taking into account the different couplings of each ensemble to the pick-up coil field:

$$\begin{aligned} \omega_M &= \frac{\omega_1 V_1 \xi_1 P_x + \omega_2 V_2 \xi_2 p_x}{V_1 \xi_1 P_x + V_2 \xi_2 p_x} \\ &= \omega_1 + \frac{v\alpha p_x}{P_x + v\alpha p_x}\Delta. \end{aligned} \tag{6.15}$$

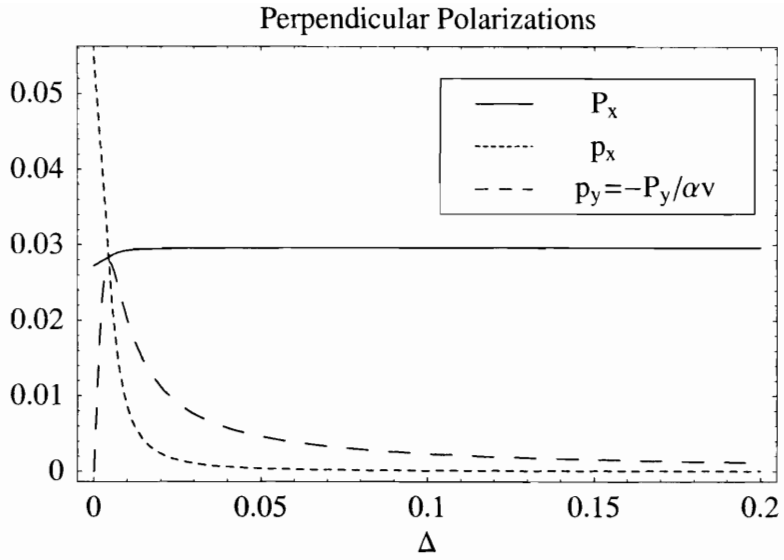

Figure 6-30: Numerical solutions for the steady state perpendicular polarizations of the two ensembles 1 and 2, as a function of the Zeeman detuning Δ of ensemble 2. We used the following realistic parameters: $\alpha = 27.8/444$, $v = 6/4$, $p_{z,0}/P_{z,0} = 1.2$, $\tau_{RD} = 10$ s, $T_2 = 240$ s.

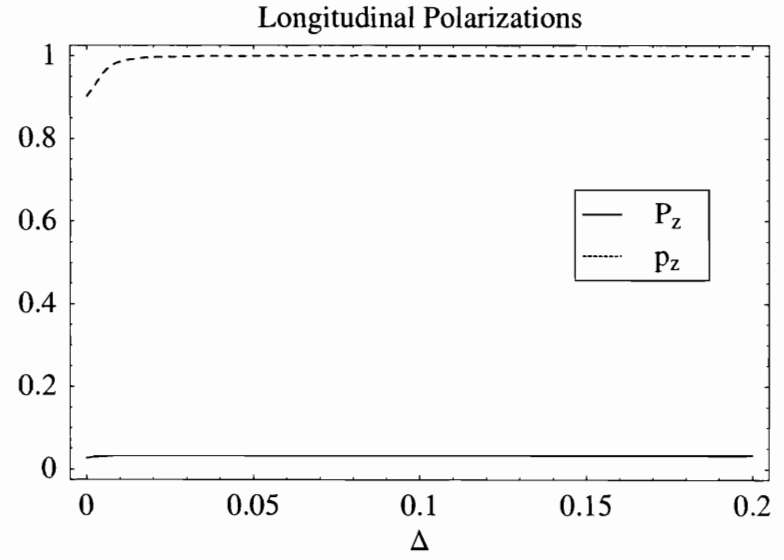

Figure 6-31: Numerical solutions for the steady state longitudinal polarizations of the two ensembles 1 and 2, as a function of the Zeeman detuning Δ of ensemble 2. We used the following realistic parameters: $\alpha = 27.8/444$, $v = 6/4$, $p_{z,0}/P_{z,0} = 1.2$, $\tau_{RD} = 10$ s, $T_2 = 240$ s.

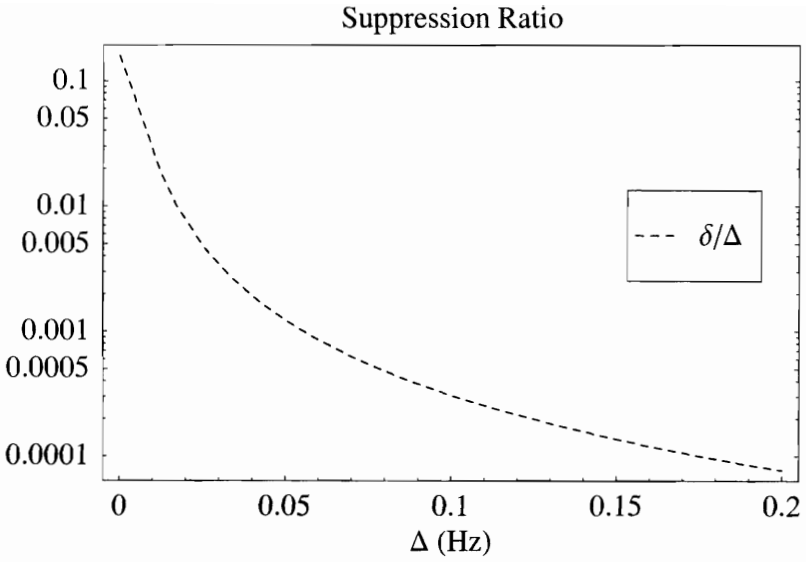

Figure 6-32: Ratio of the maser detuning δ to the Zeeman detuning Δ of ensemble 2. We used the following realistic parameters: $\alpha = 27.8/444$, $v = 6/4$, $p_{z,0}/P_{z,0} = 1.2$, $\tau_{RD} = 10$ s, $T_2 = 240$ s.

In Figs. 6-30 and 6-31 we present the steady state, numerical solutions for the two polarizations $\vec{p}$ and $\vec{P}$, as a function of the detuning, Δ, for realistic parameters. Notice that p_x is significantly different from zero only when the pick-up coil drive is almost resonant with the local Zeeman frequency ω_2. p_x reaches its maximum for $\Delta = 0$, where the maser frequency shift $\delta = \omega_2 - \omega_1$ vanishes. This accounts for the dispersive-like shape of the frequency shift, which is not caused by a sudden change in the steady state polarizations (p_x goes through a maximum for zero detuning and then continuously decreases for negative detunings), but is a consequence of the change in sign of the frequency difference Δ.

6.7.2 Light Stability and Maser Frequency Stability

In Sect. 2.1 we mentioned that both ^{129}Xe and ^{3}He in the pump bulb interact strongly with polarized Rb through the Fermi contact interaction. This interaction

produces a frequency shift in the noble gas Zeeman levels which is proportional to the Rb magnetization [84, 69]:

$$\delta\omega_{ng}^{Rb} = (\kappa_{ng} - 1)\gamma_{ng}\frac{8\pi}{3}\hbar\gamma_{Rb}[\mathrm{Rb}]P_{Rb} \tag{6.16}$$

The enhancement factor, κ_{ng}, differs greatly for the two noble gas species: $\kappa_{He} = 5$ and $\kappa_{Xe} = 726$ [84, 85]. For pump bulb temperatures of approximately 114° C, $[\mathrm{Rb}] \approx 1.4 \times 10^{13}$, and using $\gamma_{Rb} = 2\pi$ 466 kHz/G we obtain $\delta\omega_{He}^{Rb} = 4.5$ mHz and $\delta\omega_{Xe}^{Rb} = 294$ mHz. $\delta\omega_{Xe}^{Rb}$ detunes the ^{129}Xe precession frequency in the pump bulb away from the maser bulb frequency, making the oscillation of ^{129}Xe in the pump bulb negligible. The same is not true for ^{3}He which can be brought back on resonance with the ^{3}He maser frequency by a small gradient. For detunings smaller than $1/T_2$ this leads to a significant maser frequency shift. Figure 6-32 shows that near resonance the ratio $\delta/\Delta \approx 0.1 - 0.01$. Hence, a 1% instability of the Rb magnetization in the pump bulb shifts the ^{3}He maser by $4.5 - 0.45$ μHz. Effects of this magnitude unacceptably link the stability of our maser to the laser stability and the temperature stability of the pump bulb.

The full scale of these Rb induced shifts can be observed by blocking the laser light for a few seconds when the maser is in operation. In one instance, we measured an immediate ^{3}He frequency shift of about 500 μHz and a complete disruption of the ^{3}He maser amplitude stability.

As we already mentioned, we eliminate these shifts with the help of a small longitudinal coil on the pump bulb. This coil locally shifts the Zeeman frequency of ^{3}He in the pump bulb sufficiently far from the Zeeman frequency of ^{3}He in the maser bulb that the fringe pick-up coil field becomes ineffective in exciting pump bulb coherence.

6.8 Assessment of Co-Magnetometry

In this section we present a first assessment of co-magnetometry in the new $^{129}Xe/^{3}He$ maser. We already discussed the importance of co-magnetometry for rejection of common mode magnetic field noise in Sect. 4.4. Presently we believe that co-magnetometry limitations have three possible origins: (i) the imperfect spatial overlap of the masing ensembles; (ii) the spatial inhomogeneity of the pick-up coil field; and (iii) the presence of the co-located noble gas species.

In Sect. 4.4.2 we amply discussed the first point and we found that the slow diffusive transport of polarization combined with a localized source of polarization in the maser bulb may cause the centers of the masing ensembles to be separated in the $\hat{y}$ direction (the direction of the polarized inflow). We begin our assessment by showing that this prediction is verified and that co-magnetometry improves with lower pressures and faster diffusion, as expected. However, the interpretation of the data in terms of our diffusion model is not straightforward and further experimental investigation is needed to improve our understanding.

Next, we note that the same effects explained by point (i) can probably also be explained considering the spatial inhomogeneity of the pick-up coil field. Although we do not have a complete model supporting this, in Sect. 6.8.2 we draw on the intuition built in the previous section to show that co-magnetometry along $\hat{y}$ may be compromised by variations in the pick-up coil field in that direction. This is true even in the case of perfectly overlapping masing ensembles. Section 6.8.3 concludes our discussion with an assessment of the co-magnetometry limitations due to the co-located species.

Cell Name	$D_{M,He}$ (cm^2/s)	$D_{M,Xe}$ (cm^2/s)	Total Fill Pressure (Torr)
B_1	1.45	0.32	715
B_3	0.69	0.17	1725

Table 6.9: Maser bulb diffusion coefficients and total fill pressures for cells B_1 and B_3. The breakdown of the gas pressures for these cells was given in Tab. 6.7.

6.8.1 Co-Magnetometry Limitations Ascribable to Diffusion

Figure 6-33 shows the frequency shift observed on the ^{3}He maser when a linear magnetic field gradient dB_z/dy of increasing intensity is applied to the maser cell.[7] This frequency shift was measured in cells B_1 and B_3, whose gas fill pressures and noble gas diffusion coefficients are listed in Tab. 6.9. No measurable shifts were observed when dB_z/dy and dB_z/dz gradients were applied.[8]

During the measurements the ^{129}Xe frequency was locked to a reference value ω_{Xe}^{ref} by adjusting the correction B_z^{corr} to the main magnetic field. B_z^{corr} must satisfy the following equation,

$$\omega_{Xe} - \omega_{Xe}^{ref} = \gamma_{Xe}\left(B_z^{corr} + \frac{dB_z}{dy}\langle y_{Xe}\rangle\right) = 0, \tag{6.17}$$

where the center of a noble gas polarization along $\hat{y}$ is:

$$\langle y_{ng}\rangle = \frac{\int_{V_M} yP_\perp(\vec{r})d^3\vec{r}}{\int_{V_M} P_\perp(\vec{r})d^3\vec{r}}. \tag{6.18}$$

[7]The narrow dispersive feature due to peripheral pick-up coil field, shown in Fig. 6-26, was eliminated by applying a local longitudinal magnetic field to the pump bulb, as discussed in Sect. 6.7.

[8]This represents an improvement in co-magnetometry with respect to the previous maser, in which sizable ^{3}He frequency shifts were observed when applying dB_z/dz gradients to the cylindrical maser cells whose symmetry axis was oriented along $\hat{z}$ [34]. The spherical symmetry of our cells improves co-magnetometry in the $\hat{z}$ direction.

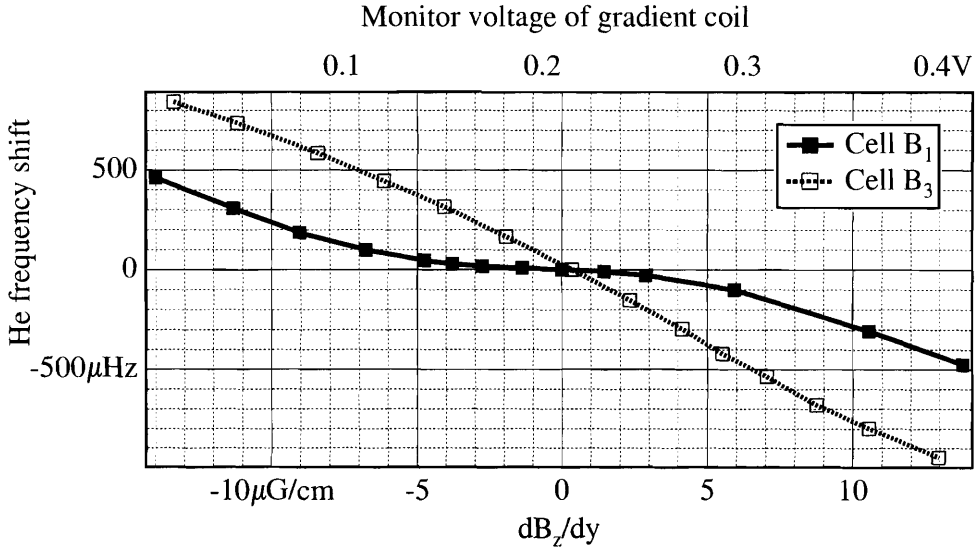

Figure 6-33: ^{3}He maser frequency shift when the ^{129}Xe maser is phase-locked and a linear magnetic field gradient is applied to the maser cell. (Typical uncertainties in plotted points are $\pm 2\mu$Hz.) Perfect co-magnetometry would imply no shift at all.

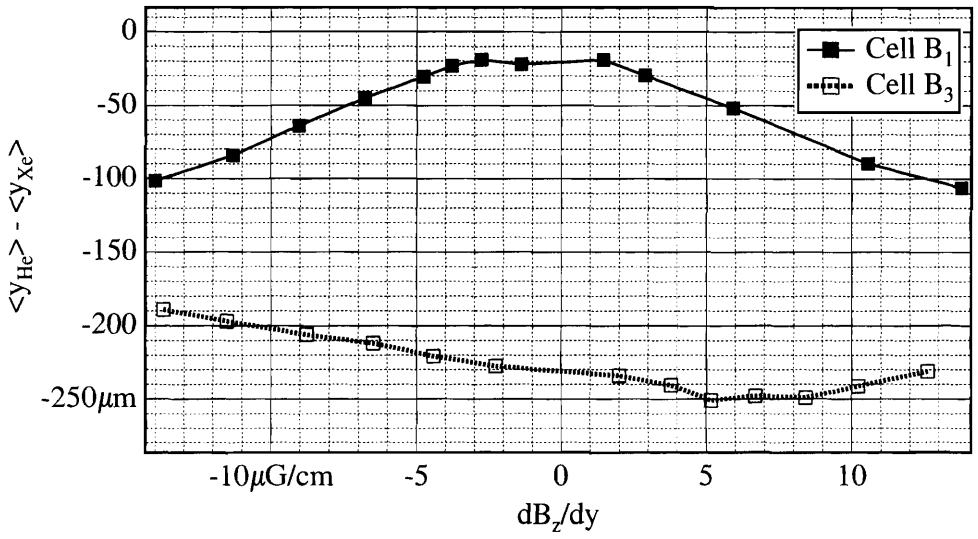

Figure 6-34: Distance between the centers of polarization for the two species, obtained using the ^{3}He maser frequency shifts in Fig 6-33 and the formula: $\langle y_{He} \rangle - \langle y_{Xe} \rangle = \delta\omega_{He}/(\gamma_{He}\, dB_z/dy)$.

The ^{3}He frequency shift due to the gradients is therefore:

$$\begin{aligned} \delta\omega_{He} &= \omega_{He} - \frac{\gamma_{He}}{\gamma_{Xe}}\omega_{Xe}^{ref} = \gamma_{He}\left(B_z^{corr} + \frac{dB_z}{dy}\langle y_{He}\rangle\right) \\ &= \gamma_{He}\frac{dB_z}{dy}\left(\langle y_{He}\rangle - \langle y_{Xe}\rangle\right). \end{aligned} \tag{6.19}$$

This equation was used to calculate the distance between the centers of polarization shown in Fig. 6-34. In the region of best magnetic field homogeneity the sensitivity of the low pressure cell to magnetic field gradients is suppressed by one order of magnitude with respect to the sensitivity of the higher pressure cell.

Figure 6-34 indicates that in both cells the center of the ^{3}He masing ensemble lies below the center of the ^{129}Xe masing ensemble as shown in Fig. 6-28. Hence, on average, the ^{3}He atoms are more displaced towards the transfer tube than the ^{129}Xe atoms. This is surprising given the higher diffusion coefficient of ^{3}He. A possible explanation is that the ^{3}He atoms radiate before they have had a chance to motionally average their position over the whole cell. Another plausible explanation is that ^{3}He atoms in the transfer tube possess some residual coherence able to displace the center of the ^{3}He polarization. We note however that on cell B_3 we installed choke coils on the transfer tube, which should limit this effect.

We presently lack a theory describing the steady state spatial distribution $P_\perp(\vec{r})$ of a masing ensemble taking into account both diffusion and a localized source of polarization. In Sect. 4.4, we solved the simpler problem for the center of polarization in a spherical cell with radius r_0 and a disk-like source of polarization that subtends an angle θ_0 from the center of the cell. We assumed that the polarization has a finite interaction time τ. A plausible choice for τ, is the effective decoherence time T_2^*. This is attractive especially considering Fig. 6-34 in which the centers of polarization, at least for cell B_1, seem to be sensitive to magnetic field gradients

much like the decoherence rates. However, when we calculate $\langle y_{He} \rangle - \langle y_{Xe} \rangle$ (using the T_2^* values in Tab. 6.7 and Eq. (4.75)) we find $\langle y_{He} \rangle - \langle y_{Xe} \rangle = 17$ μm and 41 μm, for cell B_1 and B_3, respectively. The order of magnitude is roughly correct for cell B_1, but it is definitely wrong for cell B_3. Moreover, both differences are positive, suggesting that ^{129}Xe, in theory, is the species that should be more localized towards the entrance of the transfer tube.

In conclusion, we have shown that co-magnetometry can be dramatically improved by using low gas pressures and by carefully shimming the gradient coils to obtain the longest possible decoherence times. However, a deeper understanding of the role played by diffusion in co-magnetometry can be gained only with a more extensive experimental study of co-magentometry.

6.8.2 Co-Magnetometry and the Effects of a Spatially Inhomogeneous Pick-Up Coil Field

In this section we analyze, in a different regime, the consequences of the theory outlined in Sect. 6.7.1. We suppose that there is a significant variation of pick-up coil field between points y_1 and y_2, and we assume that these two points are sufficiently close to each other that an applied gradient only creates a small shift $\Delta = (y_2 - y_1)\gamma_{ng} dB_z/dy < 1/T_2$ between ω_1 and ω_2. We are then in the linear regime of Eq. (6.12) in which the following equation is valid:

$$\delta(\Delta) \approx v \frac{p_{z,0}}{P_{z,0}} \frac{\Delta}{1 + v\frac{p_{z,0}}{P_{z,0}} + (1-\alpha^2)\frac{\tau_{RD_1}}{T_2 \alpha^2}}. \tag{6.20}$$

Notice that if the pick-up coil field were homogeneous ($\alpha = 1$) the frequency shift from ω_1 would be the weighted average of a null shift with weight $V_1 P_{z,0}/(V_1 P_{z,0} +$

$V_2 p_{z,0}$) and shift Δ with weight $V_2 p_{z,0}/(V_1 P_{z,0} + V_2 p_{z,0})$. Suppose, for instance, that $p_{z,0} = P_{z,0}$ and $V_1 = V_2$, the shift would then be $\Delta/2$, as one may have guessed. In other words, the maser behaves as if both ensembles were located at the intermediate position $(y_2 + y_1)/2$. However, when the pick-up field is not the same ($\alpha \neq 1$) at points y_1 and y_2 the frequency shift depends on the τ_{RD} and T_2 of the gas species. This has consequences when we consider co-magnetometry. In order to see it we look at a situation in which there are ensembles of both species at both points y_1 and y_2. We also assume for simplicity that $p_{z,0}^{Xe} = P_{z,0}^{Xe}$ and $p_{z,0}^{He} = P_{z,0}^{He}$. We lock the ^{129}Xe frequency to a reference value ω_{Xe}^{ref} by adjusting the intensity of the main magnetic field with a correction B_z^{corr}, that is

$$\omega_{Xe} - \omega_{Xe}^{ref} = \gamma_{Xe} B_z^{corr} + \delta\left(\gamma_{Xe} \frac{dB_z}{dy}(y_2 - y_1)\right) = 0, \tag{6.21}$$

where $\delta(\Delta)$ is the approximate shift defined in Eq. (6.20). The frequency shift obtained in ^{3}He, even when using the co-magnetometer, is

$$\delta\omega_{He} \approx \gamma_{He} \frac{dB_z}{dy}(y_2 - y_1) v \left(\frac{1}{1 + v + (1-\alpha^2)\frac{\tau_{RD1}^{He}}{T_2^{He}\alpha^2}} - \frac{1}{1 + v + (1-\alpha^2)\frac{\tau_{RD1}^{Xe}}{T_2^{Xe}\alpha^2}} \right).$$

Since the pick-up field is not homogeneous ($\alpha \neq 1$) co-magnetometry does not remove the effect of the magnetic field gradient along $\hat{y}$. This effect therefore yields another possible explanation for the shift in Fig. 6-33 and suggests two possible ways to improve co-magnetometry: keeping the atoms in a region of very homogeneous pick-up field, or realizing the matching condition $\tau_{RD1}^{He}/T_2^{He} = \tau_{RD1}^{Xe}/T_2^{Xe}$. Although this rough model does not lead to a quantitative prediction (it is hard in our maser to come up with a sensible estimate for the distance $y_2 - y_1$; the effect of motional averaging should also be taken into account), it does make a strong case for trying to

prevent masing in regions of varying pick-up coil field intensity, such as the transfer tube.

6.8.3 Shifts Due to the Co-Located Species

In Sect. 4.5 we showed that by choosing a spherical shape for the maser bulb we could prevent maser self-interaction, implying that the maser frequency of one species does not depend on the magnetic induction of its own longitudinal magnetization. This makes each maser more stable, but also limits co-magnetometry. In fact, the ^{129}Xe co-magnetometer is insensitive to the magnetic field fluctuations induced on ^{3}He by the ^{129}Xe longitudinal magnetization and it also detects changes of the ^{3}He longitudinal magnetization that do not perturb the ^{3}He maser.[9] Here, we will estimate these limitations of co-magnetometry.

The simple maser theory of Sect. 2.3 suggests that this limitation should not affect the long term stability of the maser, since the equilibrium longitudinal polarization $P_{z,eq}$ given in Eq. (2.37) does not depend on the flux of incoming atoms, or on $P_\perp$, which are most likely to change or drift. $P_{z,eq}$ only depends on geometric quantities and the noble gas decoherence time, which are likely to remain constant. However, P_z can experience fluctuations around its equilibrium value and these are tightly related to the small fluctuations in $P_\perp$, as we saw in Sect. 2.3.4. Since the maser amplitude is proportional to $P_\perp$, we estimate[10] the medium term stability of P_z by studying that of $P_\perp$. In the long run, as we have already mentioned, we expect P_z to be more stable than $P_\perp$.

Figures 6-35 and 6-36 show the fractional stability of the maser signals from cell B_1 for a three day data set already analyzed in Sect. 6.6.2. For cell B_1, we

[9]The use of a third, co-located species could resolve this issue, but we will not investigate that possibility here.

[10]Unlike $P_\perp$, P_z cannot be measured when the maser is in operation.

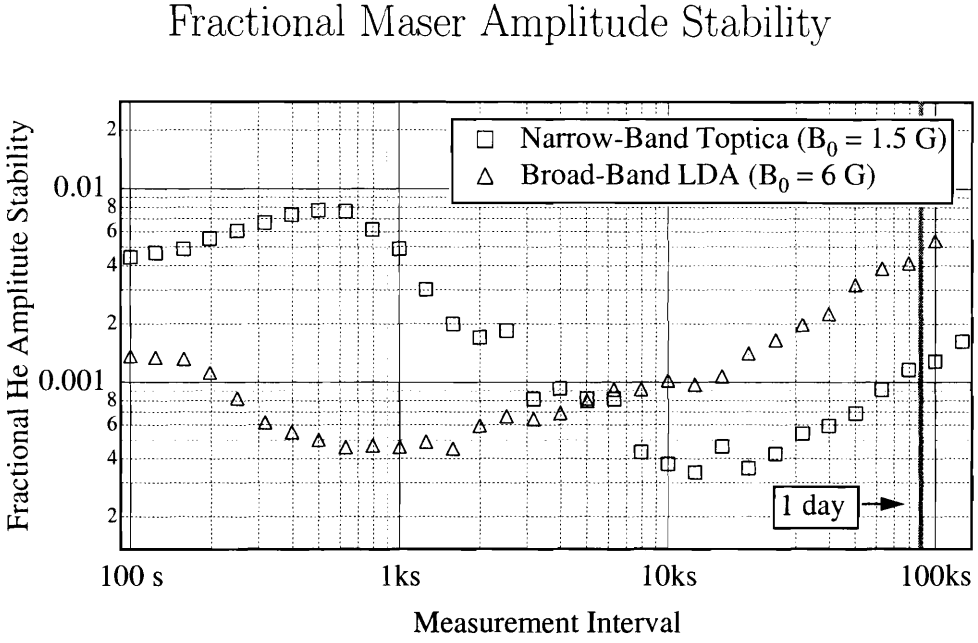

Figure 6-35: Fractional stability of the ^{3}He maser amplitude for two data sets approximately three days long. In one data set we used the Toptica narrow-band laser for optical pumping and a magnetic field of $B_0 \approx 1.5$ G. In the second data set we used the borad-band LDA and a higher magnetic field of $B_0 \approx 6$ G.

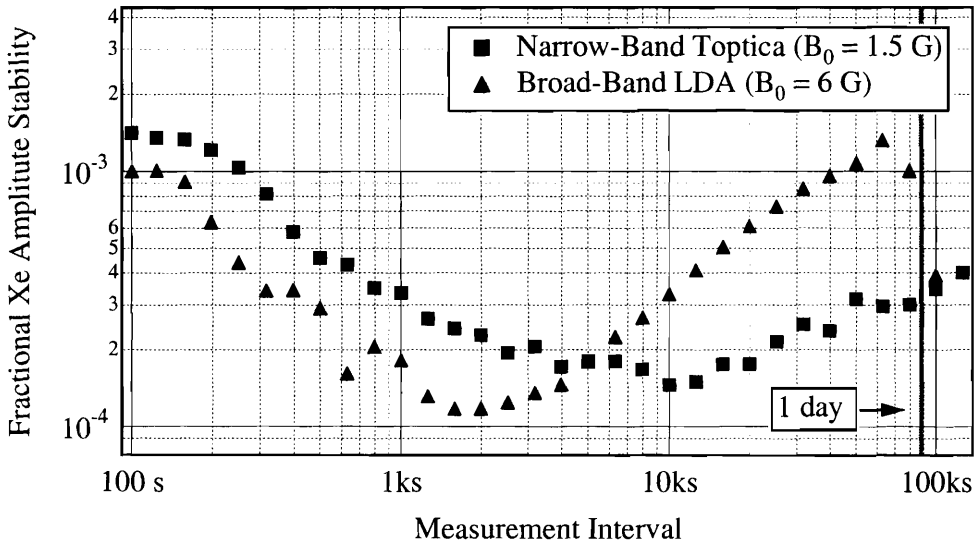

Figure 6-36: Fractional stability of the ^{129}Xe maser amplitude for two data sets approximately three days long. In one data set we used the Toptica narrow-band laser for optical pumping and a magnetic field of $B_0 \approx 1.5$ G. In the second data set we used the borad-band LDA and a higher magnetic field of $B_0 \approx 6$ G.

estimate that the magnetic induction of either species is on the order of 1 μG (see Tab. 4.4). The frequency noise induced on the free-running maser by the two longitudinal magnetizations is therefore of order a few mHz times their fractional stability. Interestingly, we find that the frequency noise from fluctuations of P_z at 10,000 seconds may be as big as a fraction of a μHz.[11] In the next section we show that the ^{129}Xe/^{3}He maser is affected by this level of noise, but other mechanisms could also account for it. Therefore the impact of imperfect co-magnetometry on medium term frequency noise remains an open question.

6.9 Assessment of Frequency Stability Achieved to Date

In this section we report on the frequency stability of the new ^{129}Xe/^{3}He maser and we give a preliminary assessment of its sensitivity to Lorentz invariance violation ("LI sensitivity" for short). For definiteness, we concentrate on two data sets. The first data set (DS1) was collected over three days, using cell B_1 at a magnetic field $B_0 \approx 1.5$ G; optical-pumping was performed with the narrow-band Toptica laser delivering approximately 250 mW of light to the cell.[12] The second data set (DS2) was collected over little more than a day ($\approx 10^5$ s) using cell B_2 at a magnetic field $B_0 \approx 6$ G; optical-pumping was performed with the broad-band LDA delivering approximately 10 W of light. Other parameters characterizing the two runs are listed in Tab. 6.10.

[11] For a measurement interval $\tau = 10,000$ s a simple estimate is: $\delta\nu_{He} \approx 1\ \mu\text{G}\ \gamma_{He}(\delta R_{Xe}/R_{Xe} + \delta R_{He}/R_{He}) \approx 550$ nHz.

[12] Degradation of the tapered amplifier, occurring for the second time in a year of operation (see Sect. 5.3.1), had reduced the output power from approximately 350 mW. Use of the Toptica narrow-band laser source was discontinued shortly after taking this data.

Description	Parameter	DS1	DS2	Units
Cell name	-	B_1	B_3	-
Magnetic field	B_0	1.5	6	G
Maser Frequency	ν_{He}	4,710	19,607	Hz
	ν_{Xe}	1,710	7,119	Hz
Decoherence time	$T^*_{2,He}$	73	88	s
	$T^*_{2,Xe}$	175	229	s
Circuit quality factor	Q_{He}	16.4	12.8	-
	Q_{Xe}	15.6	25.6	-
Maser power	W_{He}	0.47×10^{-9}	30×10^{-9}	erg/s
	W_{Xe}	7.2×10^{-9}	62×10^{-9}	erg/s
Daily thermal noise	$\sigma_\nu^{tot}(1\,\text{day})$	150	18	nHz

Table 6.10: Main parameters characterizing a ^{129}Xe/^{3}He maser data set (DS1) collected using the narrow-band Toptica laser and a second data set (DS2) collected using the broad-band LDA.

The phase residual[13] of DS1 is shown in Fig. 6-37. Figure 6-38 shows the phase residual after a fit eliminating possible frequency correlations with the maser amplitudes (see Eq. (4.2)) and a constant frequency drift. Frequency noise generates the meander of the ^{3}He phase. After carrying out the fit and thus removing frequency fluctuations due to amplitude instability and a constant frequency drift, the maser phase meander is reduced. This confirms, as we pointed out in Sect. 4.1, that accounting for amplitude correlations enhances our ability to discern LI violating daily modulations in the ^{3}He free-running frequency.

The Allan deviation of the ^{3}He frequency for DS1 is presented in Fig. 6-39. The dotted line with the characteristic slope decreasing as $\tau^{-3/2}$ is a fit of the phase noise (see Tab. 2.2). For measurement intervals $\tau \gtrsim 400$ s the phase noise becomes negligible and frequency noise dominates the maser performance. The continuous line indicates the calculated white thermal frequency noise (decreasing as $\tau^{-1/2}$),

[13]We have performed a linear fit of the ^{3}He maser phase. The residual is the time integral of the time dependent maser frequency disturbances, such as noise and, possibly, the daily sidereal modulations which would be an indication of LI violation.

$\nu_\nu^{tot}(\tau)$, which is expected in our free-running maser and takes the following form:

$$\sigma_\nu^{tot}(\tau) = \sqrt{[\sigma_\nu^{He}(\tau)]^2 + \left[\frac{\gamma_{He}}{\gamma_{Xe}}\sigma_\nu^{Xe}(\tau)\right]^2}, \tag{6.22}$$

where

$$\sigma_\nu^{ng}(\tau) = \frac{1}{\pi T_2^*}\sqrt{\frac{k_B T_M}{2W_{ng}\tau}}, \tag{6.23}$$

$$W_{ng} = \frac{\hbar\omega_M}{2}\frac{[ng]V_M P_{z,0}}{T_1}\left(1 - \frac{\tau'_{RD}}{T_2}\right) \tag{6.24}$$

are the thermal noise and the maser power expressions introduced in Eqs. (2.70) and (2.44), respectively. Equation (6.22) reflects the fact that the free-running species is affected by the thermal noise of the co-magnetometer, as well. The $\tau^{-3/2}$ slope of the Allan deviation for ^{129}Xe in Fig. 6-39 demonstrates that the ^{129}Xe phase lock removes the frequency noise from the ^{129}Xe frequency. Co-magnetometry transfers this noise to the ^{3}He maser by overcorrecting the magnetic field, hence the factor of γ_{He}/γ_{Xe} in Eq. (6.22).

In order to verify that the ^{129}Xe/^{3}He maser in DS1 was limited by thermal noise we operated the masers at higher power and lower thermal noise, as Eq. (6.23) indicates. This goal was achieved by using the broad-band LDA instead of the Toptica laser and by quadrupling the main magnetic field, which turned out not to deteriorate the noble decoherence times (see Tab. 6.10). The phase residuals of DS2 in Figs. 6-40 and 6-41 show a dramatic improvement in the SNR with respect to DS1. The Allan deviation of the ^{3}He frequency in Fig. 6-42 indicates that thermal noise is not the limiting factor in DS2 and that long term frequency instabilities can be accounted for using amplitude correlations and a linear frequency drift. The instability of the LDA causes the maser amplitudes to be more unstable in DS2 than

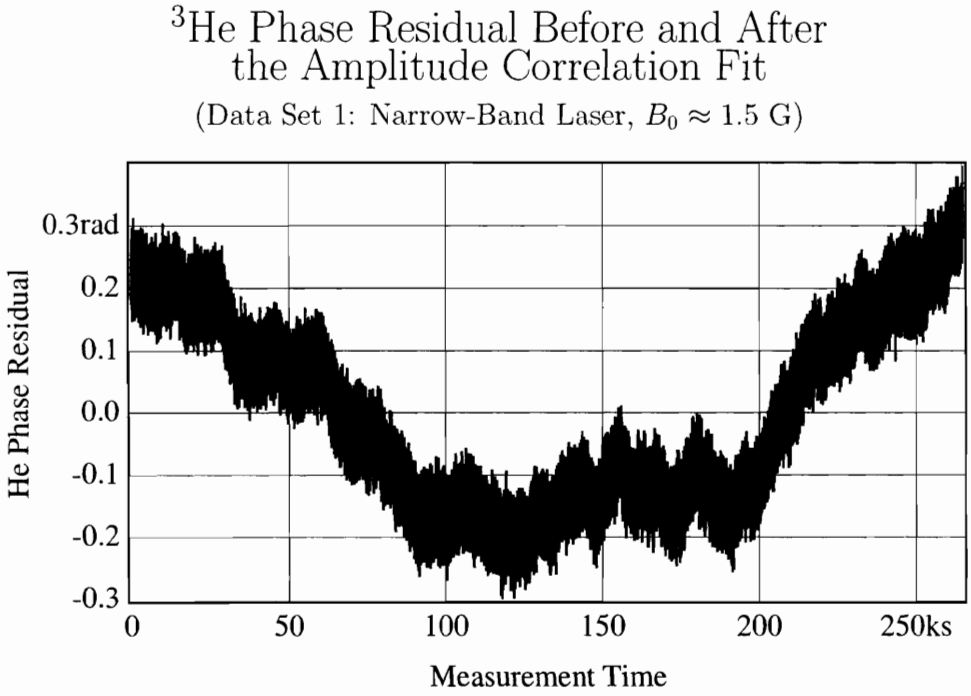

Figure 6-37: Residual of the ^{3}He maser phase. Frequency noise generates the long term meander of the ^{3}He phase, while phase noise is responsible for the short term jitter.

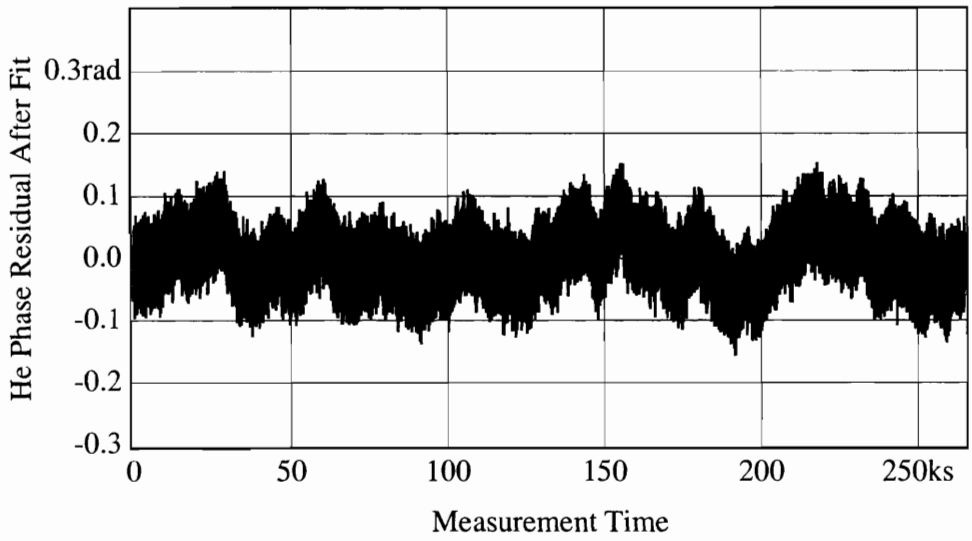

Figure 6-38: Residual of the ^{3}He maser phase after a fit eliminating possible frequency correlations with the maser amplitudes and a constant frequency drift (see Eq. (4.2)). After carrying out the fit, the meander is smaller than in Fig. 6-37, suggesting that the frequency noise ascribable to amplitude instabilities and a constant frequency drift has been rejected from the maser frequency.

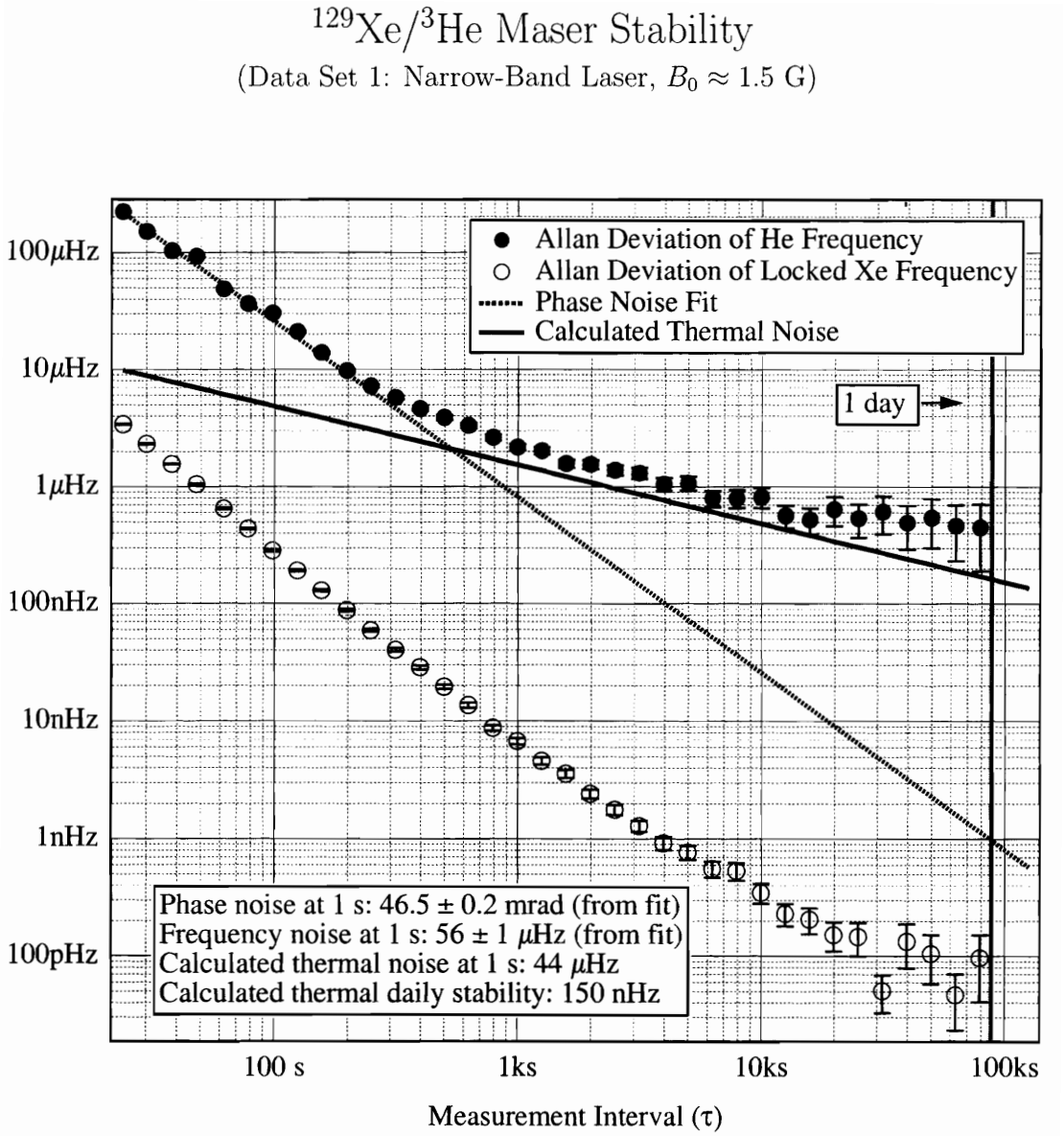

Figure 6-39: Allan deviation of the ^{3}He frequency for DS1. The dotted line is a fit of the initial phase noise. Its characteristic slope decreases as $\tau^{-3/2}$ (see Tab. 2.2). The $\tau^{-3/2}$ slope of the Allan deviation for the ^{129}Xe frequency demonstrates that the ^{129}Xe phase lock removes the frequency noise from ^{129}Xe. The continuous line indicates the calculated white thermal frequency noise (decreasing as $\tau^{-1/2}$), $\nu_{\nu}^{tot}(\tau)$, calculated using Eq. (6.22). In in this data set the maser frequency stability appears to be limited by thermal frequency noise.

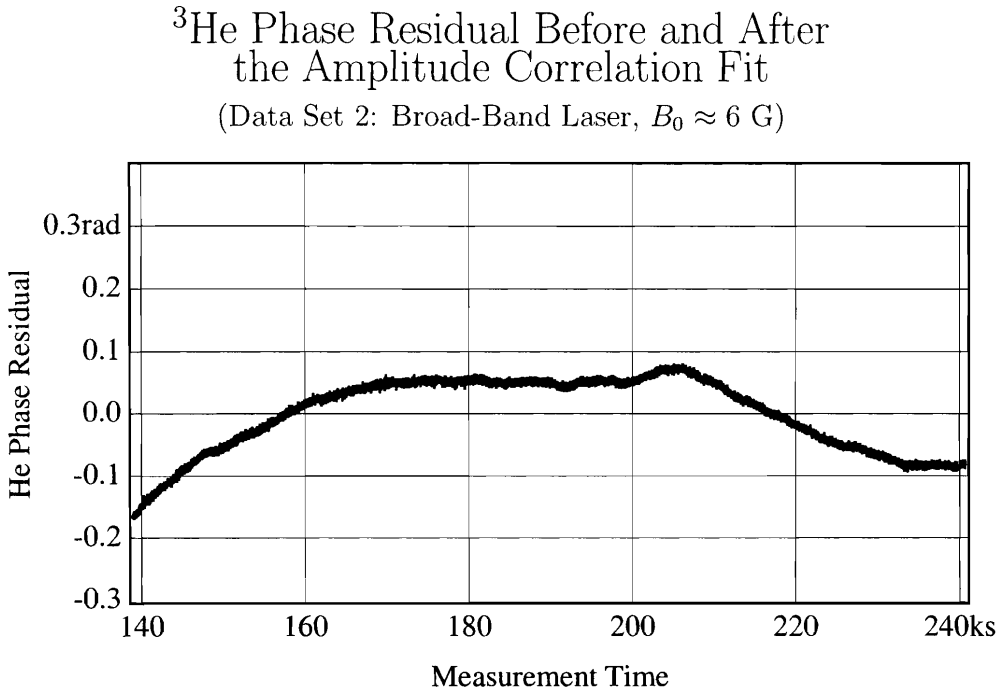

Figure 6-40: Residual of the ^{3}He maser phase. Frequency noise generates the long term meander of the ^{3}He phase, while phase noise is responsible for the short term jitter.

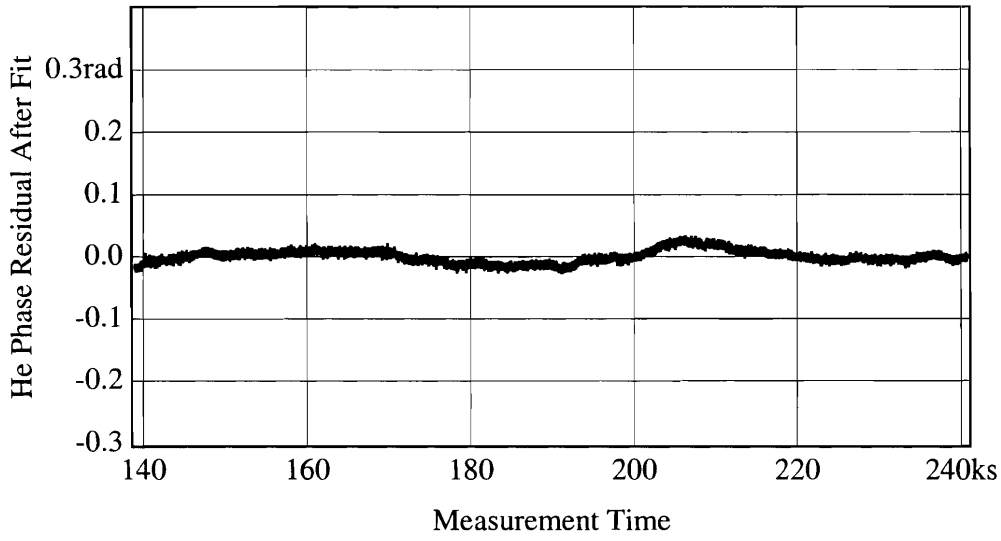

Figure 6-41: Residual of the ^{3}He maser phase after a fit eliminating possible frequency correlations with the maser amplitudes and a constant frequency drift (see Eq. (4.2)). After carrying out the fit, the meander is smaller than in Fig. 6-40, suggesting that the frequency noise ascribable to amplitude instabilities and a constant frequency drift, has been rejected from the maser frequency.

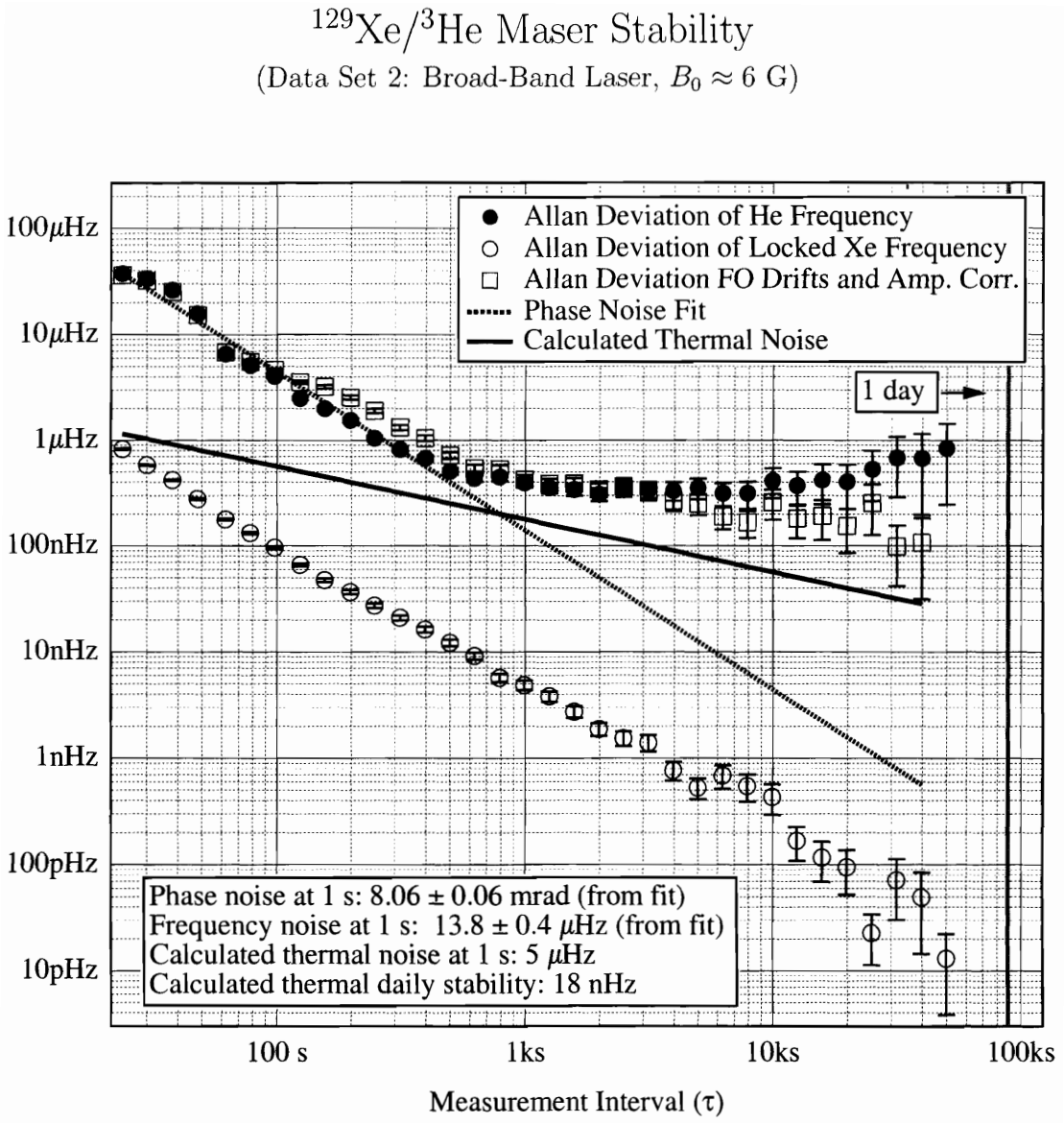

Figure 6-42: Allan deviation of the ^{3}He frequency for DS2. The dotted line is a fit of the initial phase noise. Its characteristic slope decreases as $\tau^{-3/2}$ (see Tab. 2.2). The $\tau^{-3/2}$ slope of the Allan deviation for the ^{129}Xe frequency demonstrates that the ^{129}Xe phase lock removes the frequency noise from ^{129}Xe. The long term instability of the ^{3}He maser frequency is due to the instability of the maser amplitudes (see Figs. 6-35, 6-36, 6-40, and 6-41) since fitting out (FO) the amplitude correlations (and a frequency drift) improves the Allan deviation (empty squares). The continuous line indicates the calculated white thermal frequency noise (decreasing as $\tau^{-1/2}$), $\nu_{\nu}^{tot}(\tau)$, calculated using Eq. (6.22). In this data set the maser frequency stability does not appear to be limited by thermal frequency noise, but by another white frequency noise source as we learn from the FO Allan deviation, whose slope decreases as $\tau^{-1/2}$.

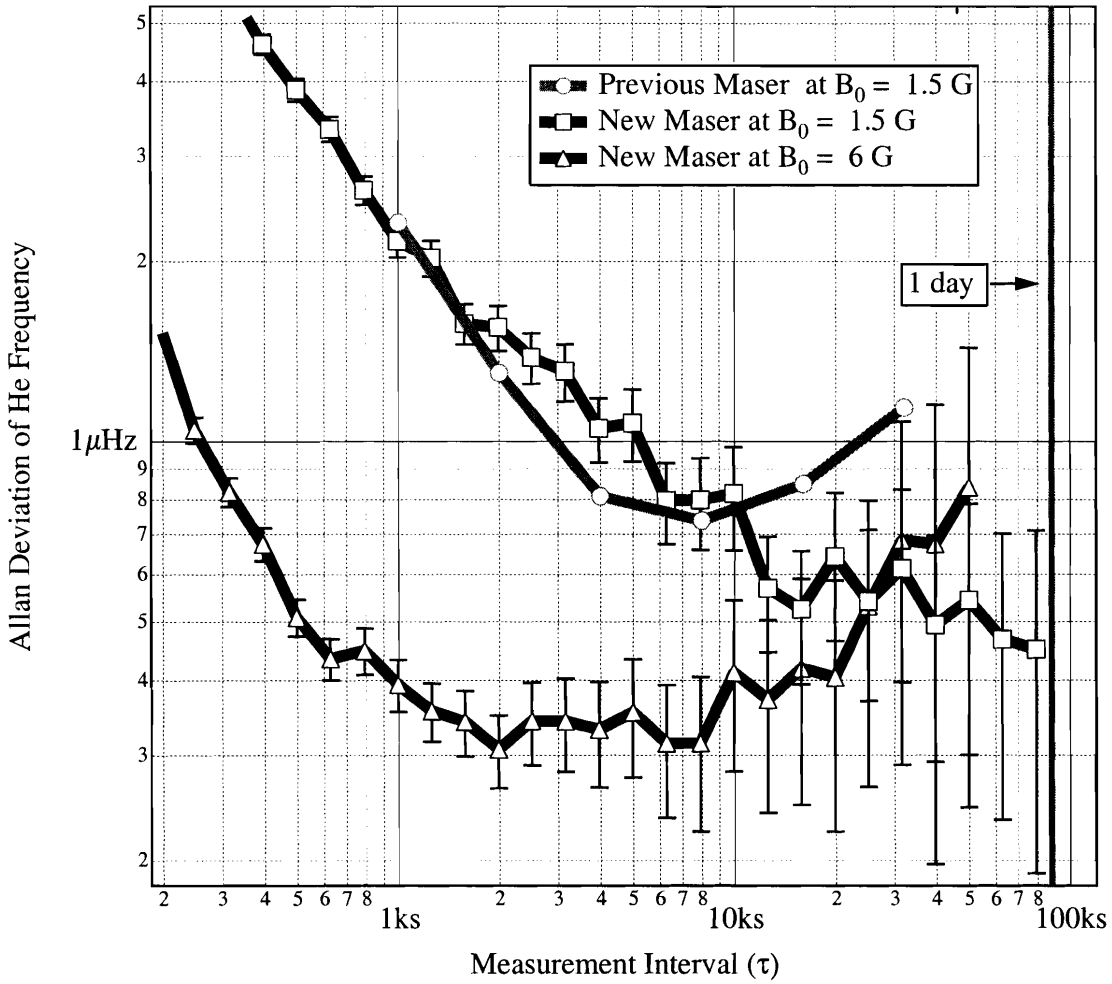

Figure 6-43: Comparison of the Allan deviations for DS1, DS2, and the average Allan deviation of the previous maser (see Sect. 4.1). Stability of the new maser at one day, when the stable narrow-band laser is employed, is a factor of 3 to 5 better than the previous maser's stability. When the new maser is operated at higher magnetic field and higher power (thanks to better optical-pumping from the broad-band LDA) the frequency stability for measurement intervals of 1,000 s improves by a factor of about 7 with respect to the previous system. Unfortunately, instabilities caused by the LDA spoil the long term stability.

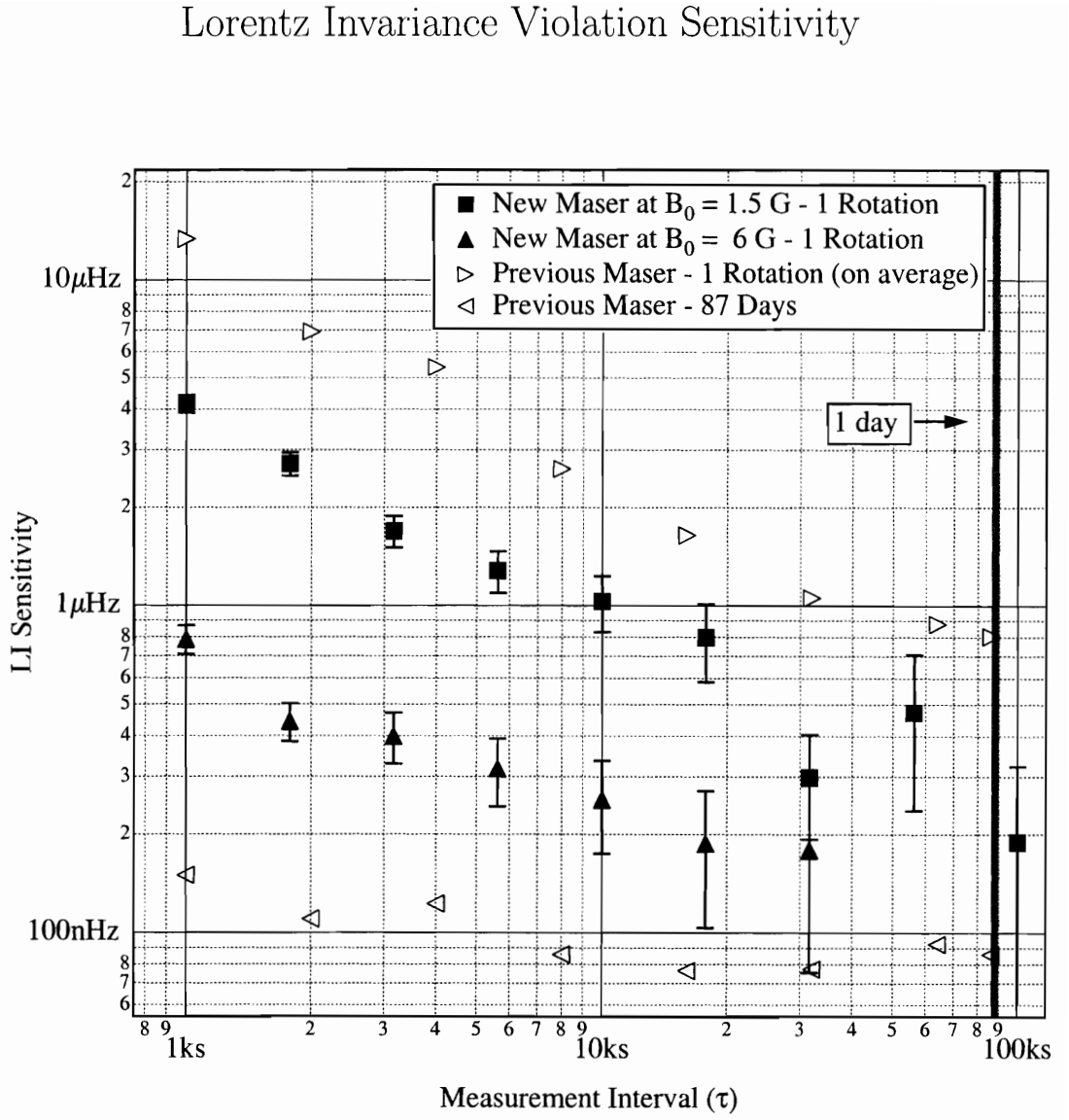

Figure 6-44: Comparison of Lorentz invariance violation sensitivity for DS1, DS2, and the average LI sensitivity of the previous maser (see Sect. 4.1). We carried out an LI analysis similar to that introduced in Sect. 4.1. We divided the data sets into samples of several fictitious rotation periods and performed the LI analysis on each data set for each rotation period. The new $^{129}Xe/^{3}He$ maser, when operated at sufficiently high maser power appears to have the potential for an increased LI sensitivity with respect to the previous maser.

in DS1, as we saw in Figs. 6-35 and 6-36.

A comparison of the Allan deviations for DS1, DS2, and the average Allan deviation of the previous maser (see Sect. 4.1) is presented in Fig. 6-43. DS1 shows that the stability of the new maser at one day, when the stable narrow-band laser is employed, is a factor of 3 to 5 better than the previous maser's stability. On the other hand, when the new maser is operated at higher magnetic field and higher power the frequency sensitivity for measurement intervals of $1,000$ s improves by a factor of about 7 with respect to the previous system.

In order to extract preliminary indications of LI sensitivity, with the limited data available, we carried out an LI analysis similar to that introduced in Sect. 4.1. We divided the two data sets into samples of shorter, fictitious rotation periods and performed the LI analysis on each data set for each fictitious rotation period. Figure 6-44 shows that the LI sensitivity for a rotation period of 30,000 s is a factor of 4 or 5 better then in the previous maser. A similar improvement is expected for a rotation period of 1 day, but several days of data would be needed to verify this prediction.

6.10 Looking Ahead

In this chapter we have shown that the new temperature control system performs very well. The choice of materials for the new oven, maser and pump blocks, tubing, and insulation proved excellent. The new system is mechanically very robust.

The power and frequency stabilization schemes for the Toptica narrow-band laser gave good results. However, the laser itself turned out to be too delicate for intensive use in the $^{129}Xe/^{3}He$ maser, which during LI tests needs to operate continuously for several months. During a testing period of about a year, slow deterioration of the

laser's tapered amplifier happened twice and low laser power prevented us from consistently operating our masers at sufficiently high powers. Nevertheless, our results with the Toptica laser confirm that the stability of narrow-band lasers is highly desirable. Future use of such lasers in the ^{129}Xe/^{3}He maser should be reconsidered when more robust lasers with output powers greater than 1 W become available.

The model describing the double-bulb ^{129}Xe/^{3}He maser that we developed in Ch. 4 is useful for developing an understanding of the transport of polarization between the two bulbs, for investigating the different behavior of the two species, and for defining the effective time scales of the masers, such as bulb escape times, T_2^*, T_L, etc. The model is sufficiently reliable to make order of magnitude predictions,[14] but is still too incomplete to enable fine optimization of maser geometry, gas pressures, and operating temperatures. The weak points of the model are two: (i) the unreliability of the optical pumping simulation, due to the well-known limitations of the theory of spin-exchange optical pumping; and (ii) the loss of ^{129}Xe polarization due to interaction with unpolarized Rb in the (warm) transfer tube, which is not included in the model. The latter effect was clearly observed for the first time in the new maser and ultimately prevented us from operating the maser at the high temperatures ($T_P \approx 140^\circ$ C) for which the maser had been originally designed. A new model addressing both problems, or a new maser design allowing for cooling of the transfer tube, while maintaining excellent overall temperature stability, should be considered in the future.

High maser powers were recently obtained, as we saw in the last section, by using the broad-band LDA and significantly raising the main magnetic field. The new gra-

[14]For instance, the model predicts that using a large pump bulb volume would favor the ^{3}He maser, which has always been the maser with worse SNR. As expected, the new design delivered unprecedented ^{3}He maser powers.

dient coils enabled us to maintain high field homogeneity even at this higher field. Thus, we diminished the effects of thermal frequency noise to an unprecedented level. This will enable us to study more effectively the other sources of frequency noise still limiting the $^{129}Xe/^{3}He$ maser stability. On this subject, we have demonstrated the suppression of one order of magnitude in sensitivity to magnetic field gradients, obtained by using lower gas pressures than in the past. We also discovered a mechanism coupling optical pumping light instability with maser frequency instability and we removed this effect by installing an extra coil on the pump bulb (the effectiveness of this scheme should be properly assessed in the future). Admittedly, ambient magnetic field fluctuations and the intrinsic instabilities of the LDA still cause frequent disruption of the masers' stability and a better understanding of co-magnetometry and better control of the LDA must be developed. Nevertheless, our latest assessment of frequency stability looks quite promising, since we have shown that there is no fundamental frequency noise that should prevent us to achieve, in the near future, an improvement by a factor of 5 or 10 in Lorentz invariance violation sensitivity.

Appendix A

Bound on Lorentz and CPT Violating Boost Effects for the Neutron

F. Canè, D. Bear, D. F. Phillips, M. S. Rosen, C. L. Smallwood,
R. E. Stoner, R. L. Walsworth, and V. A. Kostelecký

"*Bound on Lorentz and CPT Violating Boost Effects for the Neutron*,"
Physical Review Letters 93, 230801 (2004).

Bound on Lorentz and *CPT* Violating Boost Effects for the Neutron

F. Canè, D. Bear, D. F. Phillips, M. S. Rosen, C. L. Smallwood, R. E. Stoner, and R. L. Walsworth
Harvard-Smithsonian Center for Astrophysics, Cambridge, Massachusetts 02138, USA

V. Alan Kostelecký
Physics Department, Indiana University, Bloomington, Indiana 47405, USA
(Received 29 August 2003; published 30 November 2004)

A search for an annual variation of a daily sidereal modulation of the frequency difference between colocated ^{129}Xe and ^{3}He Zeeman masers sets a stringent limit on boost-dependent Lorentz and *CPT* violation involving the neutron, consistent with no effect at the level of 150 nHz. In the framework of the general standard-model extension, the present result provides the first clean test for the fermion sector of the symmetry of spacetime under boost transformations at a level of 10^{-27} GeV.

DOI: 10.1103/PhysRevLett.93.230801 PACS numbers: 06.30.Ft, 11.30.Cp, 11.30.Er, 32.60.+i

The invariance of the laws of nature under transformations between inertial reference frames that differ in relative velocity ("boosts") is an essential feature of Lorentz symmetry, along with invariance under rotations. Experimental tests of boost invariance, such as the Kennedy-Thorndike experiment [1], have been performed for many years with increasing precision [2]. These experiments typically search for a variation of the velocity of light with the laboratory velocity and test boost invariance in the context of classical electrodynamics. However, the fundamental role of Lorentz symmetry in physics makes it desirable to test boost invariance for other systems, such as massive particles with spin.

In this Letter, we present a high-sensitivity experimental test of boost invariance for the neutron, which we interpret in the context of the standard-model extension (SME) [3], a general theoretical framework that allows a comprehensive and systematic study of the implications of Lorentz-symmetry violation at observable energies. The SME provides a widely accepted formalism for the interpretation and comparison of experimental searches for violations of Lorentz symmetry and associated violations of *CPT* symmetry (the product of charge conjugation, parity inversion, and time reversal). The SME has been applied to many systems, including mesons [4], photons [2,5], and leptons [6–8], as well as the neutron [9,10] and proton [11]. An observable Lorentz violation could be a remnant of Planck-scale physics. One attractive origin is spontaneous Lorentz breaking in a fundamental theory [12], but other sources are possible [13].

Our experiment consists of a long-term monitoring of the frequencies of colocated ^{3}He and ^{129}Xe Zeeman masers as the Earth rotates and revolves around the Sun. We search for a specific signature of a violation of boost invariance: an annual variation of the nuclear Zeeman splitting, modulated at the frequency of the Earth's daily sidereal rotation. Such an effect could arise from couplings of the ^{3}He and ^{129}Xe nuclear spins (each largely determined by a valence neutron) to background tensor fields, including a dependence of the Zeeman frequencies on the instantaneous velocity (magnitude and direction) of the laboratory. The appeal of the noble-gas maser experiment is the excellent absolute frequency stability [10,14,15], and thus the sensitivity to small, slow variations in the magnitude of Lorentz-violating spin couplings.

Using the two-species noble-gas maser, we recently constrained the possible rotation-symmetry-violating couplings of the neutron spin with respect to an inertial reference frame based on the Earth [10]. Here, we choose a Sun-based inertial reference frame, which allows us to study cleanly—for the first time in the fermion sector—the symmetry of spacetime with respect to *boost* transformations. (The pioneering work of Berglund *et al.* [16] does not distinguish between the boost and rotation effects to which it is sensitive.) Our experiment's rest frame moves with the Earth around the Sun at a velocity of magnitude $v_{\oplus}/c = \beta_{\oplus} \simeq 9.9 \times 10^{-5}$, and the Lorentz transformation that describes the change of coordinates from the laboratory frame to the Sun-based frame includes both a rotation, $\mathbf{R}$, and a boost along the velocity $\vec{\beta}$.

The most general, coordinate-independent Hamiltonian, H, containing the Zeeman effect (from an applied magnetic field $\vec{B}$) and Lorentz-symmetry-violating couplings of the noble-gas nuclear spins, $\vec{I}$, including leading terms to first order in $\vec{\beta}$, takes the simple form

$$H = \vec{I} \cdot (\gamma \vec{B} + \mathbf{R}(t)\vec{\lambda}_{\odot} + \vec{\beta}(t)\mathbf{R}(t)\Lambda_{\odot}). \qquad (1)$$

Here, the vectors $\vec{I}$ and $\vec{B}$ are expressed in the lab frame, whereas the explicit Lorentz-symmetry-violating vector $\vec{\lambda}_{\odot}$ and 3×3 matrix $\Lambda_{\odot}$ have elements that are combinations of SME coefficients, which may be determined in terms of fundamental Lorentz-violating interactions [17,18], and are assumed constant in the Sun frame. The second term of Eq. (1) leads to a rotation-dependent modulation of the maser frequency. The third term contains cross couplings, in which the rotation induces daily sidereal modulations of the maser frequencies, while the boost transformation induces a sinusoidal variation of the

daily modulation amplitude over the course of the sidereal year [19] as the direction of the velocity of the Earth varies with respect to the Sun. Terms from higher rank tensors (such as a yearly modulation in the maser frequency—for which our maser does not have the stability to set strong limits) have been neglected.

We refer the reader to previous publications [10,14,15] for details on the design and operation of our two-species noble-gas Zeeman maser. Here, we provide a brief review. Colocated ensembles of ^{129}Xe and ^{3}He atoms at pressures of hundreds of millibar are held in a double-chamber glass cell placed in a homogeneous magnetic field of $\sim$1.5 G. Both species have spin-1/2 nuclei and the same sign nuclear magnetic dipole moment, but no higher-order electric or magnetic nuclear multipole moments. In one chamber of the glass cell, the noble-gas atoms are nuclear-spin polarized by spin-exchange collisions with optically pumped Rb vapor [20]. The noble-gas atoms diffuse into the second chamber, which is surrounded by an inductive circuit resonant both at the ^{3}He and ^{129}Xe Zeeman frequencies (4.9 and 1.7 kHz, respectively). For a sufficiently high flux of population-inverted nuclear magnetization, active maser oscillation of both species can be maintained indefinitely.

Because of the generally weak interactions of noble-gas atoms with the walls and during atomic collisions, the ^{3}He and ^{129}Xe ensembles can have long Zeeman coherence (T_2) times of hundreds of seconds. It is thus possible to achieve excellent absolute frequency stability with one of the noble-gas masers by using the second maser as a comagnetometer. For example, Zeeman frequency measurements with a sensitivity of $\sim$100 nHz are possible with averaging intervals of about an hour [15]. This two-species noble-gas maser can also serve as a sensitive NMR gyroscope [21]: the above quoted frequency stability implies a rotation sensitivity of 0.13 deg/h.

For the boost-symmetry test, we choose a set of laboratory coordinates (t, x, y, z), such that the $\hat{x}$ axis points south, the $\hat{y}$ axis points east, and the $\hat{z}$ axis points vertically upwards in the laboratory [22]. With the reasonable approximation that the orbit of the Earth is circular, the rotation, $\mathbf{R}$, from the Sun-centered celestial equatorial frame to the standard laboratory frame is given by

$$R^{jJ} = \begin{pmatrix} \cos\chi\cos\omega_\oplus T_\oplus & \cos\chi\sin\omega_\oplus T_\oplus & -\sin\chi \\ -\sin\omega_\oplus T_\oplus & \cos\omega_\oplus T_\oplus & 0 \\ \sin\chi\cos\omega_\oplus T_\oplus & \sin\chi\sin\omega_\oplus T_\oplus & \cos\chi \end{pmatrix}. \quad (2)$$

In this equation, $j = x, y, z$ denotes the spatial index in the laboratory frame, while $J = X, Y, Z$ denotes the spatial index in the Sun-centered frame using celestial equatorial coordinates. The Earth's sidereal angular rotation frequency is $\omega_\oplus \simeq 2\pi/(23\text{ h }56\text{ min})$, and $\chi \simeq 47.6°$ is the colatitude of the laboratory, located in Cambridge, Massachusetts. The time $T_\oplus$ is measured in the Sun-centered frame from the beginning of the sidereal day, which begins when the $\hat{y}$ and $\hat{Y}$ axes align.

The velocity 3-vector of the laboratory in the Sun-centered frame is

$$\vec{\beta} = \beta_\oplus(\sin\Omega_\oplus T, -\cos\eta\cos\Omega_\oplus T, -\sin\eta\cos\Omega_\oplus T). \quad (3)$$

Here, $\Omega_\oplus$ is the angular frequency of the Earth's orbital motion. The time T is measured by a clock at rest at the origin, with $T = 0$ taken at 2:35 AM (U.S. Eastern Standard Time), March 20, 2000 [23]. The angle between the XY celestial equatorial plane and the Earth's orbital plane is $\eta = 23.4°$. We have ignored the laboratory's velocity due to the rotation of the Earth, whose magnitude, $\beta_L = r_\oplus\omega_\oplus\sin\chi/c \simeq 1.1 \times 10^{-6}$ (where $r_\oplus$ is the radius of the Earth), is 2 orders of magnitude smaller than the orbital velocity.

We assume that the Lorentz-violating coefficients of $\vec{\lambda}_\odot$ and $\mathbf{\Lambda}_\odot$ are static and spatially uniform in the Sun frame, at least over the course of a solar year. The corresponding coefficients in the laboratory frame thus acquire a time dependence due to both the Earth's rotation and its revolution around the Sun. We also assume observer Lorentz covariance; hence direct Lorentz transformations yield the coefficients in the laboratory frame.

In the boost-symmetry test, we used the ^{129}Xe maser as a comagnetometer to stabilize the magnetic field, which was oriented along the y axis (i.e., west to east). Thus the leading Lorentz-violating frequency variation of the free-running ^{3}He maser was given by

$$\delta\nu_{\mathrm{He}} = \delta\nu_X\sin\omega_\oplus T_\oplus + \delta\nu_Y\cos\omega_\oplus T_\oplus, \quad (4)$$

where

$$\delta\nu_X = k[\lambda_s + \beta_\oplus(\Lambda_{ss}\sin\Omega_\oplus T + \Lambda_{sc}\cos\Omega_\oplus T)], \quad (5)$$

$$\delta\nu_Y = k[\lambda_c + \beta_\oplus(\Lambda_{cs}\sin\Omega_\oplus T + \Lambda_{cc}\cos\Omega_\oplus T)].$$

Here $\lambda_c, \lambda_s, \Lambda_{ss}, \Lambda_{sc}, \ldots$, are combinations of Sun-frame Lorentz-violating coefficients of $\lambda_\odot$ and $\mathbf{\Lambda}_\odot$, and $k = -8.46 \times 10^{32}$ nHz/GeV [10].

We note that Eqs. (4) and (5) cleanly distinguish the effects of rotation alone (terms proportional to λ_c and λ_s) from the effects of boosts due to the Earth's motion (terms proportional to Λ_{cc}, Λ_{cs}, Λ_{sc}, Λ_{ss}). In addition, these equations indicate that the sensitivity of our experiment to violations of boost-symmetry is reduced by a factor of $\beta_\oplus \simeq 10^{-4}$ with respect to the sensitivity to rotation-symmetry violation. However, for models of Lorentz violation that are isotropic in the frame of the cosmic microwave background [24], our experiment has greater sensitivity to boost-symmetry violation than to rotation-symmetry violation.

As discussed in [10], we acquired noble-gas maser data in four different runs spread over about 13 months (see Fig. 1). Each run lasted about 20 d, and we reversed the direction of the magnetic field after the first $\sim$10 d in each run to help distinguish possible Lorentz-violating effects from diurnal systematic variations. We fit this data to Eq. (4). Table I lists, for each run, the mean values we

determined for $\delta\nu_X$ and $\delta\nu_Y$, the amplitudes of sidereal day modulations of the ^{3}He-maser frequency due to Lorentz-violating coefficients in the $\hat{X}$ and $\hat{Y}$ directions (Sun-centered frame). For each run, $\delta\nu_X$ and $\delta\nu_Y$ correspond to a very good approximation to a single high-precision measurement of the X and Y components of $\delta\nu_{\mathrm{He}}$ performed at the mean time T_j.

Next, we fit the values of $\delta\nu_X$, $\delta\nu_Y$, and T_j in Table I to Eq. (5), thus obtaining the fit parameters reported in Table II and shown graphically in Fig. 1. We treated all fit parameters as independent and we extracted energy bounds for Lorentz-violating coefficients disregarding the possibility of accidental mutual cancellations. This analysis yielded no significant violation of boost invariance, with a limit of about 150 nHz on the magnitude of an annual modulation of the daily sidereal variation in the ^{3}He-maser frequency.

To confirm that our result is consistent with the null hypothesis (i.e., no Lorentz-violating effect), we performed two checks. First, we generated 10 000 faux ^{3}He-maser data sets including sidereal day frequency variations drawn from a normal distribution of zero mean but with standard errors for $\delta\nu_X$ and $\delta\nu_Y$ at each time T_j equal to the corresponding values found in the experiment. For each faux data set, we calculated the χ^2 of the fit to Eq. (5) and found that the value $\chi^2 = 0.30$ from the real experimental data is highly probable for a system in which there is no daily sidereal modulation of the ^{3}He-maser frequency at the experiment's level of sensitivity. In the second check, we performed a series of F tests to estimate the probabilities that the values of the fit parameters, determined from the maser data, arise entirely from statistical fluctuations. For all fit parameters, the F tests yielded probabilities greater than 30%, whereas it is customary to consider that a fit parameter is significantly different from zero only if the F test probability is smaller than 5% or 1%.

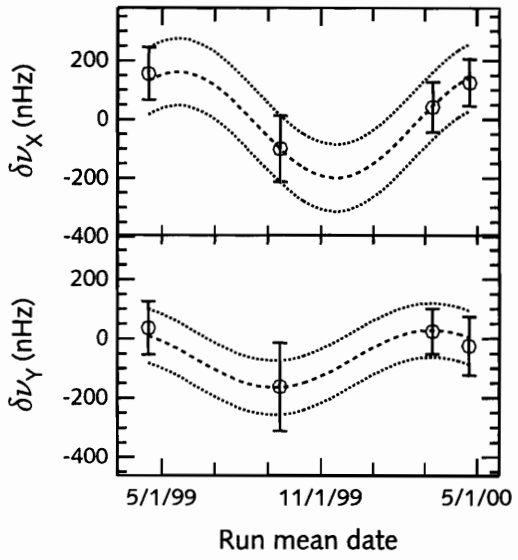

FIG. 1. Time course of the mean values of $\delta\nu_X$ and $\delta\nu_Y$. For each plot the dashed line is the best fit obtained from Eq. (5), using the fit parameters λ_c, λ_s, Λ_{cc}, Λ_{cs}, Λ_{sc}, and Λ_{ss} (see also the fit results in Table II). Dotted lines indicate the 1σ confidence bands for the fit model.

We also performed a series of checks for systematic effects, including sidereal day and year variations in maser temperature and signal amplitude (e.g., driven by variations in the optical-pumping laser). Temperature fluctuations in the ^{3}He and the ^{129}Xe detection circuit can induce small maser-frequency shifts. Accurate temperature monitoring over the course of the 13-month experiment showed a maximum 1.6 mK sidereal day variation of maser temperature, corresponding to a maximum sidereal day ^{3}He-maser-frequency modulation of about 4 nHz, which is an order of magnitude smaller than our statistical sensitivity. A careful analysis of the maser amplitude showed a lack of phase coherence in sidereal day modulations over the 13-month data set, and hence an insignificant systematic sidereal-year variation in the ^{3}He-maser frequency.

To interpret this test of boost invariance, we follow the conventions of Ref. [25], Appendix C, which allows us to relate the maser frequencies to the various SME coefficients for Lorentz and *CPT* violations. In particular, the neutron—and hence the frequency of each noble-gas maser—is sensitive to Lorentz and *CPT* violations controlled by the SME coefficients b_Λ, $d_{\Lambda\Sigma}$, $H_{\Lambda\Sigma}$, and $g_{\Lambda\Sigma\Gamma}$ [17]. Table II shows the corresponding bounds provided by our experiment to combinations of Sun-frame SME coefficients, including the clean limit of $\sim 10^{-27}$ GeV on boost violation.

In conclusion, we used colocated ^{3}He and ^{129}Xe Zeeman masers to perform a high-sensitivity search for a violation of boost invariance of the neutron. We found no significant sidereal annual variation in the free-running ^{3}He-maser frequency at a level of approximately 150 nHz. This result provides the first clean test of boost symmetry for a fermion, and, in the context of the general standard-model extension, places a bound of about 10^{-27} GeV on 11 previously unexplored coefficients among the 44 coefficients describing possible leading-order Lorentz- and *CPT*-violating couplings of the neutron. Significant improvements may be possible with a

TABLE I. Mean and standard error of the two quadratures $\delta\nu_X$ and $\delta\nu_Y$ of the sidereal day ^{3}He-maser-frequency modulations, for each of four runs. T_j indicates the mean date of the jth run.

T_j	$\delta\nu_X$ (nHz)	$\delta\nu_Y$ (nHz)
4/15/99	156 ± 90	37 ± 90
9/15/99	-100 ± 112	-162 ± 148
3/10/00	42 ± 86	25 ± 76
4/22/00	125 ± 80	-25 ± 99

TABLE II. Limits from the present work on Lorentz violation of the neutron, expressed in terms of (i) the fit parameters of Eqs. (4) and (5), i.e., coefficients for the general Lorentz-symmetry-violating vector $\vec{\lambda}_\odot$ and $\Lambda_\odot$ (both in the Sun frame); and (ii) combinations of Sun-frame SME coefficients for Lorentz and *CPT* violation (defined in Appendix B of Ref. [18]). Bounds on rotation-symmetry violation are set by the limits on λ_c and λ_s, whereas bounds on boost-symmetry violation are determined from Λ_{cc}, Λ_{cs}, Λ_{ss}, and Λ_{sc}.

Measurable combinations of SME coefficients	Fit parameters	Fit results (GeV)
$\tilde{b}_Y - 0.0034\tilde{d}_Y + 0.0034\tilde{g}_{DY}$	λ_c	$(8.0 \pm 9.5) \times 10^{-32}$
$-\tilde{b}_X + 0.0034\tilde{d}_X - 0.0034\tilde{g}_{DX}$	λ_s	$(2.2 \pm 7.9) \times 10^{-32}$
$-\cos\eta[(\frac{1}{2}\tilde{b}_T + \frac{1}{2}\tilde{d}_- - \tilde{g}_c - \frac{1}{2}\tilde{g}_T) + (\tilde{g}_T - 2\tilde{d}_+ + \frac{1}{2}\tilde{d}_Q)] + \sin\eta(\tilde{d}_{YZ} - \tilde{H}_{XT})$	Λ_{cc}	$(-1.1 \pm 1.0) \times 10^{-27}$
$-\tilde{H}_{ZT}$	Λ_{cs}	$(0.2 \pm 1.8) \times 10^{-27}$
$[(\frac{1}{2}\tilde{b}_T + \frac{1}{2}\tilde{d}_- - \tilde{g}_c - \frac{1}{2}\tilde{g}_T) - (\tilde{g}_T - 2\tilde{d}_+ + \frac{1}{2}\tilde{d}_Q)]$	Λ_{ss}	$(-1.8 \pm 1.9) \times 10^{-27}$
$\cos\eta(\tilde{H}_{ZT} - \tilde{d}_{XY}) - \sin\eta\tilde{H}_{YT}$	Λ_{sc}	$(-1.1 \pm 0.8) \times 10^{-27}$

^{21}Ne/^{3}He Zeeman maser [26], with masers located on a rotating table [27], or with space-based clocks [28].

We acknowledge support from NASA Grants No. NAG8-1784, No. NAG3-2878, No. NAG3-2194, and No. NAG8-1770, DOE Grant No. DE-FG02-91ER40661, and the Smithsonian Institution.

[1] R. J. Kennedy and E. M. Thorndike, Phys. Rev. **42**, 400 (1932).
[2] D. Hils and J. L. Hall, Phys. Rev. Lett. **64**, 1697 (1990); J. A. Lipa *et al.*, Phys. Rev. Lett. **90**, 060403 (2003); H. Müller *et al.*, Phys. Rev. Lett. **91**, 020401 (2003).
[3] D. Colladay and V. A. Kostelecký, Phys. Rev. D **55**, 6760 (1997); **58**, 116002 (1998); V. A. Kostelecký and R. Lehnert, Phys. Rev. D **63**, 065008 (2001); V. A. Kostelecký, Phys. Rev. D **69**, 105009 (2004).
[4] KTeV Collaboration, H. Nguyen, in *CPT and Lorentz Symmetry II*, edited by V. A. Kostelecký (World Scientific, Singapore, 2002); OPAL Collaboration, R. Ackerstaff *et al.*, Z. Phys. C **76**, 401 (1997); BELLE Collaboration, K. Abe *et al.*, Phys. Rev. Lett. **86**, 3228 (2001); *BABAR* Collaboration, B. Aubert *et al.*, hep-ex/0303043; FOCUS Collaboration, J. M. Link *et al.*, Phys. Lett. B **556**, 7 (2003); V. A. Kostelecký, Phys. Rev. Lett. **80**, 1818 (1998); Phys. Rev. D **61**, 016002 (2000); **64**, 076001 (2001).
[5] S. M. Carroll *et al.*, Phys. Rev. D **41**, 1231 (1990); V. A. Kostelecký and M. Mewes, Phys. Rev. Lett. **87**, 251304 (2001).
[6] H. Dehmelt *et al.*, Phys. Rev. Lett. **83**, 4694 (1999); R. Mittleman *et al.*, Phys. Rev. Lett. **83**, 2116 (1999); G. Gabrielse *et al.*, Phys. Rev. Lett. **82**, 3198 (1999); R. Bluhm *et al.*, Phys. Rev. Lett. **82**, 2254 (1999); **79**, 1432 (1997); Phys. Rev. D **57**, 3932 (1998).
[7] B. Heckel, in *CPT and Lorentz Symmetry II*, edited by V. A. Kostelecký (World Scientific, Singapore, 2002); L.-S. Hou *et al.*, Phys. Rev. Lett. **90**, 201101 (2003); R. Bluhm and V. A. Kostelecký, Phys. Rev. Lett. **84**, 1381 (2000).
[8] V. W. Hughes *et al.*, Phys. Rev. Lett. **87**, 111804 (2001); R. Bluhm *et al.*, Phys. Rev. Lett. **84**, 1098 (2000).
[9] V. W. Hughes *et al.*, Phys. Rev. Lett. **4**, 342 (1960); T. E. Chupp *et al.*, Phys. Rev. Lett. **63**, 1541 (1989).
[10] D. Bear *et al.*, Phys. Rev. Lett. **85**, 5038 (2000); **89**, 209902 (2002).
[11] D. F. Phillips *et al.*, Phys. Rev. D **63**, 111101 (2001).
[12] V. A. Kostelecký and S. Samuel, Phys. Rev. D **39**, 683 (1989); Phys. Rev. Lett. **63**, 224 (1989); Phys. Rev. D **40**, 1886 (1989); V. A. Kostelecký and R. Potting, Nucl. Phys. **B359**, 545 (1991); Phys. Rev. D **51**, 3923 (1995).
[13] For reviews of approaches to Lorentz and *CPT* violation, see, for example, *CPT and Lorentz Symmetry I*, edited by V. A. Kostelecký (World Scientific, Singapore, 1999); *CPT and Lorentz Symmetry II*, edited by V. A. Kostelecký (World Scientific, Singapore, 2002).
[14] R. E. Stoner *et al.*, Phys. Rev. Lett. **77**, 3971 (1996).
[15] D. Bear *et al.*, Phys. Rev. A **57**, 5006 (1998).
[16] C. J. Berglund *et al.*, Phys. Rev. Lett. **75**, 1879 (1995); L. R. Hunter *et al.*, in *CPT and Lorentz Symmetry I*, edited by V. A. Kostelecký (World Scientific, Singapore, 1999).
[17] V. A. Kostelecký and C. D. Lane, Phys. Rev. D **60**, 116010 (1999).
[18] R. Bluhm *et al.*, Phys. Rev. D **68**, 125008 (2003).
[19] The sidereal-year lasts 365 d, 6 h, 9 min, and 9.5 s.
[20] T. E. Chupp *et al.*, Phys. Rev. A **38**, 3998 (1988); G. D. Cates *et al.*, Phys. Rev. A **45**, 4631 (1992).
[21] K. F. Woodman *et al.*, J. Navig. **40**, 366 (1987).
[22] The coordinate system adopted here differs from that used in our earlier work, Ref. [10].
[23] At this instant, Earth crossed the equatorial plane during the vernal equinox. T and $T_\oplus$ are equivalent, modulo the sidereal day period.
[24] An example of such a model expressed in terms of standard-model extension coefficients consists of two background tensor fields (b_Λ and $d_{\Lambda\Sigma}$) with the following simple relationships: $d_{XX} = d_{YY} = d_{ZZ}$, $d_{TT} = 3d_{XX}$, $b_T = 4md_{XX}$, where m is the mass of the neutron and all other terms are zero. For this model, our experiment has an order of magnitude greater sensitivity to boost-symmetry violation than to rotation-symmetry violation, despite the factor of $\beta_\oplus \simeq 10^{-4}$.
[25] V. A. Kostelecký and M. Mewes, Phys. Rev. D **66**, 056005 (2002).
[26] R. E. Stoner and R. L. Walsworth, Phys. Rev. A **66**, 032704 (2002).
[27] Successful tests of Lorentz symmetry have been performed using rotating tables. See, e.g., Ref. [7].
[28] R. Bluhm *et al.*, Phys. Rev. Lett. **88**, 090801 (2002).

Bibliography

[1] F. Canè, D. Bear, D. F. Phillips, M. S. Rosen, C. L. Smallwood, R. E. Stoner, R. L. Walsworth, and V. A. Kostelecký, Phys. Rev. Lett. **93**, 230801 (2004).

[2] T. Chupp, R. Hoare, R. Walsworth, and B. Wu, Phys. Rev. Lett. **72**, 15 (1994).

[3] R. Stoner, M. Rosenberry, J. Wright, T. Chupp, E. Oteiza, and R. Walsworth, Phys. Rev. Lett. **77**, 3971 (1996).

[4] D. Bear, T. E. Chupp, K. Cooper, S. DeDeo, M. Rosenberry, R. E. Stoner, and R. L. Walsworth, Phys. Rev. A **57**, 5006 (1998).

[5] T. E. Chupp, E. R. Oteiza, J. M. Richardson, and T. R. White, Phys. Rev. A **38**, 3998 (1988).

[6] T. G. Walker and W. Happer, Reviews of Modern Physics **69**, 2 (1997).

[7] G. Cates, R. Fitzgerald, A. Barton, P. Bogorad, M. Gatzke, N. Newbury, and B. Saam, Phys. Rev. A **49**, 4631 (1992).

[8] E. R. Oteiza, Ph.D. thesis, Harvard University, 1992.

[9] D. Colladay and V. A. Kostelecký, Phys. Rev. D **55**, 6760 (1997).

[10] D. Colladay and V. A. Kostelecký, Phys. Rev. D **58**, 116002 (1998).

[11] V. Kostelecký and R. Lehnert, Phys. Rev. D **63**, 065008 (2001).

[12] V. A. Kostelecký, Phys. Rev. D **69**, 105009 (2004).

[13] O. W. Greenberg, Phys. Rev. Lett. **89**, 231602 (2002).

[14] O. W. Greenberg, Phys. Lett. B **567**, 179 (2003).

[15] V. Kostelecký and S. Samuel, Phys. Rev. D **39**, 683 (1989).

[16] V. Kostelecký and S. Samuel, Phys. Rev. Lett. **63**, 224 (1989).

[17] V. Kostelecký and S. Samuel, Phys. Rev. D **40**, 1886 (1989).

[18] V. Kostelecký and R. Potting, Nucl. Phys. B **359**, 545 (1991).

[19] V. Kostelecký and R. Potting, Phys. Rev. D **51**, 3923 (1995).

[20] *CPT and Lorentz Symmetry I, II*, edited by V. Kostelecký (World Scientific, Singapore, 1999, 2002).

[21] V. A. Kostelecký and C. D. Lane, Phys. Rev. D **60**, 116010 (1999).

[22] D. F. Phillips, M. A. Humphrey, E. M. Mattison, R. E. Stoner, R. F. C. Vessot, and R. L. Walsworth, Phys. Rev. D **63**, 111101 (2001).

[23] R. Bluhm, V. Kostelecký, and N. Russell, Phys. Rev. Lett. **82**, 2254 (1999).

[24] D. Bear, R. E. Stoner, R. L. Walsworth, V. Kostelecký, and C. D. Lane, Phys. Rev. Lett. **85**, 5038 (2000).

[25] D. Bear, R. E. Stoner, R. L. Walsworth, V. Kostelecký, and C. D. Lane, Phys. Rev. Lett. **89**, 209902 (2002).

[26] W. Happer and W. Wijngaarden, Hyperfine Interactions **38**, 435 (1987).

[27] A. Baranga, S. Appelt, M. Romalis, C. Erickson, A. Young, G. Cates, and W. Happer, Phys. Rev. Lett. **80**, 13 (1998).

[28] J. Vanier and C. Audoin, *The Quantum Physics of Atomic Frequency Standards* (IOP Publishing, Ltd., Bristol, 1989).

[29] M. V. Romalis, Ph.D. thesis, Princeton University, 1997.

[30] M. A. Rosenberry, Ph.D. thesis, University of Michigan, 1999.

[31] E. Condon, Physical Review **43**, 648 (1933).

[32] T. Stein, J. Carrico, E. Lipworth, and M. Weisskopf, Physical Review **2**, 1093 (1970).

[33] B. Chann, I. A. Nelson, L. Anderson, B. Driehuys, and T. G. Walker, Phys. Rev. Lett. **88**, 113201 (2002).

[34] D. C. Bear, Ph.D. thesis, Harvard University, 2000.

[35] G. Cates, S. Schaefer, and W. Happer, Phys. Rev. A **37**, 2877 (1988).

[36] T. W. Kornack and M. V. Romalis, Physical Review Letters **89**, 253002 (2002).

[37] R. E. Stoner, Appendix A, Ref. [34].

[38] H. Goldstein, *Classical Mechanics* (Addison–Wesley, New York, 1981), Sect. 7.2.

[39] V. Kostelecký and S. Samuel, Phys. Rev. Lett. **66**, 1811 (1991).

[40] L. Ryder, *Quantum Field Theory* (Cambridge University Press, Cambridge, 1996), Sect. 2.5.

[41] D. Linde, *CRC Handbook of Chemistry and Physics* (CRC press, Boca Raton, 2004).

[42] L. Foldy and S. Wouthuysen, Phys. Rev. **78**, 29 (1950).

[43] V. A. Kostelecký and C. D. Lane, preprint IUHET 404 (April 1999).

[44] T. Schmidt, Z. Physik **106**, 358 (1937).

[45] V. A. Kostelecký and M. Mewes, Phys. Rev. D **69**, 016005 (2004).

[46] J. D. Jackson, *Classical Electrodynamics* (John Wiley and Sons, New York, 1999), Sect. 11.7.

[47] P. Wolf, S. Bize, A. Clairon, G. Santarelli, M. E. Tobar, and A. N. Luiten, Phys. Rev. D **70**, 051902 (2004).

[48] C. D. Lane, Phys. Rev. D **72**, 016005 (2005).

[49] G. Saathoff, S. Karpuk, U. Eisenbarth, G. Huber, S. Krohn, R. M. Horta, S. Reinhardt, D. Schwalm, A. Wolf, and G. Gwinner, Phys. Rev. Lett. **91**, 190403 (2003).

[50] L.-S. Hou, W.-T. Ni, and Y.-C. M. Li, Phys. Rev. Lett. **90**, 201101 (2003).

[51] R. Bluhm and V. Kostelecký, Phys. Rev. Lett. **84**, 1381 (2000).

[52] H. Muller, S. Herrmann, C. Braxmaier, S. Schiller, and A. Peters, Phys. Rev. Lett. **91**, 020401 (2003).

[53] H. Muller, Phys. Rev. D **71**, 045004 (2005).

[54] P. Wolf, F. Chapelet, S. Bize, and A. Clairon, hep-ph/0509329, 2005.

[55] R. J. Kennedy and E. Thorndike, Phys. Rev. **42**, 400 (1932).

[56] R. P. Feynman, R. B. Leighton, and M. Sands, *The Feynman Lectures on Physics, Vol. 1* (Addison–Wesley, Redwood City, CA, 1989), Sects. 15–2 and 15–3.

[57] D. Hils and J. Hall, Phys. Rev. Lett. **64**, 1697 (1990).

[58] J. A. Lipa, J. A. Nissen, S. Wang, D. A. Stricker, and D. Avaloff, Phys. Rev. Lett. **90**, 060403 (2003).

[59] K. Woodman, P. Franks, and M. Richards, J. Navig. **40**, 366 (1987).

[60] Sect. 11.8 in Ref. [46].

[61] S. Weinberg, *Gravitation and Cosmology* (John Wiley and Sons, New York, 1972), Sect. 3.1.

[62] L. Schiff, Phys. Rev. Lett. **4**, 215 (1960).

[63] L. Schiff, Proc. Nat. Acad. Sci. **46**, 871 (1960).

[64] B. Heckel in Ref. [20].

[65] C. B. Alcock, V. P. Itkin, and M. K. Horrigan, Canadian Metallurgical Quarterly **23**, 309 (1984).

[66] T. J. Killian, Phys. Rev. **27**, 578 (1926).

[67] D. Phillips, G. Wong, D. Bear, R. Stoner, and R. Walsworth, Rev. Sci. Inst. **70**, 2905 (1999).

[68] R. Stoner and R. Walsworth, Phys. Rev. A **66**, 032704 (2002).

[69] J. P. Holman, *Heat Transfer* (McGraw-Hill, New York, 1968).

[70] M. Wagshul and T. Chupp, Phys. Rev. A **49**, 3854 (1994).

[71] C. C. Bouchiat and M. A. Bouchiat, Phys. Rev. A **2**, 1274 (1970).

[72] S. Chapman and T. G. Cowling, *The Mathematical Theory of Non-uniform Gases* (Cambridge University Press, Cambridge, 1970).

[73] E. W. Weisstein. *Bessel Function of the Second Kind.* From MathWorld. A Wolfram Web Resource, http://mathworld.wolfram.com/.

[74] W. H. Press, B. P. Flannery, S. A. Teukolsky, and W. T. Vetterling, *Numerical Recipes in Fortran 77* (Cambridge University Press, Cambridge, 1992), Sect. 19.5.

[75] M. Romalis and W. Happer, Phys. Rev. A **60**, 1385 (1999).

[76] J. A. Stratton, *Electromagnetic Theory* (McGraw–Hill, New York, 1941).

[77] G. P. Wong. *Manual for coating glass cells with OTS*, http://www.cfa.harvard.edu/Walsworth/Papers/OtherDocuments.html.

[78] M. S. Rosen, Ph.D. thesis, University of Michigan, 2000.

[79] M. Romalis, E. Miron, and G. Cates, Phys. Rev. A **56**, 4569 (1997).

[80] P. T. Callaghan, *Principles of Nuclear Magnetic Resonance Microscopy* (Oxford University Press, Oxford, 1991).

[81] H. Ott, *Noise Reduction Techniques in Electronic Systems* (John Wiley and Sons, New York, 1988).

[82] A. Abragham, *Principles of Magnetic Resonance* (Oxford University Press, Oxford, 1961).

[83] S. R. Schaefer, G. D. Cates, T. Chien, D. Gonatas, W. Happer, and T. G. Walker, Phys. Rev. A **39**, 5613 (1989).

[84] M. V. Romalis and G. D. Cates, Phys. Rev. A **58**, 3004 (1998).